Far-Ultraviolet Spectroscopy of Saturn's Moons Rhea and Dione

Thesis

Far-Ultraviolet Spectroscopy of Saturn's Moons Rhea and Dione

Submitted for the degree of Doctor of Philosophy

in Astronomy and Astrophysics

R. Mark Elowitz, BSc, MSc

Submitted October 2018

Declaration

I hereby declare that, except where explicit attribution is made, the work presented in this thesis is entirely my own.

Robert Mark Elowitz

Abstract

This thesis presents the first analysis of spatially resolved, far-UV reflectance spectra of Saturn's icy satellites Rhea and Dione collected by the Cassini Ultraviolet Imaging Spectrograph (UVIS) during targeted flybys. The objective of this geochemical survey of Rhea's and Dione's leading and trailing hemispheres is to identify and explain the broad absorption feature centred near 184 nanometres. The secondary objective is to determine the presence of any minor impurities within the ice layers of these satellites by characterizing the location in wavelength space and shape of the 165-nm absorption edge due to pure water ice. To determine the precise position of the mid-point of the absorption edge, derivative spectroscopy is applied to the Cassini UVIS spectra. The presence of any non-water-ice molecules within the ice matrix and/or changes in the structure of the ice grains should cause a shift from the nominal position of the 165-nm absorption edge, or alter the slope of the absorption edge. The 165-nm absorption edge and 184-nm absorption feature have been observed in disk-integrated spectra of Rhea and other icy satellites in the Saturnian system. However, as of to date, there has been no satisfactory explanation for the 184 nm absorption feature. Cassini UVIS reflectance spectra are compared with modelled spectra derived using far-UV spectra of thin-ice specimens collected in laboratory experiments and Hapke theory. The results of the modelling show that the UVIS observations can be modelled by two molecules: simple chloromethanes beneath a layer of water ice or hydrazine monohydrate mixed in solid phase with water ice. A detailed analysis based on the astrochemistry and geomorphology of Rhea and Dione show that chloromethane molecules on their surfaces is difficult to explain, since their presence would require active subsurface oceans and an extensive network of fractures through their thick ice shells. On the other hand, hydrazine monohydrate is easier to explain since it can be produced via irradiation of ammonia ice by

energetic particles originating from Saturn's magnetosphere environment. It is also shown in the research that hydrazine can also be produced on Saturn's largest moon Titan by irradiation of ammonia ice, or by chemical reactions involving water-ice and solid ammonia ice. Several possible alternative scenarios based on an analysis of both sinks and sources of chloromethane molecules and hydrazine are presented in this thesis.

Acknowledgments

I dedicate this thesis to my mother and brothers, whose gracious support, both financially and in spirit, provided me the ability to successfully complete my research.

The following people deserve my thanks for providing the support needed to accomplish this research.

My supervisors, Professor Nigel Mason and Dr. Amanda Hendrix, for their advice and guidance. Their help has allowed me to complete this thesis in a timely matter without any significant issues or problems. I am grateful to Professor Mason for financial support allowing me to make visits to The Open University campus as required by my research degree program.

Many thanks to Dr. Bhalamurugan Silvaraman and his team for providing laboratory data used in this work.

Finally, to the administrative staff of the Research Degree Office at The Open University that provided assistance with logistics in support of my doctorate degree.

Table of Contents

List of Tables

List of Figures

CHAPTER 1

INTRODUCTION

Rhea and Dione are two of Saturn's mid-sized satellites and have been subject of the Voyager mission and several close flybys during the recent Cassini-Huygens mission. Voyager discovered several bright streaks that were interpreted as ice that evolved from the interiors of Rhea and Dione along fractures in their ice shells (Birnbaum, 1982). Subsequent flybys showed that these bright streaks were actually fracture cliffs with fresh water-ice exposed as darker material falls off of their walls. The fractures may have been the result of past endogenic activity on Rhea and Dione. The Voyager flyby of Saturn's moons showed the icy moons of Saturn to be heavily cratered, with the exception of Enceladus (Birnbaum, 1982). Imagery from Voyager showed a variation in crater density on several of the icy bodies, which implied either a non-uniform distribution in the impactors, or possible or subsequent surface modification. The extensive white wispy streaks discovered on Dione during the Voyager flyby of Saturn were, at the time, interpreted to be large fractures in the moon's ice crust through which water has escaped, and refroze as frost. The fractures, grooves and bright streaks (bright, linear or curved lineaments) found on Voyager imagery of Dione and Rhea were interpreted to be due to possible past endogenic activity and/or volcanism that deposited liquid (or pyroclastic) material along fissures and fractures on the two satellites (Smith *et al*., 1981, 1982; Plescia, 1983; Stone & Miner, 1981). However, recent Cassini Imaging Science Subsystem (ISS) (Porco *et al*., 2004) high-resolution imagery confirmed the major geological features imaged by the Voyager spacecraft (Wagner *et al*., 2005) and showed that the bright streaks were the result of dark material falling off the walls of the fractures, exposing fresh water ice. Recent Cassini flybys of mid-sized icy satellites showed the twin satellites Rhea and Dione to be ice-covered bodies that orbit Saturn with a velocity that is slower relative to

the co-orbiting plasma generated in Saturn's magnetosphere. Thus, the moon's trailing hemisphere is preferentially irradiated by plasma and cold ions while the leading hemisphere is irradiated with neutral particles and possible E-ring material. Radiolysis, micrometeoroid bombardment, melting/vaporization, and sputtering of icy satellite surfaces (Figure 1.1) leads to physical and chemical changes in the nascent ices as well as producing defects (e.g. bubbles and voids) (Johnson & Quickenden, 1997). In particular water-ice and organic molecules in the ice can be dissociated by energetic electrons and other high-energy particles, leading to the formation of more complex molecules (Cooper *et al*. 2008; Cassidy, *et al*. 2010).

These physical and chemical transformations may be observed by monitoring the UV and IR spectra of the satellite's icy surfaces by spacecraft (Hendrix & Hansen, 2008). UV spectroscopy provides unique information about the molecular structure and electronic transitions of chemical species, and such spectra are sensitive to variations due to their chemical bonding, molecular environments and molecular conformations. Therefore, it may be possible to characterize the chemical composition and structure of the surface "regolith" of planetary bodies through identification of chemical species by comparing spectra recorded under analogous laboratory conditions with spectra recorded by spacecraft. Many molecules that are suspected to be present in the icy surfaces of moons in the outer solar system (Dalton, 2008) have broad absorption features due to electronic transitions that occur in the far-UV portion of the spectrum. To determine which molecular species might be present within the upper ice layers on Rhea and Dione, modelled spectra derived from laboratory measurements of thin-ice samples should be compared with UVIS spectra collected under conditions similar to those encountered at the surface of Rhea.

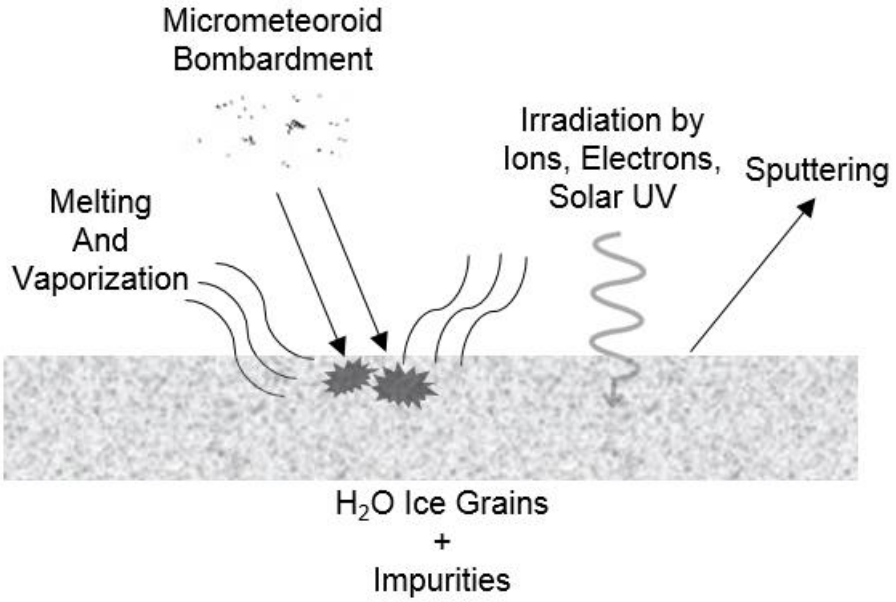

Figure 1.1: Processes that occur on the surfaces of icy satellites in the Saturnian environment. Bombardment of icy surfaces of satellites by charged particles and micrometeorites all contribute to the spectral signature of reflected light. In laboratory experiments, I can simulate the effects of charged particle bombardment on ice. It is also possible to conduct experiments that simulate bombardment of ice samples by small micrometeorites. Figure adapted from Figure 1, J. Geophys. Res. Planets, 121, 1865-1884.

1.1 Rhea and Dione

The "regolith" of Rhea and Dione is dominated by water-ice as evident by the steep absorption edge seen in full-disk integrated spectra in the far-ultraviolet (far-UV) region of the spectrum (see Chapter 5). The absorption edge occurs near a wavelength of 165 nanometres (nm), with a strength that depends on the size of the ice grains and degree of contaminants within the ice matrix. The far-UV reflectance spectra of Rhea and Dione also show a weak, broad absorption feature centred near 184 nm. This absorption feature has been reported in previous disk-integrated observations of several icy satellites (e.g. Phoebe; Hendrix & Hansen, 2008) in the Saturnian system, but, to date, its origin has not been explained. The 184-nm absorption feature observed in Phoebe (Figure 1.2) does not appear to be explained by various ice mixtures of water, tholins, carbon, kerogen, or poly-HCN (Hendrix & Hansen, 2008).

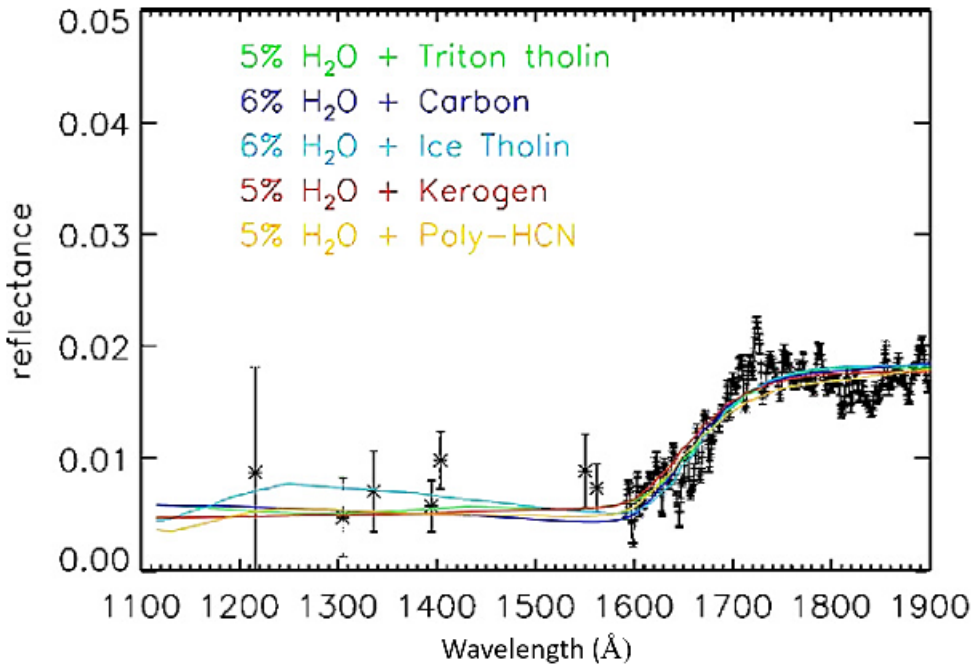

Figure 1.2: Model spectral fits to Cassini UVIS spectra of Phoebe show that tholins, carbon, kerogen, poly-HC cannot explain the 184-nm absorption feature. Figure from Hendrix & Hansen 2008.

A similar absorption feature has been reported in carbonaceous chondrite meteorites (Wagner, *et al*. 1987), which could be due to the presence of phyllosilicates and hydrated minerals. Since no laboratory absorbance measurements of these minerals were collected in the lab in support of this research, it was not possible to compare spectra of phyllosilicates and hydrated minerals with Cassini UVIS data. An absorption feature, similar to the 184-nm feature seen in the far-UV spectra of Rhea and Dione, has been previously reported in water-ice (Pipes *et al*., 1974; Wagner *et al*., 1987). However, it should be noted that the optical constants for hexagonal and amorphous water-ice derived by Warren (1984) are very sparse for wavelengths greater than 170 nm, placing constraints on the accuracy of modelled spectra of these types of ice. It is therefore not possible to determine if the 184-nm absorption feature is actually due to the structure of water-ice. For these reasons, it is postulated that the 184-nm absorption feature seen in the disk-integrated spectra of Rhea and Dione is due to a non-organic UV absorber. In this research, I present for the first time spatially-resolved far-UV spectra of the icy surfaces of Saturn's moons

Rhea and Dione. I further show that the 184-nm absorption feature can be explained by two inorganic molecules, including simple chloromethane molecules and hydrazine monohydrate.

CHAPTER 2

THE SATURNIAN SYSTEM AND ITS ICY MOONS

2.1 Overview of the Saturnian System

The planet Saturn is the sixth planet from the Sun with a perihelion of approximately 9.54 astronomical units (with 1 AU equal to the mean distance between the Sun and Earth), and an aphelion distance of about 10 AU (JPL Horizons: https//ssd.jpl.nasa.gov). The mean equatorial radius of Saturn at the one-bar surface level is 60268±4 km (Seidelmann, *et al*. 2006). The rapid rotation of Saturn with a period of 10h 39m 22.4s (JPL Horizons) and fluid state results in a high degree of flattening with a value of 0.09796 (JPL Horizons). Saturn also has the lowest density of all the planets in the Solar System, with a value less than water. Saturn's outer layers are composed of approximately 76% hydrogen and 21.5% helium, with trace amounts of water, ammonia, and methane, similar to the primordial solar nebula composition (Fortney & Hubbard, 2003). The interior of Saturn is at high enough pressure to form liquid metallic hydrogen and a molecular hydrogen layer. The liquid metallic hydrogen is thought to be responsible for the generation of Saturn's magnetic field, through a dynamo process created from the resulting conductivity (Hubbard and Smoluchowski, 1973; Celliers, *et al*. 2018). The magnetosphere is the origin of energetic electrons and protons that irradiate the surfaces of Saturn's icy satellites, causing complex chemical reactions to take place. Like Jupiter, Saturn radiates more energy than it receives from the Sun. The likely cause is due to the Kelvin-Helmholtz mechanism – i.e. gravitational potential energy. However, this mechanism can't explain the total amount of energy radiated by Saturn. One possibility is that of "helium rainout" (i.e. the helium is miscible in the hydrogen) that occurs deep inside Saturn's interior. The falling helium releases additional energy (i.e. conversion of potential to kinetic energy due to the falling helium droplets, and release of latent heat due to condensation of helium in

Saturn's interior) that can account for Saturn's total radiated energy output (Fortney & Hubbard, 2003). A solid core composed of rock and/or ice is expected to exist at the centre of Saturn. The mass of the core is predicted to be between 15 and 20 Earth masses (Hubbard *et al*. 2009).

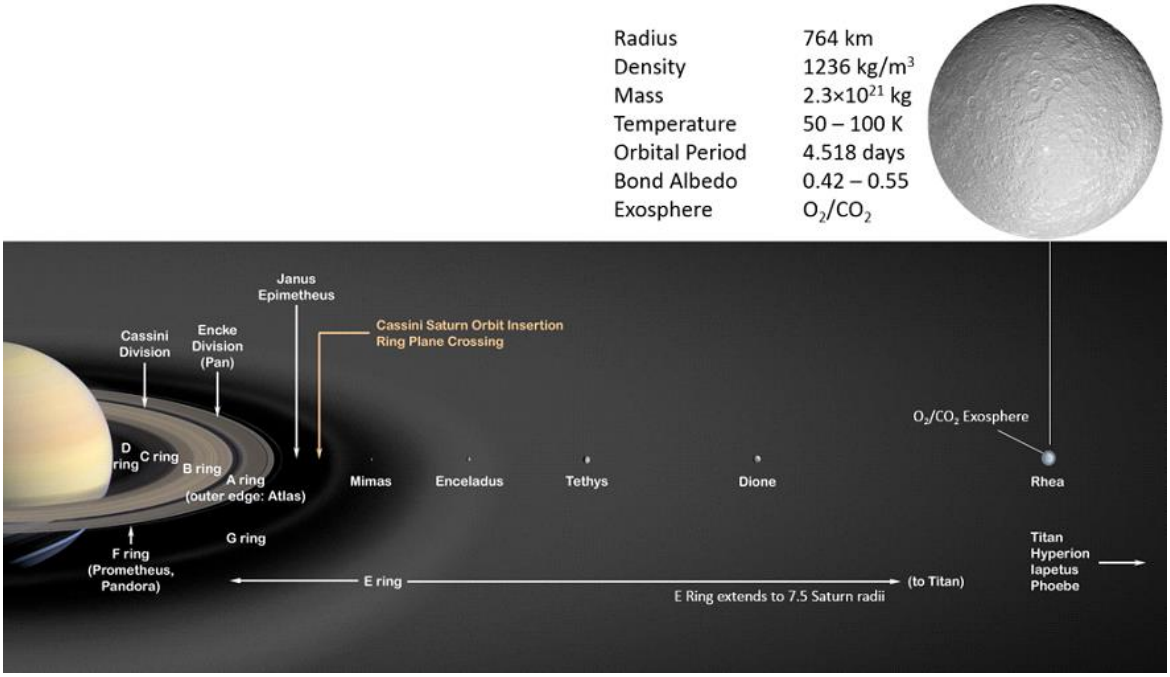

Figure 2.1: Diagram showing the location of three mid-sized icy satellites in the Saturnian system. Tethys, Dione and Rhea share similar surface features, but Rhea is located at greater distances than the other two mid-sized moons. Thus, Rhea received less irradiation from Saturn's plasma environment. The small icy moon Enceladus orbits within Saturn's E ring and is the source of the ring's icy particles. Part of the ejected material from Enceladus does not fall back onto its surface, but instead provides a source of ice grains to the E ring. Saturn's second largest moon Rhea orbits at the outer boundary of the E ring. Figure courtesy of NASA/JPL. Modified by R. Mark Elowitz.

The most spectacular feature of the Saturnian system (Figure 2.1) is the planet's extensive ring system. In contrast to the tenuous D, E, and G rings, Saturn's main rings A, B, C, and F all have large optical depths (>0.1) (Nicholson, *et al*. 2000). These rings have a radial extent that range between 1.2 to 2.3 Saturn radii. Both Voyager and Cassini observed permanent and transient structures within the rings, with the later due to gravitational interactions between small moons and ring particles (Jerousek, *et al*. 2016). The composition of the main rings is primarily water-ice. The composition of Saturn's E

ring is dominated by small water-ice grains of centimetre size and above with minor amounts of silicates, ammonia, carbon dioxide molecular nitrogen, hydrocarbons, and possibly carbon monoxide as measured by Cassini's Cosmic Dust Analyser/Mass Spectrometer (Hillier, *et al*. 2007). Similar to the sparse O_2 and H_2 atmospheres of the rings created by solar UV light dissociating water-ice molecules, an OH atmosphere is produced when high-energy ions ejected from Enceladus irradiate water-ice molecules (Johnson, *et al*. 2006). The small moon Enceladus (radius of ~504 km) plays a significant role in the Saturnian system. Its south polar plumes of water-ice grains (Figure 2.2) and gas particles experience dissociation, ionization, sputtering and acceleration (Bagenal and Delamere 2011, Cravens *et al*. 2011).

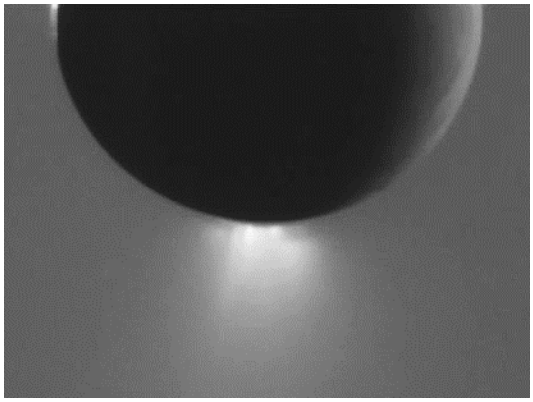

Figure 2.2: Cassini ISS image showing the plumes of Enceladus. The view shows the leading hemisphere of Enceladus with the north pole oriented up. The image was obtained at a high solar phase angle of 149 degrees, and the spatial resolution of the image is 2 km. The image was collected on May 10, 2015. Figure courtesy of NASA/JPL/Space Sciences Institute.

2.1.1 Saturn's Icy Satellites

Saturn has over 60 satellites, ranging from small irregular moons, to mid-sized icy moons, to Saturn's largest moon Titan hosting a thick atmosphere with a pressure of about 1.5 bars composed mostly of molecular nitrogen and methane (Carrasco, *et al*. 2018). The mid-sized moons of Saturn all share common properties. These moons are all dominated by water-ice on their surfaces (as revealed by the steep 165-nm absorption edge observed

in far-UV spectra; Hendrix, *et al*. 2018; Hendrix and Hansen, 2008) and in their interiors, which leads to low mean densities that range between approximately 1.0 g/cm^3 to about 1.6 g/cm^3.

Rhea is Saturn's second largest moon with a mean radius of 763.8±1 km and a mean density of 1.236±0.005 g/cm^3 (Roatsch et al. 2009). Rhea orbits Saturn at a radial distance of about 8.75 Saturn radii with a velocity of 8.48 km/s (calculated from Rhea's radial distance from Saturn) that is slower relative to the co-orbiting plasma (65.5 km/s for the azimuthal component; Roussos et al. 2008) generated in Saturn's magnetosphere. The surface temperature of Rhea ranges from about 40 K to 100 K (Teolis, et al. 2011) such that it is composed of an ice mantle with a high visible geometric albedo of 0.949±0.003 (Verbiscer, A., et al. 2007). This albedo is consistent with a surface composed mostly of water ice, a hypothesis supported by the measurement of infrared absorption features; e.g. Fink et al., 1976).

Saturn's moon Dione orbits closer to Saturn than Rhea (Figure 2.1). The mass density of Dione is higher than that of Rhea, at 1.478±0.003 g/cm^3 and its mean radius of 561.4±0.4 km (Roatsch et al. 2009) is smaller than Rhea. Dione has a wide range of geomorphology, including tectonic fractures, terrain of varying crater densities, and a tenuous exosphere composed of O_2 and CO_2, similar to Rhea (Teolis and Waite, 2016). One of the most spectacular features of Dione are the bright pattern of icy cliffs (Figure 2.3), which may indicate that the satellite experienced tidal stresses over geologically long periods of time.

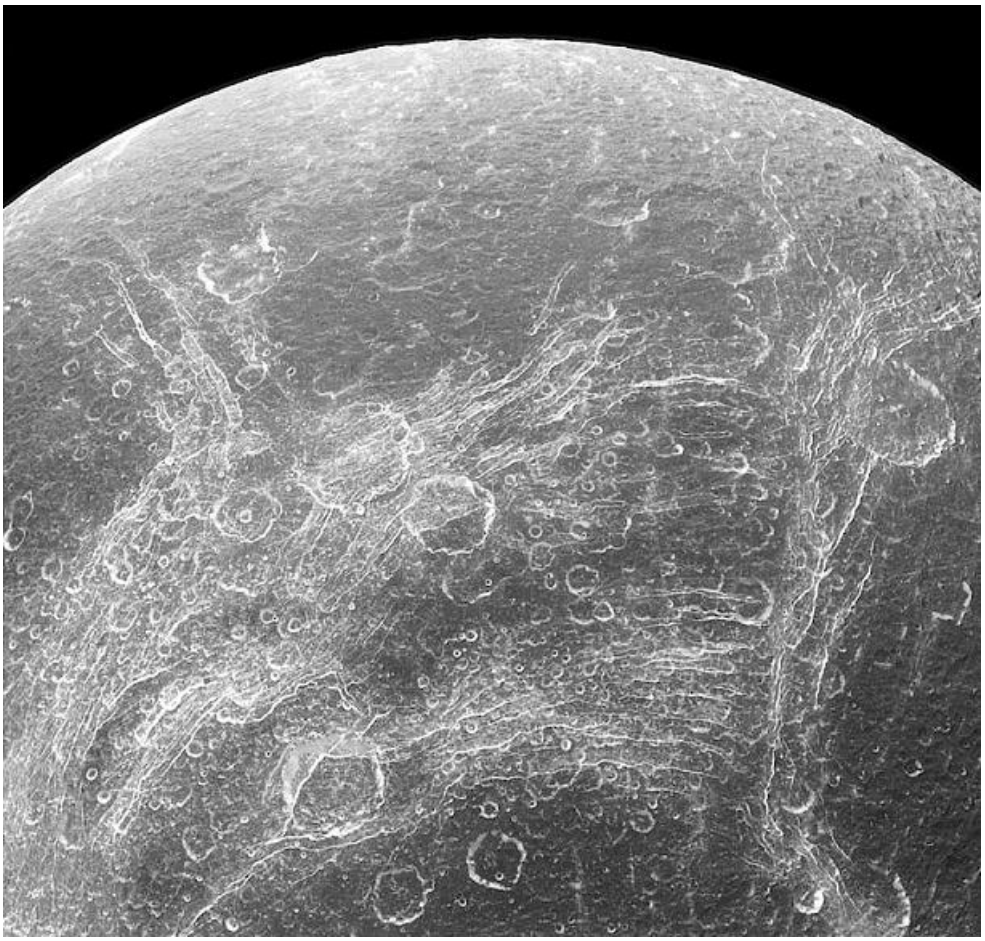

Figure 2.3: Cassini Imaging Science Subsystem (ISS) image of Dione showing bright linear features (or chasmata), whose origin may be associated with past tidal stresses over geological time spans caused by the satellite's orbital evolution. Image courtesy of NASA/JPL and deconvolved by R. Mark Elowitz to enhance the linear features.

The geomorphology on Rhea and Dione are similar, with asymmetries between their leading and trailing hemispheres. This implies that the chemical composition and evolutionary histories of Rhea and Dione were probably very similar. Both Rhea and Dione have trailing hemispheres that are darker than their leading hemispheres with bright wispy terrain. These bright streaks are chasmata (ice cliffs) that have a tectonic origin in that they were probably formed as a result of extensional fracturing of the moons surfaces (Collins *et al*. 2009). Rhea's anti-Saturn side has two large impact basins, Mamaldi (~500 km in diameter) and Tirawa (~360 km in diameter). The Mamaldi basin is older and more degraded than Tirawa, which is located to the southwest of Mamaldi. Since the Tirawa impact basin overlaps Mamaldi, by the principle of superposition it is geologically

younger. The Tirawa impact basin is similar to the large impact basin on Tethys, known as Odysseus. Several large impact craters on Tethys, Dione and Rhea (Phillips, *et al*. 2012) have appeared to have undergone some degree of relaxation (Figure 2.4).

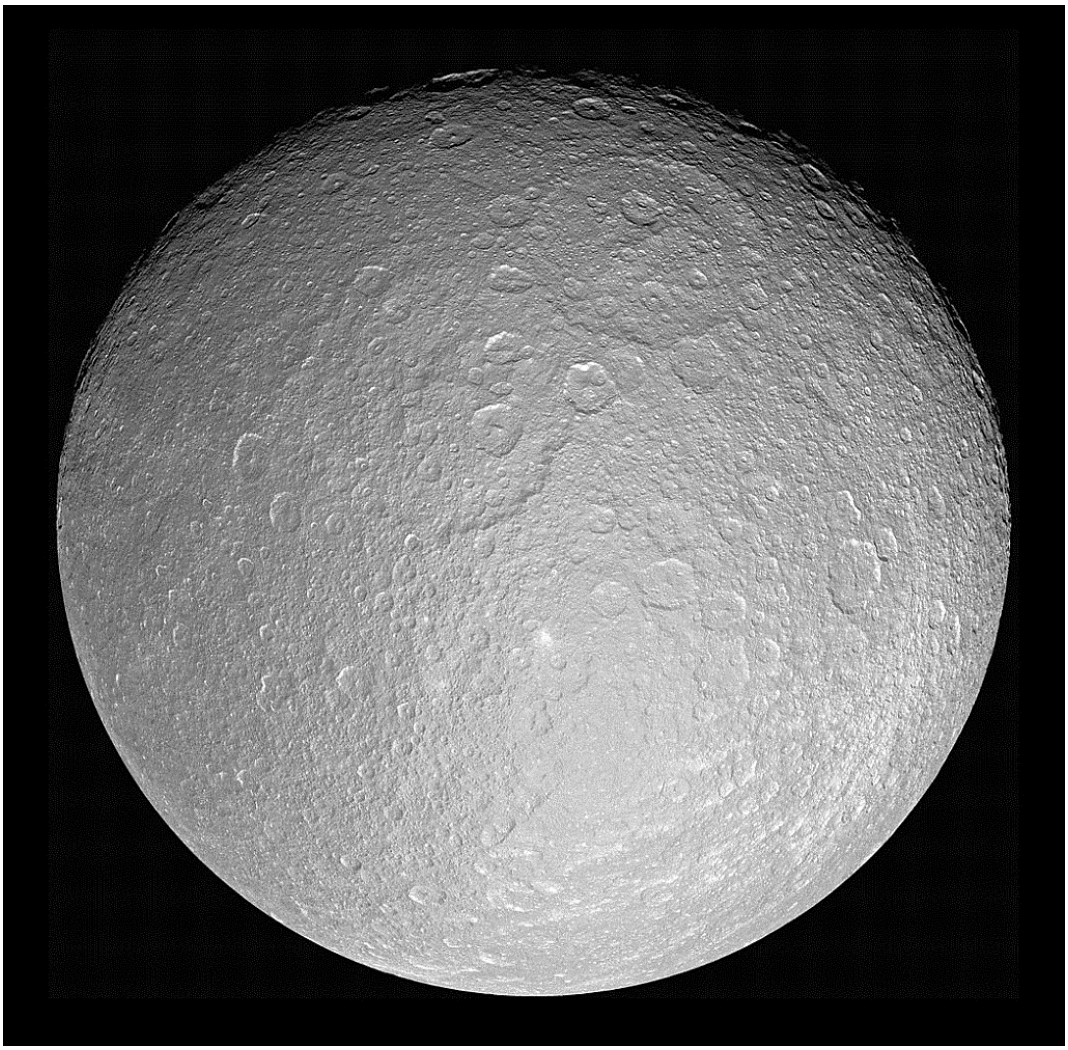

Figure 2.4: Cassini ISS image showing two large impact craters that have appeared to have undergone relation. Image deconvolved by R. Mark Elowitz to enhance detail. Image courtesy of NASA/JPL.

Crater relaxation is a sign the past endogenic activity occurred on these three icy satellites. Data from crater relaxation studies can be used to compare the thermal histories of icy satellites. The discovery of potential chemicals associated with deep sub-surface liquid layers on icy satellites, including chlorine-based salts and ammonia could lend supporting evidence that relaxed craters observed on Rhea and Dione are linked with past endogenic activity. Furthermore, viscous relaxation may have shallowed the observed fault

slopes on Rhea, Dione and Tethys implying past global heating events during their histories, since viscous relaxation is dependent on a high heat flux (Consolmagno, 1985; Schenk, 1989; Nimmo *et al*., 2010; White *et al*., 2013).

Many of the icy satellites show a copious number of impact craters on their surfaces, and tectonic features and regions of sparsely cratered plains are observed on only a few satellites that have apparently undergone endogenic activity. The Voyager missions revealed that impact craters were the dominant geological landscape on the ice satellites, except for Saturn's small icy moon Enceladus. Vast regions on Enceladus appeared to be crater free, and many craters showed signs of viscous relaxation (Johnson, 2005). Voyager discovered unusual wispy like features across the trailing hemispheres on both Rhea and Dione, although the spatial resolution of the Voyager imagery was insufficient to determine the origin of these geological features. The Voyager mission also found a dichotomy in brightness between the trailing and leading hemispheres of the mid-sized icy moons Rhea, Dione and Tethys (Morrison, 1982). Later during the Voyager mission, both Enceladus and Mimas were also found the have slightly brighter trailing sides. The origin, nature and distribution of darker materials seen on several satellites during the Voyager mission was not understood. Geological features related to extensional stress, faults and valleys on Rhea, Dione and Enceladus suggested that endogenic activities took place during the evolutionary history of these satellites (Morrison, 1982). However, until the Cassini mission the nature of the apparent endogenic activities was not well understood. The mid-sized icy satellite Dione has a pronounced crater-lineament relationship, stronger than any other mid-sized icy satellites with the exception of Enceladus (Spencer *et al*. 2009). Post-Voyager, it was thought Rhea underwent the least amount of endogenic activity during its past evolution when compared to all moons with a diameter greater than 1000 km. However, several large scarps and/or linear features were noted in some of the Voyager imagery of Rhea. The lineaments appeared to be parallel with respect to each

other, and were speculated to be caused by extensional forces followed by compression (Moore *et al*. 1985). Cassini images and digital elevation maps produced from the images revealed that the long wispy structures seen in Voyager imagery appeared to be correlated with graben and/or extensional fault systems. These fault systems had the interesting property of trending north-south (Moore and Schenk, 2007; Wagner et al. 2007). The Cassini data clearly demonstrated a relationship between the so-called "Megascarps" identified by Moore *et al*. (1985) and the north-south ridges/faults on Rhea's northern trailing hemisphere. This provided the first evidence for past endogenic activity on Rhea. In the case of Dione, Rhea and Iapetus, diurnal tidal stresses do not play a significant role, and the majority of tectonic features are apparently ancient. This implies that the tectonic features observed on the surfaces of these moons are the result of volumetric changes, reorientation and/or despinning and not present-day tidal stresses. Cassini digital elevation maps produced by images of Rhea's surface do not show any signs of plains. This appears to support the perception that no resurfacing due to cryovolcanic activity has occurred on Rhea. IR/UV colour ratio images of Rhea's trailing hemisphere (Schenk *et al*., 2011) show that the wispy terrain corresponds to graben, as revealed by the bluish colour of graben walls and outer flanks. The rimwalls of relatively young impact craters are characterised by bluish colours seen in the IR/UV ratio images. This photometric property tends to fade with age on Rhea's surface. Cassini IR/Green/UV three colour maps (Schenk, *et al*. 2011) of the five inner midsize icy satellites show asymmetries between the leading and trailing hemispheres of these moons. Significant deviations from the global asymmetry patterns are also present. An inherent process linked to the dynamics of the Saturnian system is the likely cause of the global asymmetry patterns seen in the three-colour composite images of the mid-sized icy satellites. The deviations from the global asymmetry patterns are due to satellite-specific processes.

Cryovolcanism is suspected to occur on some of the icy satellites of the outer solar system. The eruption of liquid and vapour phases of water and other volatiles occurs on Saturn's small icy moon Enceladus. Cassini Cosmic Dust Analyser (CDA) observations of the E-ring and the plumes of Enceladus between 2004 and 2008 showed icy dust particles (grains) rich in sodium salts (Hsu, *et al.*, 2015). The current explanation for the sodium salt (0.5 to 2% by mass) composition of the icy dust grains is that they originate from a subsurface ocean in contact with a silicate/rocky core in the interior of Enceladus (Postberg *et al*., 2009). Sub-surface oceans are also suspected to exist on other icy satellites, with internal heat supplied by the decay of radioisotopes, tidal deformation, and heat generated during the early accretional stage and the decay of short-lived radioisotopes (e.g. ^{26}Al) present during the early history of the satellite. Far-UV and IR spectroscopy can probe the surface environments of icy satellites to search for chemicals that could migrate from an internal ocean to the surface through cracks and fissures.

2.1.2 Infrared Spectroscopy of Rhea and Dione

Infrared spectral mapping of Rhea's surface has been carried out by Stephan *et al*. (2012) using Cassini's Visual Mapping Infrared Spectrometer (VIMS) over a wavelength range of 0.35 to 5.2 microns. They found identical spectral variations over the surfaces of both Rhea and Dione, implying that similar processes are responsible for producing the dark, non-water-ice component on the trailing hemispheres of both moons. The best explanation for small quantities of carbon dioxide (CO_2) and other organic substances found within the cratered terrain on both Rhea and Dione is bombardment of the icy surfaces by high-energy particles originating from Saturn's magnetosphere. Stephan *et al*. (2012) also identified a strong IR spectral signature of water-ice near steep tectonic features (e.g. scarps), and near young (fresh) impact craters. The detection of high concentrations of water-ice near tectonic features implies that the upper icy crust on Rhea has a depth of at least a few kilometres. However, the spectral observations carried out by

Stephan *et al*. (2012) only provide a limited analysis of the icy surfaces of Rhea (and Dione). Results from IR spectroscopy can be used in synergy with newly analysed far-UV spectral data (presented in this thesis) obtained from the Cassini UVIS instrument to search for additional molecules that have unique absorption features in the far-ultraviolet region of the electromagnetic spectrum.

To analyse their VIMS observations, Stephan *et al*. (2012) re-projected each VIMS observation into a map-projected spectral cube using the technique described in Jaumann *et al*. (2006). Each map-projected VIMS spectral cube was mosaicked together to create a global VIMS map of Rhea, which was then merged with the Cassini ISS base map of Rhea to create a composite mosaic. All science analysis was performed before completing the final VIMS/ISS mosaic to prevent loss of scientific information as a result of combining low signal-to-noise data from two different sensors.

Common to satellites in the outer solar system, the VIMS data clearly show strong absorption bands (located at 1.5, 2, 3 and 4.5 microns) due to water-ice absorption widely distributed over the surfaces of Rhea, Dione and Enceladus (Jaumann, *et al*. 2006; Stephan *et al*. 2012). Weak absorption features near 1.04 and 1.25 μm were also seen in a few regions containing high abundances of water-ice (Stephan *et al*. 2012). To produce maps showing the distribution of water-ice across Rhea's surface, the depths and central positions for each of the water-ice absorption features were measured. The analysis method applied to the VIMS data is frequently used in the analysis of imaging spectroscopy data to determine the abundances of ices and non-ice components on solar system bodies. No attempt was made to apply derivative spectroscopy in order to accentuate very weak absorption features that might be present in the IR spectra.

The VIMS study also involved the search for a possible non-ice component responsible for producing the dark areas across Rhea's surface on Cassini ISS imagery. The two favoured explanations within the planetary science community are that these

darkened areas are due to complex organic molecules, or igneous minerals that have undergone aqueous alteration. Recent INMS observations of organic molecules in the plumes on Saturn's moon Enceladus (Waite *et al*. 2006), and the detection of minor abundances on Saturn's two irregularly shaped moons Hyperion (Cruikshank *et al*. 2007) and Phoebe (Clark *et al*. 2005), as well as on Iapetus (Cruikshank *et al*. 2008) lend support to the existence of organic molecules within the Saturnian system. On Saturn's intermediate sized icy satellites, Dione and Rhea, the currently favoured explanation for the darkened component in the visible and towards the UV is reaction with water-ice and minor organic molecules with charged particles impacting the surfaces of the two satellites (Clark *et al*. 2008). These ions originate from plasma within Saturn's magnetosphere. Spectral analysis carried out using the VIMS data by Stephan *et al*. (2012) revealed no identification of the darkened material on Rhea based on absorption band fitting techniques. However, the reduced strength (depth) of the water-ice absorption bands and decrease in the albedo across the visible spectral bands of the VIMS spectra, indicate the presence of a non-water-ice component. To determine how pure the water-ice is on Rhea's surface, Stephan *et al*. (2012) estimated the spectral slope between 0.35 and 0.5 microns using the VIMS visible channel data,

$$Slope_{Visible} = \frac{(I/F)_{0.5\mu m} - (I/F)_{0.35\mu m}}{\Delta\lambda} \qquad (2.1)$$

where $\Delta\lambda$ is the width of the spectral region $(0.15\,\mu m)$ over which the spectral slope is calculated. The range of the visible spectral slope derived from the VIMS-VIS data, 1.1±0.01 to 1.8±0.02 (Stephan *et al*. 2012), implies that the spatial variation of organic molecules across Rhea's icy surface is the most likely cause of the range of slope values. A change in the spectral slope due to a variation in ice grain size does not seem to be supported by laboratory spectral measurements made by Hansen & McCord (2004), whose results show that water-ice has a high transparency in the visible region of the

electromagnetic spectrum (~0.5 microns), with no dependence on the size of water-ice grains. In contrast, Stephan (2006) and Stephan *et al*. (2010) found a dependence on the size of water-ice grains with the depth of absorption bands for wavelengths longer than 0.5 microns. It is found that the strength of the absorption bands (depth) tends to increase with increasing size of water-ice particles. Furthermore, as the negative slope of the spectrum beyond 0.5 microns becomes steeper, the size of the water-ice grains also increases in size. For the analysis of longer wavelengths (0.5 to 1.0 microns), the slope was calculated using an equation with identical form to that used for the visible wavelengths,

$$Slope_{Visible} = \frac{(I/F)_{0.5\mu m} - (I/F)_{1.0\mu m}}{\Delta\lambda} \qquad (2.2)$$

over the wavelength range of width $\Delta\lambda = 0.5\,\mu m$. The calculated slope over the 0.5- to 1-micron spectral range based on this equation varied from 0.8 to 1.2 with an uncertainty of 0.01 at a SNR of approximately 100.

It is interesting to note that the IR reflection peak at approximately 3.1 microns due to Fresnel reflection, which is a measure of the degree of crystallinity of water-ice is not observed (or is extremely weak) on icy satellites (e.g. Enceladus) located in the Saturnian system (Brown *et al*. 2006; Jaumann *et al*. 2008). Furthermore, Hansen *et al*. (2005) note that the strength of this reflectance peak at 3.1 microns does not vary with the abundance of the dark non-water-ice component observed on the icy satellite surfaces. In contrast, the same reflectance peak is observed in the IR spectra of icy moons located in the Jovian system. One possible explanation is that a fine layer of ice grains (with sizes less than 1 micron) have been altered by space weathering. The space-weathered ice grains may coat the surfaces of icy satellites in the colder Saturnian system, which are responsible for the muted (or absent) Fresnel reflection peak at 3.1 microns. Absorption due to larger water-ice particles is clearly seen in IR absorption spectra on icy satellites near 3 microns, and the Fresnel reflection peak results from scattering at the surface of the ice grains. This may

indicate that the muted (or absent) Fresnel reflection peak at 3.1 microns could be due to multi-scattering effects, where light is scattered at the surface of the water-ice grain, and internal scattering within the ice particle. This multi-scattering due to internal reflections could be responsible for the muted (or absent) Fresnel reflectance peak that occurs at 3.1 microns due to the crystallinity structure of the water-ice grain (Ciarniello *et al*. 2011). To search for a variation in the Fresnel reflection across the surface of Rhea, the Spectral Angle Mapper (SAM) technique (Rashmi, *et al*. 2014) was applied to the VIMS spectral cube data. The SAM method treats each spectrum as a vector (both observed and reference spectrum). In a 2-D scatter plot, each two-point spectrum becomes a point in band "A" and band "B" space (Figure 2.5).

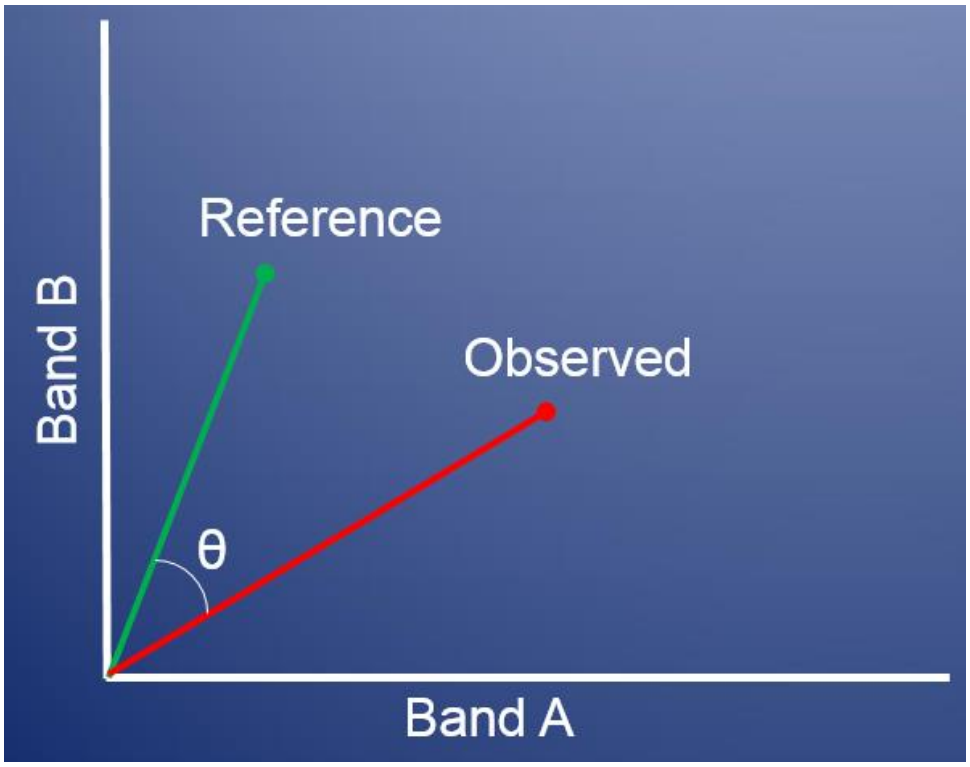

Figure 2.5: A diagram illustrating the concept of the Spectral Angle Mapper (SAM) technique of spectral mapping. The SAM method compares an observed spectrum to a reference spectrum, both represented as vectors. The smaller the angular offset between the two vectors, the closer the match between the reference and observed spectrum. The method is sensitive to the angular difference, but not the magnitudes of the two vectors.

In figure 2.5, θ represents the angular separation between the two spectra, which are mathematically treated as two separate vectors,

$$\theta = \cos^{-1}\left[\frac{\sum_{i=1}^{N} t_i r_i}{\left(\sum_{i=1}^{N} t_i^2\right)^{1/2}\left(\sum_{i=1}^{N} r_i^2\right)^{1/2}}\right] \quad (2.3)$$

where r_i and t_i represent the reference (laboratory) and observed spectrum, respectively. In the SAM method, smaller angular separations indicate more similar spectra, and a better fit between the observed and reference spectra. Spectral Angle Mapper has the advantage over other spectral mapping techniques, in that it is a pixel-by-pixel method commonly applied to imaging spectroscopy (hyper-spectral) data. Furthermore, the method is not sensitive to solar illumination effects. However, a better approach to identifying non-water-ice molecules would be the application of derivative spectroscopy, where the observed derivative spectrum is compared to a known database of reference derivative spectra of different chemical species. The derivative of the spectra accentuates any weak features that would not be readily detectable in the original spectra, by increasing the signal to background ratio of the data.

With the exception of CO_2 (identified by its narrow absorption feature near 4.26 microns), Stephan *et al*. (2012) found no other organic molecules that are suspected to be the cause of the dark, non-water-ice component in the icy surface of Rhea. The three most likely explanations for the presence of CO_2 (which has been detected in Rhea's exosphere) include chemical reactions among H_2O and another carbon-bearing compound(s) induced by radiolysis or photolysis, exogenic delivery by comets or carbon-bearing asteroids, or possibly from an endogenic source from Rhea's interior (e.g. redistribution, outgassing) (Teolis *et al*. 2010) Analysis of the VIMS IR spectral data could not confirm the presence of O_2 or ozone (O_3) within the surface ice of Rhea, although previous UV observations made by the Hubble Space Telescope (HST) have detected the presence of condensed O_3 on Rhea based on its 260 nm absorption feature. It is thought that the observed ozone is produced by UV photolysis and/or radiolysis involving charged particles from Saturn's

magnetosphere (Noll *et al*. 1997). The two absorption features in the IR (577 and 627 nm) for molecular oxygen (O_2) in the form of a condensate or trapped within Rhea's surface ice, lie within the wavelength range of the VIMS instrument. The spectral resolution of the VIMS visible channel data of 1.46 nm is sufficient to detect the two absorption bands of O_2 with a FWHM of approximately 50 nm (Brown *et al*. 2004). However, the null detection could be due to the low signal-to-noise ratio of the VIMS data, especially if the absorption features are too weak. As previously stated, the use of derivative spectroscopy could help to improve the signal-to-noise ratio, thereby accentuating any weak absorption features that may exist in the spectral data. Another possibility is that the two absorption features of O_2 are masked by the stronger spectral signature of water-ice. A search for CO_2 and ozone (O_3) was carried out using Cassini UVIS spectra in this thesis by comparing the observed spectra with model spectra based on laboratory measurements. No detection of O_3 and CO_2 was apparent (see Chapters 5 and 6).

2.1.3 Structure of Rhea's Surface Ice

The chemical structure of ice on Rhea's surface could affect the position and shape of absorption bands in ice spectra. The temperature and pressure at the time of the formation of the ice determines its phase. There are three possible structures for water-ice on icy satellites in the outer solar system – two crystalline phases and one amorphous phase. Crystalline phase ice exists in either hexagonal (Ih) or cubic (Ic). At temperatures between 100-160 K, there is a transformation from low-density amorphous water-ice to cubic crystalline ice (Jenniskens and Blake, 1996). The transformation proceeds as an endothermic reaction (i.e. energy is released upon transformation to the new crystalline form of ice), with a change in enthalpy of $\Delta H = 44 \pm 5 kJ / mol$ for the rapid transition from amorphous to crystalline ice (Jenniskens & Blake, 1996). The timescale to onset of crystallisation can be estimated using,

$$t_c = \nu_0 \exp\left(\frac{\Delta H}{R_g T}\right) \quad (2.4)$$

where $\nu_0 = 10^{-14}\ s$ is the relaxation timescale for the water-ice molecule, $R_g = 8.3144\ J\ mol^{-1}K^{-1}$ is the gas constant, and *T* is the temperature. At a temperature of 70 K, typical of Rhea's ice layer, the crystallization time scale is much greater than the age of the solar system, but for a higher temperature of 100 K, the estimated time scale for crystallisation to the cubic phase of water-ice is much less than the age of the solar system (~30 years). Thus, the cubic crystalline phase of H_2O ice is more likely to exist on icy moons located in the Jovian system. Amorphous ice is likely to be found on the surfaces of icy moons within the Saturnian system (e.g. Rhea), because their surfaces have temperatures less than 100 K, since the time of formation of the satellites. It is important to note that the transformation from amorphous to crystalline ice is not reversible, even if temperatures on the icy satellites decrease below ~135 K (the critical temperature for transformation from amorphous to crystalline ice). Both cubic and hexagonal phases of H_2O ice have nearly identical IR absorption spectra. In contrast, the IR absorption spectra for amorphous and crystalline ice structures have observable differences. The absorption bands in the crystalline ice phase are sharper, stronger and undergo wavelength shifts towards shorter wavelengths relative to the amorphous ice phase. The absorption bands in the crystalline phase of water-ice tend to decrease with temperature (Schmitt *et al*. 1998). Laboratory spectra of amorphous, crystalline, and mixtures of amorphous/crystalline water-ice are needed to explore their spectral signatures in the VUV region of the spectrum.

It is of interest to determine if crystalline ice exists on the surface of Rhea, since its presence would imply an external mechanism for its formation. It is possible that large impacts onto Rhea could have excavated crystalline ice from subsurface layers. The presence of crystalline ice could also lend support to possible cryovolcanism that might

extrude it onto Rhea's surface. Continuous bombardment of amorphous ice by micrometeoroids over long periods of time could raise the ice temperature above the critical point needed for transformation to a crystalline phase. It is also of interest to explore how crystalline ice would survive long-term bombardment by highly energetic particles from the solar wind, cosmic rays and other high-energy particles originating from the magnetospheric plasma in the Saturnian system. When high-energy particles interact with the bonds between H_2O molecules that are arranged in a regular lattice, they break the bonds, transforming the crystalline ice into amorphous ice. Since the time scale to convert crystalline ice to amorphous ice is much less than the age of the solar system, whatever process lead to the formation of any observed crystalline ice (e.g. cryovolcanic activity, large impacts) must have occurred very recently on geological timescales. The presence of water-ice in its crystalline phase on Rhea (and other icy moons in the Saturnian system) can be searched for by measuring the strength of the 1.65- micron absorption feature (i.e. the secondary minimum) arising from the crystalline structure of the ice, which is also an indicator of the temperature (Grundy and Schmitt, 1998). Unfortunately, this absorption band could not be observed using VIMS since it overlapped with one of the instrument's order-sorting filters. However, Leto *et al*., 2005, Mastrapa and Brown, 2006, Mastrapa *et al*., 2008) have shown that it was possible to discriminate between amorphous and crystalline ice by noting the shift in the 1.5 and 2.0 spectral band minimum positions. Their laboratory experiments demonstrated a shift to longer wavelengths for the crystalline form of ice at 20 K (1.51 and 2.02 microns) and 155 K (1.51 and 2.05 microns). The positions of the 1.51- and 2.02-micron absorption bands as observed with the VIMS instrument showed that water-ice was in the crystalline form for Saturn's icy satellites, with the exception of Phoebe, where contamination by non-water-ice molecules presented problems with the determination of the spectral band minima. It should be possible to mitigate problems associated with contaminants in the water-ice using the technique of derivative

spectroscopy (Chapter 5), which could improve upon the approach used by Leto *et al*., 2005, Mastrapa and Brown, 2006, Mastrapa *et al*., 2008 to determine the minima of the 1.51- and 2.02-micron absorption bands of water-ice.

Laboratory measurements made over the wavelength range 2.5-22 microns of amorphous (i.e. disordered molecular state) and crystalline (geometrically repeated patterns of water molecules in a minimum-energy configuration) forms of water-ice at temperatures ranging from 20-150 K by Mastrapa *et al*. (2009) show distinctive absorption bands across the wavelength region for both forms of the ice. They also show that some of the absorption bands associated with amorphous water-ice tend to weaken and shift to shorter wavelengths with respect to the bands in the crystalline form of water-ice. Infrared (and possibly UV) measurements of these two forms of water-ice are important to the characterisation of icy satellite surfaces for the following reasons: Crystallisation of water-ice in the deep interiors of icy moons could provide an additional heat source (since the process of crystallisation is exothermic) to maintain aqueous layers, while the minute nooks and crannies in amorphous ice provide sites where other molecules can be located within matrix. At temperatures typical of the surface of Rhea and Dione (~70-90 K from thermal models produced in Chapter 2), the timescale for the transformation of amorphous to crystalline water-ice is less than the age of the solar system. Since the trapping efficiency of other molecules is known to vary exponentially with inverse temperatures, there should be a sudden release of molecules that were formerly encased within the amorphous ice structure as the temperature rises. I do not need to worry about the transformation of crystalline water back into its amorphous form when the temperature is lowered, since crystalline ice is already in a minimum energy configuration. However, since the icy satellites are irradiated by high-energy particles (e.g. electrons and protons) originating from Saturn's magnetospheric plasma, crystalline ice can be transformed into amorphous ice.

Evidence for changes in the structure of water-ice and/or grain sizes is presented in Chapter 5 using the method of derivative spectroscopy to analyse the position and slope of the 0.165-micron absorption edge due to water-ice.

2.1.4 Exospheres of Icy Satellites in the Saturnian System

Radiolysis of water-ice molecules by solar UV photons and magnetospheric particles can lead to the production of an O_2/CO_2 exosphere. Not long after Cassini's arrival in the Saturnian system, then the Cassini Plasma Spectrometer (CAPS) (Martens *et al*., 2008) measurement of pickup ions (Jones *et al*., 2009) indicated the presence of a possible exosphere around Rhea. Pickup ions are neutral particles that become ionized through the process of ionisation by radiation from Saturn's magnetosphere, electron impact ionisation, or charge exchange with protons originating from the magnetosphere or solar wind. The pickup ions from Rhea's exosphere are swept up into Saturn's magnetosphere, and the CAPS instrument found pickup ions in the mass range of 26 to 56 Daltons. The mass range of the ions was thought to correspond to O_2^+ and CO_2^+. During the 2010 Cassini flyby of Rhea, the Ion and Neutral Mass Spectrometer (INMS) verified the existence of Rhea's O_2/CO_2 exosphere (Teolis *et al*., 2010) (Figure 2.6). In a recent paper published in Icarus, the Cassini INMS also confirmed the presence of an O_2/CO_2 exosphere around Dione with a composition and density similar to that of Rhea's exosphere (Teolis and Waite, 2016). The source of the detected molecular oxygen is believed to be from radiolysis of water-ice molecules, but the source of the carbon dioxide is not well understood.

Both Dione and Rhea are also known to have ozone (O_3) in their surface ice layers. The trapped O_2 in the surface ice leads to the eventual production of ozone as demonstrated by laboratory experiments (Cooper *et al*. 2007). The simultaneous presence of O_2 in the exospheres of Dione and Rhea (Figure 2.6) and trapped O_3 in their surface ice

lends support to radiolytic processes (Noll *et al*. 1997; Johnson and Jesser 1997). The dominant radiation source from the co-rotating plasma responsible for the production of O_2 on the surfaces of Dione and Rhea are water group ions (O^+, OH^+, H_2O^+ and H_3O^+) with energy less than 8 keV (Teolis, *et al*. 2010). Since Rhea and Dione orbit with a velocity less than the co-rotational velocity of the plasma, preferential synthesis of O_2 by radiolysis occurs on their trailing hemispheres (from irradiation and implantation of magnetospheric plasma on the trailing hemisphere; Boduch, *et al*. 2011). Although energy deposition on the icy surfaces of Dione and Rhea from electrons is much higher than water group ions, the efficiency of O_2 production from the electrons (10 eV experimental synthesis threshold; Sieger, *et al*., 1998; Orlando and Sieger, 2003) is much lower than that of the water group ions (Teolis, *et al*. 2010). The production of O_2 near the surface layer is favoured due to the easy escape of hydrogen atoms from the radiolytic process. Oxygen atoms are produced by radiolysis of H_2O molecules, and further radiolytic reactions of surface oxidants with organic molecules could lead to the production of CO_2 (Boduch, *et al*. 2011). The source of such organic molecules could be from exogenic delivery by carbonaceous material (e.g. micrometeorites). Another possibility is that carbon dioxide from an endogenic source (e.g. chemistry occurring in an aqueous reservoir in the interior of the satellite) on Rhea could be sputtered or outgassed (e.g. from a primordial source) to supply the CO_2 to the satellite's exosphere (Figure 2.6).

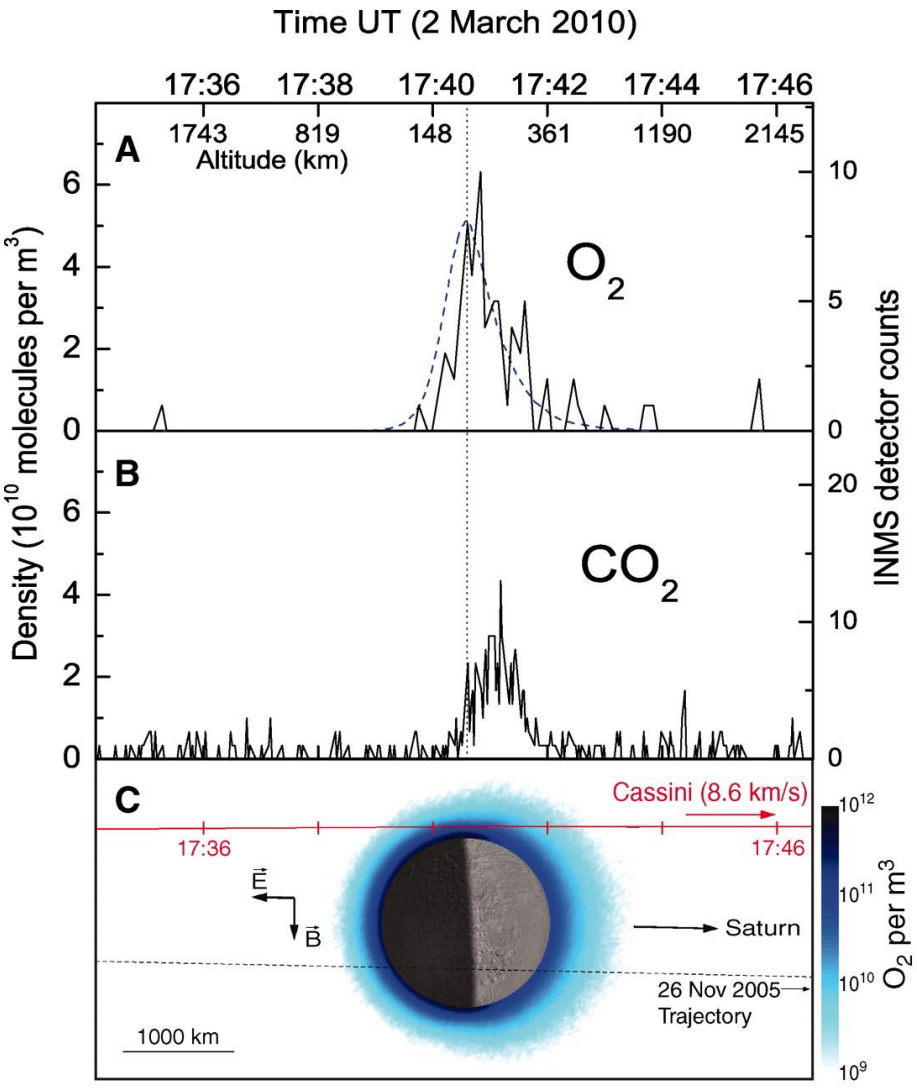

Figure 2.6: Cassini ion neutral mass spectrometer (INMS) showing molecular oxygen (O_2) and carbon dioxide (CO_2) during its March 2010 flyby of Saturn's second largest moon Rhea. The closest approach to Rhea is indicated by a dotted vertical line. The trajectory of the spacecraft is shown in the bottom pane, where Rhea's orbit is perpendicular to the page of the diagram. Teolis et al. (2010).

Teolis *et al*. (2010) modelled the magnetospheric environment through which Rhea orbits. They assumed two dominant populations of particles, protons (H^+) and water group ions (O^+, OH^+, $H_2O^+$and H_3O^+, and derived the estimated production rates of O_2 by integrating the irradiation flux and yields of the two particle groups over an energy range relevant to Saturn's magnetosphere. Their results showed a clear asymmetry in O_2 production rates between Rhea's leading and trailing hemispheres due to the higher ion flux from Saturn's magnetosphere on the trailing side of the satellite.

When an electron with energies ranging from keV to MeV interacts with an H_2O molecule, ionisation or excitation occurs. These processes produce new molecules such as H_2 or H_2O_2. The isotopically light H_2 molecules escape the gravitational acceleration (and surface) of Rhea. This, in turn, leads to an icy regolith that is oxidizing in nature. Depending on the degree of implantation into the icy surface by magnetospheric protons, some reduction also occurs. If the flux of magnetospheric protons is low, this effect is secondary to the primary ionisation and excitation resulting from electron bombardment of the surface ice layer. Further decomposition of hydrogen peroxide (H_2O_2) created from the irradiation of water-ice molecules and various secondary reactions, leads to the formation of HO_2, OH, HO_3, O_2 and O_3 (oxidising agents of interest since they may provide a source of chemical energy in outer Solar System ices; Cooper *et al*.; Chyba, 2000). The surface layer of Rhea therefore becomes more oxidised as the chemical reaction cycle between H_2O and H_2O_2 molecules continues, as H_2 is lost to space. If CO_2 is present in the surface ice layer, then the following chemical reaction can take place as a result of radiolysis (Peeters, *et al*. 2010).

$$H_2O + CO_2 \rightarrow H_2CO_3 \text{ (Carbonic acid)}$$

Further charged particle irradiation of the upper ice layer converts the carbonic acid back to carbon dioxide

$$H_2CO_3 \rightarrow CO_2 + H_2O\,.$$

For large destruction rates of H_2CO_3, a majority of the carbon exists in the form of CO_2, when equilibrium ($H_2O + CO_2 \leftrightarrow H_2CO_3$) is reached. Since the icy satellite (Rhea) is considered to be an open system, the carbon dioxide can leak (diffuse) at a slow rate into the satellite's exosphere. This could explain the presence of CO_2 in Rhea's tenuous O_2/CO_2 atmosphere. The production of CO_2 (a component of the exosphere of Rhea) via radiolysis

of carbonic acid ice is explored further in Chapter 7, where laboratory measurements of carbonic acid ice are used to search for its presence in Cassini UVIS spectra.

2.2 Thermophysical Properties of Rhea's Upper Ice Layers

To characterize the structure of Rhea's upper surface layers, a one-dimensional thermal model was used to calculate diurnal temperatures (Spencer, *et al*. 1989). The results from numerical models may be used to place constraints on the temperature range used in laboratory measurements of thin ice samples. The thermal model calculates the subsurface and surface temperature as a function of time. The diurnal surface temperatures on an icy satellite depends upon the thermal inertia,

$$\Gamma = \sqrt{k\rho c} \qquad (2.5)$$

where k is the thermal conductivity in the upper ice layers, ρ is the mass density of the ice and/or ice mixture, and c is the specific heat of the surface material. The thermal inertia is a measure of a substances ability to store heat energy, and the characteristic length scale of temperature variations within the layers just below the surface ice layer on Rhea depend on the skin depth. The skin depth depends on three thermo-physical parameters and one dynamical parameter, and is expressed as

$$d_{skin} = \sqrt{\frac{k}{\omega\rho c}} \qquad (2.6)$$

where k is the thermal conductivity, ρ the mass density, c the specific heat, and ω the angular rotation velocity. This implies that the skin depth is not uniquely determined by the thermal inertia. Values for the skin depth range from a few millimetres for asteroidal bodies to several centimetres for icy satellites.

The conductive heat flow equation is numerically solved in one dimension. The output from the model is depth versus temperature as a function of time (adapted from Spencer, *et al*. 1989).

$$c\rho\frac{\partial T(z,t)}{\partial t}=\frac{\partial}{\partial z}\left[k\frac{\partial T(z,t)}{\partial z}\right] \qquad (2.7)$$

where *c* is the specific heat capacity, *k* is the thermal conductivity and ρ is the mass density. The conductive heat flow equation has the form of a parabolic partial differential equation, and is derived from conservation of energy (i.e. from the first law of thermodynamics). The numerical solution of the heat conduction equation is carried out from the surface layer of Rhea, where the depth variable *z* = 0 to some arbitrary depth *z*, with an upper boundary condition (i.e. the surface boundary condition) given by (adapted from Spencer, *et al*. 1989)

$$k\left[\frac{\partial T(z,T)}{\partial z}\right]_{z=0}=\sigma\varepsilon T^4(0,t)-(1-A)F(t) \qquad (2.8)$$

where the left side of the boundary condition represents the subsurface conductive heat flux. The first term on the right side of the boundary condition describes the thermal radiation, where ε is the emissivity of the ice layer. Thus, the boundary condition equation states that there is an equilibrium (or balance) between the subsurface heat flux and thermal emission. The second term on the right side represents the amount of solar radiation that is absorbed by the ice layer, where $(1-A)$ accounts for the Bond albedo, and *F* is the incident solar flux on the surface layer. The lower (or base) boundary condition is given by (adapted from Spencer, *et al*. 1989)

$$k\left[\frac{\partial T(z,t)}{\partial z}\right]_{z=d}=0 \qquad (2.9)$$

which implies that the lower boundary layer is at a great enough depth to allow no spatial temperature gradient. Thus, any diurnal temperature variations take place above the lower boundary. The iterative model is run for several rotations of the body until stabilisation of the diurnal temperatures occurs – i.e. until there is no memory of the initial conditions. Since the initial release of the 1-D thermal model code by Spencer *et al*. (1989), the code

has been modified to include optional effects due to volatile cooling by sublimation, the solid-state greenhouse effect (Matson and Brown, 1989) due to penetration of the ice layer by sunlight, endogenic heat flow, an arbitrary change in insolation as a function of time, as well as thermophysical parameters that vary as a function of depth.

The models produced for Rhea assume that there is re-condensation of volatiles, and that thermal emission is from the upper surface layers only. For models that assume no solid-state greenhouse, there is no sunlight penetration below the surface layers on Rhea. However, for icy satellites where the solid-state greenhouse occurs, the temperatures of their surfaces and interiors can be higher than predicted by conventional models. A solid-state greenhouse effect occurs when sunlight increases the temperatures of relatively translucent materials with high albedos and are opaque in the thermal infrared. The upper boundary temperature used by interior models of icy moons might be closer to the solid-state greenhouse temperatures. On icy satellites with substantial solid-state greenhouse effects, thermal metamorphosis may alter the surface geomorphology.

When the subsurface temperature equals the average surface temperature, thermal equilibrium is achieved, assuming no endogenic heat sources. An endogenic heat source can be simulated by increasing the lower boundary temperature of the model. For each model simulated, the output consists of the mean power in (W/m^2), the mean output power (W/m^2), the net power out (W/m^2), the ratio of the total input energy to the total output energy, the subsurface or deep layer temperature and the mean temperature at Rhea's surface. The generated models for Rhea's upper layers are based on the solution of the 1-D time-dependent thermal diffusion equation (Spencer *et al*. 1989). The thermal conductivity of the layers is derived from the mass density, thermal inertia, and specific heat.

The one-dimensional thermal model was used to explore Rhea's leading side, with an average bolometric Bond albedo set to 0.55 and a heliocentric distance of 9.5 AU. A rotational period of 4.52 days was used, and an emissivity of 0.9 was assumed for Rhea's

upper “regolith” layers. The thermal inertia was set to 3×10^4 erg cm^{-2} $s^{-1/2}$ K^{-1} and a density of 0.5 g/cm^3, characteristic of Rhea’s “regolith” was used in the model. A small solid-state greenhouse effect was assumed – i.e. minor penetration of sunlight into the very upper ice layers on Rhea. The thermal conductivity as calculated by the 1-D thermal model is 0.00225 W/(m•K), and the calculated skin depth (the e-folding depth of temperature variations) is 1.870 cm. The skin depth and thermal inertia govern the phase and amplitude of temperature variations over the course of one diurnal cycle, and the thermal inertia is a measure of the ability of the surface layers to store energy. The thermal inertia is a function of the mass density, the thermal conductivity and heat capacity of the upper surface layers on Rhea. The numerical results of the 1-D thermal model for Rhea’s leading hemisphere are presented in Table 2.1.

The results of the diurnal temperature models of Rhea’s surface computed by myself using the Spencer 1-D time-dependent model code (Spencer *et al*. 1989) could be verified by future radiometers placed into orbit around Rhea, and from analysis of IR spectral data collected by Cassini’s Composite Infrared Spectrometer (CIRS) Focal plane 1, which covers the wavelength range 16.7 to 1000 microns. Analysis of CIRS spectra carried out using black body spectral fits indicate temperatures ranging from ~25 K (at Rhea’s southern pole) to ~70 K near the equatorial region (Howett, C. J. A., *et al*. 2016), in good agreement with my numerical thermal models.

Table 2.1: Numerical model of Rhea's leading hemisphere using a 1-D thermal modelling code.

Run	Mean Power in (W/m^2)	Mean Power Out (W/m^2)	Total Energy In/Out	Net Power Out (W/m^2)	Mean Surf. Temp. (K)	Deep Temp. (K)
0	2.181e+000	2.135e+000	0.9791	-4.557e-002	77.88	76.99
1	2.181e+000	2.181e+000	1.0001	2.712e-004	78.36	79.48
2	2.181e+000	2.181e+000	1.0000	-4.143e-006	78.36	79.47
3	2.181e+000	2.181e+000	1.0000	6.306e-008	78.36	79.47
4	2.181e+000	2.181e+000	1.0000	-9.599e-010	78.36	79.47

The simulation converges after three model runs as indicated by a unity value for the total energy input to output ratio. The calculated mean surface temperature is 78.36 K and the temperature of the deep underlying layers is 79.47 K. The minimum and maximum diurnal surface temperatures are 65 K and 97 K, respectively. Thus, it is of interest to acquire laboratory VUV ice spectra over this range of temperature, as calculated in the 1-D thermal model of Rhea's upper surface layers on the satellite's leading hemisphere. The peak equilibrium temperature achieved as calculated by the model is 107.64 K. The model is valid for Rhea's equatorial regions, where most of the Cassini UVIS observations were made.

The numerical results for Rhea's trailing hemisphere, using a bolometric Bond albedo of 0.42 are provided in Table 2.2.

Table 2.2: Numerical model of Rhea's trailing hemisphere using a 1-D thermal modelling code.

Run	Mean Power in (W/m^2)	Mean Power Out (W/m^2)	Total Energy In/Out	Net Power Out (W/m^2)	Mean Surf. Temp. (K)	Deep Temp. (K)
0	2.811e+000	2.767e+000	0.9843	-4.420e-002	82.51	81.99
1	2.811e+000	2.811e+000	1.0001	3.344e-004	82.91	84.36
2	2.811e+000	2.811e+000	1.0000	-5.932e-006	82.91	84.35
3	2.811e+000	2.811e+000	1.0000	1.048e-007	82.91	84.35
4	2.811e+000	2.811e+000	1.0000	-1.851e-009	82.91	84.35

The numerical models of Rhea's two hemispheres show differences in the diurnal surface temperatures, as well as the mean power in and out, and net power out. This is due to the asymmetry in albedo between Rhea's leading and trailing hemispheres. A plot of the diurnal surface temperatures for Day 3 for both hemispheres is shown in figure 2.7.

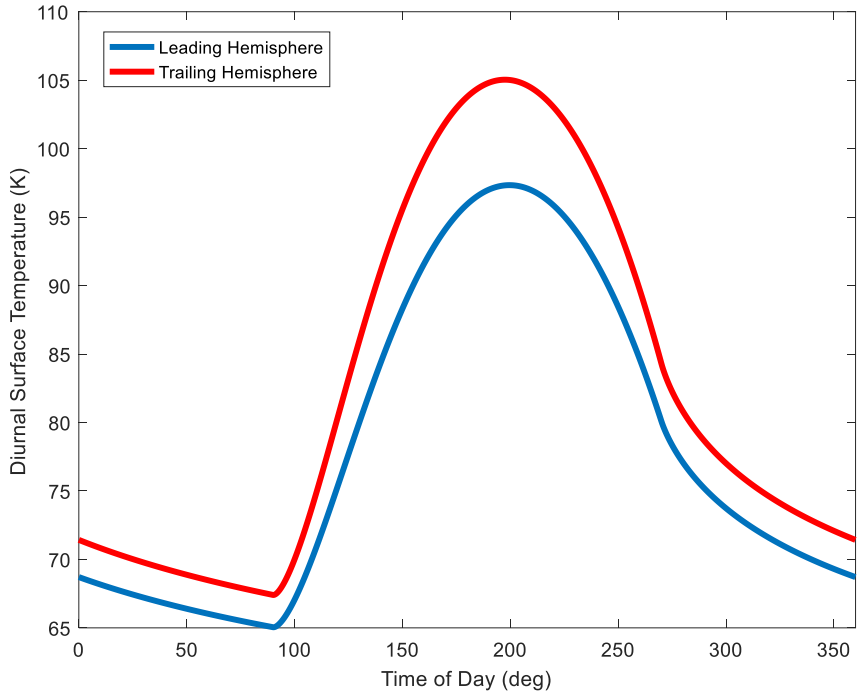

Figure 2.7: A comparison of the diurnal surface temperatures for Rhea's leading and trailing hemispheres as computed using a 1-D thermophysical model code. The difference between the two hemispheres is due to the different bolometric Bond albedos between Rhea's leading and trailing hemisphere. Temperatures on Rhea's surface can range from about 65 to 105 K, which is the temperature range for most of the laboratory ice measurements used in this research. Model produced by R. Mark Elowitz.

The difference in Bond albedo (the fraction of energy across all wavelengths incident on Rhea's surface) could be due to the asymmetry in ion/electron irradiation between the leading and trailing hemispheres on Rhea. The lower Bond albedo on Rhea's trailing hemisphere is due to the dilution of water-ice as a result of an increase in radiolysis resulting from higher ion/electron fluxes, in contrast to the satellite's leading hemisphere. The lower Bond albedo on Rhea's trailing hemisphere leads to an increase in solar radiation, since the Bond albedo considers radiation that is scattered from the surface at all wavelengths and phase angles. The increase in solar radiation leads to a slight increase in the diurnal surface temperature, relative to the leading hemisphere (Figure 2.8).

The bolometric Bond albedo map of Rhea (Figure 2.8) shows an asymmetry between the trailing and leading hemispheres. Both Cassini ISS and VIMS IR observations support the asymmetry pattern seen in the bolometric Bond albedo map. In contrast to

Tethys and Mimas, whose IR/UV spectral band ratio indicates a darkening in their southern hemispheres associated with higher thermal inertia values, Rhea's high thermal inertia is not correlated with the IR/UV ratio. Rather it is highly correlated with the Inktomi impact site in the satellite's southern hemisphere. On Dione, high thermal inertia is correlated with low latitude regions on the leading hemisphere (Howett, *et al*. 2014).

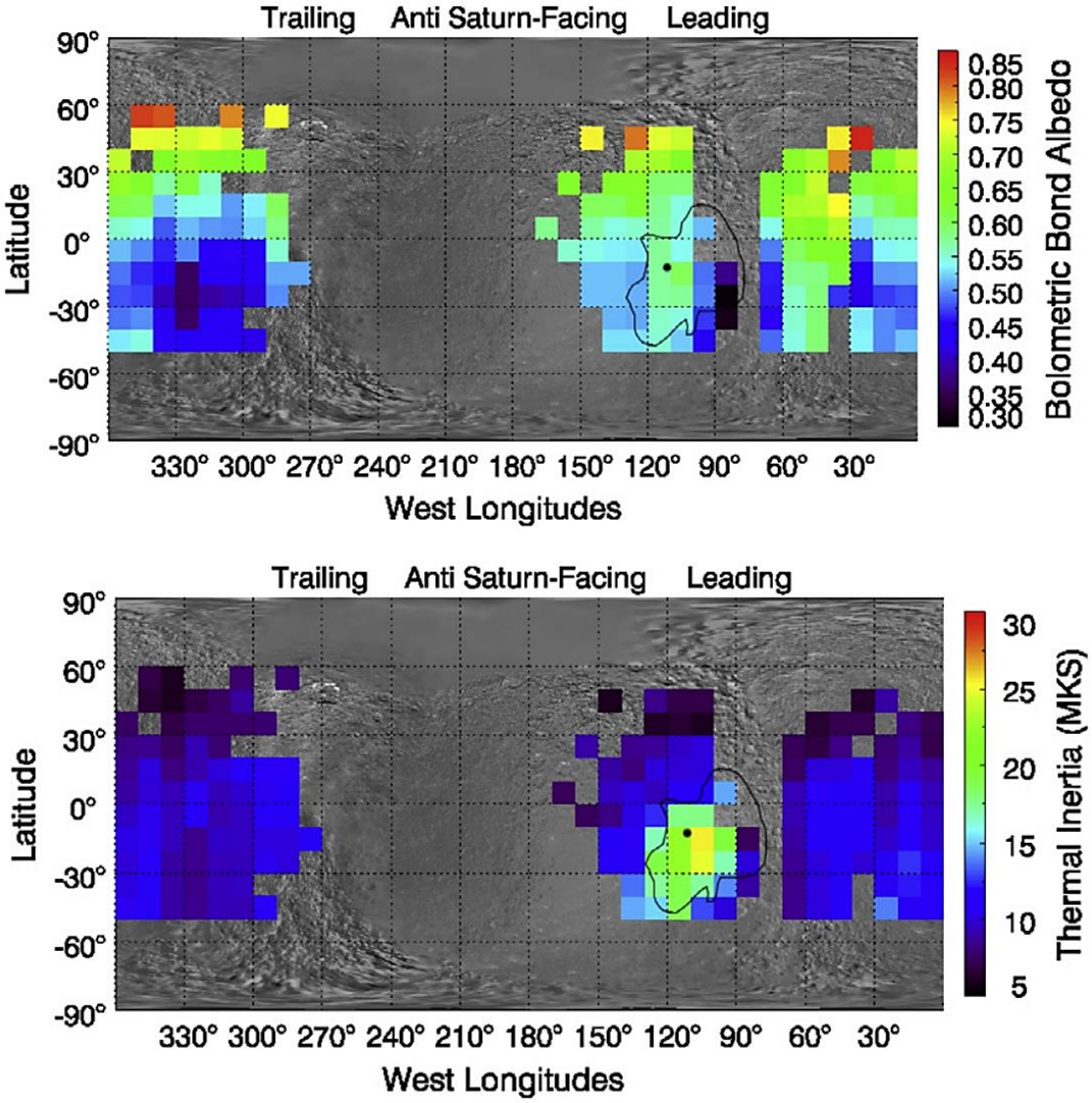

Figure 2.8: Bolometric Bond albedo (top) and thermal inertia (bottom) maps of Saturn's second largest moon Rhea. Note the high (relative to the mean background) thermal inertia at the Inktomi impact crater site (bright green/yellow region) on Rhea's leading hemisphere. Figure courtesy of Howell et al. (2014).

The anomalous high thermal inertia of the ejecta material associated with the Inktomi impact site could be due to large water-ice grains, since the thermal conductivity tends to increase as the size of the water grain increases. Since the transfer of thermal energy depends on gas conduction, the high thermal inertia observed at the Inktomi impact site is increased since Rhea is located in a near-vacuum environment. An alternative scenario for the high thermal inertia is that small ice particles are mixed together with large particles, or even large ice blocks that have high thermal inertia. If the second explanation is correct, then near-IR spectra (from Cassini's CISR instrument) should fit a non-blackbody model due to the mixture of different thermal inertia resulting from large blocks of water-ice and small water-ice grains. Model fits to near-IR spectra (Howett *et al*. 2014) tend to support the result that the radial ejecta originating from the Inktomi crater are composed of relatively small water-ice grains with similar thermal inertia values to those of Rhea's mean background. The high thermal inertia values are associated with the impact itself, which excavated larger blocks of water-ice and/or more water-rich ice composed of relatively large grains. This scenario supports the observation of strong water-ice absorption bands in the IR at the impact site (Stephan *et al*. 2012). The different water-ice grain sizes and structure as a function of geomorphology on Rhea and Dione may cause shifts in the location of the 165-nm absorption edge, which is noted in some of the Cassini UVIS reflectance spectra (see Chapter 5).

2.3 Introduction to Rhea's Internal Structure

It is of interest to characterize the internal structure of any moon since the existence of an internal ocean could have implications on the detection of chemicals on the surface originating from a deep aqueous layer. Since Rhea is the main focus of this research, I concentrate on presenting current information on its interior structure.

At present, there is no agreement on the internal structure of Rhea. Early attempts to model the internal structure of the satellite were carried out by Consolmagno & Lewis (1978), Lupo & Lewis (1979), Ellsworth & Schubert (1983) and Consolmagno (1985). These models assumed a bulk chemical composition of 60 percent (by mass) rock and 40 percent (by mass) water-ice, based on early modelling of solar abundances of the chemical elements in the solar system (Ross & Aller (1976). Recent updates of solar abundance data (Lodders 2003, Asplund *et al*. 2005) have resulted in more recent models, assuming a 50:50 rock/ice composition. However, there are difficulties with this rock-to-ice ratio, in that the condensate mean density (~1.5 g/cm^3) far exceeds the density of Rhea. The interior model based on work carried out by Consolmagno, produced an interior in which the inner 40 percent (by mass) consisted of melted water and ammonia ice. This melting would produce enough heat to differentiate the interior of Rhea. A mixture of ammonia (NH_3) and water ice produce a Eutectic melt at a temperature of 175 K (Hogenboom *et al*. 1997). This eutectic temperature would lead to migration of the fluid mixture towards Rhea's surface, resulting in partial flooding. The recent geological evidence for a resurfacing event on the trailing hemisphere of Rhea could be explained by this flooding event.

If there was solid-state convection of ice inside Rhea at some time during its past history and efficient transfer of heat produced by the decay of radioactive isotopes would occur (i.e. radiogenic heating). This would not permit the melting of water-ice (Ellsworth & Schubert, 1983). If a minor component of ammonia, in the form of NH_3 monohydrate (based on solar abundances), was present as part of a water-ice/ammonia mixture (Lewis, 1972), it would not have a major effect on the viscosity of the ice mixture, nor would it lead to global differentiation of Rhea. In other words, Rhea would remain chemically homogeneous. However, the undifferentiated scenario presents a problem in that a decrease in radiogenic heating causes Rhea's interior to contract (assuming a transformation from ice I to ice II, a rhombohedral crystalline structure of ice that is highly

ordered, and can be formed at pressures relevant to Rhea's interior over a temperature range of 190 to 210 K), which would have produced stresses that would be directed inward towards the interior of Rhea. Observations of Rhea's surface show no indications of compressional features on the surface of Rhea that would point to compressional forces.

2.3.1 The Role of Ammonia in Rhea's Interior

In this next section, I explore the melting temperature for ammonia dehydrate ($NH_3 \cdot 2H_2O$) ice using the melting curve (determined from thermodynamic properties of $NH_3 \cdot 2H_2O$ from high-pressure laboratory experiments) given in Hogenboom *et al*. (1997),

$$T_m(P) = 176.29 + 0.0243P - 7.7583\times10^{-5}P^2 \quad K \qquad (2.10)$$

where the pressure, *P*, is in units of MPa. The melting temperature of ices in the interior of an icy moon is important to determine because a lower freezing point increases the likelihood that an internal ocean may exist. Many volatile-rich moons in the solar system are likely to contain an ammonia dehydrate mixture in their interiors. The following analytical calculations assume a starting pressure of 300 MPa, a typical interior pressure for a satellite the size of Rhea. The melting point for the high-pressure limit of 300 MPa is 176.6 K, and for the low-pressure limit of 40 MPa, the melting temperature is 177.14 K. The full melting curve for ammonia dehydrate ($NH_3 \cdot 2H_2O$) is shown in Figure 2.9.

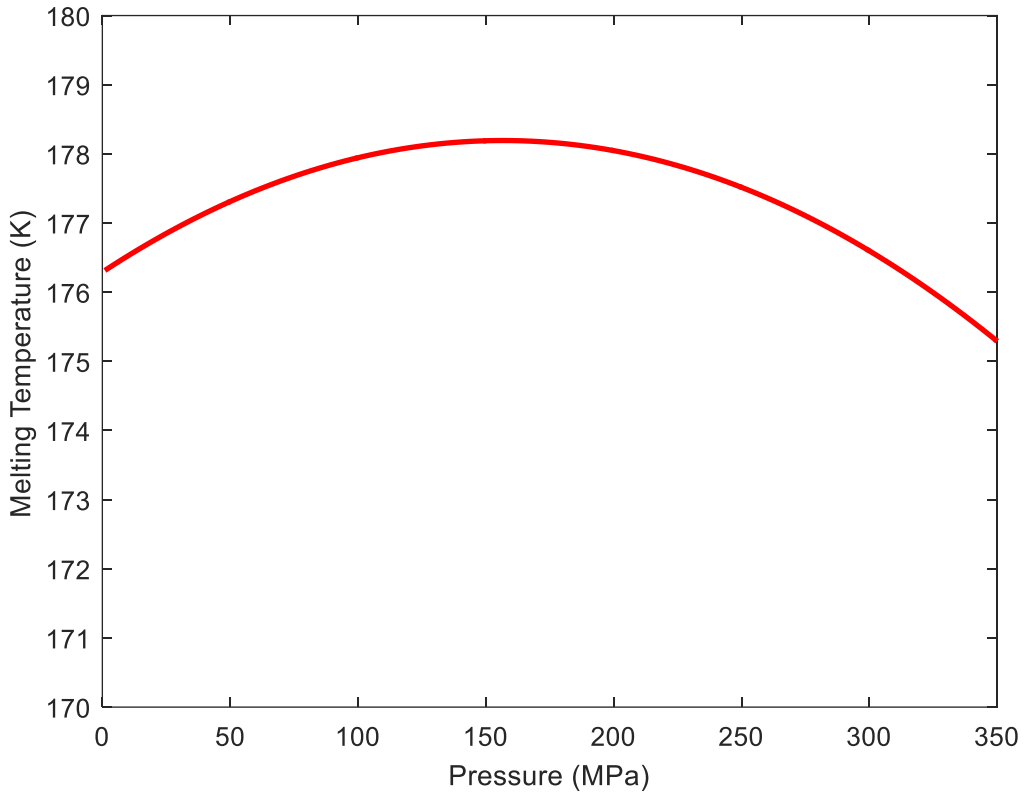

Figure 2.9: Ammonia dehydrate melting curve for temperatures and pressures relevant to the interior of Rhea. The melting curve was computed using a simple MATLAB script. The melting temperature range for this model can be reached in the deep interior of Rhea and Dione due to the heat released from the radioactive decay of long-lived radioisotopes (see Chapter 7).

The melting curve for ammonia monohydrate I, another likely candidate ammonia-water ice mixture in the interiors of icy moons, is represented by a more complex equation determined from high-pressure laboratory experiments (Hogenboom *et al.*, 1997).

$$T_m = 194.05 + 0.04326P - 0.000191974P^2 + 4.4794 \times 10^{-7} P^3 - 4.3266 \times 10^{-10} P^4 \quad (2.11)$$

The calculated melting curve for ammonia monohydrate I over pressures relevant for Rhea is shown in Figure 2.10.

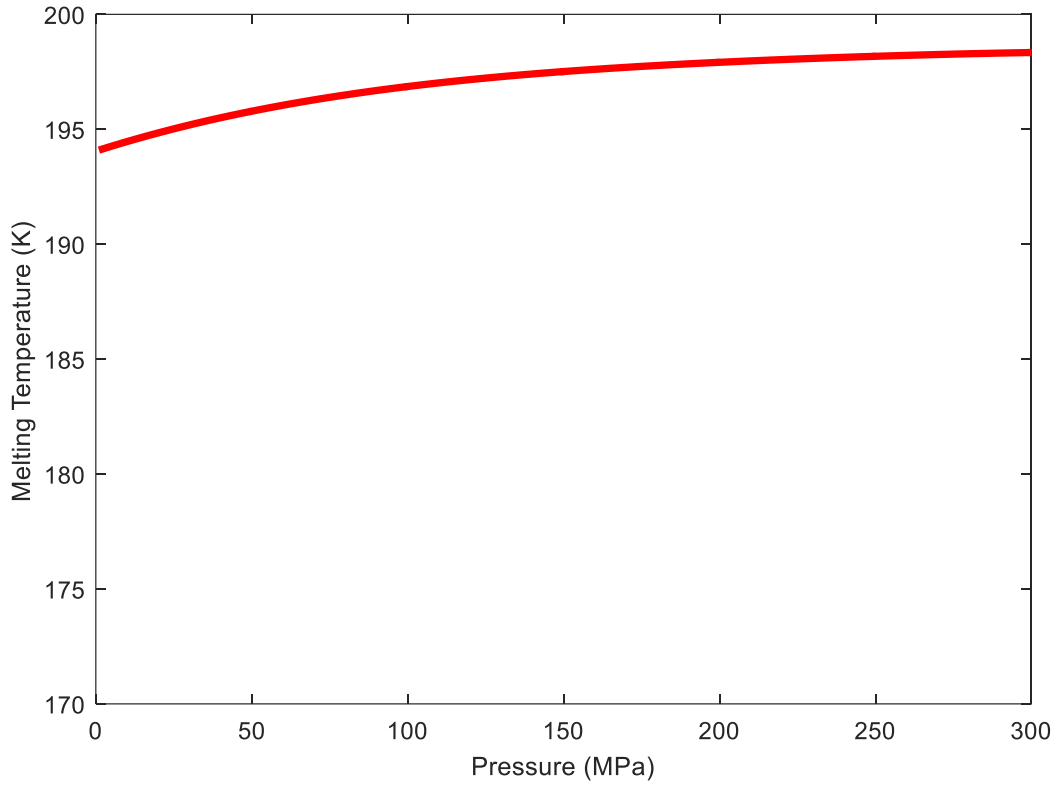

Figure 2.10: Ammonia monohydrate I melting curve for temperatures and pressures relevant to the interior of Rhea. The melting curve was computed using a simple MATLAB script. The melting temperature range for this model can be reached in the deep interior of Rhea and Dione due to the heat released from the radioactive decay of long-lived radioisotopes (see Chapter 7).

For ammonia monohydrate II, the melting curve is described by a simpler relation determined by laboratory high-pressure experiments (Hogenboom *et al*., 1997).

$$T_m = 184.22 + 0.04229P \qquad (2.12)$$

Under the wide ranges of pressures and temperatures of icy satellites in the Jovian and Saturnian systems, ammonia monohydrate could exist, in addition to ammonia dehydrate, in the interiors of these satellites. Both of these mixtures of H_2O and NH_3 are also relevant to astrobiology, in that they represent the simplest molecules that contain different hydrogen bonds present in complex macromolecules, such as DNA. Future work involving high-pressure experiments with H_2O-NH_3 mixtures of different proportions of water and ammonia are needed to explore possible geomorphological features on the surface of Rhea and other icy satellites. The melting of different ammonia-water ice

mixtures at different pressures results in the formation of eutectoid liquids. This process could lead to small changes in the physical properties of the interior of Rhea and other icy moons that lead to observable geological manifestations (Kargel *et al*. 1991, Kargel 1992). Ammonia-water mixtures have similar specific volumes of both solid and liquid phases (Croft *et al*. 1988, Hogenboom *et al*. 1997) with different phases of the ammonia-water system having pressure-related densities and compositions that differ from each other. This leads to changes in the associated buoyancies of the particular phase involved, which can alter the degree of differentiation of the mantle and crust of Rhea (in addition to other icy satellites with a high abundance of ammonia). If cryovolcanic features are observed on the surface of Rhea, the composition of ammonia-water flows could indicate the depth and pressure at which the "cryomagma" originated.

The near-Eutectic point of a water-ammonia mixture has a higher density (~0.970 g/cm^3) than water-ice, or even clathrate hydrates at a temperature near 176 K (Durham, 1993). A positive buoyancy may occur, which could lead to volatile emissions from Rhea without the requirement of a large amount of extrusive materials onto the surface of the satellite (Figure 2.11).

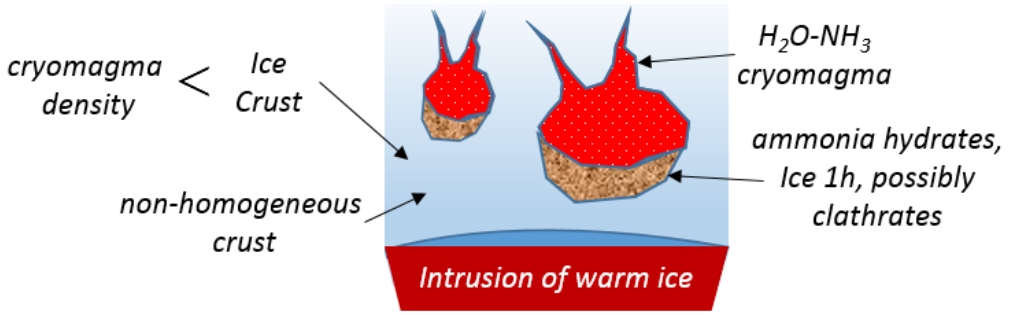

Figure 2.11: A possible scenario for production of cryomagma on Rhea. Cracks form due to a pressure build-up as the release of gas to the cryomagma increases. Figure by R. Mark Elowitz.

If volatile emissions from endogenic processes are present on the surfaces of icy satellites, ultraviolet and infrared reflectance spectra can be used to place limits on their

abundances. In Chapter 3, the basic physics of ultraviolet and infrared spectroscopy are reviewed.

This chapter has provided a detailed review of the Saturnian system and its icy moons, covering Enceladus and its water-ice geysers with minor amounts of organics, the mid-sized icy moons of Rhea, Dione and Tethys, and Titan with its nitrogen-dominated atmosphere. The mid-sized satellites are composed of mixtures of ices and silicates, with the possibility of harbouring subsurface oceans. All of the mid-sized satellites are heavily cratered, with the exception of Enceladus which stands out for having very young terrain. Rhea and Dione appear to be "twin" satellites in that they share similar photometric properties and geomorphology. Rhea and Dione also harbour thin exospheres composed of molecular oxygen and carbon dioxide, indicating a similar process for the formation of their exospheres. Tethys' very low bulk density implies that it is composed of mostly ice, and thus heating of its inside by radioactive decay would be very limited. Rhea's gravity is non-hydrostatic, and combined with uncertainties in its topography makes determination of its interior structure problematic (Tortora, *et al*. 2016). Dione's gravity is also non-hydrostatic, with a moment of inertia of ~ 0.33 (Hemingway, *et al*. 2016) and has a non-compensated ice shell. This suggests that Dione harbours a subsurface ocean (Beuthe, *et al*. 2016). Radioactive decay of the interiors of Rhea and Dione due to long-lived radioisotopes (e.g. Uranium, Thorium, and Potassium) can keep these large satellites warm (Hussmann, *et al*. 2006). Any subsurface oceans maintained by the internal heating tends to freeze over due to the slow decrease in radioactive heating, leading to small changes in the volume of these satellites. The change in volume produces near-surface extensional stress forces (Nimmo, 2004), which could explain the extensional tectonic features observed on the mid-sized icy moons of Rhea, Dione and Tethys (Collins, *et al*. 2009).

The detection of ammonia in the plumes of Enceladus shows that it does exist in the Saturnian system, and could play an important role in the sustainment of subsurface

ocean on Saturn's mid-sized icy moons due to its lower freezing point (Hussmann, *et al*. 2006).

One-dimensional thermal modelling of Rhea near surface shows that its diurnal temperature varies from about 65 to 97 K (section 2.2), providing the temperature range for choosing the appropriate laboratory data used later in this thesis. In section 2.3.1, I described the results from modelling Rhea's interior based on melting curve equations of ammonia dihydrate and monohydrate. The resulting temperature-pressure curves show that Rhea's interior can achieve the low freezing temperatures needed to produce a deep aqueous layer of a mixture of water-ice and ammonia.

CHAPTER 3

ULTRAVIOLET AND INFRARED SPECTROSCOPY

3.1 Introduction

An analysis of reflectance spectra of icy satellites requires a fundamental understanding of the physics and chemistry of UV and IR spectroscopy. This chapter deals with the underpinning chemistry and physics that is relevant to the data analysis of far-UV and IR spectra. Since comparisons with Cassini VIMS and CIRS spectra are an essential part of this thesis, a fundamental description of infrared spectroscopy is also included. A detailed description of electronic transitions (UV spectroscopy) and vibrational/ro-vibrational transitions (IR spectroscopy) is presented. A detailed understanding of spectroscopy as applied to the icy moons of the Saturnian system requires an explanation of how electronic and vibrational transitions are altered depending on the phase (solid or gas) of the chemical compound. Therefore, a discussion of how these spectral transitions are altered in the solid ice phase is included.

A fundamental description of the principle of "Derivative Spectroscopy" that was applied to the analysis of UVIS spectra in this thesis is presented. Although derivative spectroscopy has been used in the analysis of spectra in other fields of science, the technique has not yet been widely implemented within the icy satellite community. The last section of this chapter provides a detailed discussion of the fundamental physics relevant to radiolysis. Radiolysis and space weathering are two important process that occur on the surfaces of icy satellites in the outer solar system. These processes can alter the chemical composition and structure of surface ice on icy moons and thus it is necessary to understand these processes when exploring the chemical composition of surfaces of any ice moon.

3.1.1 Reflectance Spectra

Electromagnetic waves are arranged in the form of a continuum according to frequency and wavelength is known as the electromagnetic spectrum (Figure 3.1). Electromagnetic energy propagates through free space at a velocity equal to the speed of light in the form of sinusoidal waves. The relationship between the frequency and wavelength of an oscillating electromagnetic wave is given by $c = \nu\lambda \ (3.1)$, where ν is the frequency of the wave and λ is the wavelength. When an electric field couples with a magnetic field, electromagnetic waves are formed, with the electric and magnetic field perpendicular to each other and to the direction of wave propagation. The oscillating magnetic and electric fields are produced from the motion of an electron in an electric field, which propagate at right angles to each other in packets of energy called photons. The energy of a photon is given by the direct relationship, $E = h\nu \ (3.2)$, where *h* is the Planck constant, a physical constant derived from quantum mechanics as the "quantum of action". The energy of a photon can be expressed in terms of its wavelength by substitution of $\nu = c / \lambda \ (3.3)$ into the previous relation, giving $E = hc / \lambda \ (3.4)$.

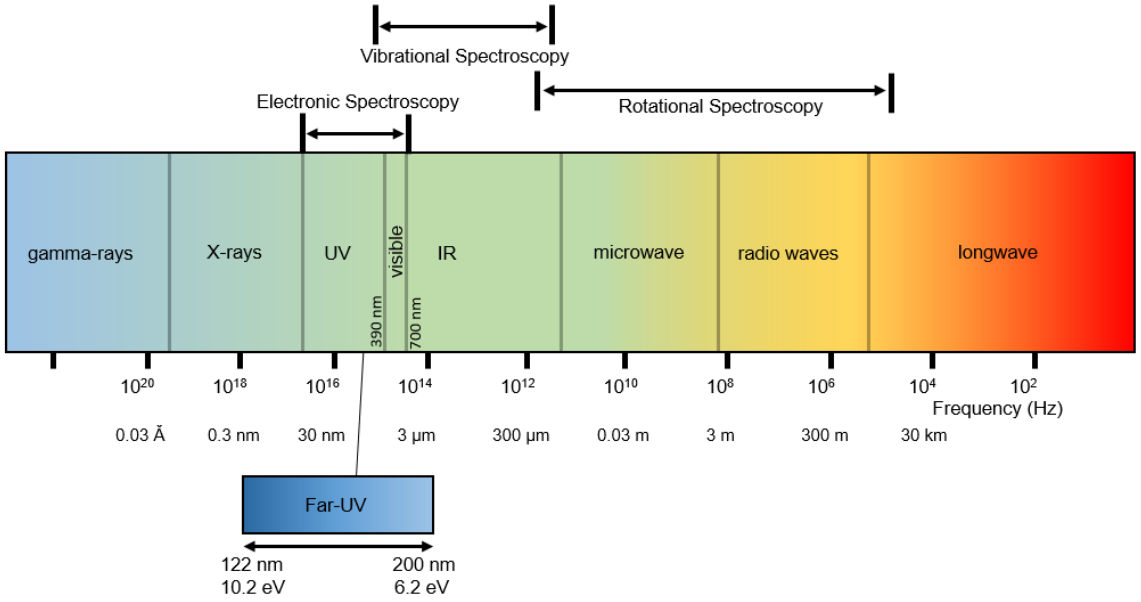

Figure 3.1: Qualitative representation of the electromagnetic spectrum. The electromagnetic spectrum consists of arbitrary divisions of electromagnetic energy according to wavelength and/or frequency. The electromagnetic spectrum ranges from the shortest wavelengths (gamma rays) to longwave radiation. Infrared spectroscopy deals with vibrational and ro-vibrational transitions. Electronic transitions involve the ultraviolet and visible portion of the spectrum. Diagram created by R. Mark Elowitz.

3.1.2 Reflectance Spectra

The foundation of reflectance spectroscopy is based on the principle of scattering. Incident photons on a chemical substance or material are scattered one or multiple times. Some of the photons are absorbed, while others are scattered from the material where they can be detected using spectrographs. The highly nonlinear nature of the scattering process (i.e. a scrambling of information) makes the retrieval of quantitative information from reflectance spectra difficult. The random walk nature of the scattering process increases the visibility of weak features in spectra not normally seen in transmission mode spectroscopy. Greater average path lengths through materials result in an increase in absorption, which can amplify weaker absorption features in reflectance spectra. This is caused by a decrease in the number of photons being absorbed at each encounter. This, in turn, increases the timescale over which the random walk process can occur – i.e. the average path length of a given photon is increased. The physical processes described here make reflectance

spectroscopy an important diagnostic tool for analysing the surfaces of planetary bodies in the solar system.

The depth of an absorption band in a spectrum depends on the abundance of the absorber. I can illustrate this by considering the case of two different minerals (including ice) occupying a given surface, one of which has an absorption band in its spectrum. As the abundance of the second mineral increases, the depth of the absorption feature in the first mineral decreases. Now I consider the case of a reflectance spectrum of a pure substance. As the diameter of particles comprising the substance increases, the depth of the absorption band tends to increase up to a maximum, followed by a decrease in its depth. The particle size of minerals (including ice) can reach a point where the first surface reflection dominates the spectral signature. This first surface reflection prevents the reflectance from reaching zero, with the exception of the case where the index of refraction of the material is unity. This concept is known as band saturation.

The location of the minima of an absorption feature can be shifted in wavelength due to a sloping continuum. The continuum of a reflectance spectrum can be thought of as a contribution from a combination of optical constants for each molecular substance in that spectrum. In reflectance spectra, it can be regarded as the background absorption onto which absorption bands are superimposed. Large absorption band features can have "wings" that also contribute to the background continuum. Nonlinear multiplicative effects arise in the case of reflectance spectra due to Beer-Lambert law (Cruz-Diaz, *et al*) and scattering

$$I_t(\lambda) = I_0(\lambda) e^{-\sigma(\lambda)N} \quad (3.5)$$

where $I_t(\lambda)$ is the transmitted intensity for a given wavelength λ, $I_0(\lambda)$ is the incident intensity, σ is the cross section, and *N* is the average column density.

This means the continuum of a reflectance spectrum should be removed using division when working with absorption or emissive features, and by subtraction when

working with absorption coefficients. Correction for a sloping continuum removes the effects resulting from wavelength shifts in the local reflectance minima.

In reflectance spectroscopy, there are four types of mixtures that can occur. In mixtures at the molecular level, the close contact of molecular mixture components can cause wavelength shifts in the adsorbate. Linear mixtures result when the chemical species are optically separated in the field-of-view of a sensor pixel – i.e. no multiple scattering occurs between components of the mixture. Multiple layers can occur when one chemical species is layered on top of another chemical species (e.g. water-ice on top of ammonia ice). The optical thickness of each layer depends on the wavelength and the physical properties of the layer. Each layer has its own transmission, reflection and absorption properties. Nonlinear mixtures of chemical substances occur when each component of the mixture is in intimate contact. The resulting spectral signature of the mixture depends on the specific optical properties of each chemical component of the mixture. In other words, the spectrum is a highly nonlinear combination of each spectrally pure member of the mixture.

The geometry of the spectral observation (including phase angle, angle of incidence and reflection) can change the proportion of single scattering to multiple scattering, and thus affect the depth of absorption bands. The change in band depth is minimized for cases where multiple scattering dominates. To first order, the depth of an absorption band, its shape and position in wavelength space are independent of the viewing angle geometry. Derivatives of reflectance spectra are insensitive to illumination artefacts resulting from varying collection geometries (Tsai and Philpot, 1998). Changes in the band depths of absorption bands are dependent on the amount of specular reflection that contributes to the total reflected light.

Based on the Hapke reflectance theory (Hapke, 1981) and the optical constants of molecules, it is possible to determine particle grain sizes and quantitative abundances by

inverting the reflectance spectra. Inversion of reflectance spectra to determine abundances and grain sizes of chemical species has been achieved using laboratory spectra (Gaffey *et al*., 1993, Sunshine *et al*., 1990).

3.1.3 Molecular Transitions and Molecular Spectroscopy

There are three fundamental transitions in molecular spectroscopy. The type of transition depends on the change in energy between the lower and upper energy levels. Electronic transitions occur in the visible to UV region of the spectrum, where the wavelength range is $\lambda \approx 0.10 - 0.78$ microns. Vibrational transitions occur in the IR, where $\lambda \approx 0.78 - 10^3$ microns. Rotational transitions are observed in the sub-millimetre region, where $\lambda \approx 10^3 - 10^6$ microns (Stedwell, and Polfer, 2017).

All of these transitions may be used to identify specific molecules in any medium since each molecule has a unique spectral 'fingerprint'. Rotational transitions (GHz) have been widely used in ground-based astronomy to identify molecules in the interstellar medium. IR spectra are widely used to identify molecules in the atmosphere of planets and form the basis of several space-based telescopes. UV spectroscopy has been less widely adopted but forms the basis of the ALICE spectrometers (Stern, *et al*., 2007; Stern, *et al*., 2008) used to explore reflectance spectra of the surfaces of comet 67P/Churyumov-Gerasimenko, the Saturnian system, and the Pluto-Charon system by the Rosetta, Cassini-Huygens and New Horizon's missions, respectively.

3.2 UV Spectroscopy

In recent years ultraviolet spectroscopy has become an important tool for analysing the icy bodies of the outer solar system. This region may be divided into the Vacuum ultraviolet (VUV) approximately 10 nm to 300 nm (Timothy, *et al*. 2013) and the far-UV

region 120 nm to 200 nm (Ozaki, *et al*. 2012). The advantage of UV spectroscopy is that it provides information about the molecular structure and electronic transitions of the chemical substance. There are a copious number of small molecules with a $\pi - \pi^*$ transition (explained later in this chapter) in the far-UV region of the spectrum, and these $\pi - \pi^*$ transitions can be used to identify the type of molecular species (Ozaki, *et al*. 2011). Since each molecule shows a unique spectrum in the far-UV and the spectra are highly sensitive to variations due to their chemical bonding, molecular environments and molecular conformations, it is possible to not only identify the molecular species but probe its environment (e.g. temperature, phase). The approximate locations of the transitions described here are illustrated in Figure 3.2.

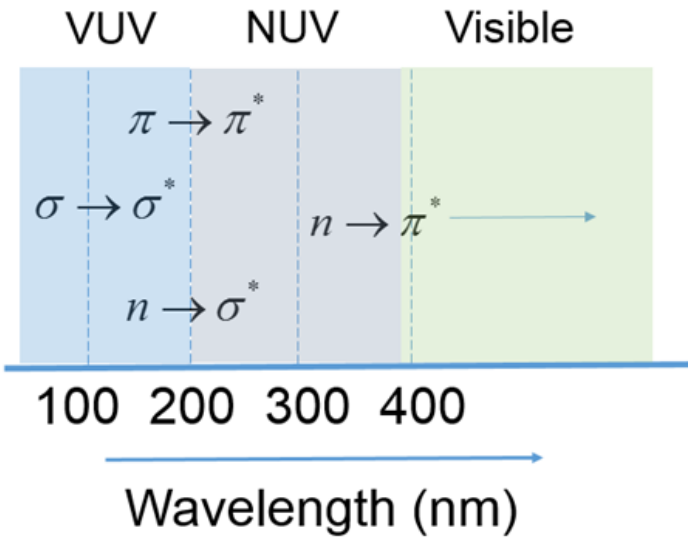

Figure 3.2: Diagram showing the region in the electromagnetic spectrum where different electron's molecular transitions are known to occur. Diagram by R. Mark Elowitz.

However, many molecules of interest to the planetary science community have broad absorption features due to electronic transitions that occur in the far-UV portion of the spectrum. These electronic transitions (Figure 3.3) result in broad absorption bands, in contrast to the sharp absorption bands that occur in the IR due to transitions between the vibrational levels of a molecule.

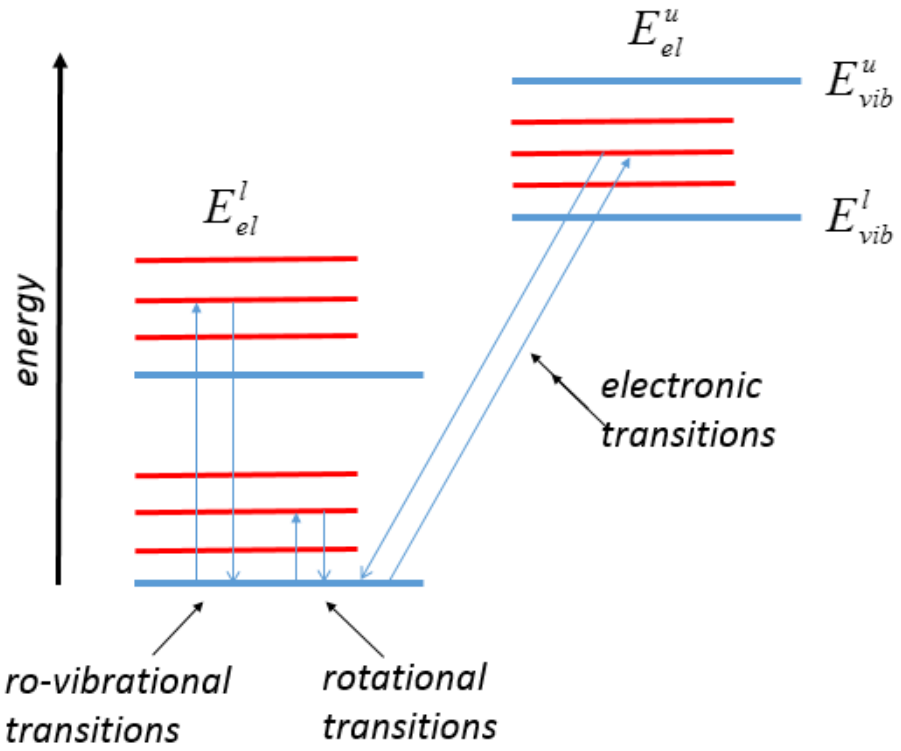

Figure 3.3: Diagram illustrating the difference between electronic transitions, which lead to broad absorption features in the far-UV and ro-vibrational transitions that occur in the infrared. Diagram by R. Mark Elowitz

Larger energy transitions between electronic states in a molecule result in higher frequency transitions (i.e. shorter wavelengths). Molecular transitions of liquid and solid phase chemicals that occur between 120-200 nm are known as far-UV transitions. For example, the electronic transition of water from the molecule's lowest energy produces strong absorption near 150 nm (in the far-UV) (Ozaki, *et al*. 2012). The strength of the absorption band is several orders of magnitude greater than the stretching band of H_2O. It is important to note that changes in the hydrogen bonding in water and molecular density lead to variations in the first electronic transition. In other words, the wavelength of the water absorption feature changes due to phase transitions in water. Far-UV spectroscopy is very useful in that many molecules exhibit strong absorption in this wavelength range. The absorption of solid phase molecules in the far-UV wavelength region between 120 – 200 nm is often very strong. There are many chemical substances that do not show significant absorption at a wavelength longer than 200 nm, but show intense absorption in the far-UV.

Furthermore, the strength and wavelength of the absorption bands are very sensitive to the concentration and temperature of the molecular compound – i.e. the molecular environment. FUV spectra are also very sensitive to variations in chemical bonding and molecular conformations (Ozaki, *et al*. 2011). Molecular conformations are any one of the infinite possible spatial arrangements of atoms in a molecule that can result from a rotation of its constituent groups of atoms about single bonds. Therefore, changes in the environment may change the molecular conformation of the molecule.

When an electron that is located in the highest occupied molecular orbital makes a transition to the lowest molecular orbital that is not occupied, the lowest energy transition typically occurs. The molecular bond (or electron pair) in the UV can be thought of as a mixture of the two contributing orbitals. The lower energy bonding orbital is denoted by (σ,π) and the associated antibonding orbital is labelled as (σ^*,π^*). Note that there is symmetry between the lower and higher energy molecular bonding orbitals. In molecular spectroscopy, the lowest orbitals that are occupied by electrons are usually the σ orbitals. The complementary antibonding orbitals with highest energy are the σ^*. The molecular orbitals denoted by π are in a higher energy state, but their corresponding antibonding orbital are in a lower energy state than the σ^* orbitals (Figure 3.4).

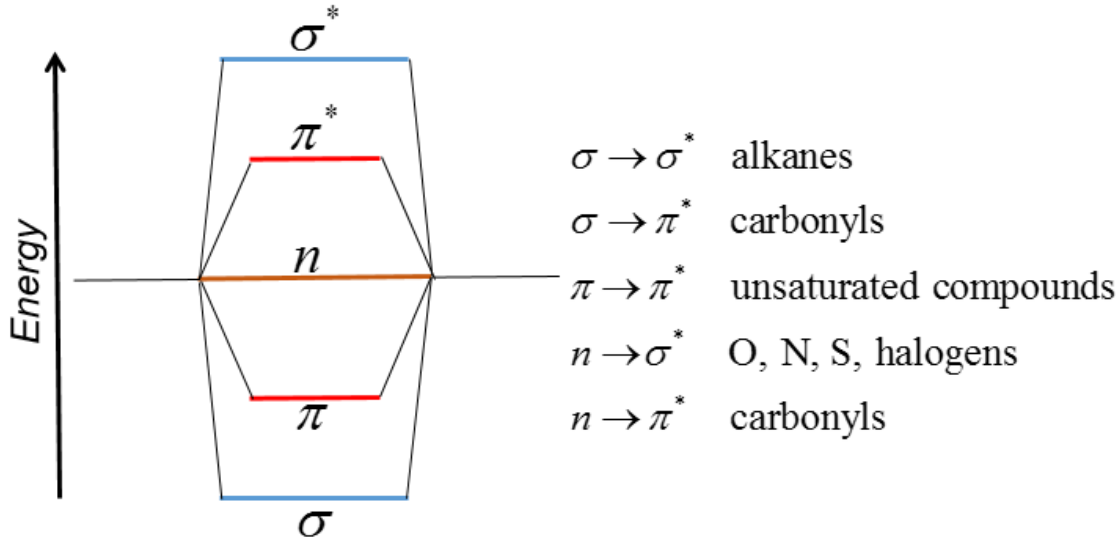

Figure 3.4: Diagram showing typical molecular electronic transitions associated with different chemical species. The possible electronic transitions occur at different relative energies.

In figure 3.4, the $\sigma \rightarrow \sigma^*$ transitions require the largest relative energy, and $n \rightarrow \pi *$ require the lowest energy. Molecules only possessing carbon-carbon single bonds are capable of undergoing $n \rightarrow \sigma^*$ transitions in the wavelength range 150 to 250 nm. Alkanes are chemicals with only hydrogen and carbon atoms. All bonds in alkanes are single. The general chemical formula used to represent alkanes is C_nH_{2n+2}. Methane (CH_4) is one example of an alkane that has been detected on icy objects in the outer solar system in both liquid (Titan) (Tokano, *et al*. 2006), as a solid, and in the form of clathrates (Oliver, *et al*. 2015). Carbonyls are organic molecules with double bonds between carbon and oxygen atoms. Carbon dioxide (CO_2) is an example of a carbonyl, and has been detected on icy objects in the outer solar system in the form of a solid ice (Cruikshank, *et al*. 2010; Filacchione, *et al*. 2016). Most halogens are produced from minerals or salts, and are highly reactive as a result of their high electronegativity of the constituent atoms of the particular chemical species within the group.

It is important to note that not all UV transitions are possible since quantum mechanical "selection rules" must be obeyed in order for an electron to transition.

Examples of quantum mechanical selection rules involve symmetry of the electronic states, symmetry properties of the particular molecule, the number of electrons that can be excited at one time, and the fact that an electron may not change its spin quantum number during a transition – i.e. a "forbidden" transition. "Forbidden transitions", such as the $n \rightarrow \pi^*$ transition in carbonyls, can be routinely observed in the UV, although at low energies. Forbidden transitions are those transitions that are not permitted according to a particular quantum mechanical selection rule, but is allowed in higher order approximations to the selection rule. In other words, forbidden transitions can occur due to the overlap of the current and future states described by quantum mechanical wavefunctions, as operated on by the transition dipole moment. Forbidden transitions have a lower probability of occurrence, and occur at much lower rates.

An example of a $n \rightarrow \sigma^*$ transition is the absorption feature near 184 nm (in the far-UV) due to methanol (CH_3OH), which can be formed by the radiolysis of water-ice and carbon molecules on the surfaces of icy satellites (Nna-Mvondo, *et al*. 2008). Methanol is an important precursor molecule that plays a key role in the formation of ribose when mixed with water and ammonia. Cometary impacts on icy satellites over the lifetime of the solar system could have delivered methanol and ammonia to their surfaces. Irradiation of ammonia, water and methanol by ions originating from Saturn's magnetosphere plasma could lead to the formation of more complex molecules, including sugars (e.g. ribose). The $n \rightarrow \sigma*$ transition in ammonia is responsible for its strong absorption at wavelengths less than 210 nm (in the far-UV). Strong absorption due to the solid phase of water occurs near 144 nm wavelength as a result of its $n \rightarrow \sigma^*$ transitions (i.e. water has two pairs of nonbonding electrons). This transition, also known as the first electronic transition of water $\left(\tilde{A} \leftarrow \tilde{X}\right)$(Ozaki, *et al*. 2011), varies with changes in the molecular density and hydrogen bond structure. The first electronic transition of water in its solid phase plays an important

role in far-UV spectroscopy of icy moons, in that the transition manifests itself as a strong absorption edge observed near 165 nm. The observed absorption edge near 165-nm shows that the icy moons in the Saturnian system are dominated by water-ice.

The $\sigma \rightarrow \sigma^*$ molecular transition of water occurs in the far-UV near 183 nm. This transition manifests itself as an absorption edge near 190 nm as observed in far-UV spectra of icy satellites in the outer solar system. In general, the energy of molecular transitions increases in the following order: $(n \rightarrow \pi^*) < (n \rightarrow \sigma^*) < (\pi \rightarrow \pi^*) < (\sigma \rightarrow \sigma^*)$. The σ-electrons are tightly bound and are localized between two atoms. The π-electrons are more delocalized with respect to the σ-electrons – i.e. they are less bound and thus transitions from π orbitals occur at lower energy (~150-250 nm). The $n \rightarrow \sigma^*$ and $n \rightarrow \sigma^*$ transitions involving non-bonding electrons or "lone pairs" have maximum absorptions that occur in the 150-250 nm region of the UV spectrum. A summary of the different electronic transitions involving the aforementioned *n*, *σ*, and *π* molecular orbitals is given in Table 3.1 below:

Table 3.1: Example electronic transitions for n, σ, and π molecular orbitals

Transition	**Wavelength Range**	**Examples**
$\sigma \rightarrow \sigma^*$	< 200 nm	C-C, C-H
$n \rightarrow \sigma^*$	160-260 nm	H_2O, CH_3OH, CH_3Cl
$\pi \rightarrow \pi^*$	200-500 nm	C=C, C=O, C=N, C≡C
$n \rightarrow \pi^*$	250-600 nm	C=O, C=N, N=N, N=O

It is important to note that the position of different absorption bands in molecules, such as H_2O, can shift when a phase transition occurs (e.g. from a gas to a solid). Thus, it takes higher energy photons (shorter wavelengths) or electrons to photo-dissociate the water molecule when it is in its solid phase (Mason, *et al*., 2006). Solid phase ammonia ice (NH_3) shows an absorption peak near 177 nm, the solid phase absorption peak at 25 K being shifted towards the shorter wavelengths, relative to the gaseous phase at room temperature (Mason, *et al*., 2006). The shift from longer to shorter wavelengths of the absorption peaks in water and ammonia during a phase transition from a gas to a solid is

due to the structure in the hydrogen bonding of the molecules. The hydrogen bonding takes on a more ordered structure during the phase transition (Mason, *et al*., 2006).

3.2.1 UV Spectroscopy of Ozone and Rhea's O_2/CO_2 Atmosphere

As an example of UV spectroscopy identifying a specific molecule in a lunar system consider the detection of ozone on Rhea. Solid O_2 is notoriously difficult to observe in astronomical environments since being a homogeneous diatomic it has no dipole moment to allow it to be detected in the IR. However, the presence of oxygen is felt to be a likely 'biomarker' distinctive of life supporting planetary system. In contrast ozone has a characteristic absorption band in the UV- the Hartley band centred around 260 nm (Teolis, *et al*., 2006). Solid ozone (O_3) is currently being studied in laboratory synchrotron facilities under environmental conditions similar to those on icy bodies in the outer solar system (e.g. NSRRC, Taiwan). Absorbance spectra obtained in the laboratory show that solid ozone not only has strong absorption near 260 nm, but weaker absorption features near 122 nm, 135 nm and 190 nm at 50 K. The 260 nm Hartley absorption feature (due to the $1\ ^1B_2 \leftarrow X\ ^1A$ transition) (Sivaraman, *et al*. 2014) has been observed on several icy satellites in the outer solar system, including Ganymede, Dione and Rhea (Figure 3.5), the first evidence for the formation of this molecule in an extraterrestrial environment. Laboratory experiments carried out by Sivaraman *et al*. (2008) show that the highest concentration of O_3 occurs at low temperatures (< 50 K), due to the confinement of oxygen atoms within the ice matrix. At higher temperatures there are more reaction pathways available due to an increase in migration of oxygen atoms in the ice, which slows down the production rate of O_3. Sublimation at temperatures greater than 80 K can also lead to loss of ozone within the ice.

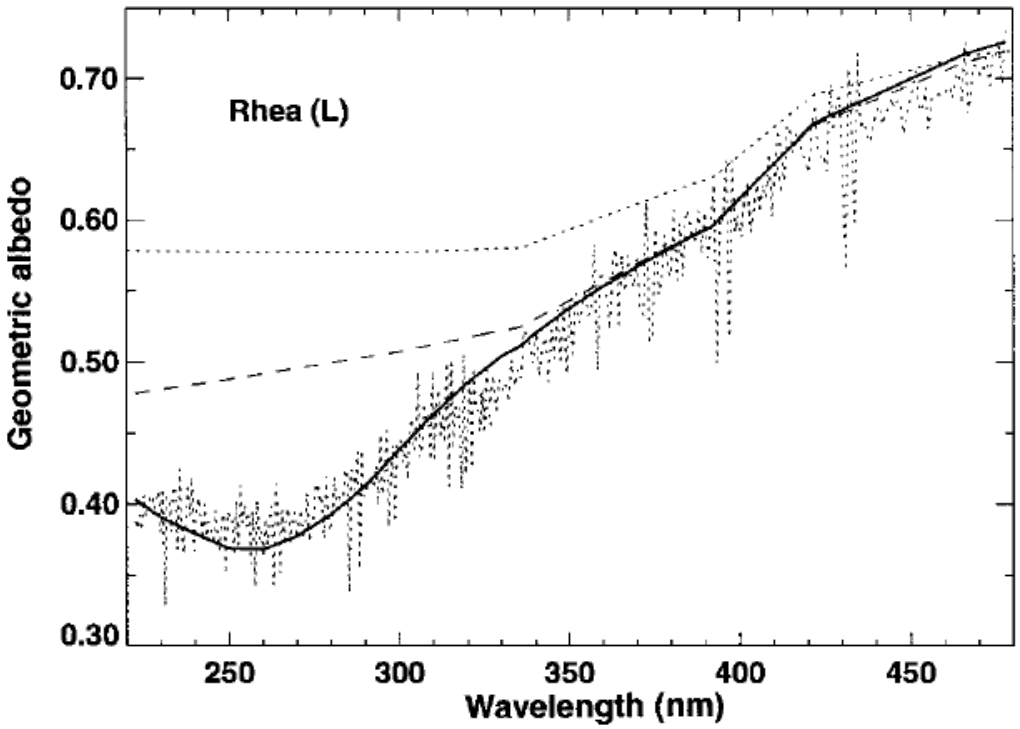

Figure 3.5: Hubble Space Telescope UV spectrum showing absorption near 260 nm due to ozone (O_3) on Rhea's leading hemisphere. The solid curve represents a model consisting of ozone (solid line) overlaid on the HST spectral measurements. The model curve was produced using a mixture of 97.5% ice and 2.5% organic residue. The residue was synthesized by irradiating water-ice and ethane (C_2H_6) using a 6 to 1 ratio, respectively. The upper dotted line represents the H_2O/C_2H_6 mixture, and the middle-dashed line represents an absorber below 477 nm with a constant slope (Noll, et al. 1997).

This discovery questions whether ozone can be used as a unique biosignature and has led to further research on the presence of ozone on other icy bodies and the mechanisms by which it may be formed.

Spectroscopic evidence for ozone has also been detected on Jupiter's moon Ganymede and Saturn's satellites Enceladus (Noll *et al*. 1997; Noll *et al*. 1996) and Dione (Noll *et al*. 1997). Noll *et al*. (1996) detected the presence of the Hartley absorption band due to O_3 on Ganymede's trailing hemisphere using the Faint Object Spectrograph (FOS) on HST. The procedure used to detect the ozone was based on the ratio of FUV spectra of the leading and trailing hemispheres of Ganymede at a particular solar phase angle. The absorption ratio clearly shows the presence of the broad absorption band centred near 260 nm due to ozone on Ganymede's trailing side (Figure 3.6).

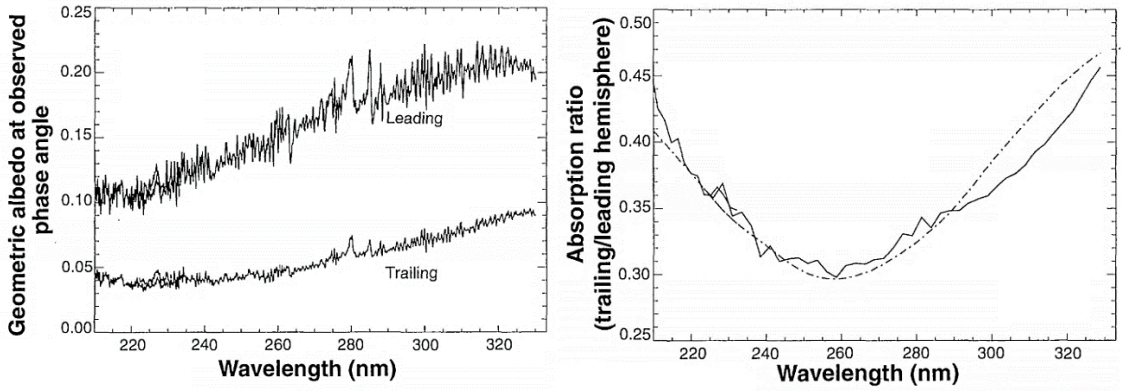

Figure 3.6: HST FOS spectra of Ganymede's leading and trailing hemispheres is shown on the left plot. The Hartley band due to ozone absorption near 260 nm can be seen in the absorption ratio plot shown on the right plot (Noll et al. 1996).

The broadening and shifting of the 260 nm band relative to the gas phase of O_3 implies that ozone is trapped in the form of a solid within the surface ice of Ganymede's trailing hemisphere. The production of ozone on Ganymede's trailing hemisphere could be due to ion irradiation or by photochemical equilibrium with O_2. The production of molecular oxygen (O_2) can take place via photolysis of water-ice molecules on the surface of icy satellites through the chemical reactions

$$\begin{aligned} 2H_2O + 2h\nu &\rightarrow 2OH + 2H \\ &\rightarrow O_2 + 4H \end{aligned}$$

where the hydrogen can easily escape the gravitational field of medium size icy moons, including Rhea. It is also possible that similar reactions can occur via the radiolysis that occurs within the high radiation environment of Saturn. The final result is the presence of O_2, with further radiolysis/photolysis leading to the formation of ozone (O_3). Early laboratory experiments were carried out by Roessler (1991), in which thin water-ice films were irradiated with high-energy protons to simulate the magnetospheric environment of Saturn. The sputtering/erosion of H_2O molecules by protons leads to the production of O_2. Post-irradiated samples of water-ice showed a decrease in the strength of absorption bands due to water-ice. Furthermore, the film specimens were observed to outgas O_2 (Rocard *et al.*, 1986; Benit *et al.*, 1991).

Further evidence for an O_2 – CO_2 exosphere surrounding Saturn's second largest moon Rhea was reported by Teolis *et al*. (2011). The authors used Cassini's Ion Neutral Mass Spectrometer (INMS) during the March 2, 2010 flyby of Rhea to detect the presence of an O_2-CO_2 exosphere. Radiolysis and/or photolysis of H_2O ice explains the presence of molecular oxygen on Rhea, but the source of carbon dioxide (CO_2) remains unclear. A possible chemical pathway to the formation of CO_2 involves the radiolysis of H_2O to form hydrogen and the OH radical. The OH radical could then react with carbon that has been exogenically delivered by carbonaceous asteroids or micrometeoroids to Rhea's surface. This reaction produces an HCO anion, which then reacts with OH to produce CO_2 and H_2, the latter escaping Rhea's exosphere.

$$H_2O \xrightarrow[Radiolysis]{} H + OH$$
$$C + OH \rightarrow HCO$$
$$HCO + OH \rightarrow CO_2 + H_2$$

Current laboratory experiments involving the irradiation of water-ice may help provide clues as to the parent molecule responsible for the production of ozone (e.g. O_2, CO_2). VUV spectra of irradiated O_2 ice collected in the lab under different temperatures, could help determine whether O_2 or CO_2 is the parent molecule responsible for the production of ozone (O_3).

3.3 IR Reflectance Spectroscopy

Infrared spectroscopy yields information about the vibrational modes and functional groups within a molecule. The stretching mode frequencies in the infrared depend directly on the strength of the bonds between two atoms in a molecule, and inversely on the reduced mass of two atoms. Thus, the frequency increases as the strength of the bond increases and as the reduced mass decreases. The intensity of an absorption feature is dependent on the efficiency of energy transfer via electromagnetic waves to

atoms involved in a vibrating molecule. The derivative of the dipole moment with respect to the internuclear distance $\left(\partial\mu / \partial x \neq 0\right)$ determines the strength of a vibrational band in molecular spectra. In other words, higher intensities of absorption involve greater changes in the dipole moment during molecular vibrations. Changing dipole moments during vibrations lead to IR active molecules. Because molecules vibrate at different frequencies due to their different structures, they can be distinguished using infrared spectroscopy. For example, carbon monoxide (CO) has a very small permanent dipole moment, but its dipole derivative is very large. Hence, this heteronuclear diatomic molecule has a very strong absorption in the infrared. The asymmetric stretch mode of CO_2 and the H-Cl stretch of HCl are also examples of IR active vibrations. On the other hand, homonuclear molecules, such as H_2, O_2, and N_2 all have zero dipole moments for all given internuclear distances and therefore, the derivative of their dipole moments is equal to zero everywhere. This is the reason why these molecules possess no vibrational and rotational electric dipole transitions. For transitions between two vibrational levels, those with the selection rule $\Delta\nu = \nu' - \nu'' = \pm 1$ have a higher transition probability than those transitions where $\Delta\nu > 1$. Those molecular transitions with $\Delta\nu = \pm 1$ are known as fundamental bands and those with $\Delta\nu > 1$ are called overtone bands. The most useful region in the infrared lies between 2.5 and 16 microns. Within this region the IR transitions between vibrational energy states originate from both stretching and bending modes. The fundamental modes are observed in the longwave-IR region, from ~7.5 to 16 microns and harmonic/combination modes are observed at shorter IR wavelengths.

In vibrational-rotational IR spectroscopy, each vibrational level is composed of a series of rotational levels (Figure 3.7). Molecular transitions between different rotational energy levels that are associated with the same vibrational level (typically $\nu = 0$) occur in rotational spectroscopy. In contrast, transitions between sets of rotational energy levels, where each rotational level is associated with different vibrational levels, occurs in

vibrational-rotational IR spectroscopy. Hence vibrational-rotational transitions display a number of spectral lines and can be represented by the notation $\nu' J' \leftrightarrow \nu'' J''$, where ν and J denote vibrational and rotational levels, respectively. The notation J'' refers to the rotational ground state and J' to levels in the excited rotational state.

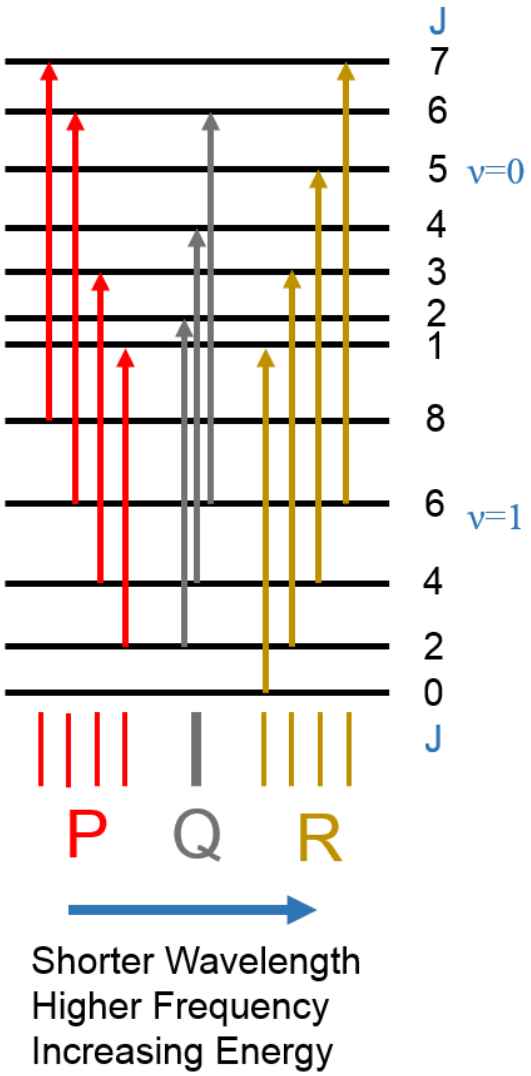

Figure 3.7: Illustration of the molecular energy levels for the carbon dioxide (CO_2) molecule showing how the P, Q, and R branches are produced in a rotational-vibrational spectrum in the IR region of the spectrum. Diagram by R. Mark Elowitz.

On examination of the molecular energy level diagram (Figure 3.7), I see that the P-branch transitions obey the selection rule $\Delta J = -1$ and the R-branch transitions follow the selection rule $\Delta J = +1$. The Q-branch obeys the selection rule $\Delta J = 0$, which is not always allowed.

The intensity (or strength) of an IR absorption feature is proportional to the change in the dipole moment during vibrations. Symmetrical bonds within a molecule with zero dipole moment exhibits very weak absorption or no absorption. Since the frequency tends to show little change with the rest of the molecule for a particular type of bond, the IR region of the electromagnetic spectrum is useful for characterizing the functional groups that exist in a molecule. The particular structure and vibrational modes of atomic bonds in molecules determine the wavelength of IR transitions for various molecules that are relevant to interstellar and planetary spectroscopy. For example, IR spectroscopy can be used to search for organic molecules in the ice layers of satellites in the outer solar system and in the atmosphere of Titan (Stephan, *et al*. 2012; Vinatier, *et al*. 2007; Vinatier, *et al*. 2010; Clark, *et al*. 2010; Dalton, *et al*. 2010). Hydrocarbon molecules are composed of only C-C and C-H bonds, yet there is a copious amount of information that can be extracted from analysing IR spectra arising from the C-H bending and C-H stretching modes. The number of normal vibrational modes for a given molecule in the gas phase with N atoms is given by $3N - 6$. For the case of a linear molecule in which rotation about its molecular axis is not observable, there are $3N - 5$ normal modes of vibration (Coates, 2006). Thus, a linear diatomic molecule has only one normal vibrational mode. When a molecule is in resonance with the frequency of vibration due to the absorption of a quantum of energy, given by the relation $E = h\nu = hc / \lambda$, a molecular vibration becomes excited. When the quantum of energy is absorbed by the molecule in its lowest energy state (or ground state), a fundamental excitation mode occurs. The first overtone is excited when two quanta of energy are absorbed, and as more quanta of energy are absorbed higher overtone modes are excited.

3.3.1 IR Spectroscopy of Water-Ice and its Role in Exploring Ice Morphology

Water-ice is the most abundant volatile on the mid-sized icy satellites in the Saturnian system. Therefore, it is important to review the major IR transitions for this polar inorganic molecule. Water (H_2O) in its gas phase has three fundamental vibrational modes, all of which are active in the IR owing to the molecule's bent structure. The symmetric stretch (ν_1) occurs at a wavelength of 2.73 microns, the asymmetric stretch (ν_3) at 2.66 microns, and the bending mode (ν_2) results in a transition at 6.27 microns (Whalley, 1968) (Figure 3.8).

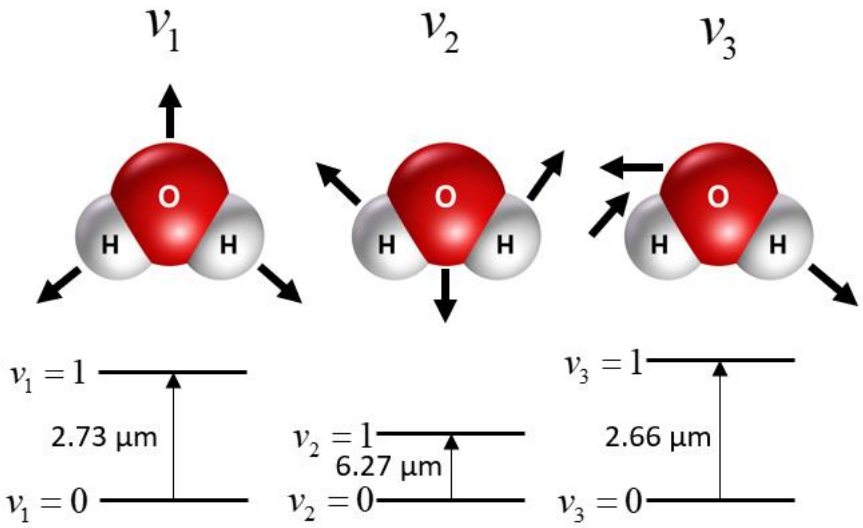

Figure 3.8: Three fundamental vibrational modes of water (H_2O).

In its solid ice phase, the mineral water-ice is capable of producing a copious number of electronic, vibrational, and rotational absorption features. Interactions with nearby water-ice molecules results in the modification of rotational transitions, and the wavelengths of the vibrational bands are shifted (Mastrapa, *et al*., 2009). Due to lattice effects in water-ice in both crystalline and amorphous form, there is additional structure. Furthermore, all transitions due to water-ice are functions of temperature (Mastrapa, *et al*., 2009). In crystalline water-ice, the 3-micron absorption band is shifted to a longer wavelength compared to that of amorphous water-ice due to the increased hydrogen

bonding (Mastrapa, *et al*. 2009). The 3-micron band has been used to determine the phase of water-ice in the interstellar medium, and could be used to determine the phase of water-ice on the icy satellites in the outer solar system.

In IR remote sensing of icy moons, light is scattered multiple times from water-ice grain boundaries, internal voids, inclusions and/or defects in the ice structure. The light that escapes from the surface ice can then be detected using IR spectrometers. The best IR absorption bands used to characterize water-ice on icy satellite surfaces would be those that are intermediate in strength without being saturated. The best candidate absorption band in the IR that satisfies this requirement is the 1.65-micron of crystalline water-ice. The 1.65-micron band is a good discriminator of water-ice in its crystalline form, since it is extremely weak or non-existent in the amorphous form of water-ice (Hansen and McCord, 2004). There are two components near wavelengths of 1.27 and 1.31 microns that are present within a weak water-ice absorption complex at 1.2-1.3 microns. However, since reflectance spectroscopy only probes the upper millimetres of an ice layer, to observe these bands due to crystalline ice would require long optical path lengths (i.e. centimetres) through the ice layer. The surface ice on an icy satellite would need to consist of relatively large ice grains and a very low abundance of impurities to observe these weak absorption features. The presence of crystalline and amorphous ice on icy satellites is governed by two competing processes, the temperature and irradiation of the icy surfaces by charged particles. Icy satellites located further from Jupiter tend to maintain the crystalline form of ice, since they receive a lower charged particle flux. Jupiter's inner moon Europa has a higher abundance of amorphous ice due to the higher charged particle flux from Jupiter's magnetosphere. Saturn's moon Enceladus has both amorphous and crystalline ice as observed in IR spectra. The discrimination between amorphous and crystalline forms of ice is based on the 1.65-micron absorption band (Grundy and Schmitt, 1998), and the Fresnel reflection peak that occurs near 3.1 microns. It is also possible to differentiate between

crystalline and amorphous ice using the 1.5- and 2.0-micron band minimum position (Leto *et al*., 2005; Mastrapa and Brown, 2006; Mastrapa *et al*., 2008). Furthermore, the reduced hydrogen bonding in amorphous ice results in a variation in the position of the infrared absorption bands between the two forms of ice (Brown & Buratti 2006). Crystalline ice is observed near the warm regions located near the sulci in the southern hemisphere, and amorphous ice is observed between the sulci (long parallel groove) regions. The crystalline form of ice can be explained by the higher temperatures, and the amorphous ice could be due to condensation of water molecules ejected from the plumes, rapid freezing due to cryovolcanism, or charged particle irradiation from Saturn's magnetosphere.

The 3.1-micron fundamental band due to the O-H stretching vibrational modes and combination with bending modes is typically saturated in IR spectra of icy moons, but there are cases where a reflectance peak can be observed near the central core of this line. Water-ice grains larger than approximately 1 micron can be identified by the appearance of the 3.1-micron Fresnel peak in IR spectra (Stephan, *et al*. 2012). The Fresnel peak can be used to discriminate water-ice grain sizes on the surface of icy satellites. The Jovian satellites, Ganymede, Europa and Callisto all show the strong Fresnel peak at 3.1 microns, indicative of larger water-ice grain sizes (>>1 micron). In contrast, the Saturnian icy moons Enceladus, Dione, Rhea, and Tethys show a muted or non-existence Fresnel peaks, independent of the varying amount dark non-ice contaminants (Brown, *et al*. 2006; Jaumann, *et al*. 2008). This effect could also be the result of space weathering of the surface material on the surfaces of the Saturnian satellites, which could produce very small particles (< 1 micron) which cover the surface material (Hansen, *et al*. 2005). This indicates that the water-ice grain sizes are much smaller relative to the Jovian satellites (~1-5 microns) (Hansen, *et al*. 2005). Although water-ice is the dominant molecular substance on the mid-sized icy moons of Saturn, other non-water-ice contaminants are

thought to be present in the surface ice. The next section reviews other IR absorption features for chemical species relevant to the icy satellites in the outer solar system.

3.3.2 Review of IR Absorption Features for Molecules Relevant to Icy Satellites in the Outer Solar System

Different molecules show characteristic IR bands and thus observation of absorption at specific wavelengths may be used to identify the molecule present, if not the actual species. Phenol and alcohol molecules tend to show sharp absorption features between 2.70 and 2.86 microns, and broad IR absorption features between 2.78 and 3.13 microns (Billes and Ziegler, 2007). Various acids have very broad IR absorption features between 2.78 and 3.57 microns. The molecular structure of amines and amides results in IR absorption features that occur over the wavelength range 2.86 to 3 microns (Parker, 1971). Molecules with absorption transitions based on the C-H bonds are common, and have absorption features that occur over the infrared region (vibrational) of the spectrum. For example, solid acetylene ice (C_2H_2) has absorption bands over the wavelength range 1.5 to 15 microns (Hudson, *et al*. 2014). This hydrocarbon has been observed in cometary comae, and is thought to originate from cometary nuclei (Mumma, *et al*. 2003). Simple hydrocarbons, including acetylene, frozen methane (CH_4; Pluto), ethane (C_2H_6; cometary comae), ethylene (C_2H_4; Titan), propane (C_3H_8; Saturn's atmosphere) have all been detected using IR spectroscopy (Hudson, *et al*. 2004). Infrared spectra of all Saturn's medium sized icy moons show absorption due to CO_2 (Cruikshank, *et al*. 2010). The O=C=O structure of the molecule produces the well-known absorption band near 4.25 microns. The 4.25-micron molecular transition of CO_2 is produced by its asymmetric stretch mode, and the 15-micron absorption feature is the result of the molecule's bending mode. The symmetric stretch mode is not IR active for CO_2, but the stretching IR mode can be active for other linear molecules.

The detection of CO_2 ice on icy satellites is important in that it provides insight into the circum-Saturnian environment, and information about the chemical pathways leading to the formation of simple and more complex organic molecules (Delitsky and Lane, 2002).

The detection of CO_2 using IR spectroscopy raises questions as to its origin in the Saturnian satellites, and thus the CO_2 known to exist in the tenuous exospheres of Rhea and Dione (Teolis and Waite, 2016). If the CO_2 is native to the Saturn system (i.e. originating from the original condensate in the solar nebula), possible sources include an amorphous mixture with other condensates, or water-ice clathrates in which the CO_2 molecule is embedded. A non-native source of CO_2 would imply irradiation of ices composed of O and C, or UV and particle irradiation (from Saturn's plasma environment) of refractory organic molecules trapped in the water-ice matrix. CO_2 may also originate from an exogenic source (i.e. implanted or deposited from impacts of objects containing carbonaceous molecules). The CO_2 could also be evaporated from a subsurface source and redeposited on the surfaces of icy satellites (Cruikshank, *et al*. 2010).

3.3.3 A Summary of IR Spectral Properties of Saturn's Icy Satellites

Infrared reflectance spectra collected by the Cassini Visual IR Mapping Spectrometer (VIMS) (Brown, *et al*. 2004) show that Saturn's mid-sized icy moons are dominated by water-ice as evident by the well-known absorption bands at 0.9, 1.04, 1.25, 1.5, 2 and 3 microns (Jaumann, *et al*. 2006). The abundance and size of the water-ice grains on the surfaces of icy satellites in the Saturnian system has been mapped using the 2-micron absorption band observed in Cassini VIMS spectra (Jaumann, *et al*. 2006). On some of the icy moons, in localized regions, carbon molecules including carbon dioxide and methane ice, as well as ammonia nitrate and organic substances, have been detected (Dalton, 2007). The identification of organic molecules containing C-H (and possibly C-N

bonds) using Cassini VIMS data on Phoebe, Iapetus and Hyperion are described in Clark *et al*. 2005; Buratti *et al*. 2008; Coradini *et al*. 2008, Cruikshank *et al*. 2008, and Cruikshank *et al*. 2007, respectively.

The presence of non-water-ice contaminants or impurities in the surface ice produces a general positive or red spectral slope between the wavelengths of 0.35 to 0.55 microns (Dalton, *et al*. 2010). A variation in water-ice grain size and degree of contaminants mixed in with water ice produces a variable spectral slope between 0.55 to 0.95 microns (Dalton, *et al*. 2010). For Saturn's moons Iapetus and Hyperion, the spectral slope is positive. The spectral slope is negative for Enceladus, and approximately zero for the mid-sized icy satellites of Mimas, Tethys and Rhea (Dalton, *et al*. 2010). A few IR spectra show a reflectance peak near 0.55 microns.

It has been speculated by Clark *et al*. 2008 and Clark *et al*. 2012 that this peak may be due to Rayleigh scattering from small iron and/or carbon nanophase particles trapped within the water-ice matrix. Iron particles that are sub-micron in size originating from meteorites are thought to oxidize when mixing with surface ice. Evidence to support this finding includes iron particles detected in the E-ring, and iron particles on escape trajectories out of the Saturnian system (Kempf et al., 2005).

Rhea and Dione orbit within Saturn's outer E-ring region and have surface dominated by water-ice with regions of their surface exhibiting low-albedo material. In contrast to Iapetus, these non-water-ice contaminants occur primarily on the trailing hemispheres of the satellites (Clark, *et al*., 2008; Stephan, *et al*., 2009,2010).

Chemicals that could explain the low-albedo contaminant in the visible/NIR and UV on Dione (and throughout the Saturnian system), include nano-phase hematite with trace amounts of CO_2 and/or NH_3 (Clark, *et al*. 2008; Hendrix, *et al*., 2009). There is no evidence for solid CO_2 on Rhea, which according to *Stephan, et al*. 2009, is most likely the

result of the spectral dominance of H_2O. Rhea and Dione both show evidence for absorption centred near 184 nm (0.184 microns) and a shift (and change of slope) of the 165-nm absorption edge due to water ice. Chapters 6 and 7 presents results from an analysis of Cassini UVIS (Ultraviolet Imaging Spectrograph; Esposito, *et al*. 2004) and CIRS (Composite Infrared Spectrometer; Jennings, *et al*. 2017) spectral data that attempts to explain the 184-nm absorption feature and change in the slope and position of the 165-nm absorption edge.

3.4 Derivative Spectroscopy

Derivative spectroscopy (Rojas, *et al*. 1988; Tsai and Philpot, 1998) is an advanced technique used to perform quantitative analysis of UV and Visible/IR spectra. The technique has not been used in the planetary science community to analyse spectral data. Chapter 6 of this thesis explores the use of spectral derivatives to characterize the 165-nm absorption edge of water-ice, and to place limits on the size of ice particles on the surfaces of icy satellites.

Taking the derivative of a spectrum can accentuate very subtle absorption features that would otherwise be very difficult to discern in the first-order spectrum. The accentuation occurs as a result of increasing the signal to background ratio. The first derivative spectrum can be used to quantitatively define the position of the inflection point of steep spectral slopes. For example, the technique of differentiating spectra in the visible-near IR has been successfully applied to defining the position of the red edge feature (a steep inflection in the spectral slope due to strong absorption of vegetation in the red band, and its high reflectivity in the near-infrared band) of vegetation (Kochubey and Kazantsev, 2012). The same technique can be applied to far-UV spectra to derive the position in wavelength space of the 165-nm absorption edge due to water-ice observed on ice satellites. Differences in the grain size and impurities tends to shift the nominal position of

the 165-nm absorption edge. The location of the first derivative peak in wavelength space is sensitive to these two physical properties of the ice mixture.

Derivative spectroscopy can be applied to a wide selection of measured spectra, from laboratory to observed spectra ranging in wavelengths from the far-UV to the infrared. First-derivative and higher-derivative spectra can be computed for spectra collected in units of absorbance (e.g. laboratory ice measurements) and reflectance spectra (e.g. space-based spectral measurements) for use in qualitative and quantitative analysis. Derivative spectroscopy provides the capability to distinguish minor absorption and spectral slope features in spectra, which are greatly enhanced in derivative space. The enhancement of subtle features allows one to distinguish spectra that at first sight appear very similar if not identical and to monitor minor changes in the spectra. Derivative spectroscopy can also be used to enhance the effective resolution, thereby allowing the discrimination of closely spaced or overlapping spectral features.

The first-derivative of a spectrum gives the rate of change of absorbance or reflectance with respect to wavelength. Thus, the units of the y-axis of the first-order derivative spectrum are absorbance or reflectance per wavelength (e.g. reflectance/nanometre, absorbance/nanometre). First-order derivatives have the property that they start and finish at zero. The derivative also passes through its zero point at the same wavelength as the maximum of the absorbance peak in a given spectrum. There are maxima and minima bands on each side of the zero-crossing point of the first derivative. These maxima and minima occur at the same wavelengths as the absorption band inflection points. All odd-order derivatives have this bipolar characteristic.

Second-order derivatives are used to determine the wavelength of minima and maxima of absorption and emission peaks in spectra. In other words, the negative band has its minima at the same wavelength as the zero-order band’s maxima. The second-

derivative also exhibits two sub-bands on either side of the main band. Even-order derivatives show strong positive or negative bands with maxima or minima at the same wavelength of the maxima of an absorbance band in a given spectrum. The observed number of bands is equal to the sum of the order of the derivative plus one.

Derivative spectra are mathematically calculated and re-calculated using different parameters. Smoothing techniques, such as the Savitzky and Golay (1964) can be applied to help mitigate the effects of noise amplification and increase the signal-to-noise ratio in the final derivative spectrum. The first derivative is effectively the rate of change of absorbance with wavelength, and can be expressed mathematically as

$$\left.\frac{ds}{d\lambda}\right|_i \approx \frac{s(\lambda_i) - s(\lambda_j)}{\Delta\lambda}, \quad \Delta\lambda = \lambda_j - \lambda_i \quad (\lambda_j > \lambda_i) \qquad (3.1)$$

where $s(\lambda_i)$ and $s(\lambda_j)$ are two different spectral pixels. Second-order derivatives should not be as sensitive to variations in solar illumination as conventional spectra at high spectral resolutions are. In other words, the derivative spectra minimize additive constants. Another characteristic of derivative spectra is their reduction in sensitivity to variable background reflectance. The derivatives, in theory, should be less affected by variations in illumination intensity due to various sun angles or surface topography (Tsai and Philpot, 1998).

The mathematical expression for the second order derivative is given by (Tsai and Philpot, 1998)

$$\left.\frac{d^2s}{d\lambda^2}\right|_j = \frac{d}{d\lambda}\left(\frac{ds}{d\lambda}\right)\Bigg|_j = \frac{s(\lambda_i) - 2s(\lambda_j) + s(\lambda_k)}{(\Delta\lambda)^3} \qquad (3.2)$$
$$\Delta\lambda = \lambda_k - \lambda_j = \lambda_j - \lambda_i \quad (\lambda_k > \lambda_j > \lambda_i).$$

The general rule for higher-order derivatives is given by

$$\left.\frac{d^n s}{d\lambda^n}\right|_j = \frac{d}{d\lambda}\left(\frac{d^{(n-1)}s}{d\lambda^{(n-1)}}\right) \quad (3.3)$$

where the derivative is typically computed using numerical iterative techniques.

The spectral derivative is highly dependent on the signal-to-noise ratio of the spectrum, but one can partially mitigate this issue by selecting the best portion of the spectrum with highest signal, combined with use of a smoothing kernel. The signal-to-noise ratio of an unsmoothed signal is usually smaller than the original signal, because the amplitude of the derivative is typically smaller. This effect is increased when the derivative of a derivative is calculated (i.e. the second-derivative). To control or mitigate this problem the differentiation of the original spectrum must be performed in combination with sufficient smoothing. There are various smoothing algorithms that can be used, including those which assume that the noise across the spectra does not vary, those that minimize the mean-squared error, and locally adaptive smoothing filters that depend on the signal-to-noise ratio at the particular locality in the spectrum. As the order of differentiation is increased, the amplitude of the noise also increases. However, if the first- or second-derivative spectrum provides a satisfactory result, then increasing to higher orders is not necessary.

Only the first-order derivative is used in the analysis of laboratory and Cassini UVIS data presented in this thesis due to limitations imposed by the noise level of the observational data.

3.4.1 Illustrative Example of the Behaviour of Derivatives

To show how derivatives are applied to the analysis of reflectance spectra, I illustrate their behaviour with a simple example. Figure 3.9 shows three artificial signals generated using the Interactive Displace Language (IDL) software package.

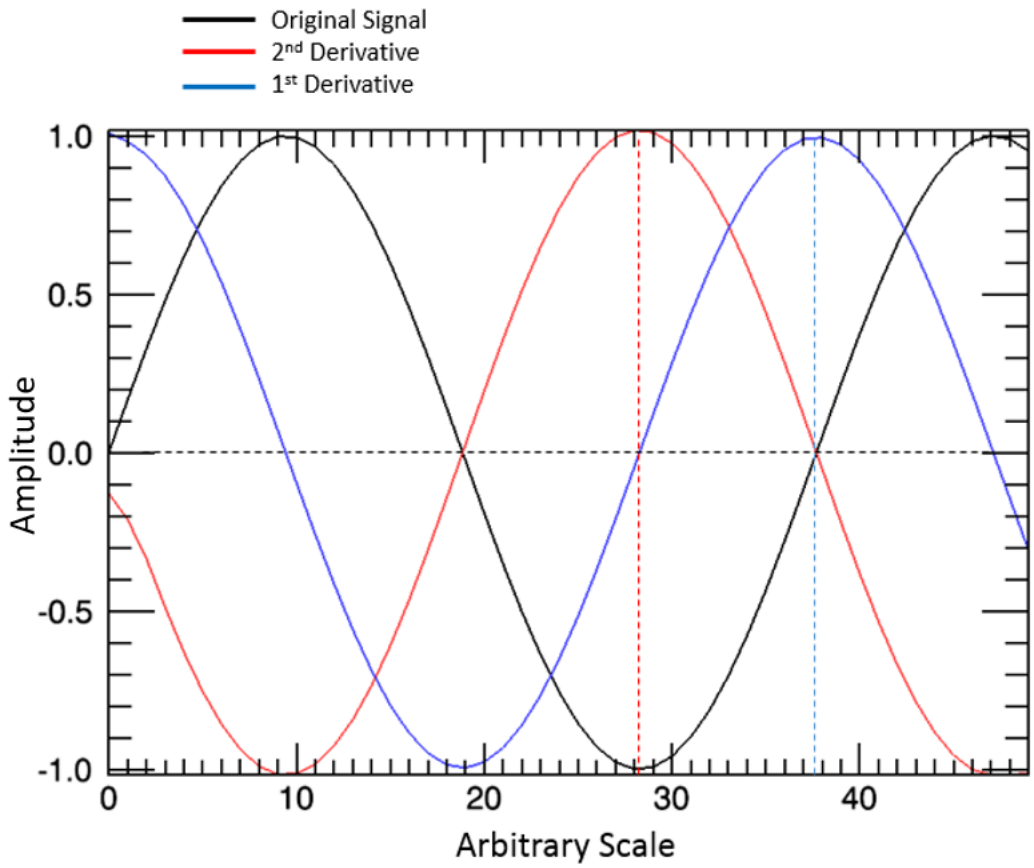

Figure 3.9: Illustrative example showing the behaviour of first and second order derivatives as applied to signal (e.g. spectral) processing.

The black curve represents part of a sinusoidal function. The minimum (representative of the minimum of an absorption band) of the function is located near 28 (a value in an arbitrary scale). The first derivative of the sinusoidal function is shown by the blue curve. The point at which the first derivative crosses the zero-point represented by the black dashed line is the location of the minimum of the original signal (black curve). There are two other zero crossing points, but I am only concerned with the minimum centred near 28 in this illustrative example. The second derivative (shown by the red curve) has its peak at the location of the minimum of the original sinusoidal function (vertical red dashed line). Thus, the first and second derivatives can be used to locate the minima or maxima of functions (signals). The behaviour of first derivatives can also be used to locate the midpoint of any given steep slope. For example, in Figure 3.8 I see that the original sinusoidal signal has a steep slope over the range 30 to 47 on the arbitrary scale. The first

derivative (blue curve) has its peak at the position of the midpoint of the steep slope (vertical blue dashed line). Thus, I have shown how first and second derivatives can be applied to any signal (e.g. spectra) to derive the quantitative locations of absorption lines and steep spectral slopes.

3.5 Radiolysis of Ice Satellites and Space Weathering

Rhea is an ice-covered moon that orbits Saturn with a velocity (8.48 km/s) that is slower relative to the co-orbiting plasma (65.5 km/s for the dominant azimuthal component; Roussos *et al*. 2008) generated in Saturn's magnetosphere. Thus, the moon's trailing hemisphere is preferentially irradiated by plasma and cold ions while the leading hemisphere is irradiated with neutral particles and possible E-ring material (Figure 3.10). Energetic particles from Saturn's magnetosphere lead to bond breaking in molecules in the surface ice, and subsequent radiolysis leads to the production of molecules, such as O_2, H_2, H_2O_2 from H_2O, or more complex organic molecules if carbon- and nitrogen-containing molecules (e.g. CH_4 and NH_3) are trapped in the ice (Cassidy *et al*. 2010).

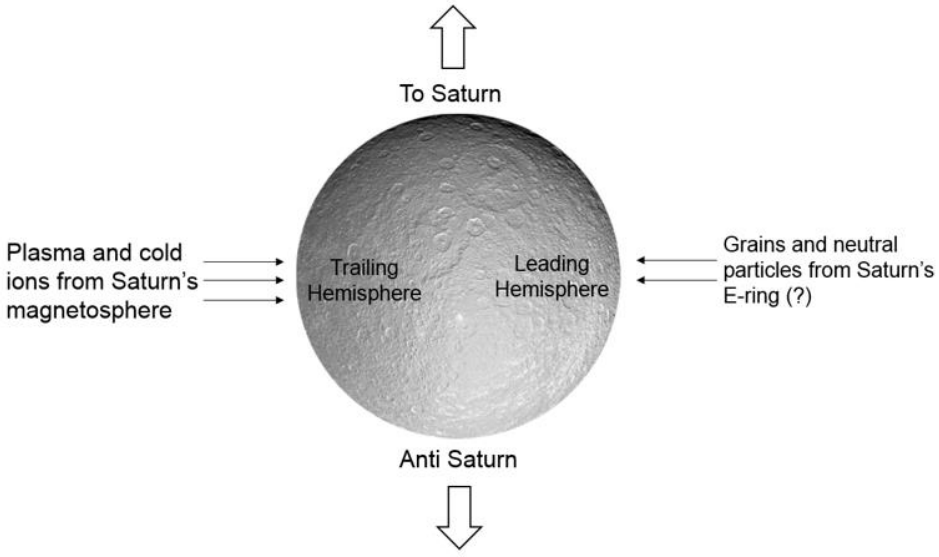

Figure 3.10: Rhea's exogenic environment relevant to the modification of the surface ice. Since Rhea orbits with a velocity that is slower with respect to the co-rotating plasma generated in Saturn's magnetospheric environment, the trailing side is preferentially irradiated with plasma and cold ions. The direction of motion is from left-to-right in this diagram. Diagram by R. Mark Elowitz.

Radiolysis of Rhea's surface may trigger physical and chemical changes in the nascent ices as well as creating defects (bubbles and voids). Annealing of surface ice layers can create vacancies (or voids) within the ice matrix (Gittus, 1978; Scherzer, 1983). These defects within the ice matrix can occur at grain boundaries, or at the interfaces in ice with contaminants. Defects within the ice can allow trapping of gas species, such as H_2O_2, O_3, O_2, and other simple molecules, in the form of bubbles. The interior surfaces of these bubbles can act as sites for chemical reactions among the trapped gases, with relatively high efficiencies. The icy surfaces of satellites are exposed to exogenic processes, including impacts by objects containing carbonaceous molecules, bombardment by E-ring grains, charged particles and plasma. Organic molecules produced by changes in the chemistry resulting from these exogenic processes can be dissociated by energetic particles leading to the formation of more complex molecules (Johnson, 1997; Johnson and Quickenden, 1997; Kouchi and Kuroda, 1990; Sack *et al*., 1992). The surfaces of icy moons can also be brightened in the visible as a result of impacts from heavier (damaging) ions with less-penetration capability (Sack *et al*., 1992). New chemical species can be implanted into the icy matrix by bombardment of charged particles, which can also drive chemical reactions, alter ice grain sizes, and sputter molecules from the surface. Such physical and chemical transformations may be observed by monitoring the UV and IR spectra of the moon's icy surface. The darkening observed in UV spectra of icy satellites is believed to be the result of bombardment of such surfaces by energetic plasma.

Rhea shares several similarities to its neighbouring satellite, Dione. VIMS spectral analysis carried out by Stephan *et al*. (2010) on the leading hemispheres of both satellites show material with a high concentration of water-ice whilst the trailing hemispheres appear to contain dark/organic molecules (including CO_2) trapped within the water-ice and geological young impact craters and tectonic features associated with relatively pure H_2O ice. It is likely that exogenic processes are common to both Rhea and Dione (Stephan, *et*

al. 2012). Analysis of the VIMS data show no correlation between the depth of the water-ice absorption band at 2 microns and variations of the spectral band ratio between visible and UV wavelengths (at 0.5 µm and 0.35 µm) (Stephan, *et al*. 2012) (Figure 3.11). This result was surprising in that the spectral signature on Rhea's trailing side should be dominated by the presence of dark (possibly organic) molecules over the near-UV to visible wavelength range.

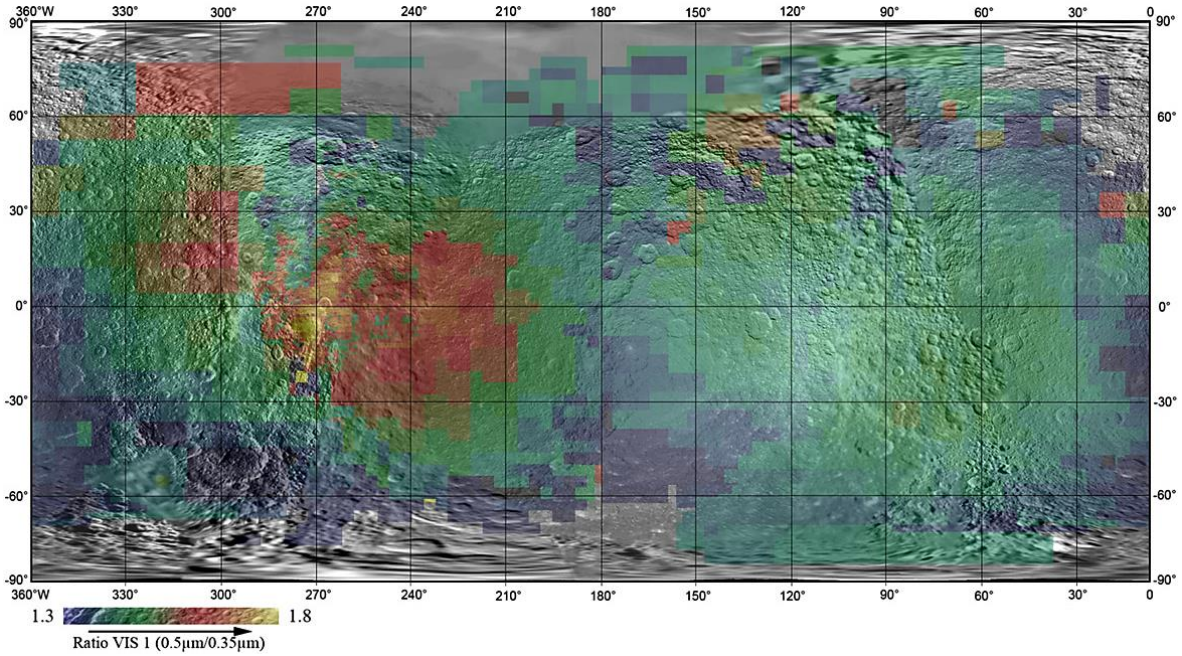

Figure 3.11: VIMS map of Rhea showing the spectral slope variation between 0.5 and 0.35 microns. The spectral slope map was merged onto a Voyager/Cassini ISS base map (Stephan et al. 2012).

At longitudes of 0 and 180 degrees, Rhea faces towards Saturn and away from Saturn, respectively. The spectral slope between 0.5 and 0.35 microns is minimum near the centres of the Saturn- and anti-Saturn-facing hemispheres. This could indicate that the central regions of the hemispheres facing and pointing away from Saturn are protected from the effects of irradiation from plasma originating from the magnetosphere of Saturn, else one would expect an increase in the spectral slope towards the UV. However, it is also interesting that the slope appears to increase on Rhea's leading hemisphere also. Thus, a process (irradiation by magnetospheric plasma, bombardment by E-ring particles, etc.) that

is common to both hemispheres (global in nature) may be currently operating on Rhea (Stephan, *et al*. 2012).

Radiolytic reactions due to high-energy particles originating from Saturn's magnetosphere, and dust impacting the trailing hemispheres of both satellites must be occurring. Space weathering due to micrometeoroid bombardment over long time spans, electrons from Saturn's magnetosphere, and possibly particles from Saturn's E-ring impact the leading hemispheres of both satellites. Impacts from asteroids and/or comets could excavate local areas of fresh water-ice from the subsurface layers. The stronger water-ice absorption bands and lower visible albedo seen in VIMS spectra of Rhea's leading hemisphere (Stephen *et al*, 2012), could be partially explained by the continuous mixing of surface layers with layers of fresh water-ice located beneath. Mixing could then result from the bombardment of micrometeorites that preferentially impact the leading surfaces of Rhea, and the icy satellites Dione and Tethys.

The orbital geometry between Saturn's E-ring and Rhea is such that at apoapsis (the furthest distance of an object from the centre of the primary body), the small E-ring particles (<1 μm) on eccentric orbits would impact the satellite's leading hemisphere (similar to Dione and Tethys) (Horanyi *et al*. 1992). The fine E-ring particles would affect Rhea's leading side in a way that would be similar to the effects caused by water group ions impacting the satellite's trailing side. This could explain the global trend of a suppressed Fresnel reflectance peak at 3.1 microns across both hemispheres of Rhea.

Saturn's radiation belt is composed of electrons with energies in the keV range that have their highest flux at approximately the radial distance of Rhea and Dione (Carbary *et al*. 2009; Paranicas *et al*. 2010). Figure 3.12 shows a numerical model of electron energy levels produced using the SATRAD model (JPL 2005). As seen in the plot of electron flux versus radial distance, there is an increase in the flux at the radial distances of both Dione and Rhea, for energies of approximately 100 keV.

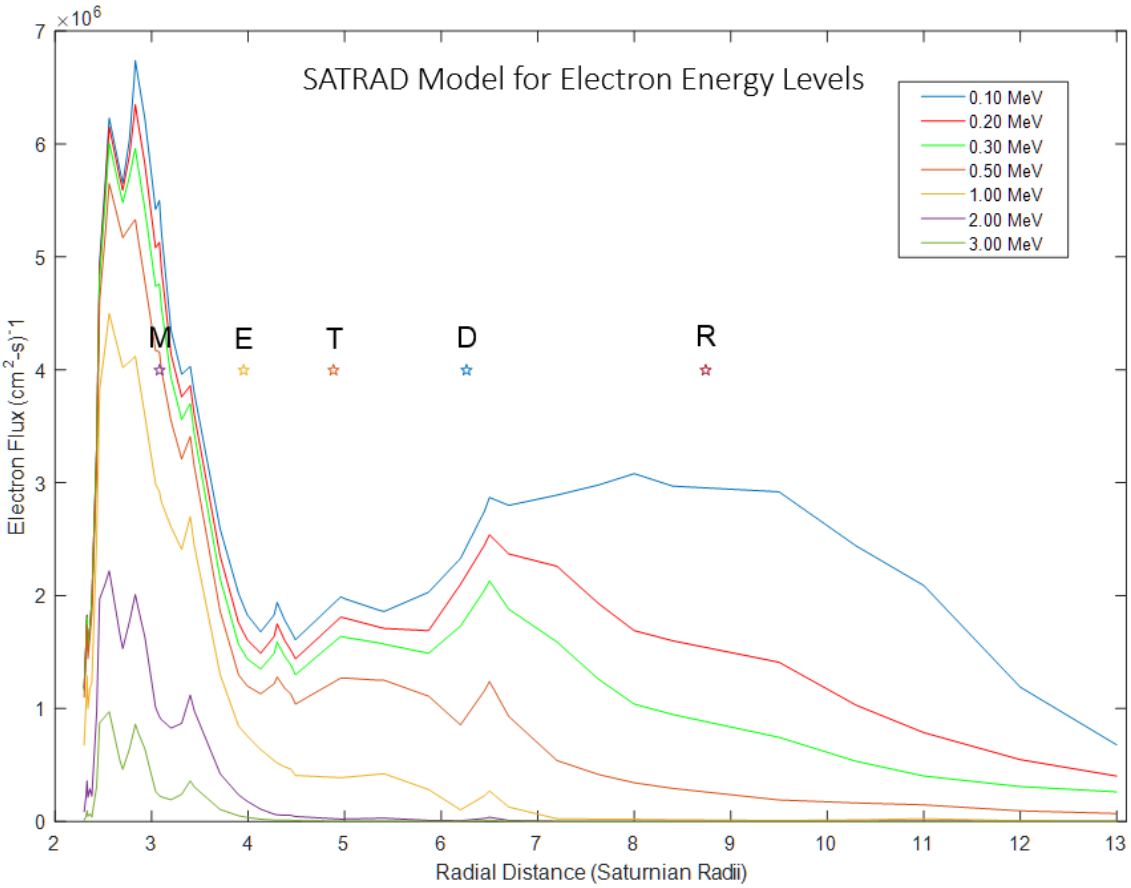

Figure 3.12: A numerical model of the electron flux at Saturn's equator as a function of radial distance for different energy ranges is computed using the SATRAD model (JPL 2005). The radial distribution of the electron flux increases to a local maximum near the locations of both Dione and Rhea, for electron energies of approximately 100 MeV. Model computed by R. Mark Elowitz.

The retrograde motion of the energetic electrons around Saturn results in their impact onto Rhea's and Dione's leading hemisphere, in contrast to magnetospheric ions that impact the trailing hemispheres of Rhea and Dione. The interaction with water-ice molecules located on the surfaces of the leading hemispheres of the two moons (i.e. sputtering of H_2O molecules) could lead to the formation of ozone (O_3) and molecular oxygen (O_2) via radiolysis. It is already suspected that such radiolysis occurs on the trailing side of Rhea, leading to the same products. This is due to the fact that both Rhea and Dione have relative velocities that are slower than the co-rotating plasma in Saturn's magnetic field. The production of O_3 on Rhea observed by Noll *et al*. (1997) could explain the global trend in the change of slope between the visible (0.50 μm) and UV (0.35 μm)

derived from VIMS observations. The change in the visible to UV slope could also explain the recent detection of O_2 in the tenuous atmosphere surrounding Rhea (Teolis *et al*. 2010).

The composition of the dark material observed on Rhea, Dione, Hyperion, Iapetus and Phoebe has not yet been identified, with the exception of minor amounts of CO_2 detected at 4.26 microns. Clark *et al*. (2005) claimed to have detected an overtone absorption band near 2.42 microns due to CN in VIMS spectra of Phoebe. However, no fundamental absorption bands of CN have yet to be detected between 4 to 5 microns. At present, the best candidate to explain the 2.42-micron feature is the hydroxyl radical OH, although wavelength calibration issues in the VIMS spectra prevent a definite determination of this absorption band (Clark *et al*. 2008a, b, 2009).

Cruikshank *et al*. (2014) modelled the dark material on Iapetus in order to explain the reddened visual spectral slope. Tholins (complex organic substances) were used in the spectral models to explain the dark material on Iapetus. However, the high spatial resolution capability of the VIMS instrument was able to separate the icy regions from the dark material in order to obtain detailed spectra of the non-water-ice component. The non-linear spectral response in the IR region of the spectrum that tholins exhibit was not seen in any of the VIMS spectra of the dark material on Iapetus. The strong absorption due to CH in the 3 to 4-micron range, a property inherent to tholins, was also not observed in VIMS spectra. In contrast, analysis performed on VIMS data by Coradini, *et al*. 2008 of Phoebe indicate the presence of the aliphatic CH stretch spectral signature at 3.53 and ~4.4 microns, which could be related to cyanide molecules. Coradini, *et al*. 2008 also claim a strong correlation between aromatic hydrocarbons (with exposed water-ice) and carbon dioxide (CO_2), and an anticorrelation between cyanide molecules and CO_2.

Many of the Saturnian icy satellites (including Rhea and Dione) appear to show a blue scattering peak in their spectra of dark material (Noland *et al*. 1974). The blue peak implies the existence of tiny particles (< 0.5 microns) mixed in with surface ice. The

existence of the blue scattering peak in the spectra of dark materials on icy satellites within the Saturnian system seems to imply a common process responsible for the scattering. A mixture of water-ice/nano-phase hematite/nano-phase metallic iron represents the best fit to the VIMS spectra of dark material mixtures on Saturn's icy satellites (Clark *et al*. 2009). Furthermore, the oxidation of iron particles to the nano-hematite state (Fe_2O_3) by the reactive dark material seen on icy moons in the Saturnian system, can explain the red slope response of UV absorption data collected for Dione (Clark *et al*. 2008). The exogenic delivery of sub-micron iron particles from meteoroid impacts could also explain the blue spectral peak due to Rayleigh scattering off small iron particles, with dimensions less than the wavelength of radiation. It is also interesting to note that the shape of the visible to near-UV (at a cut-off wavelength of 0.3 microns) spectrum would not be influenced due to organics, ammonia and CO_2 in trace amounts. Thus, Cassini UVIS/VUV spectra provide a new opportunity to search for these molecules. The lack of observational evidence for iron particles on Saturn's inner satellites could be due to shielding of the particles by ice grains originating from Saturn's E-ring as they mix with the iron particles.

Supporting evidence for the existence of iron in the Saturnian system is provided by Kempf *et al*. (2005). The team found very small particles with sizes less than 20 nm on escape trajectories out of the Saturnian system using the Cassini CDA instrument. The Cosmic Dust Analyser is capable of measuring the dust particle's chemical composition, size and velocity within the Saturnian system. Kempf *et al*. (2005) found that the small particles had a composition of iron, silicon and oxygen, in addition to minor amounts of ammonium, water-ice and possibly carbon. The iron oxide particles may originate from impacts of meteoritic dust, external to the Saturnian system, and may be responsible for the space weathering observed on several of the Saturnian icy satellites (Chapman 2004).

Irradiation from Saturn's plasma environment can alter the molecular environment in the surface layers of water-ice molecules (plus any non-water-ice impurities that may be

present). The chemical composition of the ice layer is altered over geological timescales. These two changes can alter the position of spectral absorption bands as well as the thermophysical properties and optical scattering properties of the ice by producing defects in the molecular structure of the ice.

Both energetic particle irradiation and impact weathering from micrometeoroids result in the vertical mixing of chemical reaction products due to radiolysis of the molecules present in the upper ice layer. In other words, the chemical reaction products from electron, proton and ion irradiation of water-ice molecules and impurities in the ice are buried by long-term micrometeoroid bombardment. At the same time chemical products from radiolysis are brought towards the surface by the same micrometeoroid weathering process. Hence, the radiolysis products are vertically mixed throughout the uppermost ice layers. Irradiation doses of only a few eV can lead to significant changes in the chemical composition of the ice layers over the history of the satellite (Schmitt *et al*., 1998). Thus, alteration of the molecules within the ice "regolith" has occurred many times over the lifetime of the satellite.

VIMS observations of relatively young impact craters could provide clues as to the internal structure of the outer layers of Rhea. Melosh (1989) provides an estimate of for the depth of the Inktomi impact crater of approximately one-tenth the crater's transient diameter. For a diameter of 48 km based on recent ISS imagery, this yields a crater depth of 4 km. The presence of a strong IR spectral signature due to clean water-ice, and the fact that there are no minor impurities seen in the VIMS spectra at the Inktomi impact site (Figure 3.13), implies a depth of at least 4 km for the clean ice layer.

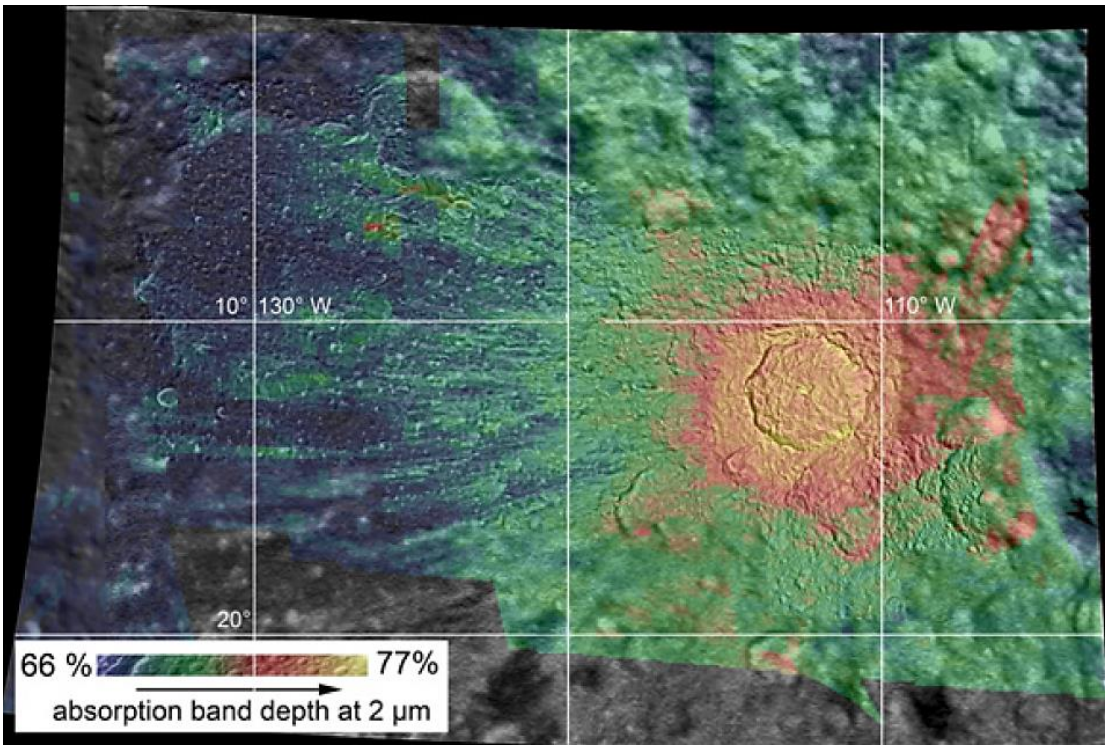

Figure 3.13: A VIMS map of the impact crater Inktomi showing the purity of water ice based on the 2-micron absorption band depth. Note the gradient in the band depth, being strongest at the centre region of the crater and decreasing outward (Stephan et al. 2012).

This 4 km deep layer of clean water-ice lies beneath a thin layer of ice subjected to space weathering from micrometeoroid bombardment. This scenario does not seem to support the common model for Rhea's interior composed of 75 percent ice and 25 percent rock/metal, homogeneously mixed with an average density of 1233±5 kg/m^3 (Anderson & Schubert, 2007; Anderson & Schubert, 2010). In contrast, a partially differentiated model of Rhea consisting of a large rocky/ice core with a uniform mixture, enclosed by a thin layer of ice (Castillo-Rogez, 2006; Iess *et al*. 2007) (Figure 3.14), appears to provide a better match to the VIMS observations. The latter model would also support an exogenic origin for the dark (possibly organic) material observed on Rhea's trailing hemisphere due to radiolytic contamination of the ice layer over a long-time span (geologically speaking).

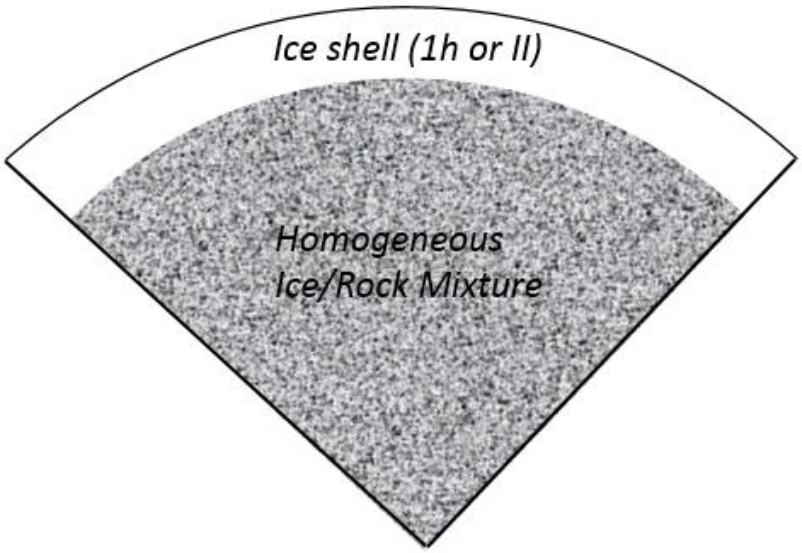

Figure 3.14: Diagram showing partially differentiated model of Rhea (figure adapted from Castillo-Rogez 2006; Iess *et al*. 2007).

3.6 Interaction of Surface Ice Molecules with Ions Originating from Saturn's Magnetosphere Environment

Incident radiation from Saturn's magnetosphere can ionise water molecules, leading to the production of H^+, H_2O^+, OH^+, and electrons. $H_3O^+ + OH$ is formed rapidly from reaction of H_2O^+ in water ice, and through the process of neutralisation OH, H, H_2, and O are formed via dissociative recombination. The following exothermic reactions can then occur (Cooper, *et al*. 2008; Johnson, 1997):

$H+OH \rightarrow H_2O$
$O+O \rightarrow O_2$
$O+H_2 \rightarrow H_2O$
$H+H \rightarrow H_2$
$O+H \rightarrow OH$
$O+H_2O_2 \rightarrow O_2+H_2O$
$OH+HO_2 \rightarrow O_2+H_2O$
$O+OH \rightarrow HO_2 \rightarrow H+O_2$
$O+HO_2 \rightarrow O_2+OH$
$OH+OH \rightarrow H_2O_2$
$H+O_2 \rightarrow HO_2$
$OH+H_2O_2 \rightarrow HO_2+H_2O$

Due to the high porosity (60-90%) of the surfaces of icy satellites, there is a large surface area available to incident ions from Saturn's magnetosphere, the geometric area being much less than the effective surface area. Diffusion of H and O can occur throughout ice grains, and large amounts of hydrogen peroxide (H_2O_2) and molecular oxygen (O_2) could therefore exist within the porous surface of an icy satellite, such as Rhea. Some of the O_2 that migrates to the interface region between the vacuum of space and the surface ice can then escape, forming the tenuous atmosphere of oxygen surrounding Rhea (Johnson *et al*., 1982; Johnson and Quickenden, 1997). The remaining O_2 is adsorbed, or is trapped as gas phase within the porous ice of Rhea. Molecular oxygen that is produced within an interior void of sub-surface ice remains in that location until it is released to the surface via radiolytic reactions induced by ion irradiation.

Ozone (O_3) can then be produced by radiolysis resulting from heavy ions, or by radiolytic reactions involving O_2 (Cooper, *et al*. 2008). Ozone can also be synthesised via a chemical pathway involving the irradiation of CO_2 (Boduch *et al*., 2011). Boduch *et al*. 2011 state that due to the low temperatures (50-100 K) at the surface of Saturn's icy satellites, it is difficult to trap O_2, thus CO_2 represents a better candidate as the parent molecule of ozone. Observational evidence of radiolysis of O_2 in surface ice due to ion bombardment from Saturn's magnetospheric plasma would be the detection of intermediate radicals, such as OH. Ozone can also be created by photolysis of O_2 that exists in the porous ice layers of icy satellites. This leads to an increase in O_3, whose abundance is constrained only by the quenching of the O (^{1}D) state. In contrast to molecular oxygen with weak absorption, ozone should, in theory, should be easier to detect as a result of its strong absorption band near 260 nm. In fact, ozone has been tentatively attributed to spectroscopic features of Ganymede (Noll *et al*., 1996; Hendrix *et al*. 1999), Rhea and Dione (Noll *et al*., 1997). The location of this band may shift, depending on the phase of

the ozone (trapped as gas bubbles within the porous ice, in solid form, or bounded to water) (Schriver *et al*., 1990).

The rate of formation and destruction of H_2 in the surface ice governs the depletion rate of H in the ice layer. This, in turn, governs the amount of OH in the form of HO_2, H_2O_2, or as OH. Hydrogen peroxide (H_2O_2) has been observed on Jupiter's moon Europa, and is produced by energetic radiation of its surface ice (Carlson *et al*., 1999). It is formed when H reacts with O_2 to form HO_2, followed by H + HO_2 to produce H_2O_2 (Moore and Hudson, 2000; Cooper *et al*., 2006). At temperatures similar to those on Saturn's icy satellites (~80 K), the most commonly proposed chemical pathway to form H_2O_2 is that of the reaction of two OH radicals (OH+OH $\rightarrow$ H_2O_2; Cooper *et al*., 2008) (Figure 3.15). The formation of hydrogen peroxide from the combination of two OH radicals can be explained by an increase in the diffusivity of the OH radicals within the water-ice lattice as the temperature rises. At lower temperatures, the OH radicals remain strongly hydrogen bonded to water molecules (Cooper *et al*., 2003). At temperatures exceeding ~100 K, experiments show a decrease in the abundance of H_2O_2 by reactive species such as OH radicals or electrons (Cooper *et al*. 2008).

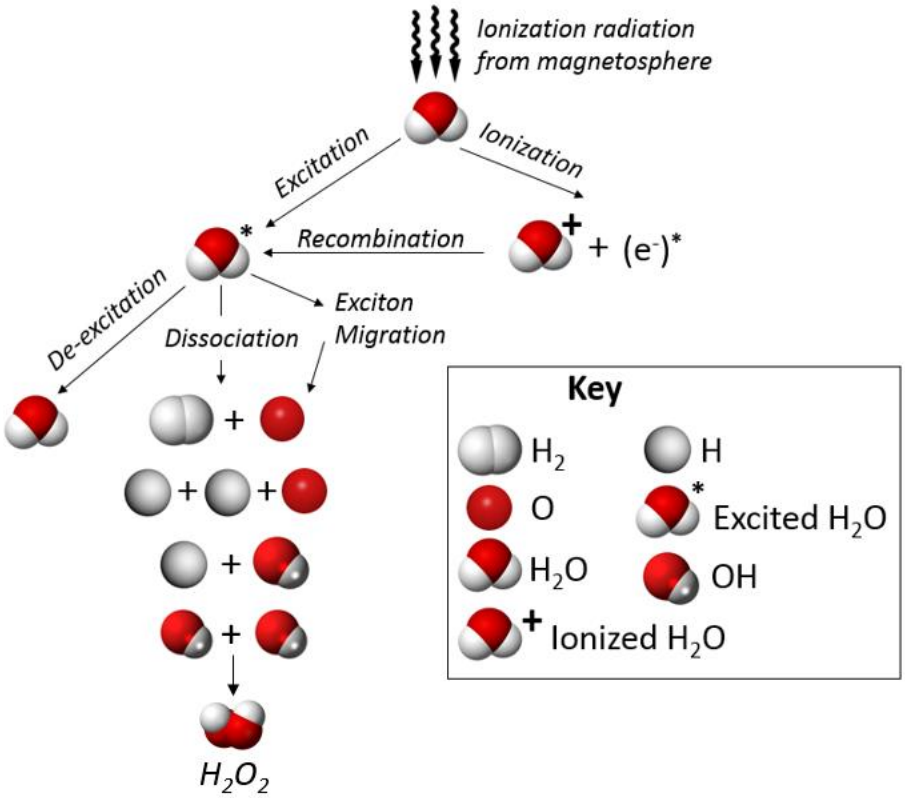

Figure 3.15: One possible chemical pathway leading to the production of hydrogen peroxide (H_2O_2) when water-ice molecules are subjected to ionizing radiation from Saturn's magnetosphere.

In contrast to the Jovian system, in the Saturnian system where the energetic particle fluxes are greater, hydrogen peroxide (H_2O_2) may be difficult to observe on Rhea and other icy satellites, since its photodissociation time scale would be much less than that of O_2, by about an order of magnitude. The form of H_2O_2 on cold icy satellites that orbit Saturn should be that of a dispersed $H_2O_2 \cdot H_2O$ compound. In contrast, on icy satellites where the surface temperatures are higher (greater than about 150 K), which occur for some of the Jovian moons, the dehydrate form of hydrogen peroxide is expected due to rapid precipitation and crystallisation. The particular phase of hydrogen peroxide in ice could be deduced by examining the 3.5-micron signature in the infrared, and from UV reflectance spectroscopy (Hendrix *et al*. 1999).

In summary, a variety of oxidizing molecules (e.g. H_2O_2, O_3, OH, HO_2, and HO_3) are all synthesised in H_2O+O_2 ices by radiolytic reactions. These oxidizing chemicals are probably part of an inventory on icy moons, including Europa and Enceladus, and may

play an important role in delivery of chemical energy to sub-surface oceans that may potentially harbour primitive life.

3.6.1 Radiolysis of Solid Carbon Dioxide Ice on Rhea

If minor amounts of carbon dioxide (CO_2) are mixed with water-ice on the surface of Rhea, then irradiation by high-energy particles from Saturn's magnetosphere can lead to chemistry involving the dissociation of H_2O and CO_2,

$$H_2O + h\nu \rightarrow OH + H$$
$$CO_2 + h\nu \rightarrow CO + O,$$

which produces ionised, excited and neutral species including HO_2, H_2O_2, O_2, H_2, HCO, O, H and ozone (O_3) (Boduch *et al*., 2011). Although the backreaction $CO + O \rightarrow CO_2$ has a very low probability of occurring, the reaction $OH + O \rightarrow H_2O$ is favoured – i.e. pure water-ice is reformed when the ice is irradiated. This increases the probability that hydrogen peroxide (H_2O_2) is produced from the dissociation of H_2O and CO_2 by ion irradiation, which allows the formation of OH radicals from the released oxygen and hydrogen atoms. Hydrogen peroxide (H_2O_2) is dissociated by solar UV photons and other energetic particles at a faster rate than it is produced from the irradiation of water-ice molecules. Thus, if it is detected within the icy surface of Rhea, it would indicate a high rate of production from radiolytic chemical reactions. A correlation of H_2O_2 with CO_2 would be consistent with laboratory measurements involving the addition of small quantities of O_2 and CO_2 to water. In laboratory experiments carried out by Moore and Hudson (2000), they found that the addition of O_2 and CO_2 to water increased the yield of hydrogen peroxide production, when irradiated with MeV protons at a temperature of 77 K. This temperature is typical of Rhea's surface, and Saturn's magnetosphere provides a source of MeV protons (Figures 3.16 and 3.17). Assuming the majority of H_2O_2 is produced by radiolysis due to MeV protons, with a penetration depth that is below the

photo-destruction depth ($\lesssim$ 200 µm), there should be accumulations of hydrogen peroxide in reservoirs just below the upper ice layer on Rhea.

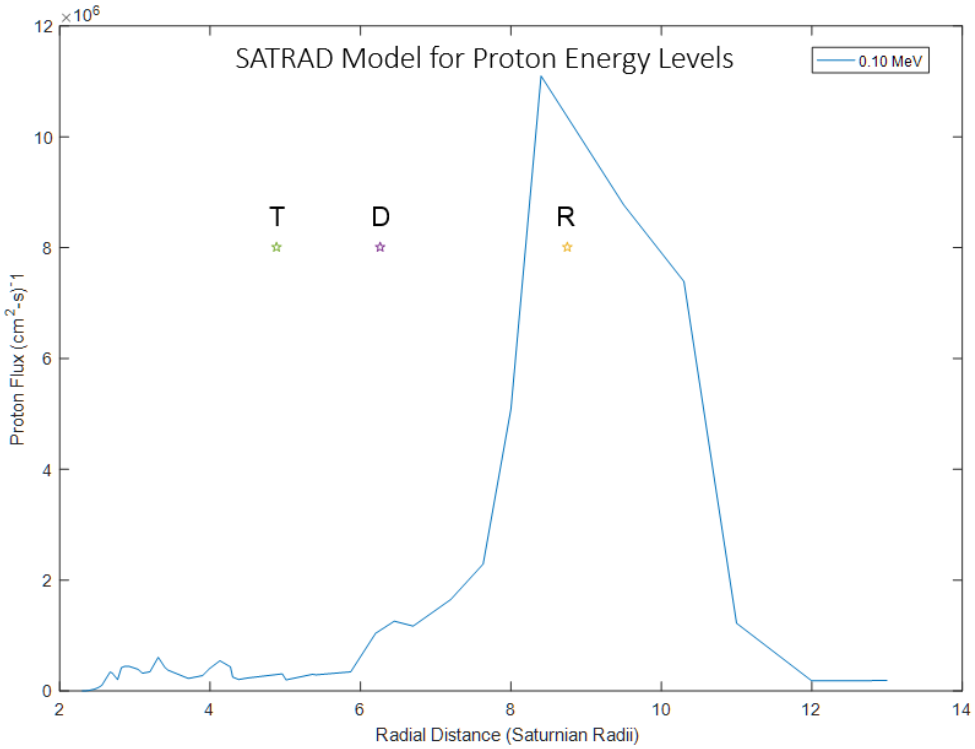

Figure 3.16: Proton flux as computed using the SATRAD numerical model (JPL 2005) at Saturn's equator as a function of radial distance. There is a broad peak in the flux distribution for 0.10 MeV protons, with the maximum amplitude at the location of Rhea. Model produced by R. Mark Elowitz.

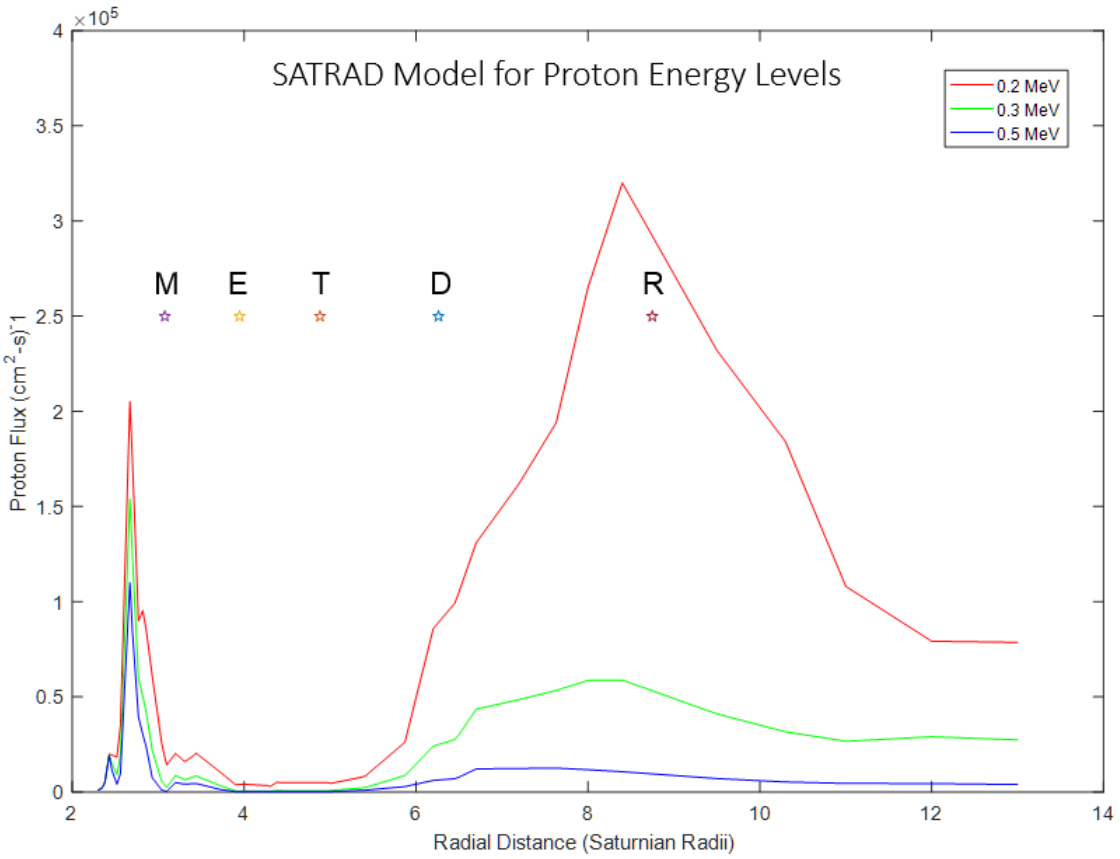

Figure 3.17: Proton flux for 0.2, 0.3, and 0.5 MeV protons. As is the case for 0.10 MeV protons, there is a dominant peak in the proton flux for 0.2 MeV protons at the location of Rhea. For 0.2, 0.3, and 0.5 MeV protons, there is a sharp peak in the flux distribution just inside the orbit of Mimas. Model produced by R. Mark Elowitz.

If Rhea's surface ice contains no CO_2 (although its exosphere is composed of O_2/CO_2), it may provide an explanation for the null detection of solid ozone (O_3) based on a recent analysis of Cassini UVIS data. If irradiation of CO_2-rich ice mixtures by charged particles from Saturn's magnetosphere does not occur on Rhea, then the formation of ozone may not occur. This is based on recent laboratory experiments, which show that O_3 is only produced when CO_2-rich ice mixtures are irradiated by ions (Boduch *et al*. 2011). On the other hand, if irradiation of water-ice on Rhea produces O_2 first, then it is possible that O_3 is formed via recombination of O and O_2. At the temperature range on Rhea's surface (~50 to 100 K), it is difficult to trap O_2, which may prevent the formation of ozone in sufficient amounts to be detectable using VUV spectroscopy (Boduch *et al*. 2011). Furthermore, the fact that Cassini's UVIS instrument does not provide sufficient

wavelength coverage to search for the strong 260 nm absorption band of ozone, limits the search to ozone's weaker absorption features. No such absorption features were found based on an analysis of Cassini UVIS spectra presented in Chapter 5.

3.7 Summary of UV/IR Spectroscopy and Exogenic Processes

This chapter has reviewed the fundamental science behind UV/Visible and IR spectroscopy. UV spectroscopy involves electronic transitions in molecules, and IR spectroscopy deals with vibrational/vibrational-rotational transitions. UV spectroscopy is very useful for studying the surfaces of solar system objects, including their composition, space weathering effects (e.g. radiolytic processes), and volatiles within ices. IR spectroscopy is used to detect the presence or absence of functional groups that are indicated by their specific vibration frequencies (e.g. C=O, NH_2, OH, CH, C-O, etc.). A thorough description of derivative spectroscopy and its utility in spectroscopy was presented. Derivatives of zeroth-order spectra can accentuate subtle features in spectra, deblend closely-spaced spectral features, and determine the positions of steep inflections and absorption bands in spectral data. Although derivative spectroscopy has been used in other fields, its use in the planetary science community is relatively new. First-order derivative spectra are used later in this thesis as part of an analysis of both laboratory and observed far-UV and IR spectra.

A thorough review of radiolysis of icy moons was also presented. The key message from the chapter is that the chemistry/scattering processes and structure of the upper surface layers of icy satellites are affected by exogenic processes. Exogenic processes that alter surface chemistry, which governs the particular spectral transitions observed in reflectance spectra, include charged particle bombardment of the surface ice by ions and electrons. These energetic particles originate from Saturn's magnetic plasma environment. The observed darkening observed in the UV on icy satellite surfaces is the result of

bombardment by energetic plasma. Due to the relative motion between the icy satellites and Saturn's co-rotating plasma, energetic electrons preferentially impact the leading hemisphere and plasma impacts the trailing side. Defects in surface ices (bubbles and voids) are created by ion irradiation, and trapped gases lead to the production of absorption features seen in UV spectra. If the optical properties of surface ice are dominated by ice grains from Saturn's E-ring then one would expect a brightening effect in the UV. However, the surface layers of Saturn's icy moons are dark in the UV portion of the spectrum. This implies the existence of a non-water-ice component of Saturn's E-ring, since water-ice is bright in the UV. Lastly, the size and structure of surface ice particles are governed by continual impacts by dark material (micrometeorites), including carbonaceous material. This "Space Weathering" modifies the surfaces of icy satellites, producing smaller particles.

CHAPTER 4

LABORATORY ICE MEASUREMENTS

4.1 Laboratory Ice Sample Measurements

The goal of this chapter is to present and describe laboratory ice spectra that are used later in this thesis to produce model spectra, which will be used to perform a comparative spectral analysis of the surface ice layers of Rhea and Dione.

In order to analyse ice spectra of planetary and lunar surfaces recorded by a spacecraft it is necessary to cross compare observational data with data recorded in the laboratory under analogous conditions. In this thesis, observational far-UV reflectance spectra recorded by the Cassini spacecraft are compared with a comprehensive set of data recorded in the laboratory. This thesis also presents a set of far-UV spectra of molecules that are known (or suspected) to exist in the Saturnian system (Chapter 5). The spectral data presented in this work contributes to our understanding of the physico-chemical nature of molecular ices in the outer solar system.

In this chapter, I start with the description of the laboratory experiment designed to collect thin ice sample data measurements, relevant to Saturn's icy satellites. A discussion of the Beer-Lambert law is included at the beginning of this chapter as it plays a fundamental role in the measurement of thin ice samples relevant to the analysis of ice spectra. A detailed description of how the laboratory vacuum-UV spectra were collected and processed is presented.

Vacuum ultraviolet spectroscopy is especially useful for characterisation of IR inactive molecules in the surface ice of Rhea, such as molecular oxygen (O_2). The formation of more complex molecules from O_2 that are connected by covalent and/or

intermolecular bonds is relevant to the study of icy satellites, since molecular structures consisting of two identical molecules bonded together (and possibly polymers) take place in chemical reactions within the surface ice layer (Silvaraman, et al. 2008). Both VUV and Infrared spectra are used to study the effects of irradiation using protons, electrons and ions on various ice mixtures.

In recording a set of VUV spectra in the laboratory it is necessary to invoke the Beer Lambert law, (Mason *et al*. 2006). The incident and transmitted beam intensities are determined, and from the known path length and number density, the photo-absorption cross sections can be calculated from the measured transmission spectra from

$$I_t(\lambda) = I_0(\lambda) e^{-nl\sigma(\lambda)} \quad (4.1)$$

where $I_t(\lambda)$ is the measured transmission spectrum, $I_0(\lambda)$ the initial intensity of the beam, n the number density (cm^{-3}), l the thickness of the ice sample, and $\sigma(\lambda)$ the photo-absorption cross-section (cm^{-2}). Solving the Beer-Lambert equation for the VUV absorption cross-section gives

$$\sigma(\lambda) = -\frac{1}{n} \ln\left(\frac{I_t(\lambda)}{I_0(\lambda)}\right) \quad (4.2)$$

where $n \approx (n_i + n_f)/2$ with n_i and n_f the average column density of the ice specimen before and after the VUV integration (in cm^{-2}). The resulting expression for the cross-section is thus independent of the path length *l*, which is accounted for in the column density, *n*. The approximation for the average densities of the ice sample is applicable to laboratory experiments where the samples are exposed to a source of VUV photons (i.e. simulating UV photolysis).

Using the optical constants for the ice specimen, the absorption coefficient, α, can be calculated using a plane-parallel approximation for the absorbing ice specimen (Mastrapa *et al*. 2008),

$$\alpha = \frac{1}{d}\ln\left(\frac{I_0}{I}\right) - \frac{2}{d}\ln\left|\frac{(n_0+n_1)(n_1+n_2)+(n_0-n_1)(n_1-n_2)e^{-2i\delta_1}}{2n_1(n_0+n_2)}\right| \quad (4.3)$$

where *d* denotes the thickness of the ice specimen, the ratio I_0 / I is the transmission spectrum, and the index of refraction for the vacuum, ice specimen, and the sample window are denoted by n_0, n_1, and n_2, respectively. The parameter δ_1 is given in terms of the frequency, the thickness of the ice sample, and the sample's index of refraction as $2\pi n_1 d\omega$.

If the structure and optical properties of the ice sample are not affected due to irradiation, and if many absorption spectra are averaged, then a simpler version of the equation for the absorption coefficient can be used (Cruz-Diaz, *et al*. 2014),

$$\alpha = \frac{1}{d}\ln\left(\frac{I_0}{I}\right) \quad (4.4)$$

where the transmission spectrum is denoted by I_0 / I and the ice specimen's thickness by *d*. The column density of the ice specimen can be calculated from the mass density of the ice, ρ_{ice}, the thickness of the ice sample at the deposition point, *d*, and the molecular mass of the ice compound, *M*.

$$N_c = \frac{d\rho_{ice}}{M\mu} \quad (4.5)$$

In this equation, $\mu = 1.66\times10^{-24}\ g$ is one "atomic mass unit", and the molecular mass is given in units of grams. From the column density, the integrated absorption coefficient of the ice sample can be calculated in terms of the band area (in optical depth) from the relation

$$\alpha_{\text{int}} = \frac{Band\ Area\,(in\,Optical\,Depth)}{N_c}. \quad (4.6)$$

The laboratory experiments carried out by Mason *et al*. (2006) demonstrated that more dimers of molecular oxygen are created in ice samples of greater thickness – i.e. the

thickness of the ice samples is the key parameter that governs the proportion of O_2 monomers and dimers. For the laboratory ice experiments described here, the measured VUV absorption cross-section σ (cm^{-2}) of a given species can be used to estimate the ice thickness *d* from the absorbing column density, *N* (cm^{-3}), the mass density of the ice ρ (g/cm^3), the molar mass of the species, m (g/mol), and the transmitted I_t and incident intensities I_0 at a specified wavelength (Cruz-Diaz, *et al*. 2014).

$$N(\lambda) = \frac{-1}{\sigma(\lambda)} \ln\left[\frac{I_t(\lambda)}{I_0(\lambda)}\right] \qquad (4.7)$$
$$d = \frac{Nm}{N_A \rho}$$

In the above equation for the ice thickness or ice penetration depth, N_A is the Avogadro number. In laboratory experiments involving absorbance measurements of thin ice samples vapour deposited onto film substrates, the pathlength (or thickness of the ice) can be determined from the number density and mass density of the ice. An alternative approach is to determine the path length (or thickness of the ice sample) from a known deposition rate, or by counting laser interference fringes of a He-Ne laser reflected off the ice sample (Mastrapa, R. M., *et al*. 2009).

The absorbance of a gas, *A*, is related to the number density and absorption cross section by the relation

$$A = \sigma N \quad (4.8)$$

where *N* is the number density of absorbing molecules, and σ is the absorption cross section. Beer's law governs the exponential decrease in the observed intensity

$$I = I_0 \exp(-Ad) \quad (4.9)$$

where *d* is the thickness of the sample, or the propagation distance of the beam. Substituting the equation for the absorbance into Beer's law yields an expression for the

transmitted intensity in terms of the number density of molecules, the absorption cross section and the absorption path length.

$$I = I_0 \exp(-\sigma N d) \qquad (4.10)$$

The absorbance is the negative logarithm of transmittance, thus

$$A = -\ln\left(\frac{I}{I_0}\right) = \ln\left(\frac{I_0}{I}\right) = \sigma N d \qquad (4.11)$$

The laboratory ice absorbance spectra can be obtained using the expression $-\ln(I / I_0)$, where I denotes the beam intensity measured with the vapour deposited film and I_0 is the beam intensity measured without the deposited film present.

The measured absorbance spectra can be used to calculate the absorption coefficient given the path length, *d*, through the ice sample using the relation (Cruz-Diaz, *et al*. 2014)

$$\alpha_\lambda = \left(\frac{A_\lambda}{\ln 10}\right) / d \qquad (4.12)$$

and the optical constant *k* can be expressed in terms of α_λ

$$k = \alpha_\lambda \lambda / (4\pi). \qquad (4.13)$$

Thus, the absorption coefficient (in units of inverse length) can be written as

$$\alpha_\lambda = \frac{4\pi k}{\lambda}. \qquad (4.14)$$

To compare the experimental absorbance spectra with far-UV reflectance spectra, the absorbance data can be converted to relative reflectance using the relation

$$R = \frac{1}{\exp[A \ln 10.]} \qquad (4.15)$$

4.2 Experimental Methodology

Experiments simulating Rhea conditions were carried out in an UltraHigh Vacuum (UHV) chamber housing a cold finger on which a Lithium (or Magnesium) Fluoride (LiF or MgF) window was attached (Figure 4.1). The chamber pressure went down to 5 x 10^{-9} mbar while temperatures down to 10 K were achieved at the LiF window. This entire system was attached to the end station of the 03A1 High Flux beamline at the National Synchrotron Radiation Research Centre (NSRRC), Taiwan. Vacuum UltraViolet (VUV) light in the 110 nm – 200 nm (6 – 11 eV) was used to probe the molecular ices that are formed at low temperatures. In order to obtain the photoabsorption spectra of simulated molecular ices, a spectrum of the LiF window, I_0, was recorded at 10 K. Then after sample deposition (i.e. the vapour from a liquid sample was allowed to form a uniform film on the LiF substrate.) another spectrum was recorded, *I*. Eventually the photoabsorption spectrum was then obtained using the Beer-Lambert law. To determine the column density, *N*, and thickness, *t*, of the ice sample the known absorption intensity, *A* (*cm mol*$^{-1}$), and density, ρ of the ice at a given temperature are used in the following two equations (Sivaraman, *et al*. 2014):

$$\begin{aligned} N &= \int \tau dv / A \\ t &= NM / N_A \rho \end{aligned} \qquad (4.16)$$

where $\int \tau dv$ is the integrated area in units of cm^{-1}, *M* is the molecular mass in units of grams, and N_A is the Avogadro number of molecules.

Molecules from liquid samples of hydrazine monohydrate, trichloromethane, tetrachloromethane and water were extracted into the gas phase before letting into the chamber to form molecular ice films. The same procedure was used to acquire VUV spectra of other chemical species relevant to icy satellites in the Saturnian system. In the case of layered ices of trichloromethane and tetrachloromethane were first deposited, respectively,

above which water molecules were deposited. Whereas in the case of mixed ices a 1:1 mixture of tricholoromethane / tetrachloromethane with water was prepared in the gas phase before deposition. All the samples were deposited at 10 K and were later warmed to higher temperatures (mostly covering Rhea diurnal temperatures) for spectral recording. Apart from the molecules given above, I have compared the known VUV spectra of various astrochemical ices with that of the Rhea and Dione spectra (Dawes, *et al*. 2018; Mason, *et al*. 2006; Pavithraa, *et al*. 2018; Sivaraman, *et al*. 2014; Sivaraman, *et al*. 2016; Sivaraman, *et al*. 2012).

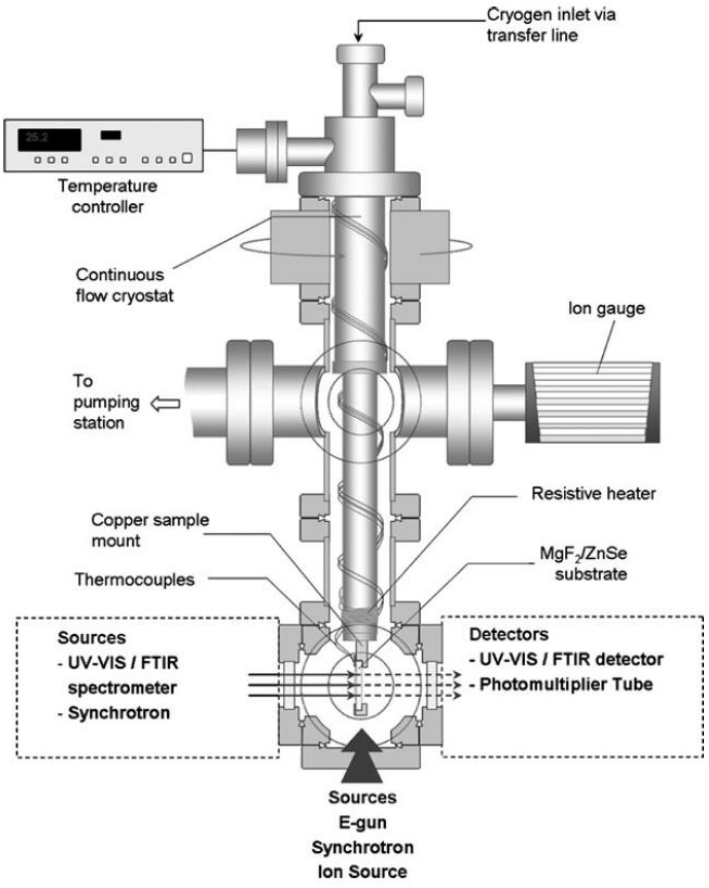

Figure 4.1: Laboratory experiment setup for collecting VUV spectroscopy of thin film ice samples under astrophysical ice conditions in the ISM and outer solar system. Figure courtesy of Nigel J. Mason, The Open University, Milton Keynes, UK.

In summary, laboratory measurements of ice mixtures deposited on thin substrates show that the position of electronic absorption bands in solid phase ice cannot rely solely on gas phase data. As ice undergoes a phase change from a gas to a solid, the absorption

cross section is known to change. Spectra collected of molecules in their solid phase do not show all the electronic states that gas phase spectra display.

4.3 Far-UV (Vacuum UV) Laboratory Ice Measurements

In this section I present the results of laboratory measurements of thin ice specimens in the far-UV (140-190 nm). The vacuum-UV spectra were collected as a joint project carried out by the Physical Research Laboratory (India), NSRRC (Taiwan) and The Open University (UK). The research program makes measurements of both far-UV and InfraRed (IR) spectra of molecules under simulated conditions relevant to the interstellar medium, cometary bodies, and icy satellites.

The ice samples presented in this chapter were selected based on their relevance to the icy satellites of the outer solar system (Table 4.1; Appendix A) (Dalton 2008). A description of the laboratory experiment setup and data collection is described in detail in Chapter 4.2. All ice samples were measured under environmental conditions similar to those encountered at the surface of Saturn's moon Rhea (approximately 70-90 K as determined from thermal modelling of Rhea's surface in Chapter 2.2). The step size used for recording the vacuum-UV ice measurements was approximately 1 nanometre. All of the spectra are archived in the AstroChemical Ices Database (ACID) (https://www.prl.res.in/~dinesh/acid/) in support of the astrochemistry Vacuum-UV program. Not all of the molecular species listed in Table 4.1 (and in Appendix A) were compared with UVIS observations, since some of these molecules were found not to have absorption features in the far-UV range of the UVIS-FUV detector.

Table 4.1: Laboratory Vacuum-UV Thin Ice Measurements (110 – 190 nm, T=40-100 K). The last column indicates if the chemical species was measured in the lab.

Primary Species	**Range of Percent of Minor Chemical Species**	**T (K)**
Water-Ice	0.5 – 20% Methyl Chloroformate	Yes
Water-Ice	0.5 – 20% Carbon Disulpfide (CS_2)	Yes
Water-Ice	0.5 – 20% Ammonia (NH_3)	Yes
Water-Ice	0.5 – 20% Carbon Dioxide (CO_2)	Yes
Water-Ice	0.5 – 20% Ozone (O_3) (solid or trapped gas bubbles)	Yes
Water-Ice	0.5 – 20% Molecular Oxygen (O_2)	Yes
Water-Ice	0.5 – 20% Nitrous Oxide (N_2O)	Yes
Water-Ice	0.5 – 20% Carbon Monoxide (CO)	Yes
Water-Ice	0.5 – 20% Methane (CH_4)	Yes
Water-Ice	0.5 – 20% Carbonic Acid (H_2CO_3)	Yes
Water-Ice	0.5 – 20% Thioanisole ($CH_3SC_6H_5$)	Yes
Water-Ice	0.5 – 20% Acetylene (C_2H_2)	No
Water-Ice	0.5 – 20% Dimethyl Ether (CH_3OCH_3)	Yes
Water-Ice	0.5 – 20% Ethyl Acetate ($C_4H_8O_2$)	Yes
Water-Ice	0.5 – 20% Diethyl Ether ($(C_2H_5)_2O$)	Yes
Water-Ice	0.5 – 20% Propargyl Alcohol (C_3H_4O)	Yes
Water-Ice	0.5 – 20% Glycerol ($C_3H_8O_3$)	Yes
Water-Ice	0.5 – 20% Trichloroethylene ($CICH=CCl_2$)	Yes
Water-Ice	0.5 – 20% Acetaldehyde (CH_3CHO)	No
Water-Ice	0.5 – 20% Phenyl Group	Yes
Water-Ice	0.5 – 20% Hydrogen Peroxide (H_2O_2)	No
Water-Ice	0.5 – 20% Hydrazine (N_2H_4) (in monohydrate form)	Yes
Water-Ice	0.5 – 20% Carbonic Acid (CH_2O_3)	Yes
Water-Ice	0.5 – 20% Formic Acid (HCOOH)	No
Water-Ice	0.5 – 20% Dimethyl Sulfoxide ($(CH_3)_2SO$)	Yes
Water-Ice	0.5 – 20% Carbon Tetrachloride (CCl_4)	Yes
Water-Ice	0.5 – 20% Chloroform ($CHCl_3$)	Yes
Water-Ice	0.5 – 20% Dichloromethane (CH_2Cl_2)	Yes
Water-Ice	0.5 – 20% Methanol (CH_3OH)	No
Water-Ice	0.5 – 20% Acetonitrile (CH_3CN)	Yes
Water-Ice	0.5 – 20% Methyl Chloroformate ($ClCOOCH_3$)	Yes
Water-Ice	0.5 – 20% Ethyl Formate ($HCOOC_2H_5$)	Yes
Water-Ice	0.5 – 20% Hydrogen Cyanide (HCN)	No
Water-Ice	0.5 – 20% Organic Tholins	Yes
Water-Ice	0.5 – 20% PAHs	No
Water-Ice	0.5 – 20% Carbonaceous grains	No

4.3.1 Reflectance Spectra of Water-Ice

To determine which molecules may be present within the surface ices of Saturn's moons Rhea and Dione, and which molecules might be responsible for producing the absorption feature between ~179 – 189 nm seen in the Cassini UVIS spectra, I present the

following series of laboratory ice spectra measured in the far-UV region from 140 to 189 nm. The laboratory spectra include irradiated and unirradiated water ice, the former being the dominant molecule present on Saturn's mid-sized icy moons. Evidence for irradiation processing on the surfaces of Rhea and Dione comes from the detection of an ozone (O_3) absorption feature near 260 nm (Noll, *et al*. 1997). Additional laboratory spectra are presented based on a list of chemical species that are suspected to exist in the Saturn system (see Table 4.1, Appendix A).

The first vacuum-UV laboratory ice spectra to be presented (Figure 4.2) are those of irradiated water-ice at temperatures of 30 K (blue line), 60 K (green line), and 130 K (red line). Since absorbance spectra can be difficult to interpret, all the laboratory spectra have been converted to relative reflectance. The most notable feature in the vacuum-UV spectrum is the steep spectral slope due to the water-ice absorption edge near ~165-nm. The ice spectrum collected at a temperature of 30 K shows a less steep spectral slope due to water-ice absorption in contrast to the other two spectra collected at 60 K and 130 K. The 165-nm absorption edge of the 60 K and 130 K lab spectra appears to be shifted towards shorter wavelengths, in contrast to the 30 K spectrum. This typically occurs for smaller water-ice grain sizes – i.e. as the grain size decreases the absorption edge tends to shift to shorter wavelengths. The spectral slope of the 165-nm absorption edge is less steep for the case of the 30 K spectral measurement.

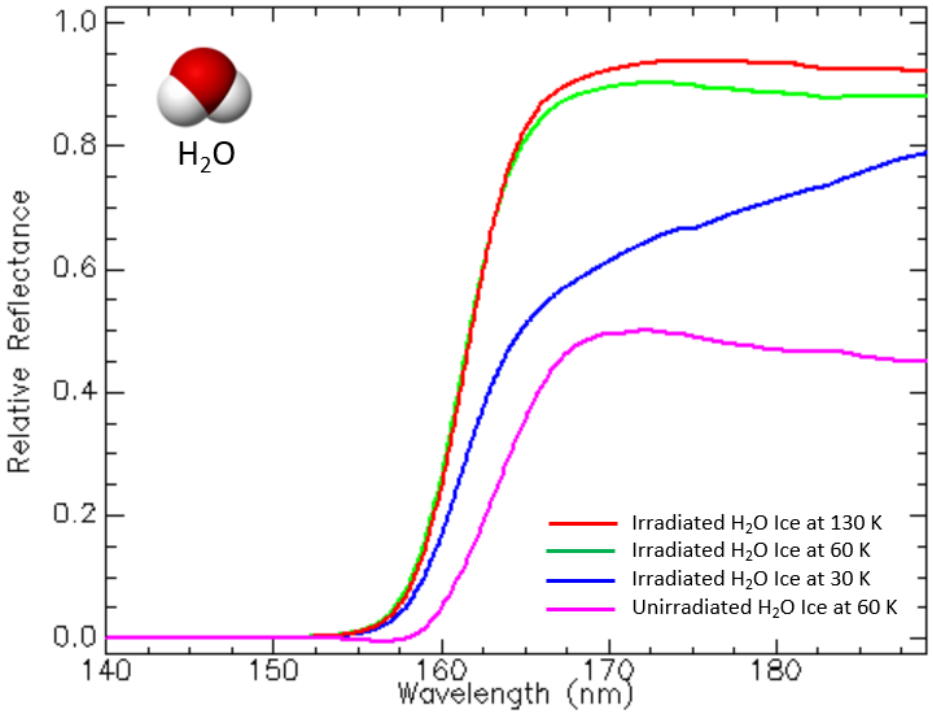

Figure 4.2: Irradiated vs unirradiated vacuum-UV water-ice spectra measured in the laboratory at conditions similar to those encountered on the surfaces of Rhea and Dione. The laboratory data is displayed as relative reflectance to allow easier interpretation of the water-ice absorption edge near 165 nm and to check for any indication of absorption between ~179 and 189 nm. The step size of the measured spectra is ~1 nm. The absorption edge of the irradiated water-ice is shifted with respect to the nominal 165-nm position due to radiolytic processing.

A qualitative assessment of the relative shift of the absorption edge due to water-ice from its nominal position near 165-nm can be made by taking the first-derivative of the laboratory spectrum (Figure 4.3). The aforementioned differences in the 30 K spectrum are reflected in its derivative's lower amplitude. The three derivative peaks of the irradiated ice spectra are shifted relative to the unirradiated absorption edge of unirradiated water-ice due to the synthesis of molecular species (e.g. H_2O_2, O_2, OH) resulting from the radiolysis of the irradiated ice.

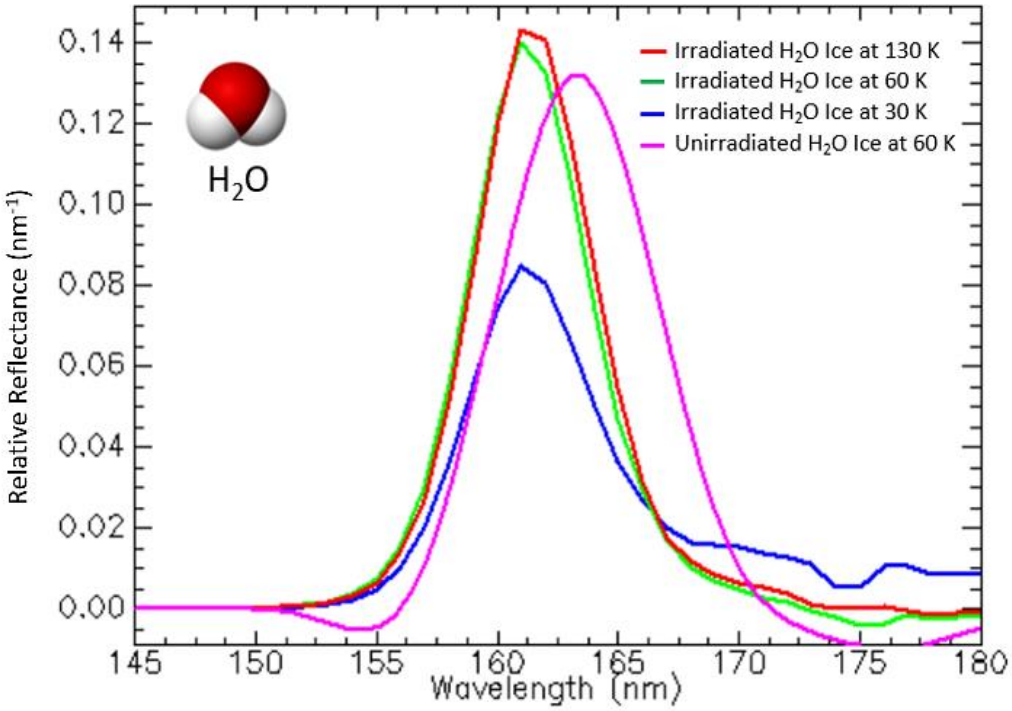

Figure 4.3: First derivatives of three irradiated water-ice spectra and one unirradiated water-ice spectrum measured in the laboratory at three different temperatures covering the range of temperatures encountered on the surface of Saturn's moon Rhea. The vertical black line represents the nominal position of the 165-nm absorption edge due to pure water-ice. The derivative peak is shifted to shorter wavelengths due to the production of radiolysis products.

4.3.2 Reflectance Spectra of Mixtures of Water-Ice and Ammonia

The next laboratory far-UV ice spectrum to be presented is a 1:1 mixture of water and ammonia ice (Figure 4.4). There is mounting evidence for possible ammonia ejected by the plumes of Enceladus (Emery *et al*., 2005; Verbiscer *et al*. 2006). Ammonia (NH_3) is also predicted to be one of the more abundant molecules incorporated into the bodies of icy objects in the outer solar system (Lewis, 1972), since its condensation temperature when mixed with water-ice is near 150 K. The vacuum-UV spectra of H_2O:NH_3 ice mixtures exhibit a steep spectral slope at wavelength beyond 180 nm. No significant variation with temperature is seen in the spectra.

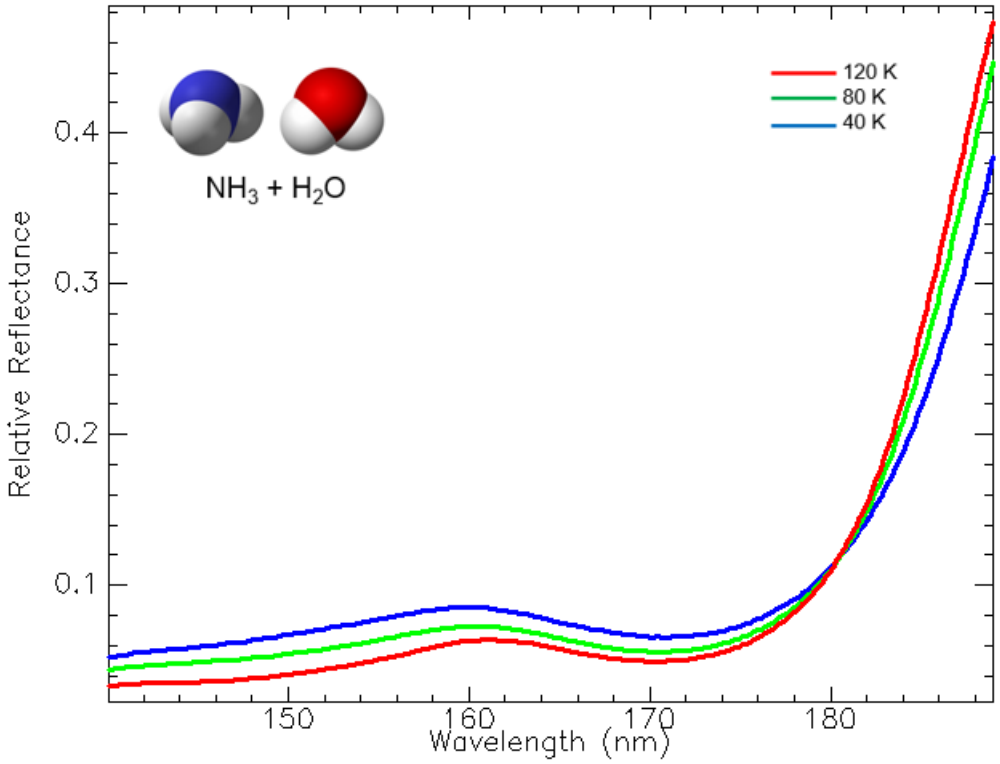

Figure 4.4: A 1:1 mixture of ammonia and water-ice measured in the laboratory at near-vacuum conditions. The thin-film ice spectra were measured at temperatures of 40 K (blue line), 80 K (green line), and 120 K (red line). The absorbance data are displayed as relative reflectance. The step size of the measured spectra is ~1 nm.

4.3.3 Reflectance Spectra of Carbon Dioxide Ice

Carbon dioxide in its solid ice phase has an asymmetric stretching mode (C-O bond) near the measured laboratory wavelength of 4.26 microns (ν_3 mode). This spectral transition has been detected on several of Saturn's icy moons using the Cassini VIMS instrument (Cruikshank, 2009). Carbon dioxide is also of interest because Rhea and Dione are known to have tenuous exospheres composed of O_2/CO_2 (Teolis & Waite 2016). The source of O_2 is radiolysis, but the source of the CO_2 is not known. To investigate the nature of CO_2 in Rhea's upper ice layers, VUV laboratory ice spectra were collected (Figure 4.5). The VUV spectra were collected at two temperatures, 30 K and 80 K, representative of the range of temperatures that can occur over Rhea's surface.

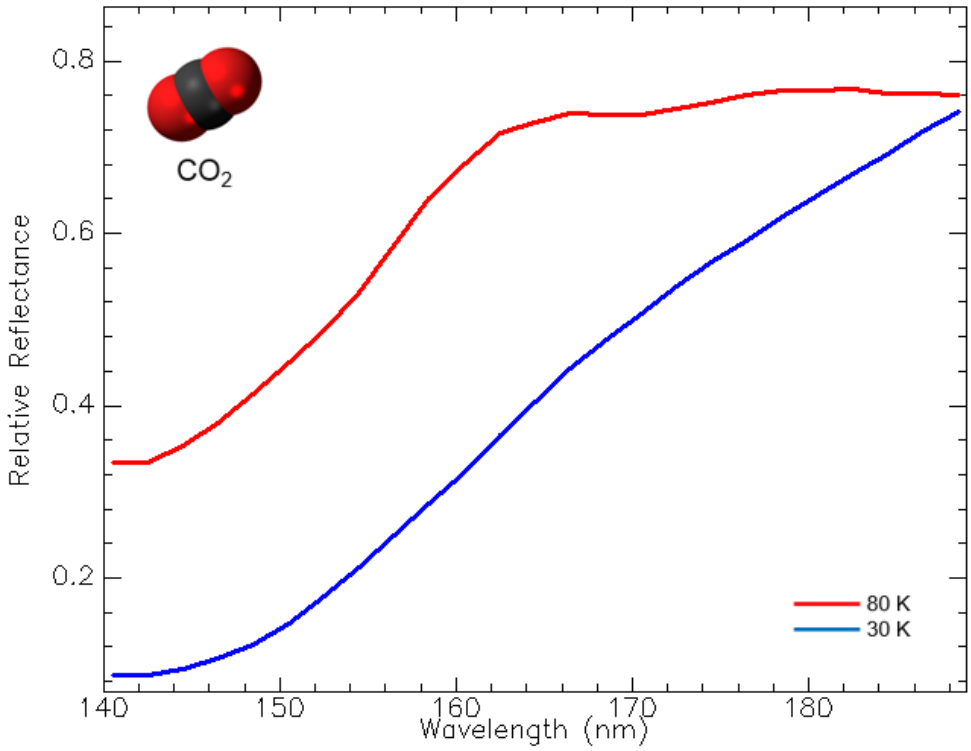

Figure 4.5: Solid ice phase CO_2 measured in the laboratory at near-vacuum conditions. The thin-film ice spectra were measured at temperatures of 30 K (blue line), 80 K (red line). The absorbance data is displayed as relative reflectance. The step size of the measured spectra is ~1 nm.

The first-derivatives of the two CO_2 ice spectra show notable differences in their structure, in both wavelength positions of their peaks and amplitudes. The steeper spectral slope of the 80 K CO_2 spectrum correlates with the higher amplitude and profile of the derivative peak (Figure 4.6). The flatter spectral slope of the low-temperature (30 K) CO_2 ice spectrum is reflected in the less pronounced structure in its first-derivative peak. Sublimation of the CO_2 ice observed in the 80 K laboratory ice spectrum could explain the notable difference in the laboratory ice spectra and the derivative peak structure. Sublimation of CO_2 trapped in Rhea's surface ice could explain its presence in the satellite's tenuous exosphere.

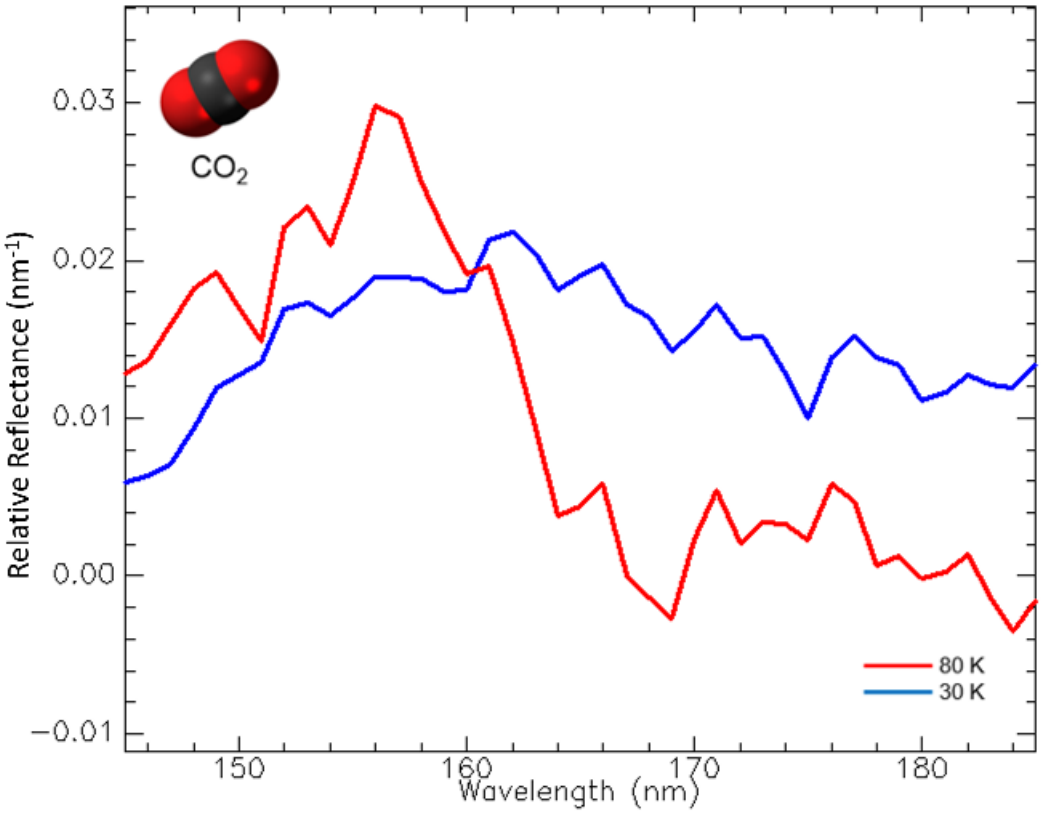

Figure 4.6: First-derivatives of the two CO_2 ice spectra at 30 K and 80 K. The position of the derivative peak can be used to quantitatively determine the position of the steep absorption edge of the 80 K CO_2 spectrum in wavelength space. The derivative spectra clearly illustrate a dependence on temperature.

Carbon dioxide is present on several icy satellites in the outer solar system (Raul, *et al*. 2012), and can be trapped in the surface ice in the form of gas bubbles, bound in the form of clathrates, or adsorbed on water-ice grains. Complexing of CO_2 by these mechanisms increases the binding energy of the molecule, making loss due to sublimation more difficult. If CO_2 is complexed in these forms on the surface of Rhea and other icy satellites in the Saturnian system, it would have a long residence time – i.e. the molecular compound would be very stable. Any free CO_2 ice that exists would be quite volatile at the temperature of Rhea's surface. The ease at which CO_2 sublimes at relatively low temperatures (~100 K) can be explain by the intermolecular forces between CO_2 molecules. The non-polar nature of the CO_2 molecule implies weak van der Waals forces between the molecules. This allows CO_2 molecules to sublime at relative low

temperatures. However, it is not clear whether free CO_2 ice can remain stable for long periods of time on Rhea's surface. A detailed analysis of laboratory ice spectra could provide insight on the stability of carbon dioxide ice on the surfaces of icy satellites in the Saturnian system.

4.3.4 Reflectance Spectra of Carbon Monoxide Ice

Carbon monoxide (CO) is a simple linear molecule and is the most abundant molecular in the interstellar medium (ISM) (Mason *et al*. 2006). CO ice is highly volatile and cannot exist in the form of free ice on Rhea's surface due to its low sublimation temperature of approximately 30 K (Martinez, *et al*. 2007), except at its polar regions where the temperature approaches 30 K. It is also possible that CO could be trapped within the amorphous water-ice matrix present on Rhea's or other icy satellites in the Saturnian system. The thermodynamics of the water-ice in which the CO and other volatiles are trapped controls the rate of outgassing, especially the transition temperature at which amorphous ice can be transformed to its crystalline phase. It is also possible that CO and CO_2 can exist at the polar regions of Rhea and other icy moons in the Saturnian system as temperatures can be as low as 30 K in these regions (Howett *et al*. 2016). Laboratory spectra of two ice samples of carbon monoxide (CO) were collected at temperatures of 30 K and 50 K (Figure 4.7), typical of the temperature range encountered at Rhea's surface.

The difference between the two laboratory spectra of carbon monoxide (CO) is most likely the result of sublimation at temperatures greater than 30 K. The CO spectrum recorded at a temperature of 50 K (red spectrum on Figure 4.7) has probably undergone sublimation.

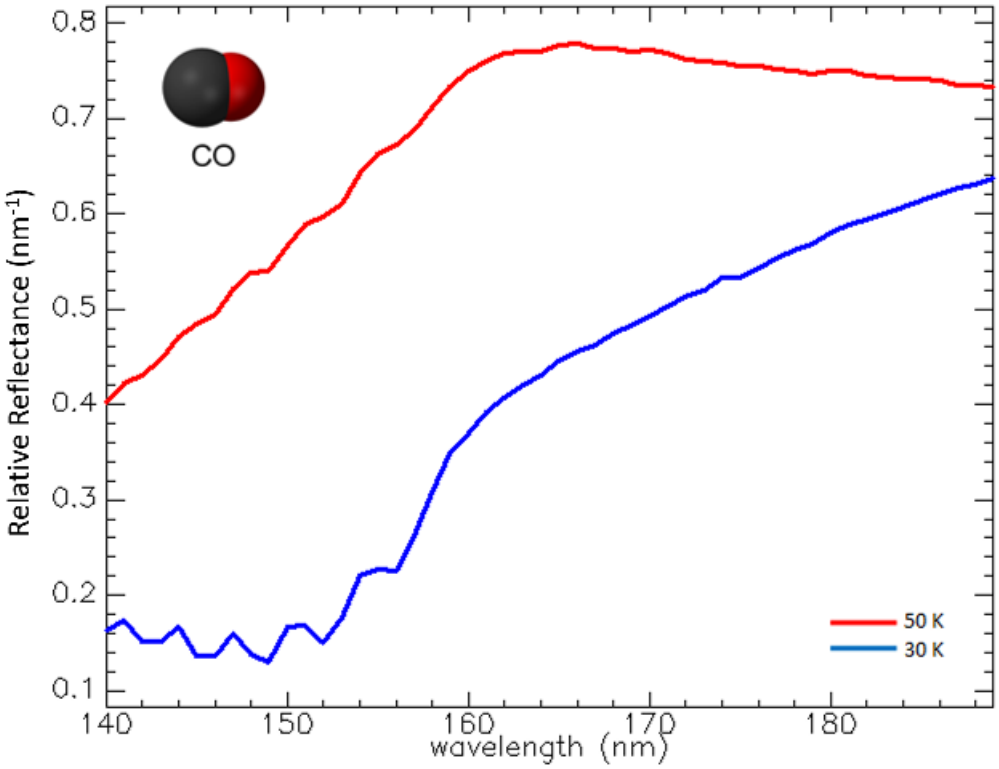

Figure 4.7: Vacuum-UV ice spectra of CO ice collected in the laboratory at temperatures of 30 K and 50 K. Rhea's temperature can approach 30 K near its polar regions, so if CO exists on Rhea it would most likely be located at the polar regions. The shape of the spectral slope appears to be dependent on the temperature. The spectra are presented as relative reflectance. The spectra were measured with a step size of ~1 nm. Note the effects of CO sublimation at the higher temperature of 50 K (red spectrum).

4.3.5 Reflectance Spectra of Hydrazine Monohydrate

A mixture of hydrazine (NH_2NH_2) and water-ice (H_2O) creates a monohydrate ($NH_2NH_2•H_2O$) via hydrogen bonding. The molecular weight of hydrazine is 32 and the monohydrate has a molecular weight of 50. Therefore, the molecular weight ratio is calculated as 32/50 = 0.64. This leads to 64 percent hydrazine assuming 100 percent monohydrate. The collection of hydrazine monohydrate is relevant to geochemical studies of icy satellites as water-ice and ammonia can lead to its production through chemical pathways in the upper ice layers of these moons (Chapter 6). Hydrazine derived salts (Aruna *et al*. 2014) are of interest in the study of internal aqueous layers known to exist in several icy satellites in the outer solar system. These salts are like ammonium-based salts in that both types of salts are highly soluble in water and relatively insoluble in nonpolar

organic solvents. They can be synthesised from chemical reactions involving the exchange of chemical bonds between the two reacting species, solid ammonium salts with hydrazine hydrate (Aruna *et al*. 2014). Hydrazine may also play an important role as an intermediate in biological systems which use ammonium as an inorganic electron donor for denitrification, which could provide a source of free energy for metabolism in extremophiles (Kartal *et al*. 2011). Both hydrazine (N_2H_4) and hydroxylamine (NH_2OH) could be widespread in Titan's environments (Jetten *et al*. 1999). Hence the study of laboratory vacuum-UV spectra of hydrazine monohydrate is of relevance to geochemical studies of icy satellite surfaces.

Three laboratory ice spectra (Figure 4.8) were collected at temperatures ranging from 50 K to 90 K, identical to the surface temperatures and pressure at the surfaces of Saturn's mid-sized icy satellites. The laboratory ice spectra show no significant differences for the three temperatures, 50 K, 70 K, and 90 K, at which they were measured. All three spectra show a steep spectral slope at wavelengths less than 165-nm, indicative of absorption due to water-ice. A weak absorption feature between ~170 nm to ~190 nm is seen in all three spectra of the hydrazine monohydrate. The presence of the absorption centred near 184 nm closely resembles the absorption feature seen in the Cassini UVIS reflectance spectra of the surfaces of Rhea and Dione (see Chapter 6).

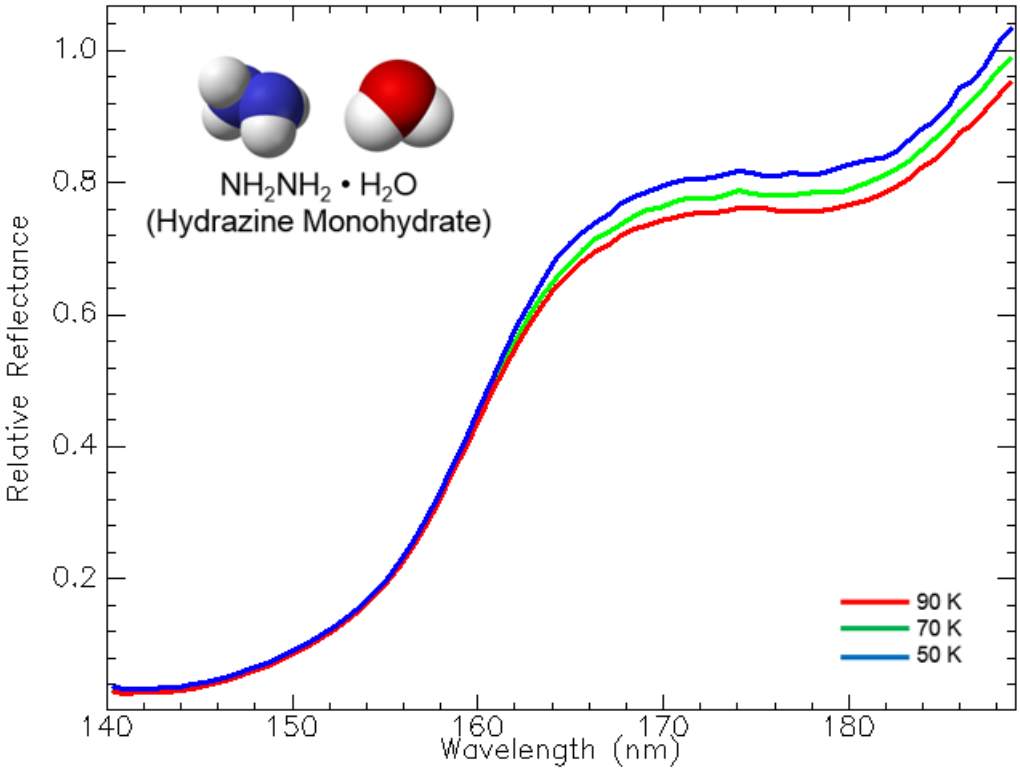

Figure 4.8: Vacuum-UV ice spectra of hydrazine monohydrate collected with a step size of ~1 nm. The spectra are presented as relative reflectance at 50 K (blue curve), 70 K (green curve), and 90 K (red curve). Note the weak absorption between ~170 – 190 nm.

The peak of the first-derivative for the hydrazine monohydrate data is shifted to shorter wavelengths relative to that for pure water-ice (Figure 4.9). This shift is due to the hydrazine component of the ice mixture. If water-ice were the only molecular substance present, I would expect the derivative peak to be located closer to the nominal 165-nm absorption edge of water-ice. Another effect that can induce the shift in the location of the derivative peak is the warm-up effect that occurs during the recording of the absorbance spectra in the laboratory. In this case, the shift is approximately 5 nm relative to the nominal 165-nm absorption edge due to pure water-ice. These effects should be accounted for when producing synthetic model spectra used to compare to UVIS observations.

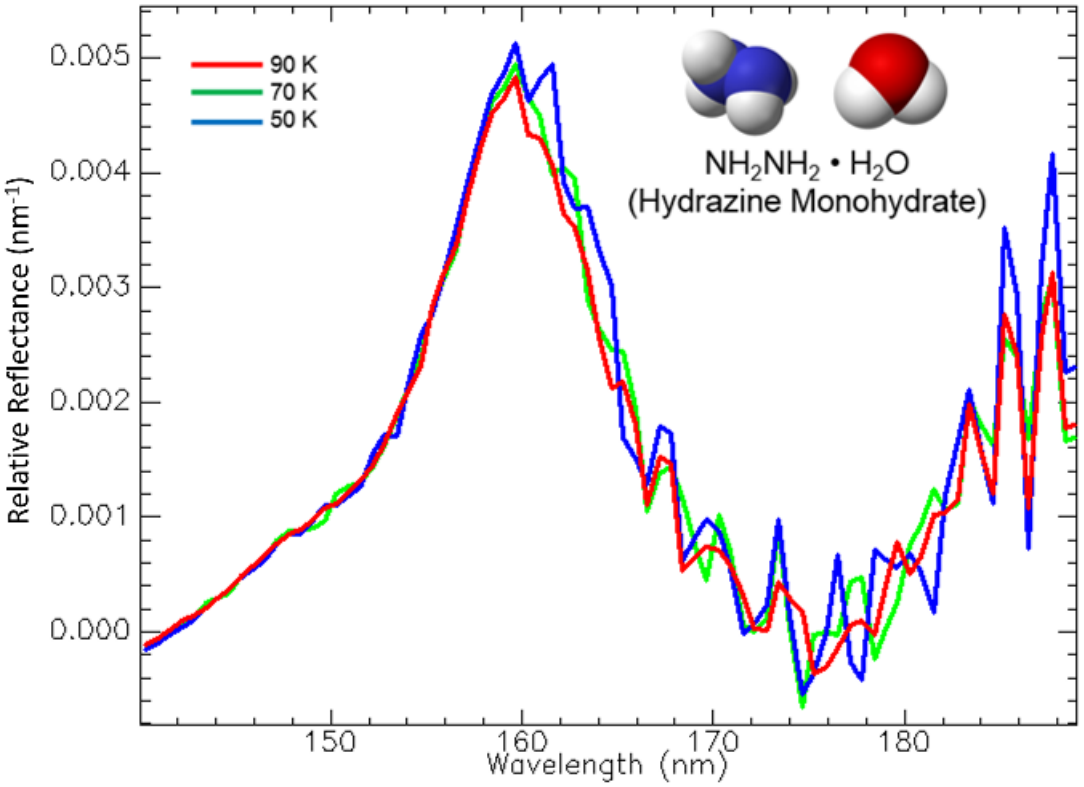

Figure 4.9: First derivative peaks for the three hydrazine monohydrate laboratory spectra. The shift of the peak towards shorter wavelengths relative to the 165-nm (dotted line) absorption edge of pure water-ice is clearly seen.

4.3.6 Reflectance Spectra of Chlorine Molecules

Chloromethane molecules, including CH_3Cl, CH_2Cl_2, and other simple chlorine molecules (e.g. CCl_4) are of interest because they are known to exist in trace amounts in meteorites (Garrison, *et al*. 2000). Organic molecules associated with meteoritic debris on the surfaces of icy bodies in the outer solar system can be converted to chloromethane molecules (e.g. CH_3Cl) with chloride and/or perchlorate in the "regolith". Chlorine molecules are highly relevant to icy satellites suspected of harbouring aqueous layers/reservoirs below their surfaces due to internal heating. Chloride-containing molecules are known to exist in terrestrial sea water (Graedel & Keene, 1996), and possibly within the internal oceans in the interiors of icy satellites. Four vacuum-UV spectra (Figure 4.10) of a mixture of Tetrachloromethane and water-ice were collected over a temperature range of 50 – 110 K that is commensurate to the surfaces of Saturn's

icy satellites. The reflectance centred near 170 nm appears to decrease in strength as the temperature increases. This may be the result of sublimation of the chlorine compound as the temperature rises. The steep absorption edge is shifted towards shorter wavelengths, relative to the nominal 165-nm absorption edge due to pure water-ice.

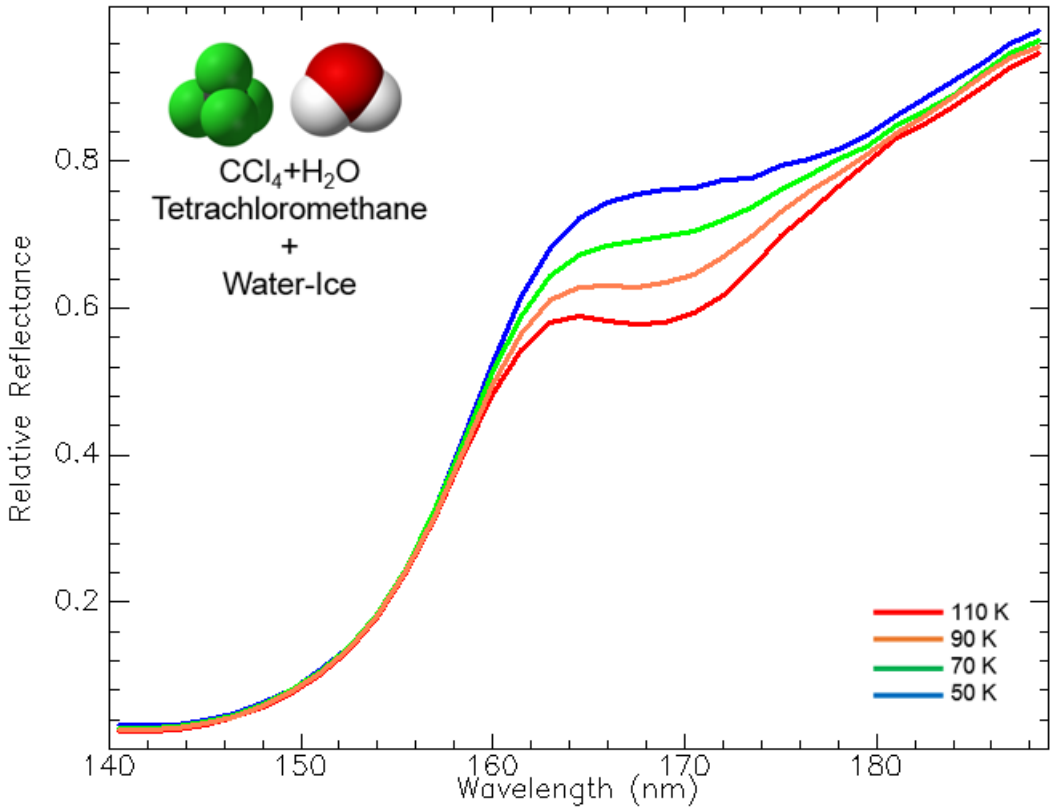

Figure 4.10: Four vacuum-UV laboratory spectra of a 1:1 mixture of water-ice and Tetrachloromethane (CCl_4+H_2O). The ice spectra were collected at four different temperatures similar to that on the surfaces of Saturn's icy satellites. The laboratory data is shown as relative reflectance to emphasise the absorption centred near 170 nm. Note the increased absorption near 170 nm as the temperature increases.

When chloromethane molecules are beneath water-ice the broad absorption feature minima shift to longer wavelengths with a minimum near 180 nm (Figure 4.11). The highest temperature laboratory spectrum shows the weakest absorption out of the four vacuum-UV spectra that were recorded over a temperature range of 50 – 110 K. The weaker absorption may be due to sublimation of the chlorine compound at higher temperatures.

It was also surprising to see a resemblance between the laboratory spectra (Figure 4.11) and the UVIS spectra of Rhea and Dione, since simple chloromethane molecules are

not one of the chemicals suspected to be present on any of Saturn's icy moons. However, there are possible scenarios that could lead to the presence of chlorine and hydrazine monohydrate molecules on Rhea and Dione, which are discussed in Chapter 6.

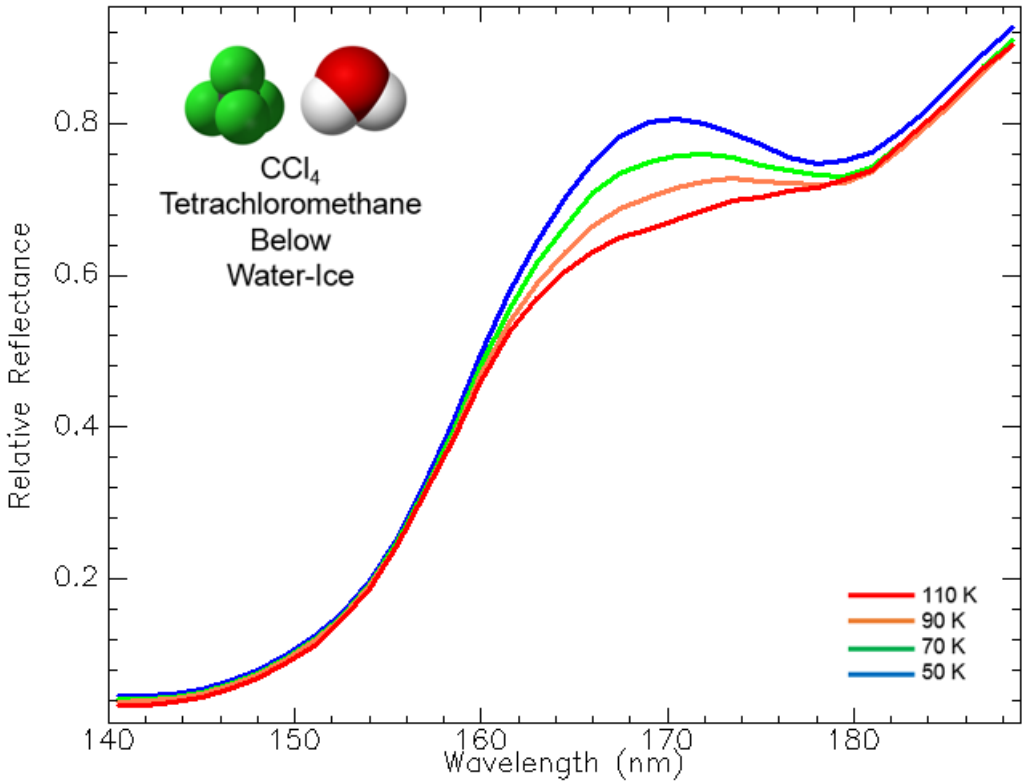

Figure 4.11: Four VUV laboratory spectra of Tetrachloromethane (CCl_4) below a layer of water-ice. The ice spectra were collected at four different temperatures similar to that on the surfaces of Saturn's icy satellites. The laboratory data is shown as relative reflectance to emphasise the absorption centred near 180 nm. Note the decreased absorption near 180 nm for the spectrum measured at 110 K.

The next VUV laboratory spectrum shown (Figure 4.12) is an ice mixture of dichloromethane (CH_2Cl_2) and water. Dichloromethane is an organic compound that is not miscible with water. This chloromethane compound is relevant to icy satellites in the outer solar system in that one possible source of dichloromethane (CH_2Cl_2) is ocean water (Moore, 2004). Thus, it is possible that CH_2Cl_2 could exist in the subsurface oceans of icy satellites. The three VUV laboratory spectra (Figure 4.12) all show the weak absorption between ~170 – 190 nm. The strength and shape of the weak absorption feature does not depend on the temperature at which the spectra were recorded. The far-UV absorption

edge in the three laboratory spectra is shifted towards shorter wavelengths relative to the nominal 165-nm of pure water-ice.

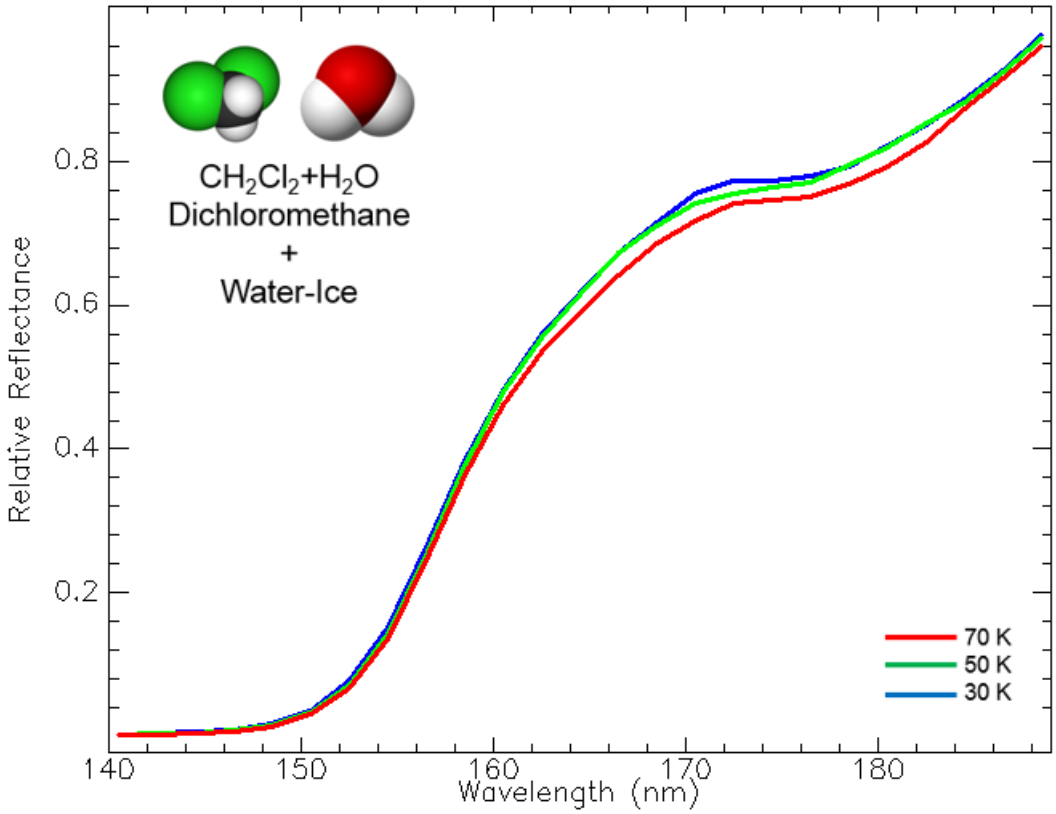

Figure 4.12: Three vacuum-UV laboratory spectra of an ice mixture consisting of dichloromethane (CH_2Cl_2) and water-ice. The sampling of the ice spectra is ~ 1 nm. The ice spectra were collected at three different temperatures similar to those on the surfaces of Saturn's icy satellites. The laboratory data is shown as relative reflectance to emphasise the absorption centred near 180 nm. The weak absorption between ~170 – 190 nm does not appear to depend on temperature.

Chloroform ($CHCl_3$) is a volatile organic compound with a tetrahedral molecular structure. Chloroform is miscible in tetrachloromethane (CCl_4) and is soluble in benzene. The melting point of chloroform is 209.7 K (Daintith, 2004). Three VUV spectra (Figure 4.13) of chloroform were collected over a temperature range of 50 – 130 K under ultrahigh vacuum conditions. The spectrum measured at 50 K shows a possible broad absorption feature that is centred near 180 nm. The spectrum recorded at 130 K shows absorption over the wavelength range of ~164 nm to 174 nm. The 165-nm absorption edge due to water ice is shifted towards shorter wavelengths due in the presence of chloroform in the ice mixture.

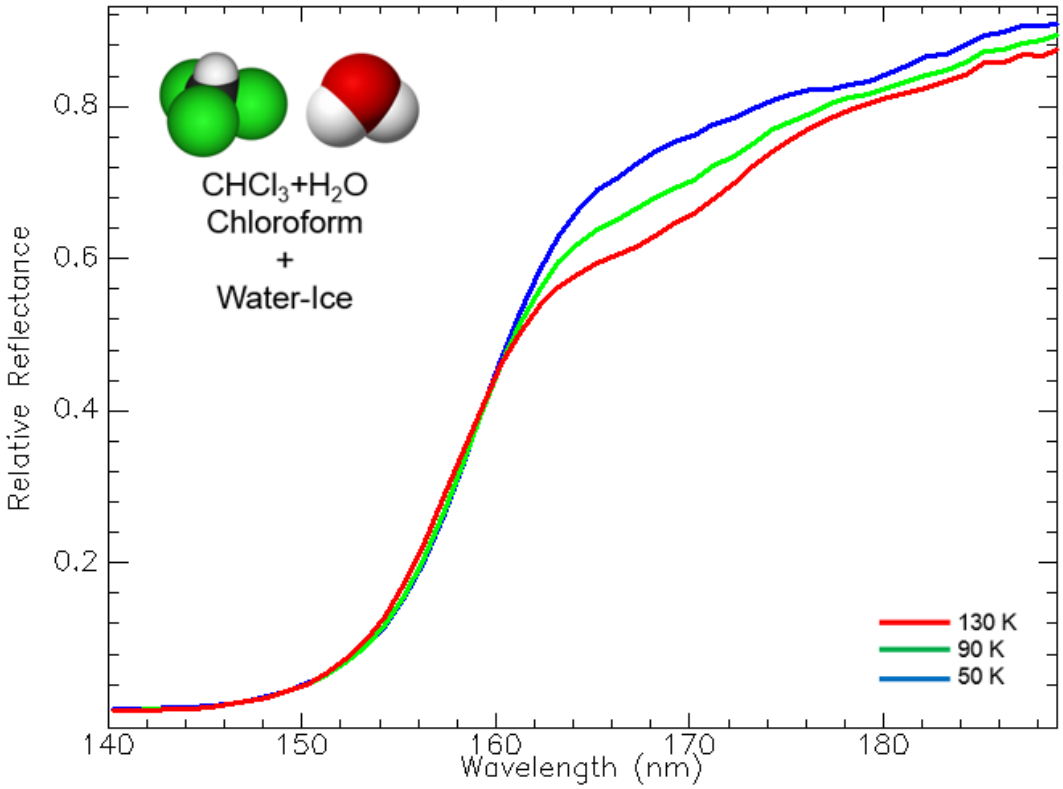

Figure 4.13: Three VUV laboratory spectra of an ice mixture consisting of water-ice and trichloromethane ($CHCl_3$) and water. The sampling of the recorded spectra was ~1 nm over three different temperatures ranging from 50 – 130 K. The spectra have been displayed as relative reflectance to allow easier interpretation of absorption features. Note the possible weak absorption centre near 180 nm in the spectrum recorded at 50 K. A broad absorption feature is apparent from approximately 164 – 174 nm in the spectrum measured at a temperature of 130 K.

The next series of chloromethane VUV spectra to be presented consists of a layer of water-ice on top a layer of chloroform ice (Figure 4.14). In this configuration, the broad absorption centred near 180 nm is readily apparent in three of the spectra, except the one recorded at the highest temperature of 110 K. This may be due to sublimation of the chloroform from the ice mixture.

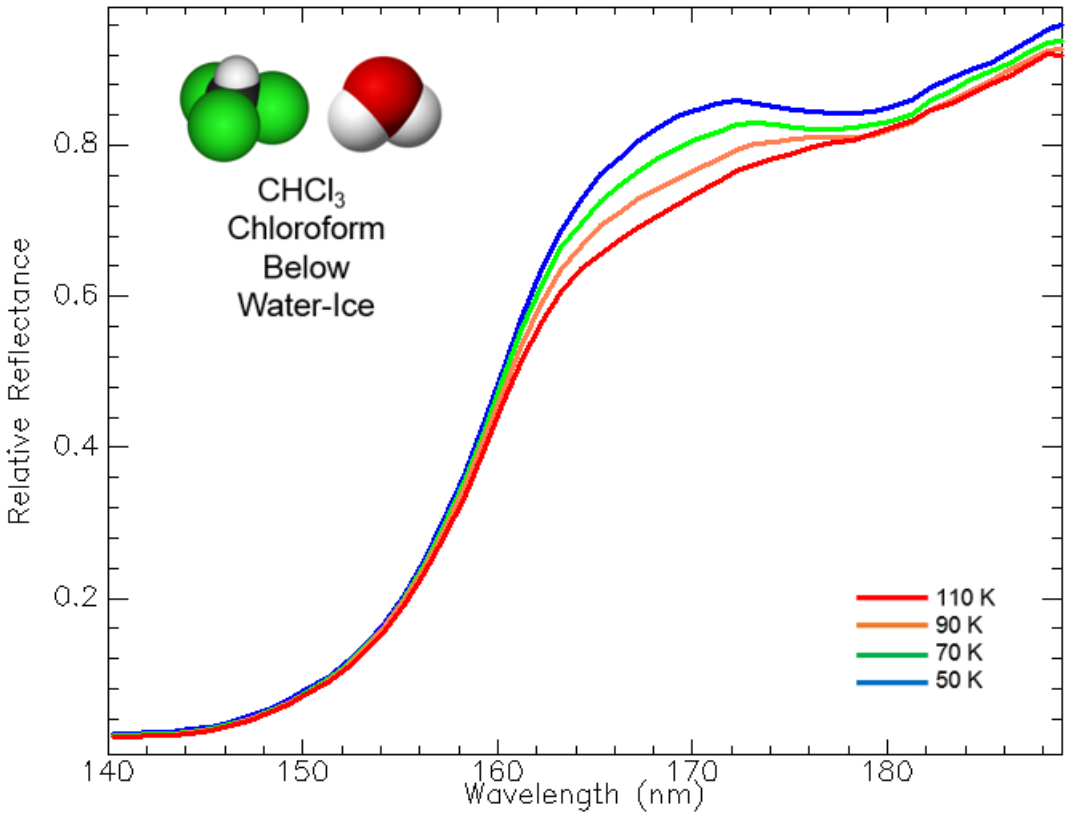

Figure 4.14: Four vacuum-UV laboratory spectra of a layer of water-ice and layer of trichloromethane or chloroform ($CHCl_3$) ice below. The sampling of the recorded spectra is ~1 nm over four different temperatures ranging from 50 – 110 K. The spectra have been displayed as relative reflectance to allow easier interpretation of absorption features. The broad absorption centred near 180 nm is readily apparent for the three spectra recorded at the three lowest temperatures. No such absorption is seen in the spectrum measured at 110 K, possibly due to sublimation of chloroform beneath the water-ice layer.

Methyl Chloroformate ($ClCOOCH_3$ or $C_2H_3ClO_2$) is a more complex chloromethane compound that does not show the same spectral signatures as the simple chlorine molecules presented previously in this chapter. Laboratory ice spectra (Figure 4.15) of methyl chloroformate recorded at temperatures of 100 K, 50 K, and 30 K appear to show no absorption features between 140 and 190 nm. Methyl chloroformate decomposes slowly in water to produce methanol, hydrogen chloride and carbon dioxide.

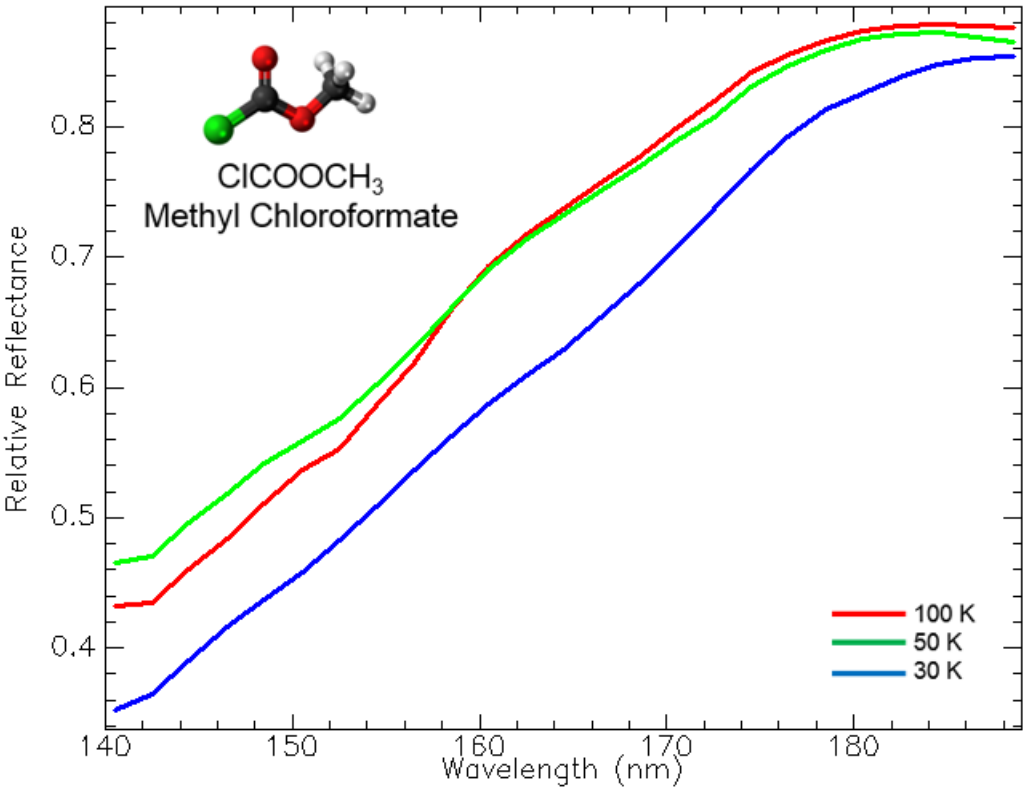

Figure 4.15: Three vacuum-UV laboratory spectra of methyl chloroformate over a temperature range of 30 – 100 K, similar to the range of temperatures encountered at the surface of Rhea and other icy satellites in the Saturnian system. The sampling of the spectra is ~1 nm, and the laboratory spectral data are displayed as relative reflectance. No absorption features are seen between 140 and 190 nm, in contrast to laboratory ice spectra of simple chlorine molecules.

4.3.7 Reflectance Spectra of Ozone (O_3)

I now present vacuum-UV laboratory spectra of solid ozone ice recorded at temperatures of 50 K and 70 K (Figure 4.16), similar to temperatures at the surface of icy satellites in the Saturnian system. The 260 nm Hartley absorption band of ozone has been seen in UV spectra of Jupiter's moon Ganymede, and on Saturn's icy satellites Dione and Rhea (Noll *et al*. 1997). Ozone is produced via photolysis and/or radiolysis of molecular oxygen (O_2) trapped in the surface ice layers of these icy moons. The O_2 is formed by radiolysis of water-ice molecules exposed to energetic electron and ion bombardment from Saturn's magnetosphere (Boduch, *et al*. 2011). However, as Boduch *et al*. 2011 point out, there may exist a chemical barrier to the production of ozone due to difficulty of trapping

O_2 in the surface ice of Saturn's icy moons. An alternative chemical pathway to the synthesis of O_3 may involve the irradiation of CO_2 present in the surface ice (Boduch *et al.* 2011). In this scenario, the ozone would be correlated with CO_2. Oxidants, such as O_2, O_3 and H_2O_2 produced by irradiation of ices, play an important role in astrobiology. Their diffusion/migration through the ice shells of icy moons to putative subsurface oceans, could sustain biological activities.

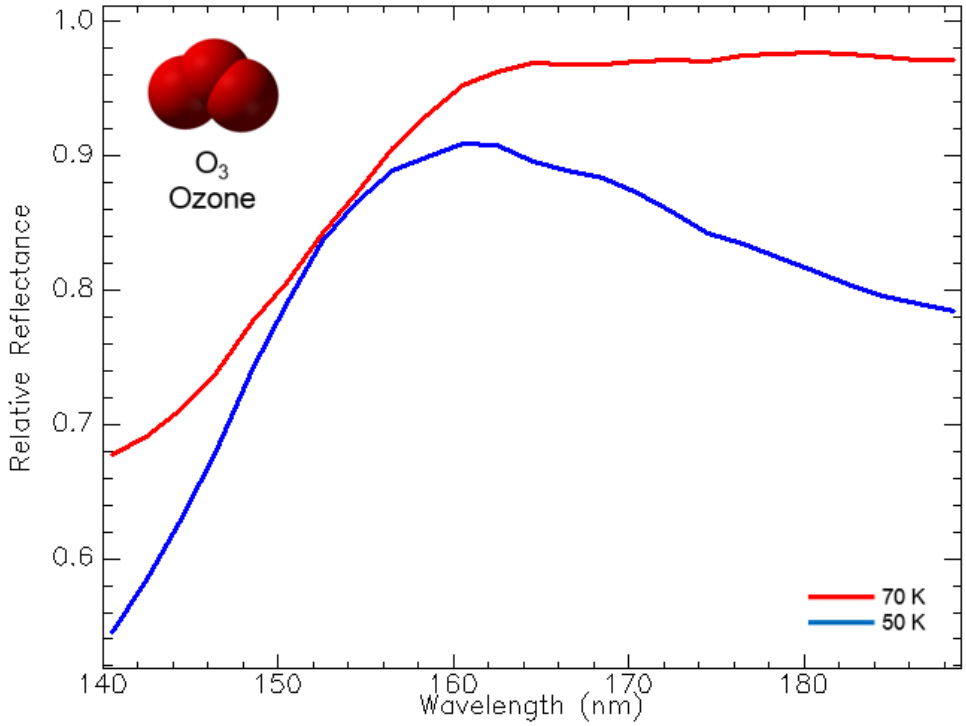

Figure 4.16: Two vacuum-UV laboratory spectra of ozone ice recorded at temperatures of 50 and 70 K, similar to the range of temperatures encountered at the surface of Rhea and other icy satellites in the Saturnian system. The sampling of the spectra is ~1 nm, and the laboratory spectral data are displayed as relative reflectance. There is no apparent absorption seen in the spectra over the wavelength range 140 – 189 nm.

The ozone spectrum recorded at 70 K (Figure 4.16) is remarkably different from the spectrum measured at a temperature of 50 K (Figure 4.16). This could be due to sublimation of the ozone from the thin film substrate as the temperature increases. However, it is readily apparent from the spectral profile that solid ozone ice cannot explain any features seen in the far-UV reflectance spectra of Rhea and Dione.

4.3.8 Reflectance Spectra of Dimethyl Ether $(CH_3)_2O$

Dimethyl ether (methoxymethane) $(CH_3)_2O$ is an organic compound, and is one of the simplest ethers. Dimethyl ether can be produced by chemical pathways involving formic acid (HCOOH), the methoxy radical (CH_3O) and methyl formate ($HCOOCH_3$). Formic acid is an important biological precursor molecule found in astrophysical environments, including cometary bodies, star forming regions, dense molecular clouds, and small bodies in the Solar System (Bergantini, *et al*. 2014). Thus, it is of interest to study its laboratory ice spectrum in the far-UV region of the spectrum. Figure 4.17 shows three laboratory ice spectra of dimethyl ether measured over a temperature range of 80 K to 115 K, similar to temperatures encountered on the icy Saturnian satellites.

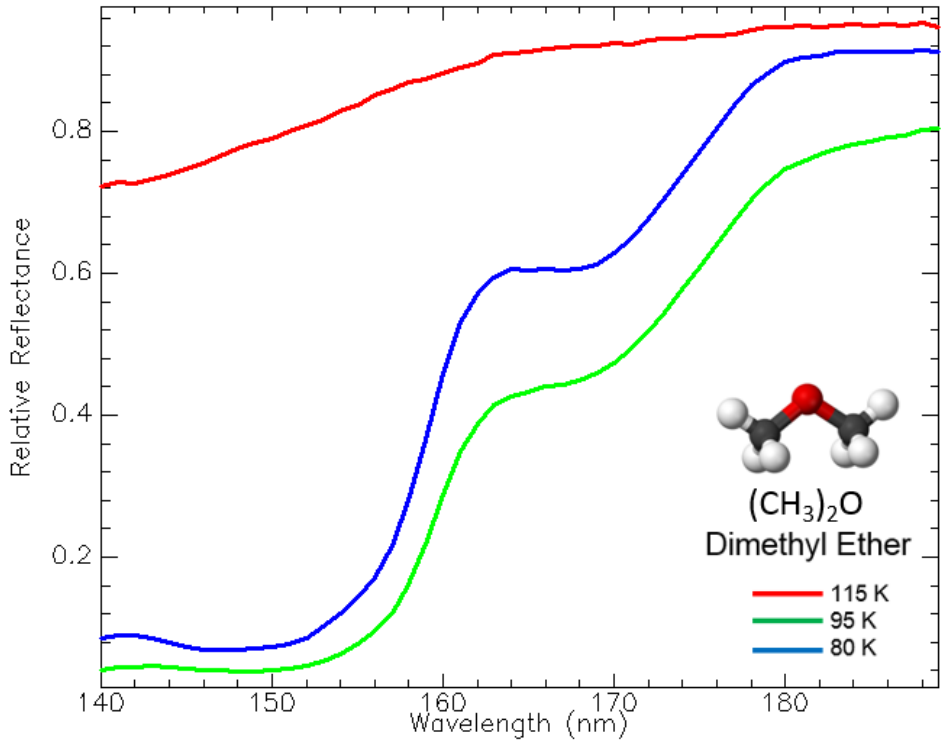

Figure 4.17: Three VUV laboratory spectra of dimethyl ether ice recorded at temperatures of 80 K, 95 K and 115 K, similar to the range of temperatures encountered at the surface of Rhea and other icy satellites in the Saturnian system. The sampling of the spectra is ~1 nm, and the laboratory spectral data are displayed as relative reflectance. The two spectra measured at lower temperatures show a complex spectral profile and a broad absorption feature with a minimum centred near 170 nm. The spectrum measured at 115 K shows no such profile or absorption feature. This may be due to sublimation of dimethyl ether as the temperature increases.

The differences between these three laboratory ice spectra can be seen by taking the first derivative of the spectra (Figure 4.18). The two derivative spectra recorded at lower temperatures (80 K and 95 K) exhibit a double peak profile due to their complex spectral slope. In contrast, the spectrum measured at 115 K shows no derivative peaks. Sublimation of the dimethyl ether could explain the lack of derivative peaks in the high-temperature spectrum.

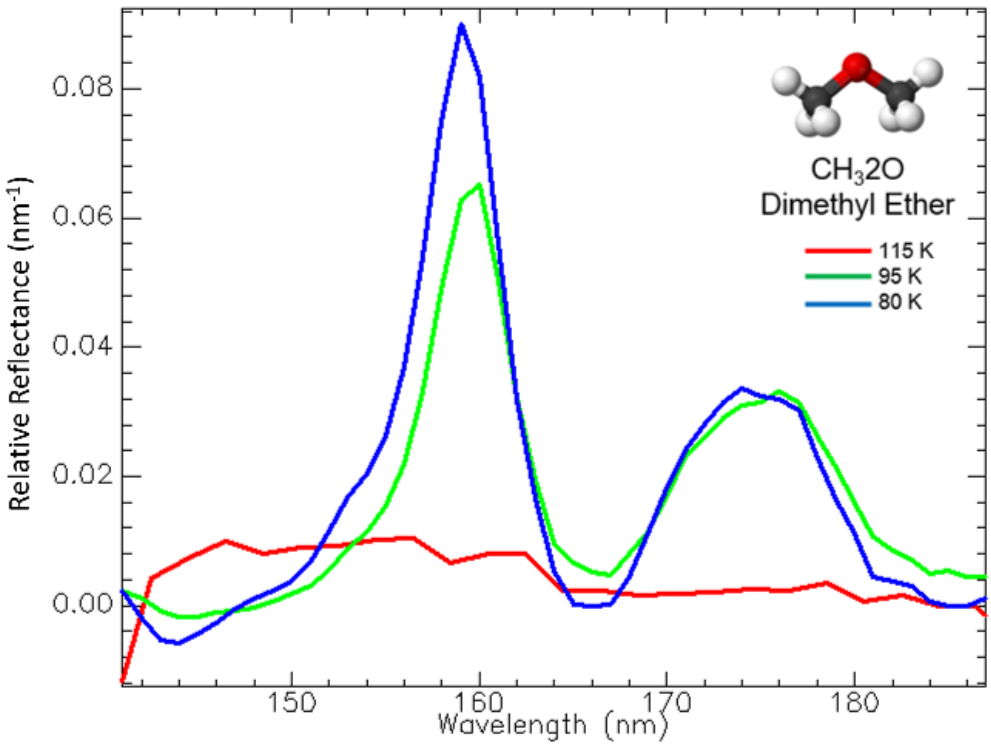

Figure 4.18: First-derivative spectra of the first-order laboratory ice spectra of dimethyl ether (CH_32O). Note the double peak profile in the two spectra recorded at lower temperatures. The double peaks are due to the complex structure in the spectral slope of the first-order laboratory spectra (Figure 4.17). The lack of complex structure in the derivative spectrum measured at 115 K is the result of sublimation of the ice as the temperature increases.

4.3.9 Reflectance Spectra of Ethyl Formate ($HCOOC_2H_5$)

Ethyl formate is another ester compound that can be formed from chemical pathways between formic acid and ethanol. Methyl formate is a complex organic molecule that is present in the interstellar medium (e.g. hot cores are star-forming regions) and in

comets (Bergantini *et* al. 2013; Biver *et al*. 2015) and is predicted to form as a result of chemical reactions between radicals, including CH_2OH, CH_3O, CH_3 and HCO. Ethyl formate may also exist on icy comets and small bodies of the solar system, and far-UV laboratory spectra can be used to search for its presence along with other molecules described previously in this chapter on the surfaces of icy satellites. Three VUV spectra (Figure 4.19) were collected over a temperature range similar to that on the surfaces of Saturn's icy satellites (~50-110 K). The three spectra show a broad absorption feature with a minimum centred near 165 nm.

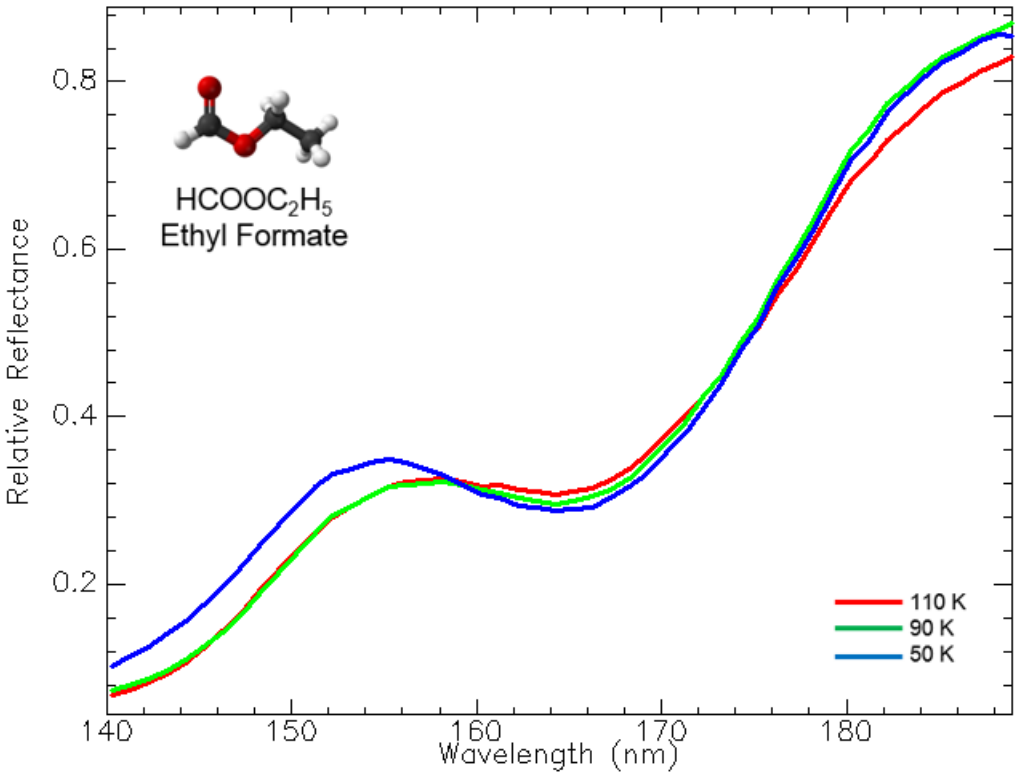

Figure 4.19: Three laboratory ice spectra recorded over three temperatures similar to the temperatures encountered at the surfaces of Saturn's icy satellites. The sampling of the spectra is ~1 nm, and the data are presented in relative reflectance. All three laboratory spectra show a broad absorption feature centred near 165 nm. Ethyl Formate does not explain the 184-nm absorption feature seen in the Cassini UVIS spectra of Rhea and Dione.

4.3.10 Reflectance Spectra of Acetonitrile (CH_3CN)

Acetonitrile (CH_3CN) has been found in protoplanetary disks around young stars (Bergner, *et al*. 2018), and studies of cometary bodies suggest that it may have been a common molecular compound in the early solar system. CH_3CN and other C-N bearing chemicals also exist on cometary objects, and in Titan's atmosphere (Hudson & Moore, 2004). It is important to study these molecules in the laboratory since they represent a large class of organic molecules found in the ISM. Far-UV laboratory spectra of acetonitrile may be used to search for its presence on Saturn's icy satellite Rhea. Radiolysis from high-energy particles from Saturn's magnetosphere would dissociate any Acetonitrile present on the surface of icy satellites, and the products would lead to the formation of many new organic species.

Two VUV spectra were measured in the lab at temperatures of 40 K and 80 K in a near-vacuum environment. The spectra are presented in Figure 4.20 in the form of relative reflectance. Both spectra show a weak absorption with a broad profile from approximately 145 – 160 nm.

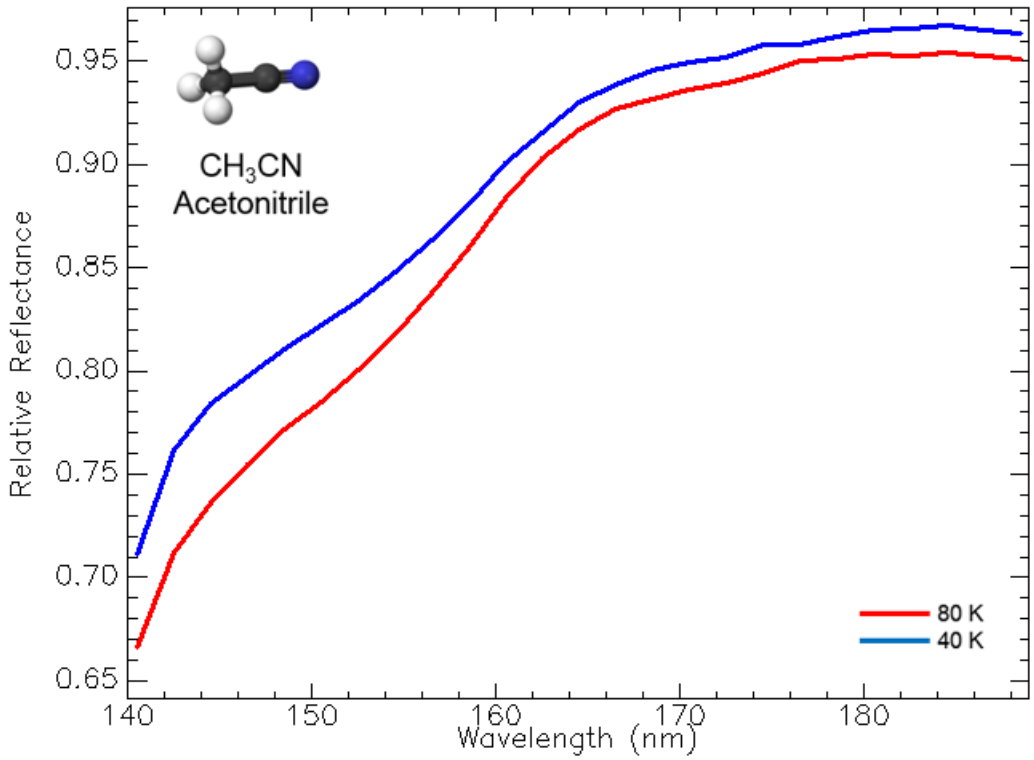

Figure 4.20: Two laboratory ice spectra of Acetonitrile recorded over a temperature range similar to that encountered at the surfaces of Saturn's icy satellites. The sampling of the spectra is ~1 nm, and the data are presented in relative reflectance. The two vacuum-UV spectra show an extremely weak, broad absorption feature, from approximately 145 to 160 nm. No absorption is seen near 184-nm.

4.3.11 Reflectance Spectra of Glycerol, Ethyl Acetate and Propargyl Ether

VUV thin ice spectra of Glycerol ($C_3H_8O_3$), ethyl acetate ($C_4H_8O_2$), and phenol (C_6H_6O) were collected over a temperature range of 60 K to 70 K (Figure 4.21). These conditions are like those at the surfaces of Saturn's icy satellites. The organic and alcohol molecules are assumed to be present in the interstellar medium and star-forming regions. Thus, they may have been incorporated into icy bodies in the outer solar system and are of interest in terms of their astrochemistry. The spectral slopes of the relative reflectance spectra do not match the spectral slopes of any of the Cassini UVIS spectra obtained over Rhea's leading and trailing hemispheres. Ethyl acetate, Propargyl ether, and glycerol therefore do not explain the broad absorption feature observed in UVIS spectra between ~175 and 190 nm.

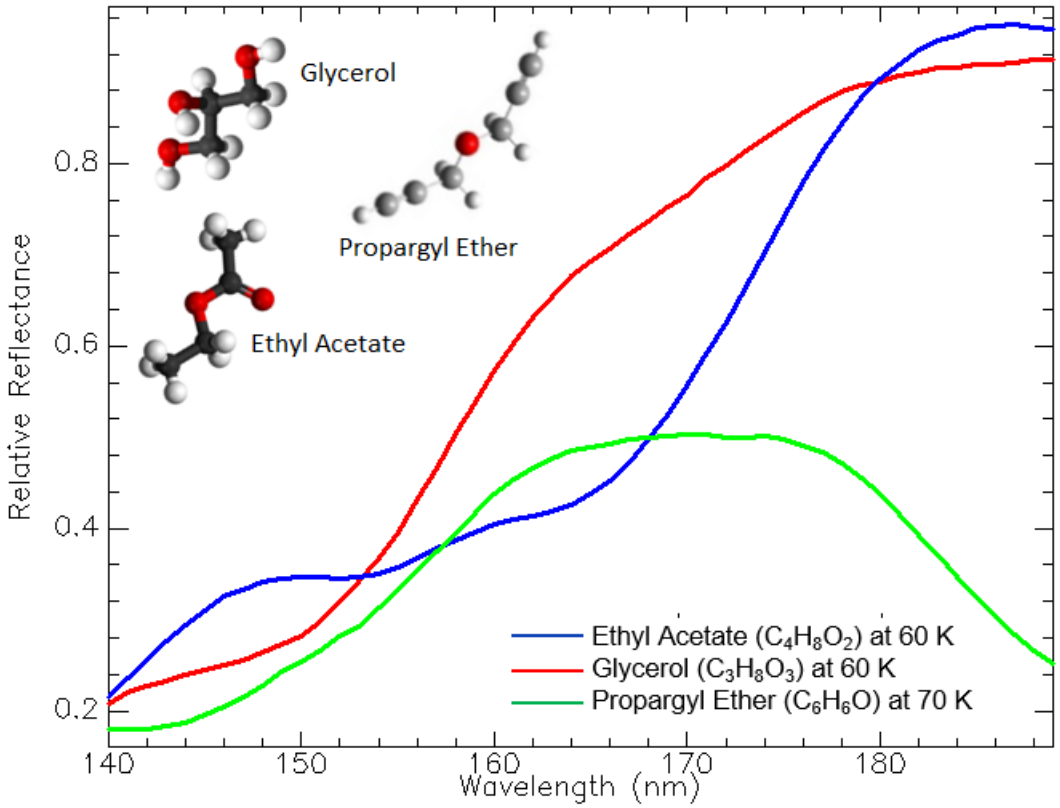

Figure 4.21: VUV laboratory ice spectra of several organic molecules recorded over a temperature range similar to that encountered at the surfaces of Saturn's icy satellites. The sampling of the spectra is ~1 nm, and the data are presented in relative reflectance.

4.3.12 Summary of Laboratory Ice Measurements

In this chapter far-UV measurements of ice mixtures deposited on thin substrates under conditions in the outer solar system have shown the positions of electronic absorption bands in the solid (ice) phase. The ice mixtures chosen were based on a list of molecules that are known (or suspected) to be present on the surface of Saturn's icy moons. Vacuum-UV (VUV) measurements of irradiated water-ice by an electron gun have been presented as a baseline reference. The irradiated water-ice spectra show a distinctive shift in the far-UV water-ice absorption edge from its nominal 165-nm position towards shorter wavelengths. The shift is also confirmed using first-derivative spectroscopy, which clearly shows a shift in the derivative peak towards shorter wavelengths relative to 165-nm. The displacement of the absorption edge from its nominal 165-nm location is the

result of the production of by-products from radiolysis, including molecular oxygen, hydrogen peroxide and other intermediate radicals.

The positions of electronic absorption features in solid phase ice can differ from those obtained on gas phase data. As ice undergoes a phase change from a gas to a solid, the absorption cross section is known to change. Thus, the solid phase ice spectra presented here may not show all the electronic states that gas phase spectra display.

A preliminary examination of the laboratory ice spectra presented in this chapter shows that simple chloromethane and hydrazine molecules appear to provide a match to the unknown absorption feature between ~170 – 190 nm. Chapter 6 of this report presents detailed comparisons between the laboratory ice spectra presented in this chapter and Cassini UVIS data collected during three flybys of Saturn's moon Rhea. A detailed discussion of the results of the comparisons, and scientific implications is presented in Chapters 6 and 7.

CHAPTER 5

CASSINI UVIS INSTRUMENT AND OBSERVATIONS

5.1 Introduction

This chapter will start by providing a detailed description of the Cassini Ultraviolet Imaging Spectrometer (UVIS) instrument. A description of the data collection process and calibration is then provided, followed by a review on how the UVIS reflectance spectra were chosen and processed for analysis. A description of where the UVIS spectra were collected on the surface of Rhea is then given, along with a detailed log of the observations. The chapter then presents for the first time, spatially-resolved far-UV spectra of Rhea's icy surface in the form of a plot that allows the reader to compare the differences in reflectance between the satellite's leading and trailing hemispheres. The differences are also illustrating by showing the first-derivative spectra of the original data.

5.1.1 Design of the Cassini UVIS Science Instrument

The Cassini Ultraviolet Imaging Spectrometer (UVIS) instrument (Figure 5.1a and 5.1b) measured radiance over two spectral channels. The extreme UV (EUV) channel measured radiance over the spectral range of 56 nm to 118 nm, and the far-UV (FUV) channel covers the spectral range from 110 nm to 190 nm. The UVIS instrument also included a Hydrogen-Deuterium Absorption Cell (HDAC) that measured the deuterium-to-hydrogen (D/H) ratio in the Saturnian system, and a High-Speed Photometer (HSP) channel that recorded stellar occultation (Esposito, *et al*. 2014). The primary use of the HSP was to study the detailed structure of Saturn's rings by recorded measurements of density profiles derived from the occultation measurements.

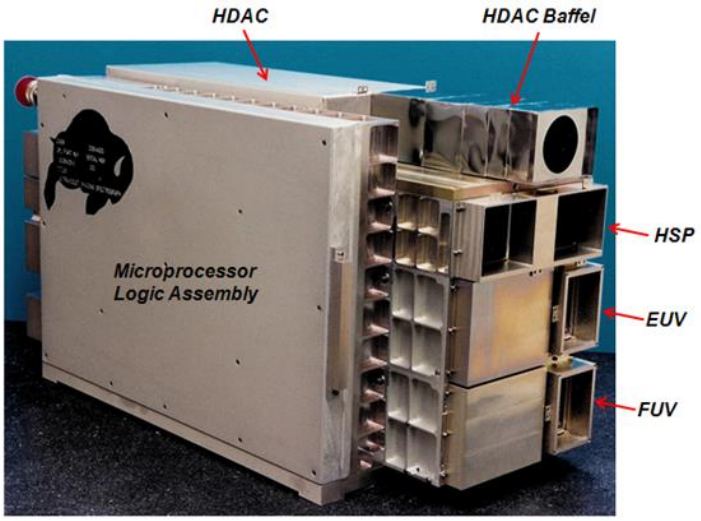

Figure 5.1a. Photograph of the Cassini Ultraviolet Imaging Spectrometer (UVIS) showing its different experiments. The microprocessor logic assembly controls the operation of the different experiments. In the diagram, HDAC is the Hydrogen Deuterium Absorption Channel, HSP is the High-Speed Photometer, EUV and FUV are the Extreme Ultraviolet and Far Ultraviolet spectrometers, respectively. Figure curtesy of the Cassini UVIS team.

Figure 5.1b. Location of the UVIS science instrument on the Cassini spacecraft. The UVIS instrument was aligned with the other science instruments to permit simultaneous observations of a given target. Figure was produced using 3-D DXF model viewer. Model courtesy of NASA.

The Rhea surface ice observations were made using the far-UV spatial-spectral instrument (FUV), which had a focal length of 100 mm for the telescope, and an entrance pupil size of 20 mm × 20 mm. The instrument's reflecting surface was coated with a combination of aluminum and magnesium fluoride (MgF_2). Magnesium fluoride is a good choice for coating UV optical surface elements due to its high transmission in the vacuum UV (VUV) region of the spectrum, down to 121 nm. Toroidal gratings coated with Al+MgF_2 that are aberration-corrected were utilised in the UVIS/FUV instrument to provide both high sensitivity and spatial resolution in the direction of the entrance slit. The gratings had 1068 grooves per millimetre and were designed to focus the observed spectrum onto an imaging microchannel plate detector. Toroidal gratings were chosen over holographic and elliptical gratings, because they produce the highest quality images for a given angle of incidence (Esposito *et al*. 2004). The toroidal gratings were used with a diffraction angle equal to zero at the centre of the detector. Holographic gratings were not selected due to the degradation of image quality for object points that are located at greater distances from the centre of the spectrometer slit. Elliptical gratings were not used because they produce only one stigmatic wavelength, in contrast to toroidal gratings, which have two stigmatic wavelengths (McClintock, *et al*. 1993). Stigmatic images over wide wavelength ranges are desired, since they represent an imaging system in which all aberrations have been minimised or eliminated. The specific wavelength range for each channel of the UVIS spectrometer sets the number of grooves in the toroidal grading to 1068 per millimetre (Esposito *et al*. 2004). The groove spacing for the grating used in the FUV spectrograph was determined using the relationship between the wavelength range, focal length, f_s, of the spectrograph and width of the detector, w_{det},

$$d = \frac{f_s}{w_{\text{det}}}\left(\lambda_2 - \lambda_1\right) \quad (5.1)$$

where $\lambda_2 - \lambda_1$ is the range of wavelengths that are imaged onto the detector. Since the UVIS/FUV spectrometer was designed (limited by mechanical constraints) so that the diffraction angle, β, was equal to zero at the detector's centre point, the angle of incidence is given by the grating equation of the form

$$d \sin \theta_i = \frac{\lambda_2 + \lambda_1}{2} \quad (5.2)$$

where θ_i is the desired angle of incidence, and *d* the spacing of the grooves on the grating. Equations 5.1 and 5.2 determine the grating spacing and angle of incidence, given the focal length of the spectrograph, the width of the detector and the wavelength coverage. The requirement of stigmatic imaging for two wavelengths at the diffraction angles $\pm\theta_{d,s}$, determined the vertical (R_V) and horizontal (R_H) radius of curvatures for the toroidal grating, based on the relationship between the two radii of curvatures, and the angle of incidence and diffraction.

$$\frac{R_V}{R_H} = \cos\theta_i \cos\theta_{d,s} \quad (5.3)$$

To obtain the desired spectrometer design for $\theta_d = 0$ at the centre of the detector, given the mechanical constraints, the structure holding the spectrograph required the angle $\theta_i - \theta_d$ to be 9.2 degrees for the EUV and FUV channels of the UVIS instrument. This configuration resulted in a subtended angle of $\Delta\theta_d = 2.45$ degrees when projected along the Rowland circle (a circle that is defined by the centre of the spectrometer grating and the tangential radius of curvature of the grating), and two locations for the stigmatic wavelengths at diffraction angles of $\theta_{d,s} = \pm 1.23$ degrees (McClintock, *et al*. 1993). The requirement to obtain the best average imaging over the detector was the primary driver for the design of the spectrometer.

The microchannel plate operated as an electron multiplier, and because it was composed of multiple channels, it provided the UVIS/FUV spectrometer with spatial resolution. To reduce the scattering of long-wavelength light within the spectrometer, cesium iodide (CsI) was used for the photocathode material in the wavelength range of 110 to 190 nanometres. Photocathode materials with higher efficiency than CsI were not chosen because they tend to have higher sensitivities to longer wavelength radiation, and internal scattering of these longer wavelengths inside the FUV instrument can dominate weak planetary FUV emissions (Esposito *et al*. 2004).

The UVIS/FUV spectrograph had three slit width settings of 75, 150 and 800 microns. The Rhea observations in this research program used the 75- and 150-micron slits, providing a $\Delta\lambda$ (the smallest resolvable element) of 2.75 and 4.8 Å̄, respectively. The instantaneous field of view provided by the 75-micron slit was 0.75 mrad, and for the 150-micron slit, 1.5 mrad. Only the 2007 Rhea flyby observations utilised the high-resolution slit mode. The detectors inside the FUV spectrograph were based on CsI with a maximum quantum efficiency of 8 percent, and the detector was mounted inside a vacuum housing with a magnesium fluorite (MgF_2) window.

The pixel size of the detector elements was 25 µm × 100 µm, and the format of the detector was 1024 spectral × 64 spatial. To avoid vignetting for object points that are off-axis, the telescope's mirror size was set at 33 mm in height × 22 mm in width. Furthermore, to reduce the amount of scattered light when limb scan measurements are being made, the telescope was equipped with internal baffles and a sunshade. The overall design of the UVIS/FUV instrument (Figure 5.2) represents a compromise between spectral and spatial (imaging) resolution, based on the constraints of volume available on the Cassini spacecraft (Esposito *et al*. 2004).

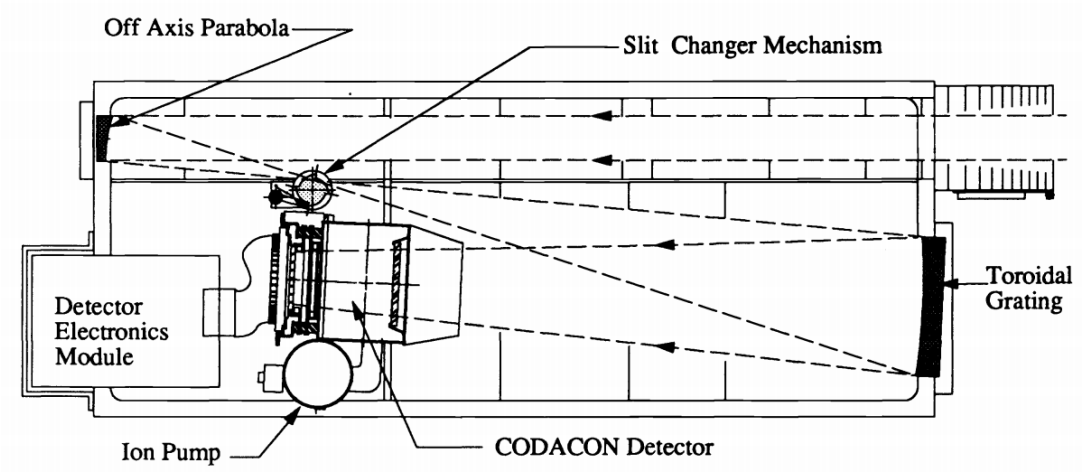

Figure 5.2: Optical design diagram for the Cassini UVIS/FUV spectrometer channel. The design represents the best compromise in spectral resolution, quality of spatial imaging, and volume/mass. Figure courtesy of McClintock et al. (1993).

A summary of the technical specifications of the UVIS FUV channel are given in table 5.1.

Table 5.1: Specifications for the Cassini UVIS/FUV instrument (Esposito et al. 2004).

Telescope	**FUV (~110-190 nm)**
Focal length (mm)	100
Entrance pupil size (mm)	20×20
Reflecting surface	Al+MgF_2
Toroidal Grating	
Size (mm)	60×60
Grating radii (mm)	300, 296.1
Grating surface	Al+MgF_2
Grooves/mm	1068
Input angle α (degrees)	9.22
Out angles β (degrees)	±2.9
Position Slits	
Slit widths (microns)	75, 150, 800
Δλ (Ä) (extended source)	2.75, 4.8, 24.9
Field of View (mrad)	(0.75, 1.5, 8)×60
Detectors	
Photocathode	CsI
% Maximum QE	8
Detector window	MgF_2
Detector size (mm)	25.6×6.4
Pixel format (λ×θ)	1024×64
Pixel size (microns)	25×100
Pulse resolution	10 μsec

5.2 Data Collection from Cassini UVIS Science Instrument

The signal (in counts/pixel) and noise (counts/pixel) recorded by the UVIS/spectrometer is described by the following equation, assuming the instrument was viewing an extended source (Esposito et al. 2004).

$$S(\lambda) = L(\lambda) \cdot F_{opt}^2 \cdot A_{pix} \cdot \tau(\lambda) \cdot q \cdot t$$
$$N(\lambda) = \sqrt{S(\lambda) + d \cdot t} \qquad (5.4)$$

Here, *F* is the focal ratio of the optical system, $L(\lambda)$ is the observed radiance of the source expressed in kilo-Rayleigh (kR) units (=$10^9/4\pi$ photons/cm^2/sr/s), A_{pix} is the area of one detector pixel (25 μm × 100 μm), *q* the quantum efficiency of the detector, *t* the integration time, $\tau(\lambda)$ the transmission of the instrument's optical system, and *N* and *b* are the noise (in counts/pixel) and dark current (counts/pixel/second), respectively. Observing through the low resolution slit (150 μm) results in greater sensitivity across the FUV wavelength range of ~110 to 190 nm with a spectral resolution of 0.48 nm. The high resolution slit mode provides a greater spectral resolution of 0.24 nm, but at the cost of lower sensitivity across the same wavelength range. The equation for the recorded signal (eqn. 5.4) can be expanded in greater detail when the pixel-to-pixel variation (also known as the flat field) is accounted for, in addition to scattered light. In this case, the recorded number of counts per pixel located at column *i* and row *j* on the detector, is given by (Esposito et al. 2004)

$$N_{counts}(i,j) = L(i,j) \cdot \frac{A_{tel} \cdot A_{slit}}{f^2} \cdot \frac{1}{n_{pixel}} \cdot FF(i,j) \cdot \tau_{sys} \cdot q \cdot \Delta\lambda \cdot t \cdot B(i,j) + S(i,j) \quad (5.5)$$

where $L(i,j)$ is the measured radiance at a pixel, A_{tel} is the telescope entrance pupil area (20 mm × 20 mm for UVIS), A_{slit} is the area of the entrance slit, f is the focal length of the telescope (100 mm for UVIS), n_{pixel} is the number of rows illuminated by the image, assuming it completely fills the spectrometer slit (60 for UVIS/FUV), $FF(i,j)$ is the flat

field (describing the non-uniformity across the detector – i.e. pixel-to-pixel variation), τ_{sys} is the combination of transmissions for the telescope mirror, grating, and window, q is a parameter that describes the efficiency of the measured counts per incident photon (i.e. the quantum efficiency of the detector), $\Delta\lambda$ is spectral width of a single detector pixel, t is the integration time, $B(i,j)$ is the recorded background signal, and $S(i,j)$ accounts for scattered light in the instrument.

Prior to the launch of the Cassini spacecraft, the FUV spectrograph was calibrated in the laboratory to measure the instrument's sensitivity. The measured sensitivity is then used to convert the recorded detector counts (DNs) to physical units using the equation

$$L(i,j) = \left[N_{counts}(i,j) - B(i,j) - S(i,j) \right] \cdot M(i,j) \quad (5.6)$$

where $L(i,j)$ is the recorded radiance of a detector pixel at pixel *i* and *j*, and $M(i,j)$ is the inverse of the sensitivity, given by

$$M(i,j) = \frac{f_{tel}^2}{A_{tel} \cdot A_{slit}} \cdot n_{pixel} \cdot \frac{1}{FF(i,j) \cdot \tau_{sys} \cdot q \cdot \Delta\lambda \cdot t} \quad (5.7)$$

where the units of the inverse of the sensitivity are kiloRayleigh/count/nm, and the other parameters in the equation are defined above (Esposito et al. 2004). The values for the inverse sensitivity are contained in the calibration files at the Planetary Data System (PDS), and include the integration time of the observation. Thus, the observed spectral data need not be in the form of a count rate before applying the calibration matrix to the observed observation.

5.3 Data Processing of UVIS Observations

The UVIS instrument recorded data using 1024 spectral channels over 64 spatial elements, with the ability to collect the spectral-spatial data over a finite time series. The

slit of the UVIS spectrometer was slewed across the target's surface to acquire the second (spatial) dimension. The spectral-spatial format of the data recorded by UVIS is illustrated in figure 5.3.

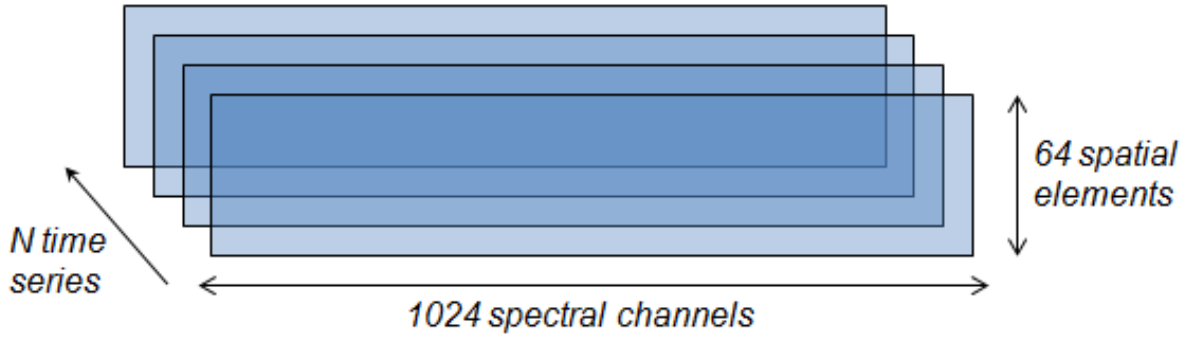

Figure 5.3. Conceptual layout of the UVIS instrument data format. Each UVIS spatial-spectral cube consists of 1024 spectral pixels, 64 pixels in the spatial dimension, over a time series (samples) corresponding to each integration of the detector array. Diagram by R. Mark Elowitz.

Each UVIS EUV/FUV data product may take the form of an image, a spectrum, or a spectral-spatial cube. Each time series sample contains both spatial and spectral information about a given scene. This is in contrast to a true hyper-spectral instrument that produces products, where each pixel within a given scene constrains both spectral and spatial information simultaneously. The spectrum derived from true hyper-spectral instruments extends over the third dimension of what is considered a spectral cube. In contrast, instruments such as Cassini's UV imaging spectrometer produce spectra by summing over all spatial elements (i.e. summing over the entire spatial dimension).

Processing Cassini UVIS data for this thesis had many challenges, especially the lack of computer software tools needed for the data reduction. With the exception of the UVIS instrument manual, processing the data was difficult due to insufficient materials in the literature covering the processing of UVIS data. One major issue was the lack of visualisation tools to enable the UVIS instrument footprint to be projected onto a real image of Rhea's surface. Most of the data collected by the Cassini UVIS instrument was meant to be processed and analysed by members of the instrument team. The few software

tools developed in-house by the UVIS team were not user friendly, and substantial time was required to learn how to apply these tools to the processing of UVIS-FUV spectral data. Assistance outside of the UVIS team was not an option as very few scientists outside the team have worked with Cassini UVIS data due to the problems described above.

The approach used to process and analyse UVIS data in this research programme involved the use of IDL (Interactive Data Language) and ENVI (ENvironment for Visualizing Images). These tools provide a flexible scripting language that can be used to manipulate spectra and imagery obtained from spectrometers and imaging systems. Using the scripting and interactive language capabilities of these two tools, the UVIS data was calibrated, background subtracted, and corrected for the solar irradiance at the distance of Saturn at the time of each observation. The processed data was then smoothed (data polishing) using the Savitzky-Golay technique (Savitzky & Golay, 1964; Gorry, 1990) to reduce the high amount of noise inherent in far-UV data.

UVIS/FUV datasets for the Rhea 2007, 2010 and 2011 flyby events were obtained from the NASA PDS archive to provide enough spatial distribution in both latitude and longitude on Rhea. A wide spatial coverage on Rhea's surface was chosen to characterise the geochemical distribution of molecules. The spectral-spatial datasets among the three flybys were also chosen based on the signal-to-noise ratio of the data, and range across the surface of Rhea (Figure 5.4). The same procedure was used in the selection of the Dione datasets.

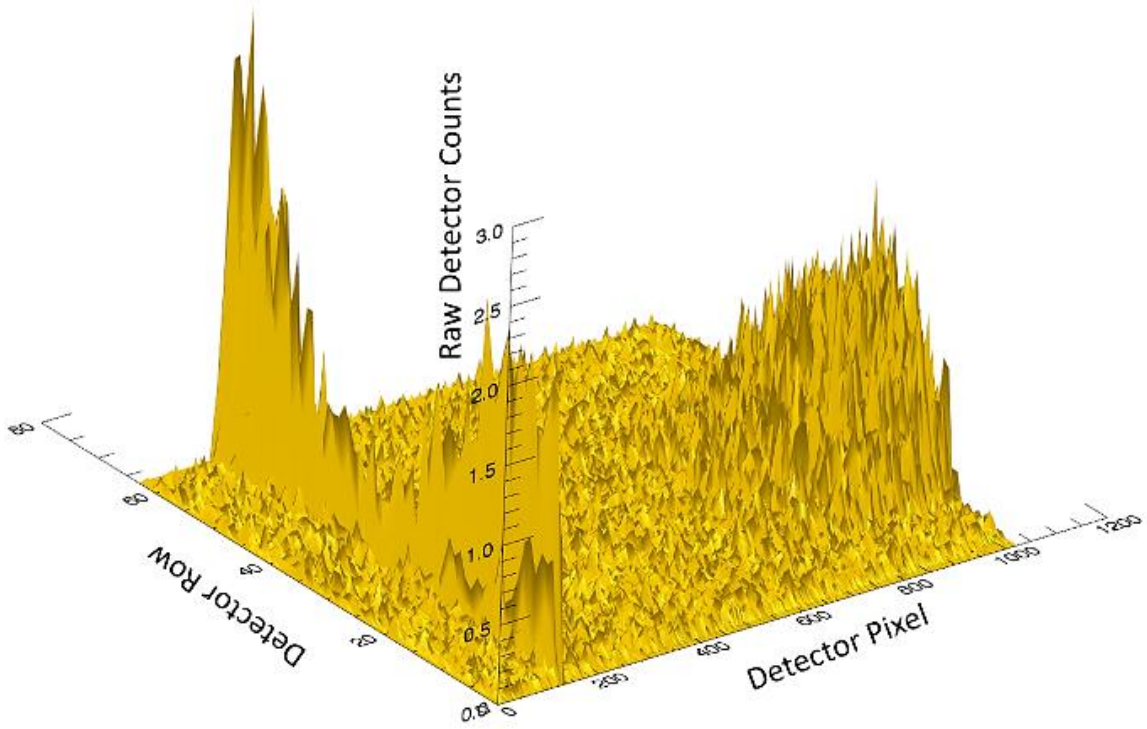

Figure 5.4: Illustration of raw, uncalibrated UVIS spectral-spatial data in the form of a three-dimensional plot. The reflected signal from Rhea is seen at the centre right side of the surface plot. The signal with a sharp profile to the left is due to the solar 1215 Lyman alpha emission line. The UVIS/FUV data has 1024 spectral channels and 64 spatial rows. The z-axis has been scaled to allow easy visualisation of the data. The interactive three-dimensional plot created using the 'surface' routine in IDL can help determine appropriate areas for background subtraction and overall data quality assessment. Diagram by R. Mark Elowitz

This methodology was applied to improve the quality in the statistical fitting of the observed spectral data with laboratory spectra of different water-ice/non-water-ice mixtures. The final data set consisted of UVIS observations with a range constraint, such that Rhea's surface filled the UVIS spectral slit field-of-view. Each UVIS/FUV raw spectrum was converted to geophysical units (kilorayleigh/Angstrom) by applying a unique set of calibration matrix coefficients (described in the previous section) to the data (Esposito, *et al*. 2014). After multiplying the observed spatial-spectral data with its associated calibration matrix, the derived calibrated data is in units of kiloRayleigh per nanometre (kR/nm). Since all of the UVIS/FUV observations of Rhea's surface filled the area of the spectral slit in the spatial dimension, the derived radiance is given by equation

4.21. The detector count rate is not derived, since the calibration file associated with each FUV observation includes correction for the integration time. All observations were corrected for particle emission (gamma rays) background from the Cassini spacecraft radioisotope thermoelectric generators (RTGs). Appropriate RTG background counts were obtained using a plot of RTG background rate as a function of time (Figure 5.5).

The count rates shown in Figure 5.5 were derived by taking an average value for an area defined by a range of FUV detector columns from 950 to 1015 over rows 2 to 60, from a series of interplanetary hydrogen observations. For the low-resolution slit, the background is systematically slightly higher than for the high-resolution slit, since the low-resolution slit is two times the width of the high-resolution slit.

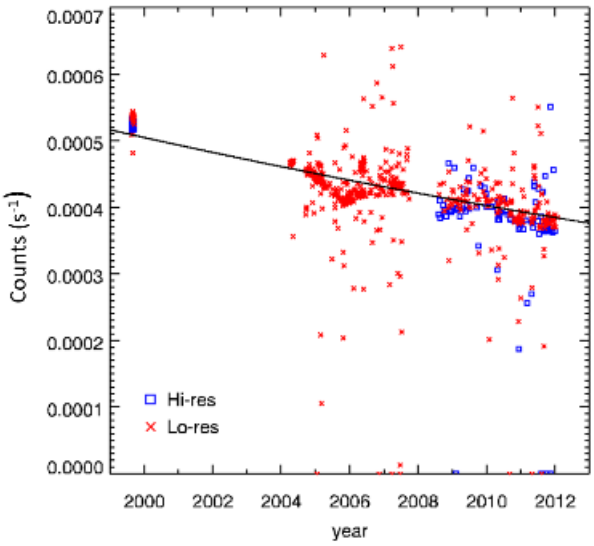

Figure 5.5: Background counts due to emission of gamma rays from Cassini's radioisotope thermoelectric generators (RTGs) used to provide power to the spacecraft. The steady decrease in the background time as a function of time agrees with the expected decay of Plutonium-238 inside the RTGs. Diagram from the "Cassini UVIS User's Guide", Laboratory for Atmospheric and Space Physics (LASP) (2014).

The recorded counts in Figure 5.5 that lie above the general decay trend (black line) are the result of background contamination from celestial objects (e.g. planets, moons, stars) that cross through the field of view of the UVIS instrument. Ring-crossing events might be another source of background contamination. Partial data dropouts/losses during downlink

result in recorded counts that tend to fall below the general decay trend (black line) shown in Figure 5.5.

Lower background counts were used for each successive fly-by (2007, 2010, and 2011) due to the expected decay of plutonium-238 within the RTGs. The sky background is subtracted from the data by looking for a region with no apparent photon-generated signal and calculating the mean pixel value for that region. Anomalous pixels were flagged before applying the calibration matrix, and interpolated across within the IDL processing environment. The calibrated spectrum for each observation was derived by summing across a given number of valid spatial elements, making sure to not include any rows near the edges of the data (Figure 5.6).

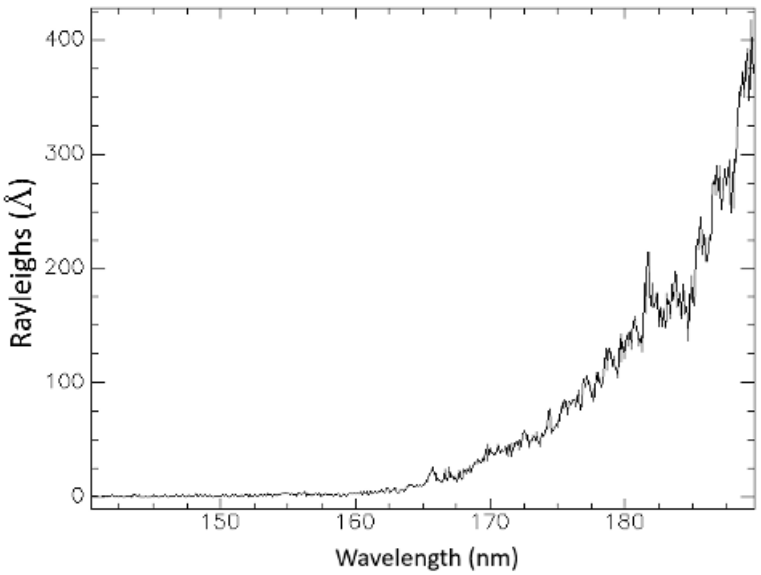

Figure 5.6: An example calibrated UVIS/FUV spectrum before solar correction. The pre-solar corrected spectrum shows weak absorption from approximately 180 to 189 nm. No smoothing has been applied to the data.

Each calibrated spectrum was then converted to I/F (reflectivity) by dividing by a solar spectrum (Figure 5.7) from the SOLSTICE instrument on the SORCE spacecraft for the given observation date (McClintock *et al*. 2000). The appropriate solar spectrum was used to account for the difference between the sub-solar longitudes facing both Saturn and the Earth at the time of each observation to account for solar variability,

$$\rho = \frac{P}{(S/\pi)} = \frac{I}{F} \qquad (5.8)$$

where ρ is the reflectance, P the calibrated FUV spectrum, and S the solar flux spectrum, where $S = \pi F$. Any correction for the filling factor was negligible since Rhea completely filled the projected slit for all observations in the dataset – i.e. there were no sub-pixel observations.

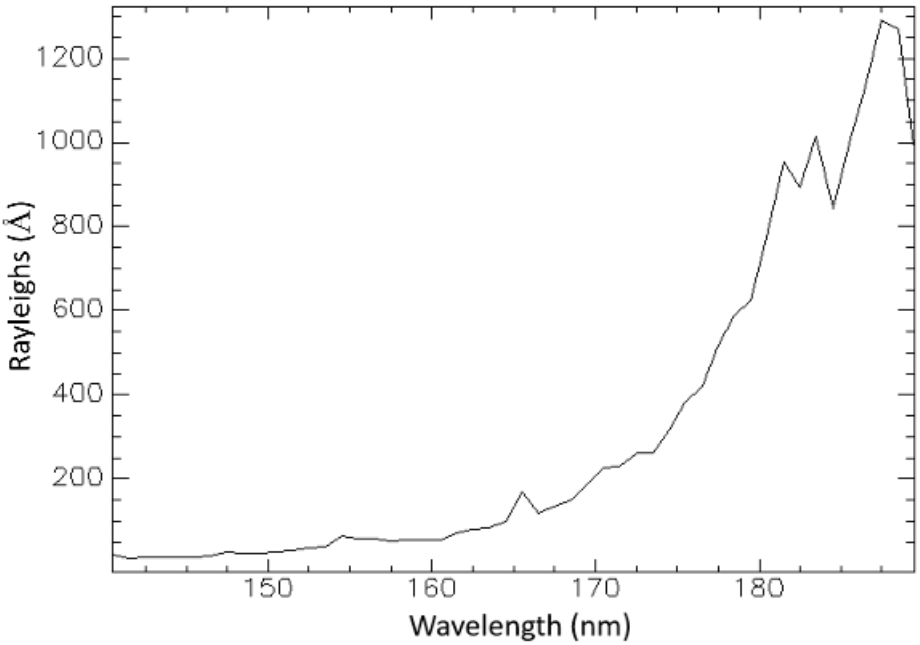

Figure 5.7: An example far-UV solar spectrum observed by the SOLSTICE (SOlar Stellar Irradiance Comparison Experiment) instrument on board the SORCE (SOlar Radiation and Climate Experiment) spacecraft. The spectrum is shown over the region of interest, from 140-189 nm.

Each solar flux corrected spectra (in I/F) was smoothed using the Savitzky-Golay method (Savitzky & Golay, 1964) to reduce noise and allow easier comparison with laboratory reference spectra (Figure 5.8). The region of interest (~150 – 190 nm) has the highest signal-to-noise, and is used in the analysis of Cassini UVIS data. A search for molecules for wavelengths short-ward of 150 nm is problematic due to noise in the far-UV data that is higher and more structured.

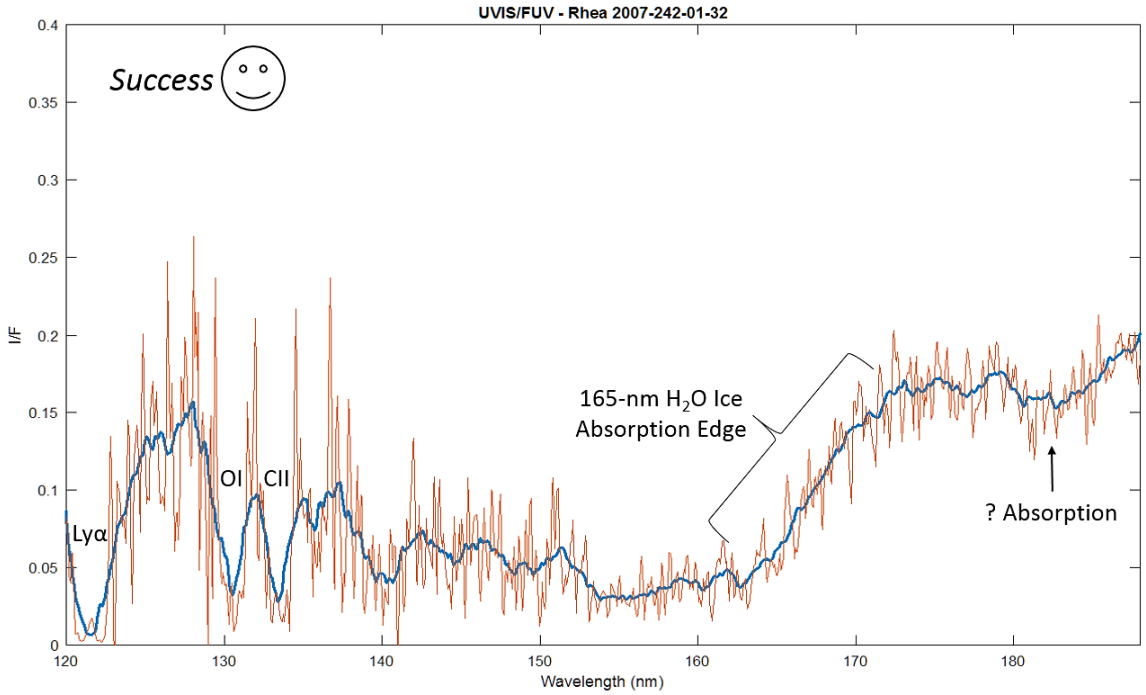

Figure 5.8: Example UVIS/FUV spectrum of Rhea corrected for solar flux and smoothed to reduce noise. The 165-nm absorption edge due to water-ice is visible and an unknown absorption feature is seen at wavelengths between ~175 and ~190 nm. Note the trend towards higher signal-to-noise beyond 150 nm.

The spectrum shown in Figure 5.8 exhibits the classical 165-nm UV absorption edge due to water-ice on the surface of Rhea. This absorption feature is due to the first electronic transition in the far-UV (denoted by $\tilde{A} \leftarrow \tilde{X}$) arising from the lowest energy site (Ozaka, *et al*. 2012). This band can be assigned to the transitions from the *n* orbital to the σ^* orbital, and to the $3s$ (Rydberg) orbital (see section 3.2 for review of UV spectroscopy). The $\tilde{A} \leftarrow \tilde{X}$ transition of water exhibits peak shifts due to phase transitions, reflecting the variation in changes in hydrogen bonding and molecular density of H_2O (i.e. it is dependent on the environment where the water is located) (Ozaka, *et al*. 2012).

5.4 Location of Cassini UVIS Observations on Rhea's Surface

The Cassini UVIS observations were carried out during the 2007, 2010 and 2011 flybys of Saturn's mid-sized icy satellite Rhea. Additional observations were carried out during 2005 and 2013. The distance to Rhea during the five flybys of Rhea ranged from

approximately 7700 km to 135721 km, and Rhea's surface filled the UVIS slit for all observations, except for the observation collected on November 26, 2005. The spectral resolution and spectral slit instantaneous field-of-view (IFOV) (UVIS high-resolution slit mode) for the Rhea observations was 0.275 nm and 0.75 mrad, respectively. The solar phase angle ranged from ~0.8 to ~65 degrees for the entire data set. The Cassini UVIS/FUV observations were selected from the Planetary Data System, an archive of data products (mostly imagery and spectra) generated from NASA space science missions. Several months were spent sorting through Cassini UVIS data in order to find the highest quality reflectance spectra of Rhea and Dione.

The selection of UVIS data was based on the signal-to-noise ratio and lack of data artefacts over a wide range of latitude and longitude on the surface of Rhea. Each candidate spectrum was carefully examined by creating a three-dimension plot of the signal within the UVIS instrument slit. The UVIS data was sampled to satisfy the requirement of collecting far-UV spectra over the leading and trailing hemispheres of the satellites to search for any asymmetries in molecular species due to preferential irradiation of the surface ice.

A log of the selected UVIS observations and their associated geospatial information in shown in Table 5.2.

Table 5.2: Geospatial data Cassini UVIS observations for the 2005, 2007, 2010, 2011 and 2013 Rhea flybys. Lat1 and Lat2 are the latitude boundaries of the observation, and Long1 and Long2 are the respective longitude boundaries. The numbers in parentheses are the sub-observer IAU West longitude for the case when the UVIS longitude footprint occupies the entire disc of Rhea. Day is Day of Year. All angles are in units of degrees.

Year	**Day**	**Time**	**Lat1 (deg)**	**Lat2 (deg)**	**Long1 (deg)**	**Long2 (deg)**
2005	330	20:29:03	-1.86	-1.20	85.17	250.03
2007	242	01:32:38	-17.34	-17.98	82.56	127.81
2007	242	01:35:31	-19.71	-13.16	79.55	134.27
2007	242	01:38:08	-16.40	-8.95	71.52	136.62
2007	242	01:40:45	-12.77	-8.55	61.76	138.16
2007	242	01:43:35	-12.20	-8.53	68.80	145.16
2007	242	01:46:08	-16.62	-12.94	71.16	148.04
2007	242	01:48:57	-16.29	-13.00	75.36	155.80
2007	242	01:51:36	-11.00	-7.67	70.24	157.45
2007	242	01:54:23	-7.90	-5.06	75.26	165.48
2007	242	01:56:57	-13.44	-10.71	80.43	169.18
2010	061	18:20:06	-48.36	50.11	278.68	316.51
2010	061	18:22:49	-43.74	61.54	274.31	326.70
2010	061	18:25:43	-39.43	70.69	288.48	336.97
2010	061	18:28:35	-43.90	72.97	0.0	353.18
2011	011	05:40:49	-33.57	-32.83	114.16	219.96
2011	011	06:04:38	1.11	2.62	115.50	271.37
2013	068	16:52:94	-7.26	84.78	0.0	325.07

The UVIS slit footprints were calculated using the Geometer tool developed by the Cassini UVIS team. Geometer uses the JPL NAIF SPICE (Space Planet Instrument Camera-matrix Events) kernels to determine the relative positions of the Cassini spacecraft and solar system bodies, the orientation of the spacecraft and solar system objects, as well as instrument pointing information (Figure 5.9) (Acton, 1996; Acton *et al*. 2017). The spacecraft kernel (SPK) was used to determine the trajectory of the Cassini spacecraft and ephemeris of Rhea for each observation. The PcK (Planet) kernels provided information about the size, shape and orientation of Rhea. The UVIS/FUV instrument field-of-view size, shape and orientation was provided in the IK (instrument) kernels. The orientation of the Cassini spacecraft during each UVIS observations was determined using the CK (Camera-matrix) kernels. Other kernels provided information about the reference frame specifications and spacecraft clock data.

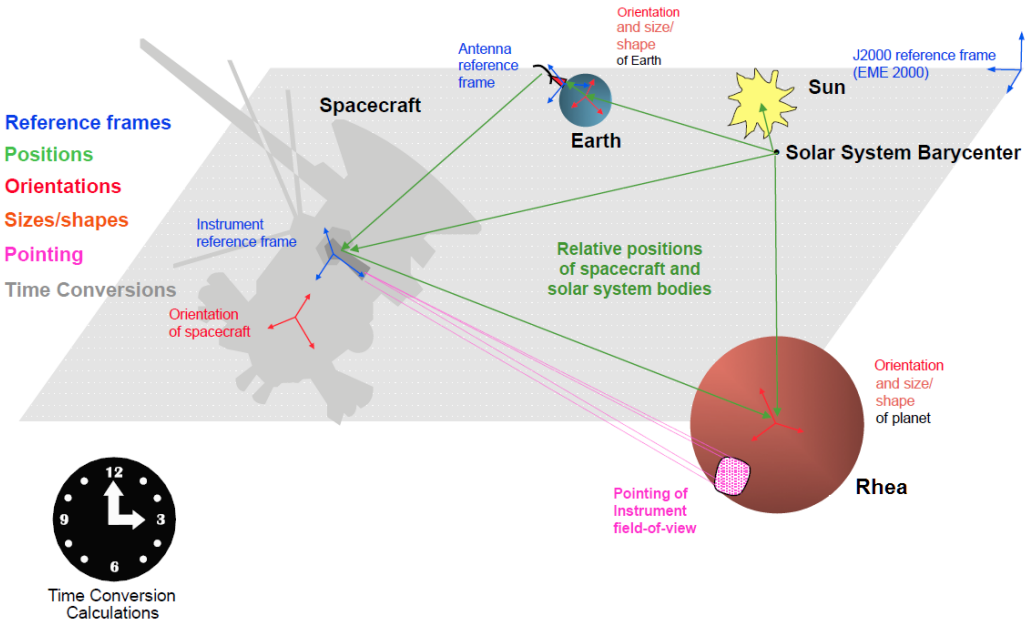

Figure 5.9: Illustration showing the basic concept behind JPL NAIF SPICE kernels used to calculate the UVIS instrument slit projection onto the surface of Rhea. Figure modified from the Navigation and Ancillary Information Facility (NAIF) "Overview of SPICE" presentation (November, 2014). Figure courtesy of NASA JPL

The Cassini UVIS/FUV instrument footprints calculated using the Geometer code and Environment for Visualisation of Images (ENVI) software are presented in Chapter 6 along with a detailed description of the analysis of comparisons of UVIS far-UV spectra with modelled spectra based on laboratory measurements.

5.5 Far-UV Observations of Rhea's Icy Surface

Table 5.3 shows the metadata for each spectrometer footprint on Rhea's surface for the UVIS dataset, with ranges that varied from approximately 7700 km to 55730 km. The solar phase angle varied from approximately 0.86 to 34 degrees. For each flyby event the best UVIS observations were chosen from the Planetary Data System (PDS) based on signal-to-noise, minimal data artefacts, and sufficient sampling over Rhea's surface to allow a geochemical survey of the satellite.

Table 5.3: Log of Cassini UVIS observations for the 2005, 2007, 2010 and 2011 Rhea flybys. Day is "Day of Year." All angles are in units of degrees.

Year	Day	Time	t (sec)	Phase (deg)	Range (km)	Incidence (deg)	Emission (deg)
2005	330	20:29:03	30.0	18.82	55729.88	17.65	1.83
2007	242	01:32:38	60.0	17.15	7698.02	22.87	30.87
2007	242	01:35:31	60.0	17.31	8478.04	20.48	33.62
2007	242	01:38:08	60.0	18.25	9249.06	19.57	34.16
2007	242	01:40:45	60.0	19.71	10065.52	19.23	34.81
2007	242	01:43:35	60.0	21.51	10989.73	14.54	33.03
2007	242	01:46:08	60.0	23.39	11850.94	14.90	37.35
2007	242	01:48:57	60.0	24.89	12827.53	9.43	34.04
2007	242	01:51:36	60.0	26.27	13766.	9.79	33.90
2007	242	01:54:23	60.0	27.4	14768.39	6.15	28.56
2007	242	01:56:57	60.0	28.69	15710.67	2.81	31.38
2007	242	02:09:59	60.0	32.33	20596.58	35.02	30.16
2007	242	02:12:39	60.0	32.92	21614.82	32.64	20.08
2007	242	02:17:56	60.0	34.04	23645.09	32.97	1.15
2010	061	18:20:06	120.0	0.86	19551.46	48.82	48.54
2010	061	18:22:49	120.0	1.17	20947.	37.46	36.78
2010	061	18:25:43	120.0	1.63	22437.14	27.19	26.38
2010	061	18:28:35	120.0	2.09	23910.67	19.04	18.74
2011	011	05:40:49	120.0	14.97	22088.86	47.25	32.40
2011	011	06:04:38	120.0	15.39	33578.73	18.74	5.91

In Table 5.4, the parameter *t* is the integration time, the parameter *Incidence* is the solar incidence angle with respect to the local target surface. The parameter *Emission* is the emission angle of the observed target at the point intersected by the UVIS instrument boresight. The parameter *Range* is the distance above the target surface on Rhea. The parameter *Phase* is the phase angle on the specified target at the observation time at the point intersected by the instrument boresight. All geometry values in Table 5.1 were computed using the JPL SPICE software suite and inserted into the corresponding metadata file associated with its UVIS data file. The ephemeris, navigational, and spacecraft clock kernels obtained from JPL NAIC facility were used in the UVIS team's *Geometer* program (Colwell, 2004) and the *Environment for Visualisation of Images* (ENVI) software (Exelis Visual Information Solutions, Boulder, Colorado) to produce a global map of UVIS instrument footprints projected on Rhea's surface (Figure 5.10 and 5.11). "Geometer" plots the 64 spatial rows of the UVIS/FUV sensor field-of-view projected onto the celestial body's (e.g. Rhea) surface. Each of the 64 spatial rows consists

of a 1024-pixel spectrum, so each UVIS observation projected onto Rhea's surface contains both spatial and spectral information. The spectrum is created by integrating (summing) across the entire spatial dimension. The map of instrument footprints provides context showing the sporadic sampling of UVIS observations covering Rhea's leading and trailing hemisphere.

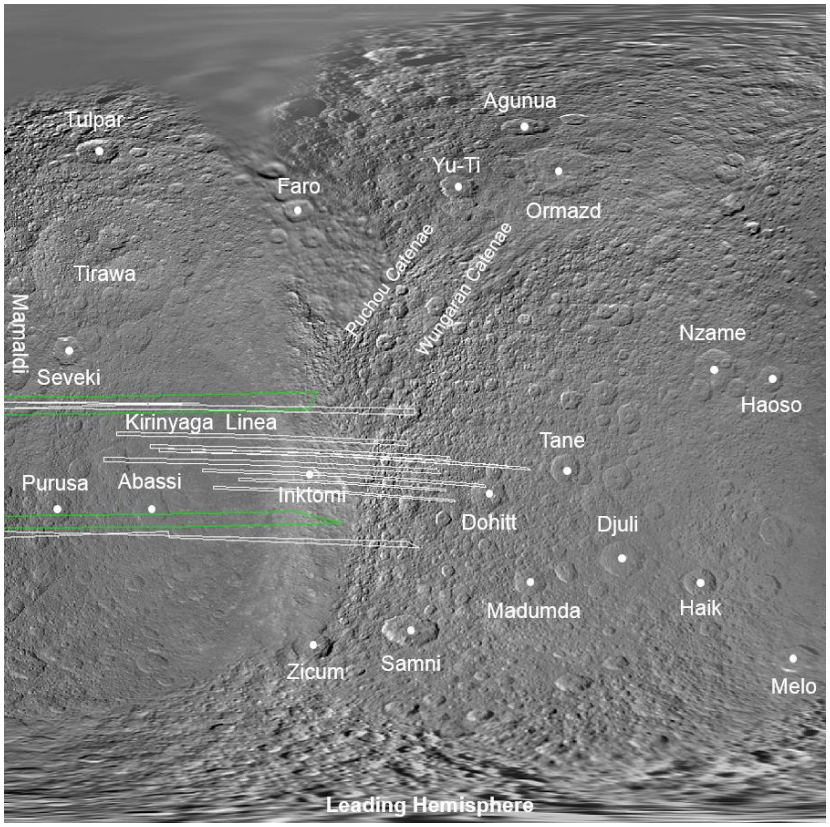

Figure 5.10: Projection of Cassini UVIS/FUV spectrometer footprints onto Rhea's leading (0 to 180 degrees longitude) hemisphere. The white footprints are for the 2010 Rhea flyby, and the green footprints are for the 2011 flyby of Rhea. The single 2005 observation is not shown due to insufficient metadata. The instrument footprints were computed using JPL NAIF SPICE kernels and the UVIS Instrument Team's "Geometer" program. The different colour boxes represent the total integrated (summed) radiation from all 64 rows of the UVIS detector.

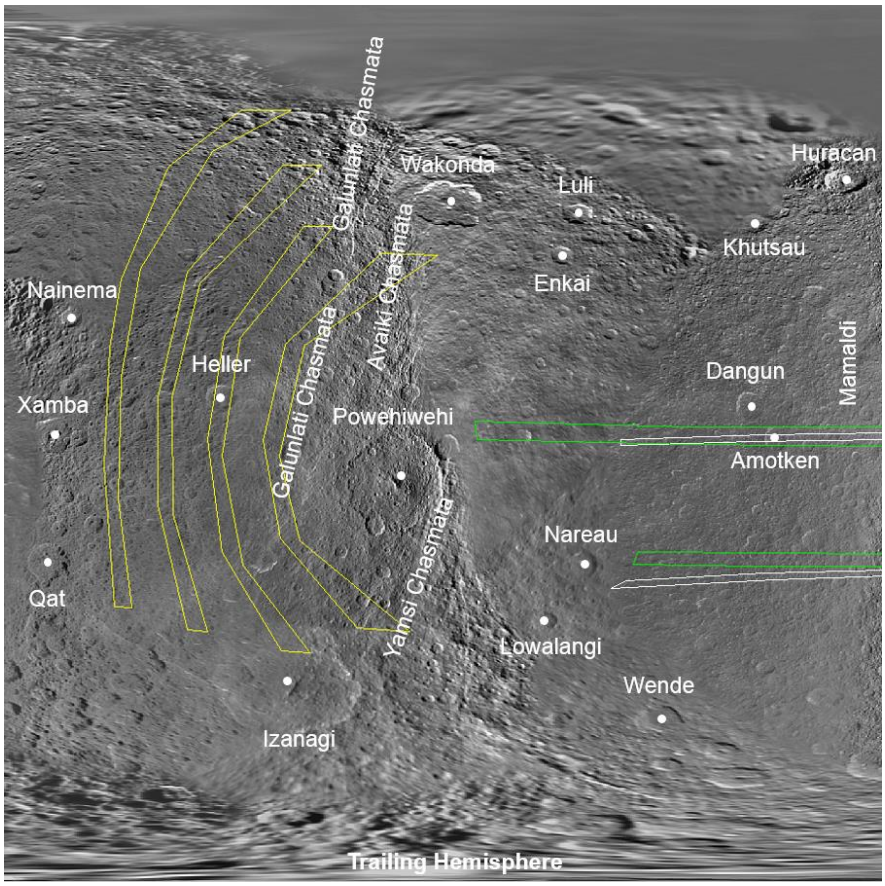

Figure 5.11: Projection of Cassini/UVIS spectrometer footprints onto Rhea's trailing (180 to 360 degrees longitude) hemisphere. The white colour footprints are for the Cassini 2007 flyby of Rhea. The yellow footprints are for the 2010 Rhea flyby, and the green footprints are for the 2011 flyby of Rhea. The single 2005 observation is not shown due to insufficient metadata. The instrument footprints were computed using JPL NAIF SPICE kernels and the UVIS Instrument Team's "Geometer" program. The different colour boxes represent the total integrated (summed) radiation from all 64 rows of the UVIS detector.

The Cassini Ultraviolet Imaging Spectrograph (UVIS) spectra were produced by the Laboratory for Atmospheric and Space Physics (LASP) and stored in the Planetary Data Science (PDS) archive for use by external scientists. The fully processed UVIS spectra are shown in Figure 5.12, and the associated first-derivative spectra are shown in Figure 5.13. Many other UVIS observations were examined, but insufficient signal-to-noise ratio prevented useful analysis of the data. Processing of the UVIS data sets and their associated first-derivatives were carried out using a high-end PC Workstation over approximately one year.

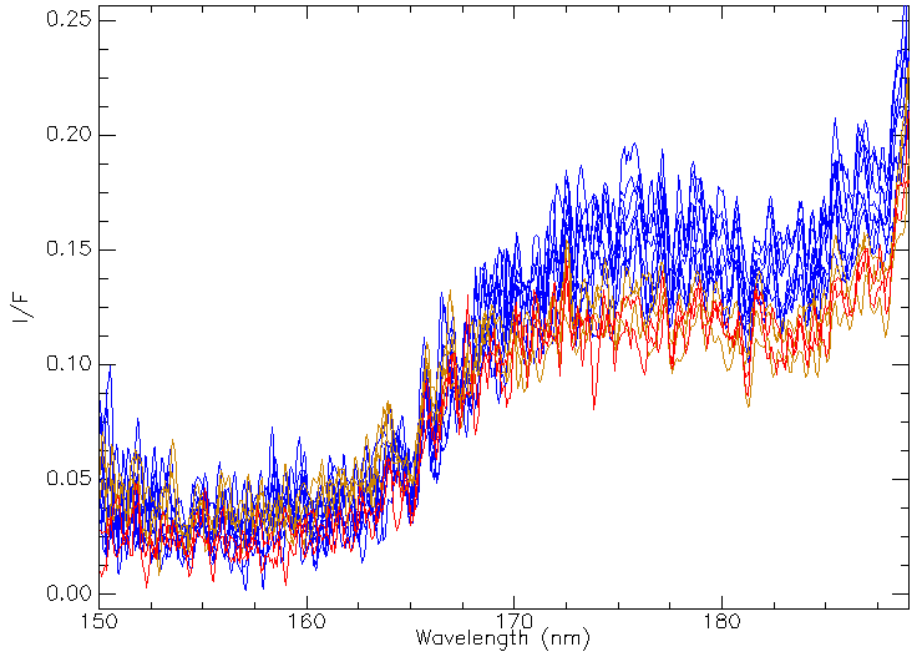

Figure 5.12: Zeroth-order (original) Cassini UVIS/FUV reflectance spectra presented in this thesis. The blue spectra correspond to Rhea's leading hemisphere, the gold colour to the trailing hemisphere, and the red colour to the transition zone between Rhea's leading and trailing hemispheres. The trailing hemisphere of Rhea shows a lower reflectance relative to the leading side of the satellite. This asymmetry could be explained by the preferential irradiation of Rhea's trailing hemisphere by charged particles originating from Saturn's magnetosphere.

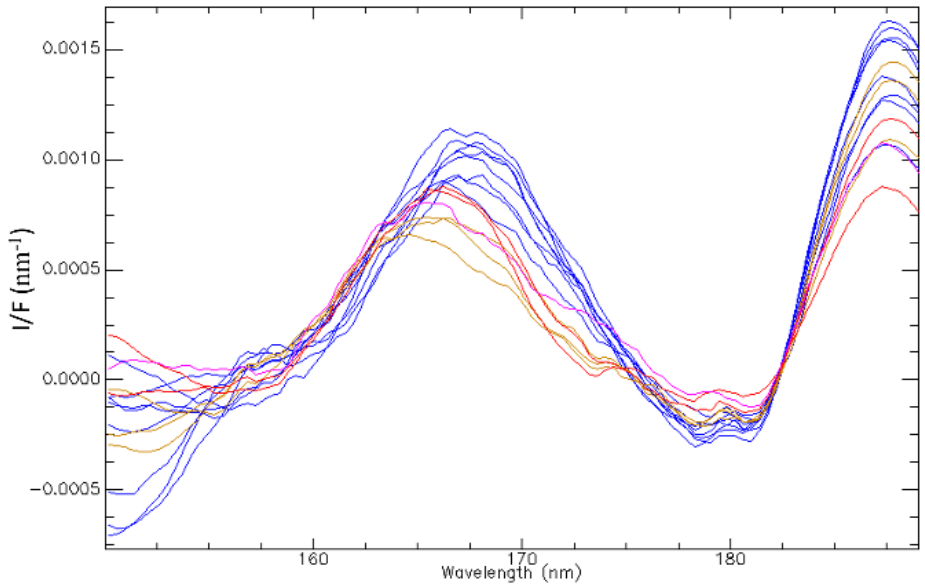

Figure 5.13: First-derivative spectra of the Cassini UVIS/FUV data presented in this thesis. To mitigate noise in the data, a Savitzky-Golay smoothing technique was applied to the data. The blue derivative spectra correspond to Rhea's leading hemisphere, the gold colour to the trailing hemisphere, and the red colour to the transition zone between Rhea's leading and trailing hemispheres. The relative shift of the first-derivative peak between the leading and trailing hemispheres is due to grain size and/or variation in minor contaminants within the water-ice matrix.

The selection of the derivative spectroscopy technique was based on an extensive literature research of different techniques over several months. The Savitzky-Golay method (Savitzky & Golay, 1964) was chosen based on its ability to damp out noise, while preserving the spectral content of the data. The Savitzky-Golay smoothing procedure was used to damp out significant noise, and the same exact smoothing parameters were applied to every observation to assure systematic results. This is the first-time use of applying the Savitzky-Golay derivative method to Cassini far-UV spectra to characterise the surfaces of icy satellites.

Processing the Cassini UVIS data presented several challenges, since very few software tools were developed to allow external investigators to work with the data. The only available documentation was the Cassini UVIS Users Guide, which described several examples of processing raw data. The best approach, based on available resources, involved the use of the *Interactive Display Language* (IDL) (Exelis Visual Information Solutions, Boulder, CO) to read in, apply calibration, and convert to I/F units for subsequent analysis.

The UVIS observations with the highest signal-to-noise were selected for processing, based on examination of three-dimensional surface plots of the spatial-spectral data (described in Chapter 4), and calculation of the signal-to-noise ratio. Many of the observations for Rhea and Dione could be eliminated after examining the three-dimensional representation of the data, which showed insufficient signal for further processing. Furthermore, most of the observations were full-disk integrated and were eliminated from further processing since the focus of this research was based on the first-time analysis of spatially resolved far-UV spectra of Rhea and Dione. Processing of the first UVIS spectrum took approximately three months, but once satisfactory results were obtained, further processing of the Cassini UVIS data sets was less problematic. To assure

systematic results, the same exact procedures were applied to all data sets used in this thesis.

The UVIS spectra are dominated by water ice as evident by the steep absorption edge near 165-nm. It is interesting to note that an asymmetry in the reflectance between Rhea's leading and trailing hemisphere is seen in both the original and first-derivative spectra (Figures 5.12 and 5.13). This asymmetry could be explained by the preferential irradiation of Rhea's trailing hemisphere by charged particles originating from Saturn's magnetospheric plasma environment. The preferential irradiation of the trailing hemisphere occurs as a result of Rhea's slower orbital velocity relative to the co-rotational plasma velocity. The first-derivative spectra show a systematic shift to longer wavelengths for UVIS spectra collected on Rhea's leading hemisphere (Figure 5.14).

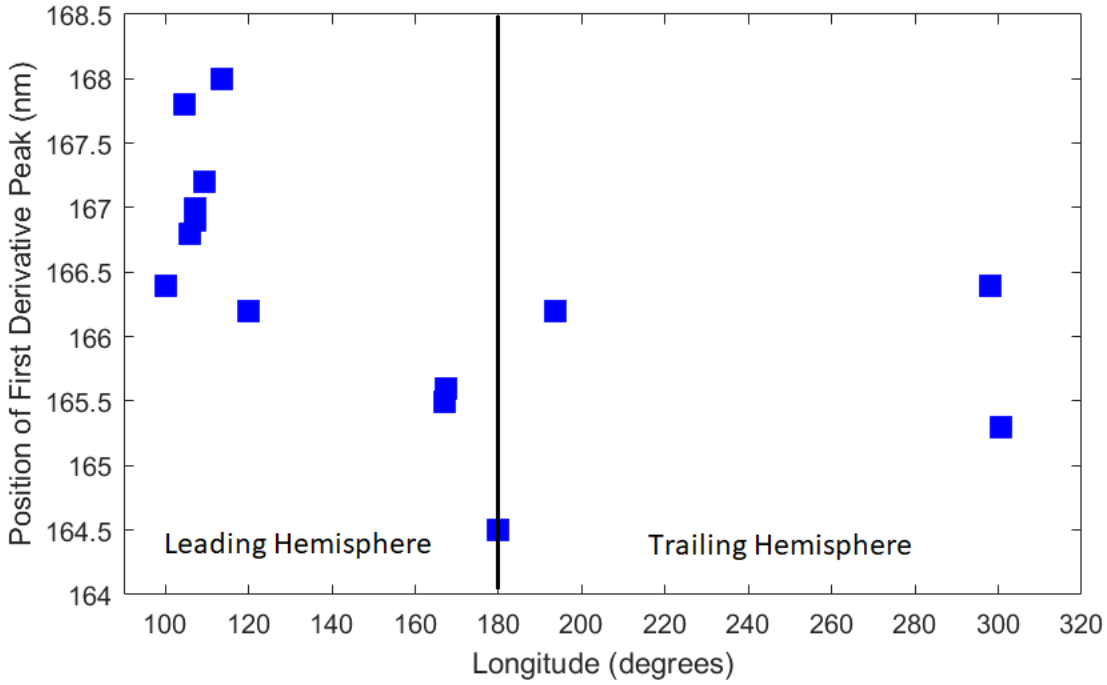

Figure 5.14: Plot illustrating the qualitative behaviour of the location in wavelength space of the first-derivative peak as a function of longitude on Rhea's surface.

In contrast, the first-derivative spectra of Rhea's trailing and transition zone between its leading and trailing hemisphere tend to show negligible to minor shifts in the 165-nm absorption edge as seen in the derivative peak (Figure 5.14). An alternative way to

illustrate the variation in the first-derivative peak as a function of location on Rhea is to display the changes on a map of the moon's surface (Figure 5.15).

The presentation of the results of the derivative analysis using two different representations provides two alternative views to those readers who are better at visualizing data in a two-dimensional representation, and to those who are more adapted to viewing numerical data in a one-dimension form.

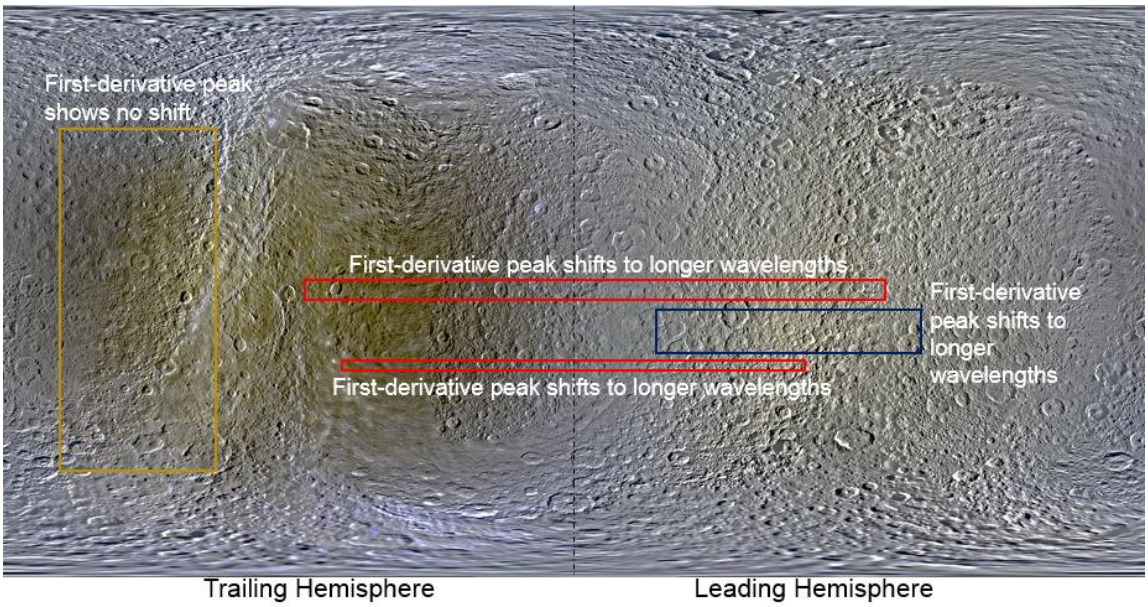

Figure 5.15: Cassini VIMS map (IR/GRN/UV) showing the behaviour of the first-derivative peak derived from UVIS spectral observations. The results indicate a distinct shift in the first-derivative peak in wavelength space for Rhea's leading hemisphere and for observations where the UVIS spectrograph slit crosses the boundary between the two leading and trailing hemispheres. The map is a cylindrical projection at 400 m/pixel at Rhea's equator. Original map provided by Dr. Paul Schenk (LPI, Houston).

In addition to the relative shift in the first-derivative peak between Rhea's leading and trailing hemispheres, there are also notable differences in the width and amplitude of the first-derivative peaks between Rhea's leading and trailing hemisphere. There are two likely reasons for this shift towards longer wavelengths of the first-derivative peak calculated for spectral observations of Rhea's leading hemisphere: the first possibility is a change in the size of water-ice grains dependent on the location on Rhea's surface. The second possibility is impurities or contaminants mixed with the water-ice matrix, which

could perturb the hydrogen bonding of the water molecules. The larger grain sizes on Rhea's leading hemisphere as seen by the shift in the derivative peak to longer wavelengths, may be the result of E-ring material coating the surface. The asymmetry in the position of the first-derivative peak between Rhea's leading and trailing hemispheres could be the result of radiolytic reactions leading to the production of impurities in the ice layer – i.e. the result of surface modifications by charged particle bombardment from Saturn's magnetosphere. The impurities in the water-ice can lead to a change in the spectral slope of the 165-nm absorption edge due to pure water-ice. This change, in turn, could lead to a shift in the position of the first-derivative peak in wavelength space.

In summary, the processed UVIS data for Saturn's icy moon Rhea shows that the icy satellite's surface is dominated by water-ice as seen by a steep absorption edge located near 165 nm. All of the processed UVIS spectra of Rhea show a broad absorption feature between approximately 179 to 189 nm, for which there is no apparent asymmetry between the leading and trailing hemispheres – i.e. the weak absorption feature is seen in all far-UV spectra, regardless of the observation site on Rhea. This indicates a systemic process is responsible for the absorption over this wavelength region. The systemic process may be endogenic in origin, or an exogenic source capable of producing a similar broad absorption feature over both hemispheres on Rhea's surface. A comparative spectral analysis between the Cassini UVIS data and modelled spectra based on the laboratory data presented in Chapter 5, will be presented in Chapter 6. The comparative analysis will show that two chemical species that have never been observed in the outer solar system, provide a possible explanation for the unknown absorption feature near 184 nm that is seen in the far-UV spectra of Rhea (and the nearby icy satellite Dione).

CHAPTER 6

A COMPARATIVE ANALYSIS BETWEEN CASSINI UVIS DATA AND LABORATORY ICE MEASUREMENTS

6.1: Introduction

This chapter presents a comparative spectral analysis between model spectra created using the laboratory ice data presented in Chapter 4 and the Cassini UVIS observations shown in Chapter 5

Ultraviolet reflectance spectra are sensitive to the upper most layers of icy satellites, where the interaction of incident radiation with water-ice and organics produce broad absorption features in the observed spectra. These icy surfaces are subject to radiolysis and photolysis from high-energy particles (originating from Saturn's magnetospheric plasma) and solar UV photons, exogenic delivery of organics from micrometeoroid bombardment, and transfer of material from Saturn's E-ring. On some icy moons, endogenic processes may still be ongoing and can lead to the possible migration of fresh water-ice, salts/brines (NaCl, $NaHCO_3$, Na_2CO_3; Postberg *et al*. 2009), and organic molecules (CO_2, CO, NH_3, CH_4, N_2, H_2CO; Waite *et al*. 2009; Glein *et al*. 2008) up to their surfaces, material that can be transported across the lunar surface and beyond. For example, the plumes of Enceladus are thought to distribute molecules from the satellite's interior onto its surface, and into Saturn's E-ring (Postberg *et al*. 2009). Thus, molecules that have migrated to the surfaces on icy satellites may be observable using far-UV spectroscopy.

The UVIS spectra presented in Chapter 5 show that the surface "regolith" of Rhea and Dione is dominated by water-ice (Figure 6.1) as evident from the steep absorption

edge near 165 nm. The surfaces of Dione, Tethys and Enceladus are also dominated by water-ice as evident by the presence of the 165-nm absorption edge.

Another interesting finding from the analysis of UVIS far-UV spectra is the presence of a broad, weak absorption feature between ~178 and 189 nm. This absorption feature has also been observed in far-UV spectra of Enceladus, Mimas, Tethys, Phoebe, and Dione satellites (e.g. Phoebe; Hendrix & Hansen, 2008) in the Saturnian system but, to date, its origin has not been explained and this is the main topic of this thesis.

Analysis of the far-UV spectrum of Enceladus shows that its surface ice is dominated by water-ice that is purer than that on the surfaces of Rhea, Dione and Tethys (Figure 6.1). This is to be expected as water-ice grains on the surface of Enceladus are being replenished by active water-ice geysers. An absorption feature, similar to the 184-nm absorption seen in icy satellites, has been previously reported in water-ice (Pipes *et al*, 1974; Hapke *et* al, 1981; Wagner *et al*., 1987). However, the optical constants for water-ice derived by Warren (1982, 1984) are very sparse for wavelengths greater than 170 nm.

Saturn's irregular moon Phoebe also shows the 184-nm absorption feature, which does not appear to be explained by various mixtures of tholin and ice, water-ice and carbon, water and kerogen, and water plus poly-HCN (Hendrix & Hansen, 2008). Carbonaceous chondrite meteorites also show a similar absorption feature near 184 nm, which could be due to the presence of phyllosilicates and hydrated minerals (Wagner, et al., 1987). However, since no laboratory absorbance measurements are available for carbonaceous substances, it is not possible to further explore this possible explanation for the 184-nm absorption in Rhea's ice.

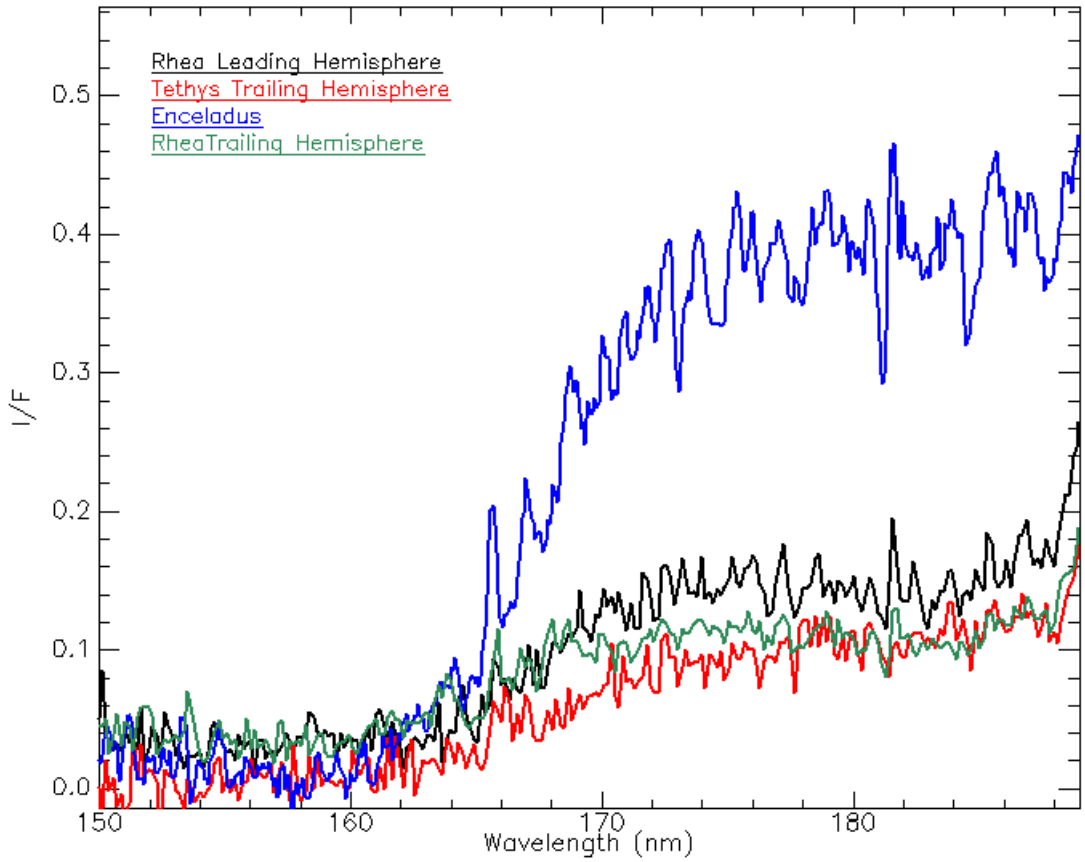

Figure 6.1: Far-UV reflectance spectra of Rhea, Tethys, and Enceladus showing the domination of water-ice on their surfaces as evident by the 165-nm absorption edge. The spectra are shown in units of absolute reflectance (I/F). The high reflectance of Enceladus is due to fresh water-ice (relative to Rhea and Tethys) on the moon's surface. The spectrum of Rhea shows a broad absorption feature between 174 and 189 nm. The absorption is not apparent in the far-UV spectrum of Enceladus and Tethys.

This chapter presents possible explanations for the 184-nm absorption feature (Figure 6.2) observed in the far-UV spectra of Rhea and Dione based on a comparative analysis of the laboratory ice measurements with the Cassini UVIS observations presented in Chapter 5. A description of the chemical pathways leading to the formation of molecules found to provide possible explanations for the absorption band between ~179 nm and 189 nm, and the spectral slope of the 165-nm absorption edge due to pure water-ice (Figure 6.2), is presented.

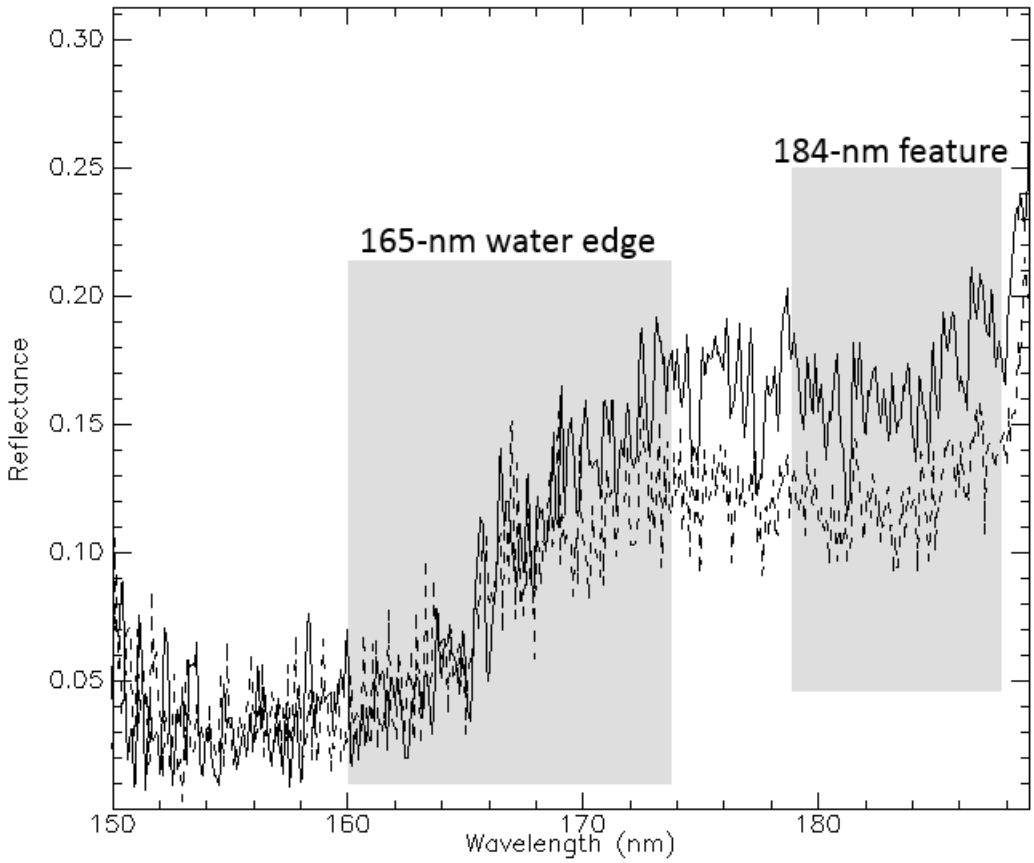

Figure 6.2: Cassini UVIS far-UV reflectance spectra of Rhea's leading (solid line) and trailing (dashed line) hemispheres (from derived results presented in Chapter 5). The spectra are dominated by the 165-nm absorption edge due to water-ice. A weak, broad absorption feature over the wavelength range of ~179 – 189 nm is also observed in both spectra. The difference in reflectivity is possibly the result of preferential irradiation of Rhea's trailing hemisphere as it orbits within the plasma produced by Saturn's magnetosphere.

6.2: Modelling of Water-Ice Grain Size on the Surface of Rhea Using Simple Beers Law Relations

Models of the far-UV absorption edge due to pure water-ice were created using Beers law and the measured absorbance (described in Chapter 5). Based on the derivative analysis of UVIS reflectance spectra presented in section 5.2, the location of the far-UV absorption edge of water-ice is shifted to wavelength slightly beyond 165-nm for data collected over Rhea's trailing hemisphere and the transitional region across both hemispheres. The leading hemisphere UVIS spectra show no shift in the first-derivative

peak relative to the nominal 165-nm position of the water-ice absorption edge. One possibility for this is a different grain size in the water ice of the two hemispheres. As the water-ice grain size increases, the UV absorption edge should shift towards longer wavelengths (Figures 6.3 and 6.4) as the depth of the absorption band increases (i.e. decreasing reflectivity). The far-UV absorption edge due to water-ice observed in UVIS spectra of Rhea's surface can be compared with modelled spectra to provide a rough estimate of the grain size. The modelled spectra were produced using a VUV laboratory absorbance spectrum and Hapke's formulism (described in Chapter 4). It is assumed that minor contaminants within the ice matrix do not alter the size of the water-ice grains.

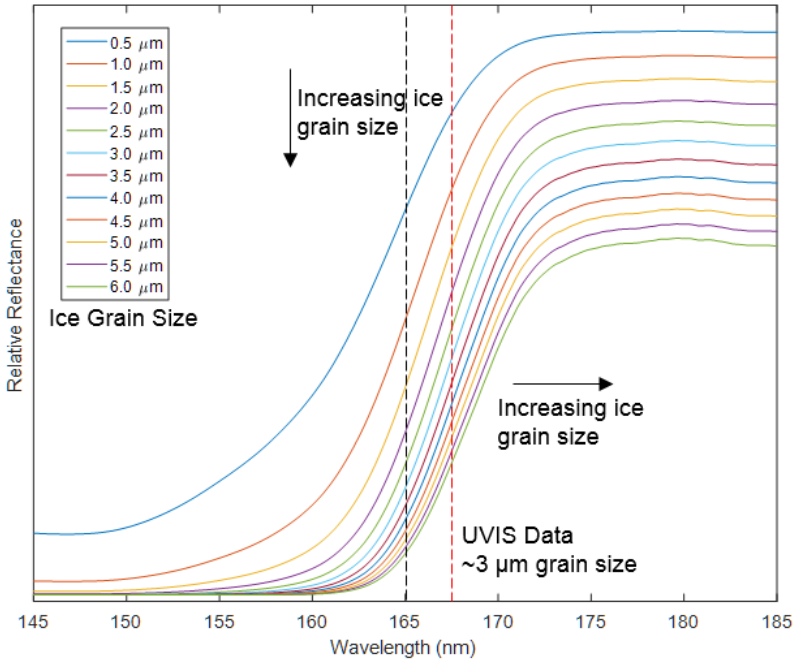

Figure 6.3: Modelled spectra of pure water-ice showing the effect of changing grain size on the depth of the water absorption band and shift in the UV absorption edge. As the particle grain size increases the UV absorption edge shifts to longer wavelengths. The depth of the absorption band due to water-ice increases as the grain size increases.

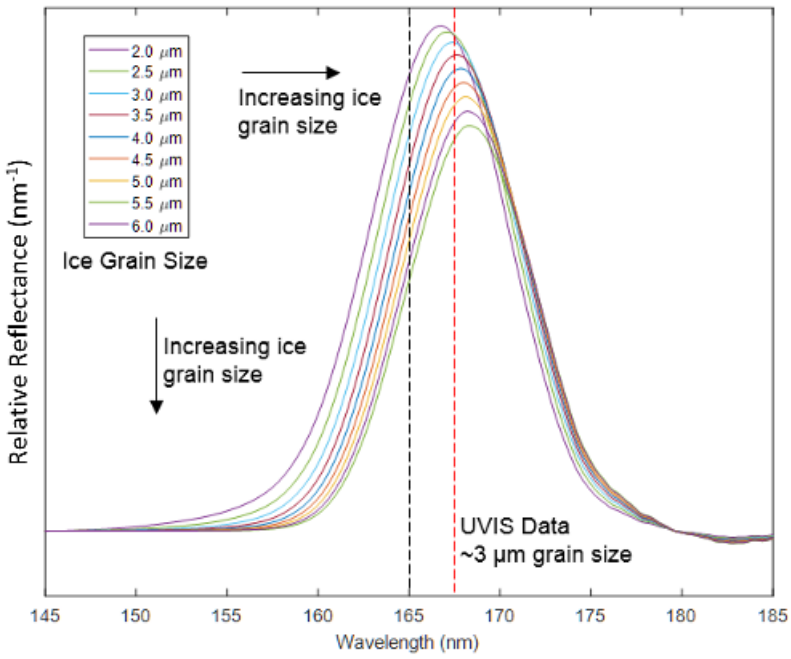

Figure 6.4: Illustration showing the behaviour of the first-derivative of the modelled far-UV absorption edge of water-ice (Figure 6.3). Note the shift of the peak of the derivative to longer wavelengths as the grain size increases. The amplitude of the derivative peak decreases as the modelled grain size increases (i.e. absorption increases or reflectivity decreases). The 3 μm grain size represents the average of the shift in the derivative peak for the UVIS data used in producing modelled spectra.

A qualitative and quantitative analysis of the modelled UV absorption edge of irradiated water ice can be performed by taking the first derivative of the modelled spectra (Figure 6.4). The location of the first-derivative peak in *wavelength space* determines the position of the water ice absorption edge seen in far-UV spectra of icy satellites. A first-derivative analysis of modelled spectra of water-ice illustrates the change in the amplitude of the derivative peak and its wavelength as the size of the water-ice grain size changes (Figure 6.4). Differences in the water ice grain sizes and impurities produces shifts in the position of the H_2O ice absorption edge (Hendrix and Hansen 2008). In Figure 6.3, the steep spectral slope of the 165-nm absorption edge of water ice shifts to longer wavelengths as the size of the ice grains increases. This is reflected in the position and amplitude of the derivative peak (Figure 6.4). The derivative peak of several UVIS observations sampled from Rhea's leading and trailing hemispheres were compared with the modelled derivative

peak shown in Figure 6.4. The black dashed line indicates the nominal position of the 165-nm absorption edge of pure water-ice and the red dashed line represents the location of the derivative peak of the average of all of the UVIS first-derivative spectra across both hemispheres on Rhea. The shift of the derivative peak towards longer wavelengths with respect to the nominal 165-nm location of pure water-ice indicates large grain sizes and/or possible non-water ice contaminants in the surface ice on Rhea. The results from the derivative analysis indicate an average grain diameter of about 3 microns for Rhea, with a range in grain sizes from 1 to 5 microns.

The UVIS spectra of Rhea's trailing hemisphere show a slight shift in the first-derivative peak to longer wavelengths, relative to the nominal 165-nm absorption edge of water-ice, with the exception of Rhea's leading hemisphere. The shift in the derivative peak appears to depend on the specific sampling site of the UVIS observations. The shift could be caused by fresh water-ice brought to the surface from impacts, space weathering effects, or radiolytic processing of the ice regolith. Modelled spectra of the behaviour of the UV absorption edge indicate that ice grains may exist on Rhea's surface that range from about 1 to 5 microns, with smaller grains distributed over Rhea's leading hemisphere. The size of the water-ice grains used in producing the model spectra used in the comparative analysis with UVIS observations are based on an average grain size of approximately three microns.

6.3: Modelling of Water-Ice/Chlorine and Water-Ice/Hydrazine Mixtures on the Surface of Rhea

To determine the properties of water-ice on Rhea, a model of the water-ice albedo bi-directional reflectance spectrum was developed using Hapke theory. Hapke's theory (Chapter 4) is based on a radiative transfer photometric model that describes how light scatters in a semi-transparent medium. The Hapke model (Hapke 1981, 1986, 1993) is

frequently used to model regoliths of planetary bodies and icy surfaces of satellites in the outer solar system (Hendrix and Hansen, 2008). The reflection from the surface of an icy moon depends on several factors that are included in Hapke's formalism (Hapke, 1981, 1986, 1993). These include the direction of the light source (e.g. phase angle), the shape of ice grains, the topology of the surface ice layer, and the chemical composition of the ice "regolith". The chemical composition of the ice layer is described by the optical constants $n(\lambda)$ and $k(\lambda)$, which are a function of wavelength. $n(\lambda)$ and $k(\lambda)$ are the real and imaginary components of the index of refraction, respectively. The optical constants (n, k) enter into Hapke's equation (Hapke 1981, 1986, 1993) through the single-scattering albedo. The single-scattering albedo is a function of the internal and external scattering coefficients, which depend only on the optical constants. The single-scattering albedo can be thought of as the probability that light interacting with a grain (or particle) is scattered instead of absorbed when an interaction takes place between individual grains and incident photons. In addition to its dependence on the optical constants through the internal and external scattering coefficients, the albedo also depends on the internal transmission, which is itself dependent on the absorption coefficient of the ice (or "regolith") and the size of the ice (or "regolith") grain.

A model of the far-UV absorption edge due to water-ice based on computation of the bi-directional reflectance using Hapke's model equation and the following procedure is now described (Figure 6.5).

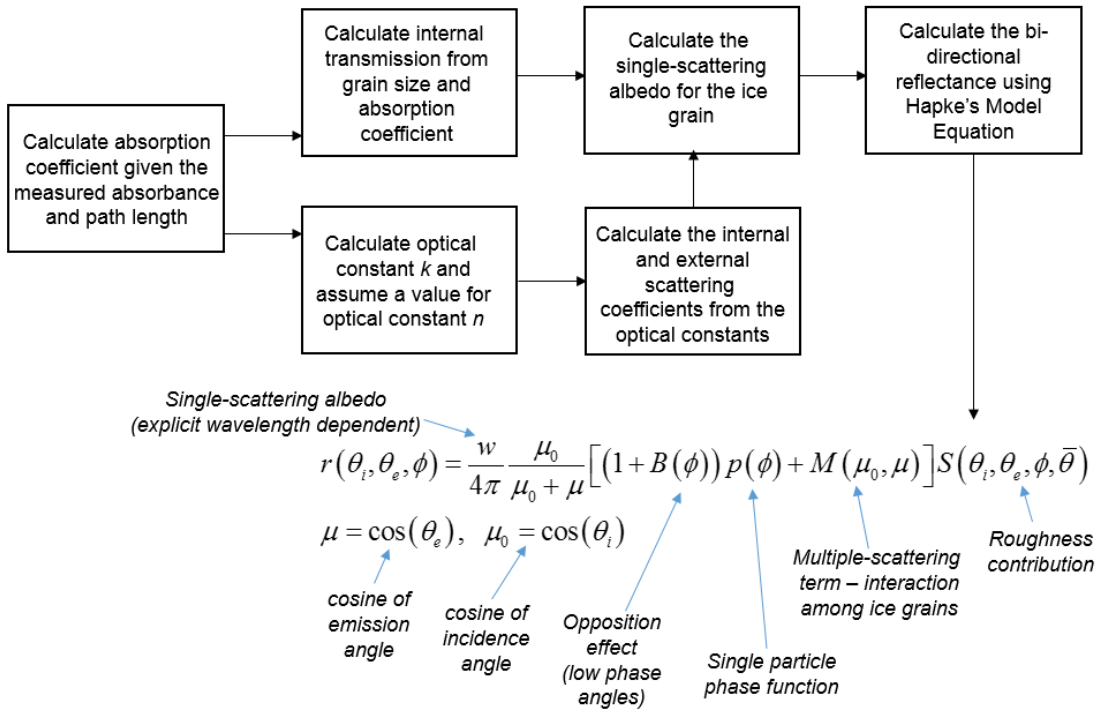

Figure 6.5: Diagram showing the various parameters involved in calculating the bi-directional reflectance of an ice layer using Hapke's model (Hapke 1981, 1986, 1993). Figure created by R. Mark Elowitz.

It is first necessary to calculate the absorption coefficient given the measured absorbance spectrum measured in laboratory experiments,

$$\alpha = \left(\frac{A}{\ln(10.)} \right) / d \qquad (6.1)$$

where A is the measured absorbance spectra and d is the photon path length. Using the absorption coefficient and assuming a particular water-ice grain size, a, the internal transmission in the grain, τ_i is

$$\tau_i = \mathrm{e}^{-\frac{2a\alpha}{3}} \qquad (6.2)$$

where α is the absorption coefficient. The internal transmission factor can be thought of as the total fraction of radiation that enters a single grain and reaches another surface in the duration of one transit. Assuming a value for the optical constant n representative of water-ice, and using the calculated absorption coefficient from equation 6.1 the optical constant k is found from the following expression,

$$k = \frac{\alpha\lambda}{4\pi} \quad (6.3)$$

where λ is the wavelength of the radiation incident on the surface. Using the optical constants (*n*, *k*), the internal (s_i) and external (s_e) scattering coefficients, which are required in order to model the single-scattering albedo of the ice grain (Hendrix 2008; Liu *et al*. 2016), are then given by

$$s_i = 1 - \frac{4}{n(n+1)^2} \quad s_e = \frac{(n-1)^2 + k^2}{(n+1)^2 + k^2} + 0.05 \quad (6.4)$$

The single-scattering albedo (Hapke 1981, 1986, 1993) is one of the most important terms in Hapke's model, and is dependent on the chemical composition and grain size of the ice "regolith".

$$w = s_e + (1 - s_e)\frac{(1 - s_i)\tau_i}{1 - s_i\tau_i} \quad (6.5)$$

In the equation for the single-scattering albedo (*w*), τ_i is the internal transmission factor. It is interesting to note that there is an explicit dependence of *w* on the wavelength. The ratio between scattering and absorption in the total extinction of the ice layer is governed by the single-scattering albedo – i.e. the ratio of the scattering coefficient to the extinction coefficient. For mixture of multiple ices, the single-scattering albedo can be modified by a weighted sum of the individual components of the ice mixture.

Using the equations described above, and the cosines of the incidence and emission angles of the radiation, and the phase angle, it is possible to generate modelled far-UV spectra of water-ice using Hapke's formula. However, in addition to the information described here I also require data on the single particle phase function, a multiple-scattering (i.e. interaction among ice grains) parameter, roughness contribution factor, and for low phase angles, an opposition effect term. At scales that are less than the detector's spatial resolution, the contribution of roughness/texture of the surface layer is considered

in Hapke's model. This "roughness parameter" is a function of the incidence angle, emission angle, phase angle, and the average macroscopic roughness slope of scales at the sub-pixel level. The roughness term assumes that the scales on which the roughness occurs are valid for geometric optics, and that the local facets are large relative to the mean size of the ice grains. Another assumption is that the facets are tilted at random angles. The roughness parameter also assumes that multiply-scattered light between surface facets is negligible, which may not be valid for icy surfaces. Given this additional information Hapke's equation (Hapke 1981, 1986, 1993) may be used to simulate the far-UV absorption edge due to water-ice on the surface of an icy satellite.

$$R(i,e,g) = \frac{w}{4\pi}\frac{\mu_0}{\mu_0+\mu}\left[\left(1+B(\phi)\right)p(\phi)+M(\mu_0,\mu)\right]S(i,e,\phi,\bar{\theta}) \qquad (6.6)$$

Here, *w* is the single-scattering albedo, μ and μ_0 the cosines of the emission (or reflectance) and incidence angles, $B(\phi)$ the opposition effect parameter (Domingue *et al*., 1998), $p(\phi)$ the single grain phase function, $M(\mu_0,\mu)$ the contribution from multiple scattering, and $S(i,e,\phi,\bar{\theta})$ the contribution from roughness at scales less than the detector's spatial resolution (i.e. the contribution for macroscopic roughness). In other words, *S* is the contribution for macroscopic roughness. The roughness parameter represents the mean slope angle within a single pixel. It can be thought of as a microscale roughness parameter (Verbiscer and Veverka, 1992), from the grain size to a few millimetres. Thus, the roughness parameter depends on the ice grain organisation. The phase function, $p(\phi)$ depends on the asymmetry parameter, *b* and the backscattering fraction, *c*. The two-parameter (*b* and *c*) Henyey-Greenstein phase function (Domingue *et al*. 1991; Hapke 1981, 1986, 1993) for single grains is commonly used in the planetary science community.

$$p(\alpha) = \frac{1+c}{2}\frac{1-b^2}{\left(1+2b\cos\phi+b^2\right)^{3/2}} + \frac{1-c}{2}\frac{1-b^2}{\left(1-2b\cos\phi+b^2\right)^{3/2}} \quad (6.7)$$

The behaviour of the phase function depends on the shape of the ice grains, their composition and internal structure. The single-scattering albedo, ω, depends on the size and microstructure of ice grains, as well as the particle composition. It is the only wavelength-dependent Hapke parameter used in modelling spectra.

The Hapke model can be extended to intimate mixtures of particles of different composition by expressing a weighted average of the single-scattering albedo.

$$w = \frac{\sum_i p_i \sigma_i w_i}{\sum_i p_i \sigma_i} \quad (6.8)$$

In the equation for the weighted average of the single-scattering albedo, p_i is the volume percent of each species, σ_i is their absorption cross-section, and w_i the single-scatter albedo of each species in the mixture. It should be noted that this is a weighted average for a linear mixture of ices, and does not account for mixing of different ices at the molecular level. In nonuniform ices, different chemical species (e.g. H_2O and CO_2) may be mixed at a granular level – i.e. as an "intimate mixture." This induces multiple scattering of solar photons from each chemical species in the ice mixture, before emerging from the surface to the observing sensor. Therefore, the resulting spectrum shows absorption bands from both chemical species in the mixture. In addition, different ices may be mixed at the molecular level, which can produce a shift in the central wavelength of one of the minor (contaminant) species present in the reflectance spectrum.

It is the dark surfaces (low in albedo) at UV wavelengths of many bodies in the outer solar system that are most suitable for Hapke analysis. However, oddly enough, these low albedo surfaces in the UV also lead to the low signal-to-noise found in far-UV observations. This means that multiply-scattered light can lead to Hapke model solutions

that are ambiguous – i.e. the multiply-scattered light is very weak and typically one can get by with using a much simpler modelling of singly-scattered light. In the modelling of the UV absorption edge seen in the Cassini UVIS observations of Rhea, it is assumed that the particle phase function does not depend on the wavelength, although there may be minor changes in its amplitude.

It should also be noted that the use of the Hapke model to produce model spectra has a few drawbacks. The Hapke theory does not allow an unambiguous fit to the UVIS measurements. For example, the Hapke model does not consider polarisation in the coherent backscattering – i.e. the Hapke model used in this research is assumed to be a scalar one. Furthermore, the Hapke model takes an unphysical methodology to describe the scattering of electromagnetic radiation from a discrete random medium. The theory does not follow the formulism of the macroscopic Maxwell equations, but instead uses a series of simplistic equations to provide a 'back of the envelope' solution to a very complex problem of electromagnetic scattering of radiation. This makes Hapke theory difficult to validate against controlled laboratory experiments, since no physical parameters related to the macroscopic Maxwell's equations are used. However, the relatively simplistic approach is used in comparing model spectra with observational data as the approach represents the standard methodology used by the planetary science community.

6.4: Results of Comparative Spectroscopy of Chlorine/Hydrazine Model Spectra with Cassini UVIS Spectra

Model spectra of hydrazine monohydrate and trichloromethane below a layer of water-ice were fitted to the UVIS data using the grain size derived from derivative spectroscopy and a set of best-fit Hapke parameters. To reduce noise in the UVIS data, a *Savitzky-Golay s*moothing filter (Savitzky & Golay, 1964; Gorry, 1990) was applied to each UVIS spectrum. The Savitzky-Golay method applies a least squares (digital

smoothing polynomial) fit to the data. The filter uses a weighting method based on a polynomial of a given degree. A polynomial least squares fit within the filter window is applied to the noisy spectrum. The spectral data (i.e. the noisy signal) is then convolved with the smoothing filter to produce the final smoothed spectrum, with minimal loss of spectral features. Tests using the Savitzky-Golay smoothing procedure showed it to perform better than basic smoothing filters based on box averaging and running mean.

Limited phase cover observations did not permit a satisfactory fit to derive Hapke parameters needed to produce modelled spectra. Attempts to use the limited phase angle coverage resulted in a wide range of Hapke parameters that fit the UVIS phase curve data equally well within the statistical error of the data. The non-uniqueness of solutions based on the Hapke model results when the photometric measurements are too sparse. In other words, the phase angle data is too limited in relation to the range in phase angle data required to constrain the multi-parameter Hapke model. The Hapke parameters that are unconstrained due to limited phase angle coverage (e.g. coherent backscatter opposition effect, asymmetry of the phase function of the ice grains, and macroscopic roughness parameter) couple with other Hapke parameters that lead to solutions which are statistically similar. As a result of the aforementioned problems, an alternative methodology was used to obtain the Hapke parameters. Since Rhea and Dione share similar geomorphology based on Cassini high-resolution ISS imagery, and both mid-sized icy satellites have an O_2/CO_2 exosphere (Teolis & White, 2016; Teolis, *et al*. 2010), it is assumed that these two satellites have similar compositional and photometric properties. Both Rhea and Dione exhibit brighter leading hemispheres, and show very little limb darkening at low phase angles. This implies that multiple scattering is not dominant on their surfaces (Buratti, 1984). Furthermore, a similar trend in albedo variation is observed across Dione and Rhea, with the leading hemispheres showing a brighter appearance. The brighter hemispheres are most likely caused by a deposition of pure water-ice from

Saturn's E-ring (Howett *et al*. 2014). Buratti and Veverka (1984) derived similar photometric properties (based on similarities in the shape of the phase curves) for Rhea and Dione, implying similar surfaces. The authors also show that Dione and Rhea are similar when the phase parameters, *b* and *c* are plotted on a two-dimensional scatter plot. Both Rhea and Dione are closely together, showing significant differences from Tethys, Mimas, and Enceladus. Buratti and Veverka (1984) also showed similarities between Rhea and Dione based on similar Voyager Orange/Violet average colour ratios. Therefore, the Hapke parameters derived for Dione are used in producing model spectra used in the comparison with Cassini UVIS observations of Rhea. Table 6.1 summarises the Hapke parameters used for the three UVIS observations presented in this thesis.

Table 6.1: UVIS observation data and Hapke model parameters used in creating modelled spectra. The asymmetry parameter for the width of the forward and backward scattering lobes, and the relative amplitude of the scattering lobes is denoted by b and c, respectively. The roughness parameter (in radians) is denoted by S. Phase is the phase angle (in degrees) at the time of observation. Incidence and Emission are the incidence and emission angles of the UVIS observation. The Hapke parameters for the modelled spectra are b = 0.35, c = 1.00, S = 0.35 radians, h = 0.457, and $B0$ = 0.95.

Observation	**Phase (deg)**	**Incident (deg)**	**Emission (deg)**
26 Nov 2005 20:29 UT	18.8	17.4	20.0
30 Aug 2007 01:32 UT	17.1	22.9	30.9
30 Aug 2007 01:35 UT	17.3	20.5	33.6
30 Aug 2007 01:38 UT	18.2	19.6	34.2
30 Aug 2007 01:40 UT	19.7	19.2	34.8
30 Aug 2007 01:43 UT	21.5	14.5	33.0
30 Aug 2007 01:46 UT	23.4	14.9	37.3
30 Aug 2007 01:51 UT	26.3	9.8	33.9
02 Mar 2010 18:20 UT	0.86	48.82	48.5
02 Mar 2010 18:25 UT	1.63	27.2	26.4
11 Jan 2011 05:40 UT	15.0	47.2	32.4
30 Aug 2007 01:54 UT	27.4	6.1	28.6

The first comparison between UVIS/FUV spectral data and laboratory thin ice sample measurements is shown for a distant flyby of Saturn's second largest moon Rhea. The UVIS far-UV spectrum was collected at a distance of 55730 km and a phase angle of approximately 18.8 degrees. The integration time for the observation is 30 seconds, using

the high-resolution slit. The UVIS/FUV slit field of view crosses the boundary between Rhea's leading and trailing hemispheres near the satellite's equator (Figure 6.6). The impact craters Mumbi and Amotken are transected by the slit field of view.

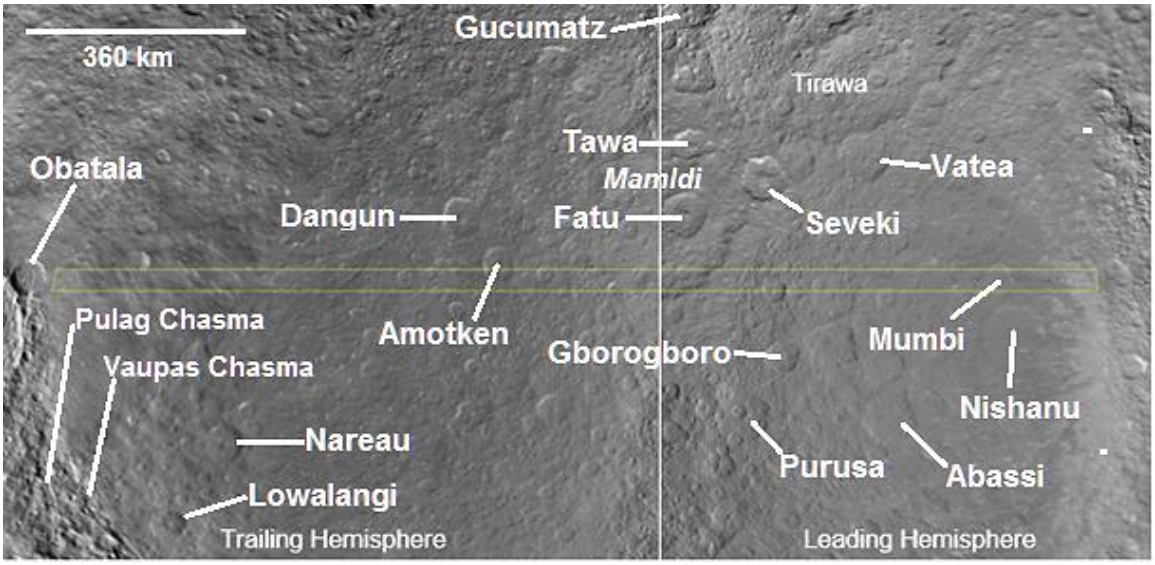

Figure 6.6: Cassini UVIS/FUV slit field of view (FOV) for observation collected on November 26, 2005 at 20:29 UT as calculated by the UVIS team Geometer code (Chapter 5). The UVIS/FUV slit field of view cross the boundary between the leading and trailing hemisphere on Rhea. The FOV passes through the impact craters Amotken and Mumbi (67.2 km diameter; location 1.9˚S, 131.2˚W). As is the case for all the UVIS observations, the instrument field of view displayed on the map represents the integrated (sum) of reflected light of all the detector spatial rows over the range of phase angles during the observation.

Three models were produced using the measured absorbance for two molecules located just beneath a layer of water-ice. The chlorine molecules measured were tetrachloromethane (CCl_4) and trichloromethane (CH_3Cl) at a temperature of 70 K under near vacuum conditions. The third model created was for Hydrazine Monohydrate ($NH_2NH_2{\cdot}H_2O$). The theoretical models were based on Hapke's formulism (Hapke 1981, 1986, 1993), using the measured vacuum-UV absorbance collected from laboratory experiments. Since the laboratory ice mixtures were dominated by water-ice, an index of refraction of 1.4 at a wavelength of 184 nm (Warren & Brandt, 2008; Warren 1984) was used in producing the modelled spectra. As shown in Figure 6.7, all three molecules provide reasonable fits to the November 26, 2005 UVIS observation over the wavelength

region of interest (~160 – 189 nm). The slight mismatch in the fits between 150 and 160 nm are not of concern, since this region of the UVIS data are quite noisy, and issues with background subtraction can cause minor variations in the reflectance.

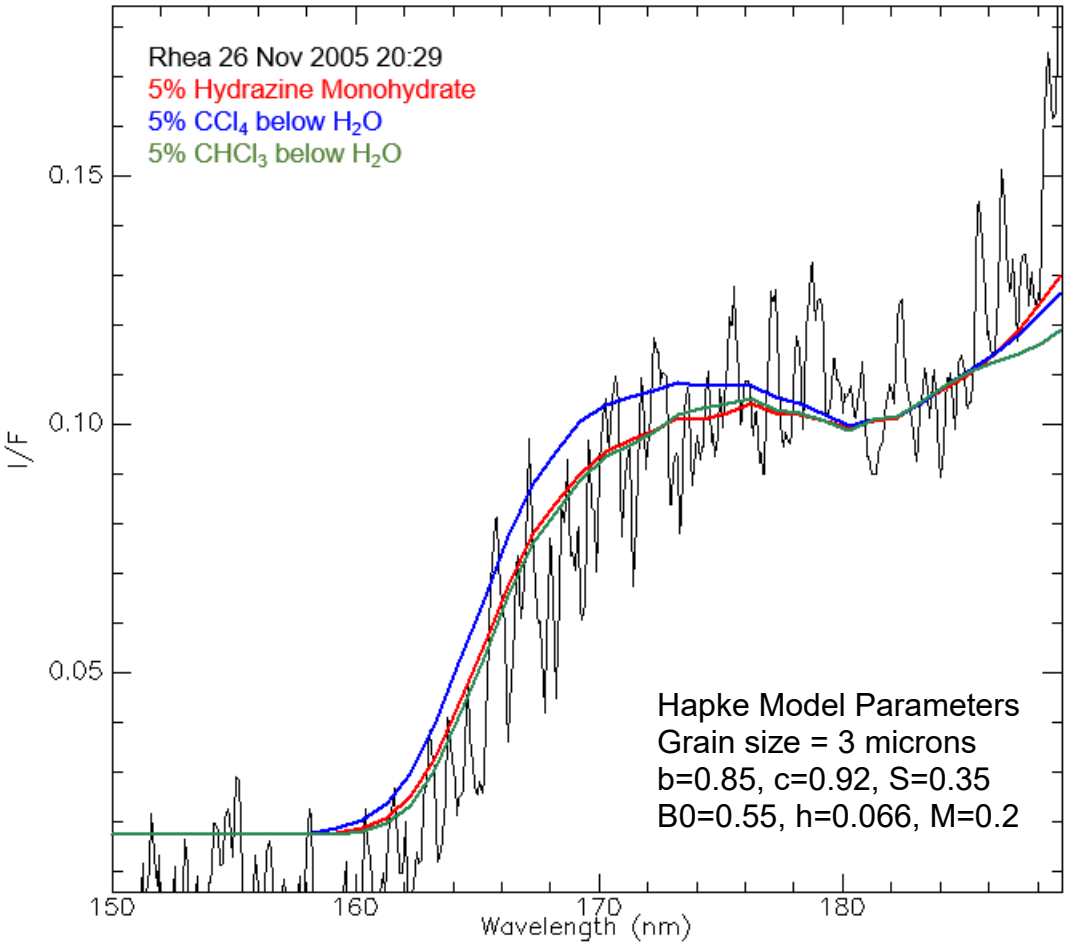

Figure 6.7: Theoretical model fits to the November 26, 2005 20:29 UT UVIS observation for two chloromethane molecules, and hydrazine monohydrate. The UVIS/FUV slit field of view crosses the boundary between Rhea's leading and trailing hemisphere. Both CCl_4 and hydrazine monohydrate fit the broad absorption feature centred near 184 nm. The thin ice layers of the two chloromethane molecules were located just below a layer of water-ice. The pathlength used in the model spectra was approximately 0.2 microns and the grain size for the ices was 3 microns, determined from derivative spectroscopy of UVIS observations.

Analysis of the modelled fits to the UVIS data show that both hydrazine monohydrate and simple chloromethane molecules can explain the broad, relatively weak absorption seen between ~179 and 190 nm (seen in UVIS data presented in Chapter 5). No other molecules presented in Chapter 5 of this dissertation can explain the absorption

feature centred near 184 nm. This was a surprising result, as it was not suspected that chlorine molecules and/or hydrazine monohydrate could be present on the surface of icy satellites, including Rhea.

Hydrazine monohydrate is less problematic to explain than chloromethane molecules. There are various chemical pathways that can lead to the formation of hydrazine monohydrate on the surface of icy satellites. For example, if minor amounts of ammonia are present within the bulk composition of water-ice chemical reactions among NH_3 and H_2O in solid phase can produce $NH_2NH_2{\cdot}H_2O$ (Loeffler and Baragiola, 2010). The detailed chemical reactions that could lead to the formation of hydrazine are discussed later in Chapter 7. Another possible source of hydrazine monohydrate is Saturn's largest moon Titan. Titan is known to have a thick atmosphere composed mostly of nitrogen with minor amounts of methane and trace abundances of other hydrocarbons. It is possible that hydrazine could be produced by chemical reactions among these nitrile and other organic molecules and transported from Titan to Rhea's surface. This scenario assumes that the hydrazine is not destroyed by UV light or bombardment by energetic particles in Saturn's magnetosphere environment.

If simple chlorine molecules are present at the surface of Rhea, they are more difficult to explain. Possible sources include exogenic delivery by asteroids and micrometeorites rich in chondritic composition (Garrison *et al*., 2000), or complex chemical reactions among minor quantities of CH_4 (methane) and the chlorine (Cl_2) within the upper surface layers of Rhea.

The possible discovery of hydrazine monohydrate and/or chloromethane molecules at one geographical location could be peculiar to the local geomorphology. However, further analysis of Cassini UVIS/FUV data at different locations on Rhea lead to the same conclusion drawn from model fits to the November 26, 2005 observation. Analysis of model fits to UVIS/FUV data collected on August 30, 2007 indicate the presence of

hydrazine monohydrate and/or trichloromethane on Rhea's leading hemisphere. The data collected during the close flyby of Rhea during August 30, 2007 provided some of the highest resolution, far-UV spectra from the Cassini mission. The highest resolution UVIS observation for the dataset analysed in this thesis occurred on August 30, 2007 01:32 UT at a range of 7698 km and phase angle of 17.1 degrees. The integration time was 60 seconds using the high-resolution slit state. Figure 6.8 shows the UVIS/FUV slit field of view, which passes just south of the impact crater Inktomi and transects several other impact craters.

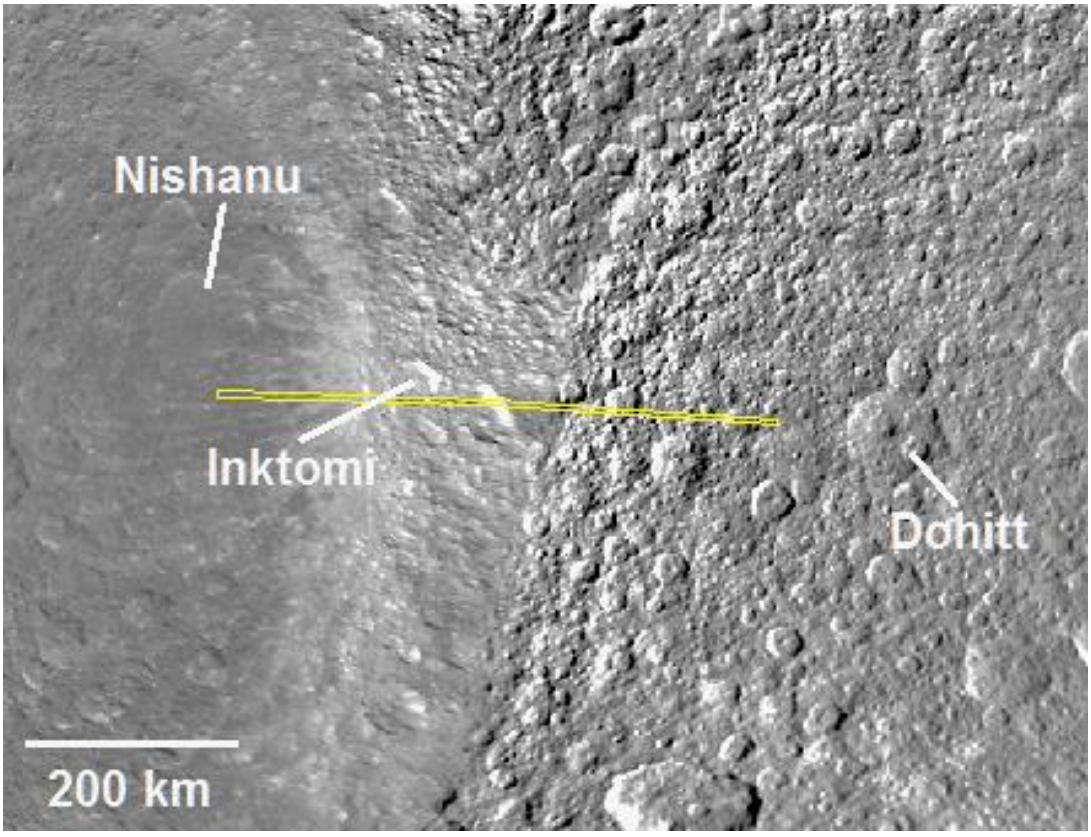

Figure 6.8: Cassini UVIS/FUV slit field of view (FOV) for the August 30, 2007 01:32 UT observation. The slit field of view is located on Rhea's leading hemisphere, and is calculated using JPL SPICE kernels and the Geometer computer code developed by the Cassini UVIS team. The FOV passes through the southern rim of the 47.2 km diameter impact crater Inktomi located at 14.1˚S, 112.1˚W.

A "chi-by-eye" examination of the comparative spectral plots for the modelled and observed spectra in Figure 6.9 shows that hydrazine monohydrate, or simple

chloromethane molecules located beneath a layer of water ice, can explain the broad absorption feature between ~178 to 189 nm. The model spectra of the three molecules also fits the overall spectral slope of the 165-nm absorption edge due to water-ice, which is displaced from its nominal wavelength due to the UV absorbers, or possibly grain size effects.

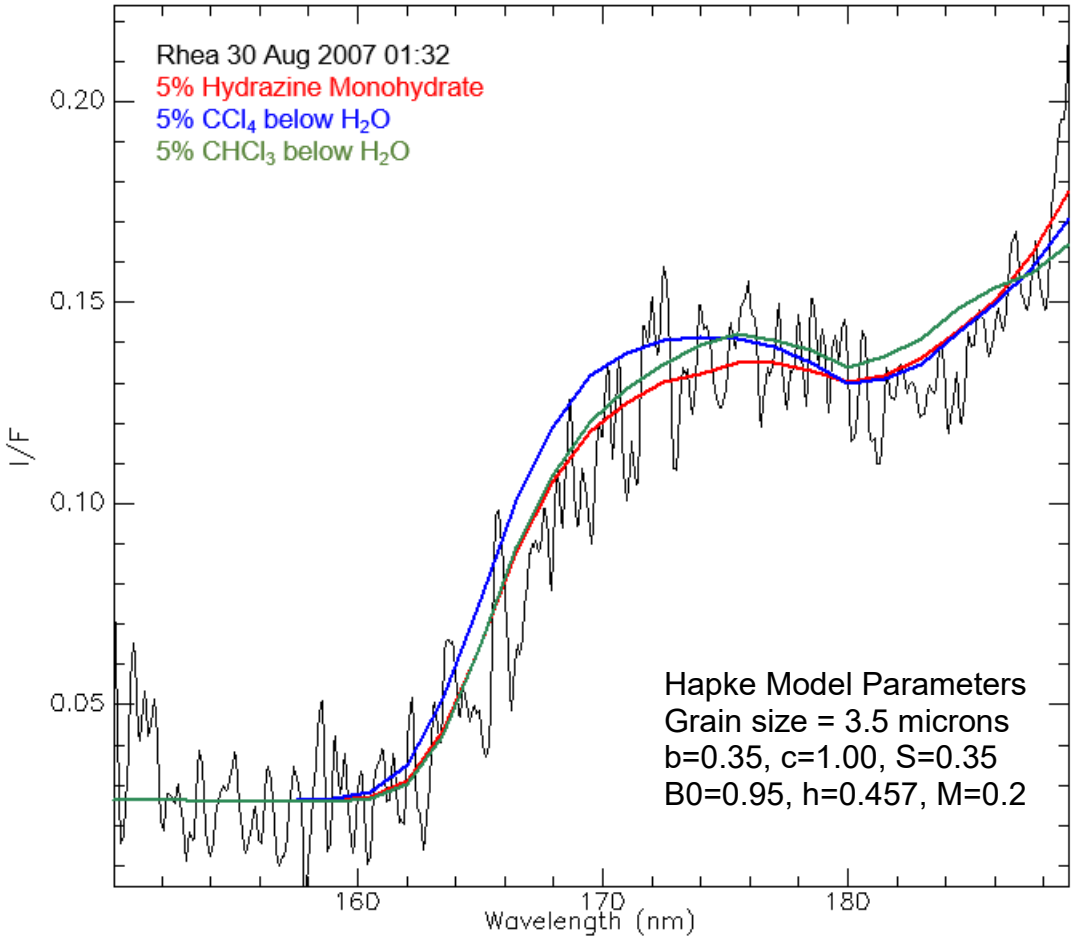

Figure 6.9: Theoretical model fits to the August 30, 2007 01:32 UT UVIS observation for trichloromethane and tetrachloromethane under water ice, and hydrazine monohydrate. The modelled spectra are based on Hapke's formulism and laboratory measurements of the absorbance. All three molecular molecules could explain the absorption between ~179 and 189 nm, although hydrazine monohydrate provides the best fit to the UVIS spectrum.

The UVIS/FUV slit field of view for the August 30, 2007 01:35 UT observation is shown in Figure 6.10. This observation was carried out at a distance of 8478 km from Rhea at a phase angle of 17.3 degrees. The integration time was 60 seconds using the high

resolution slit mode. The UVIS/FUV slit field of view for this observation is located on Rhea's leading hemisphere and passes through the impact crater Chingaso.

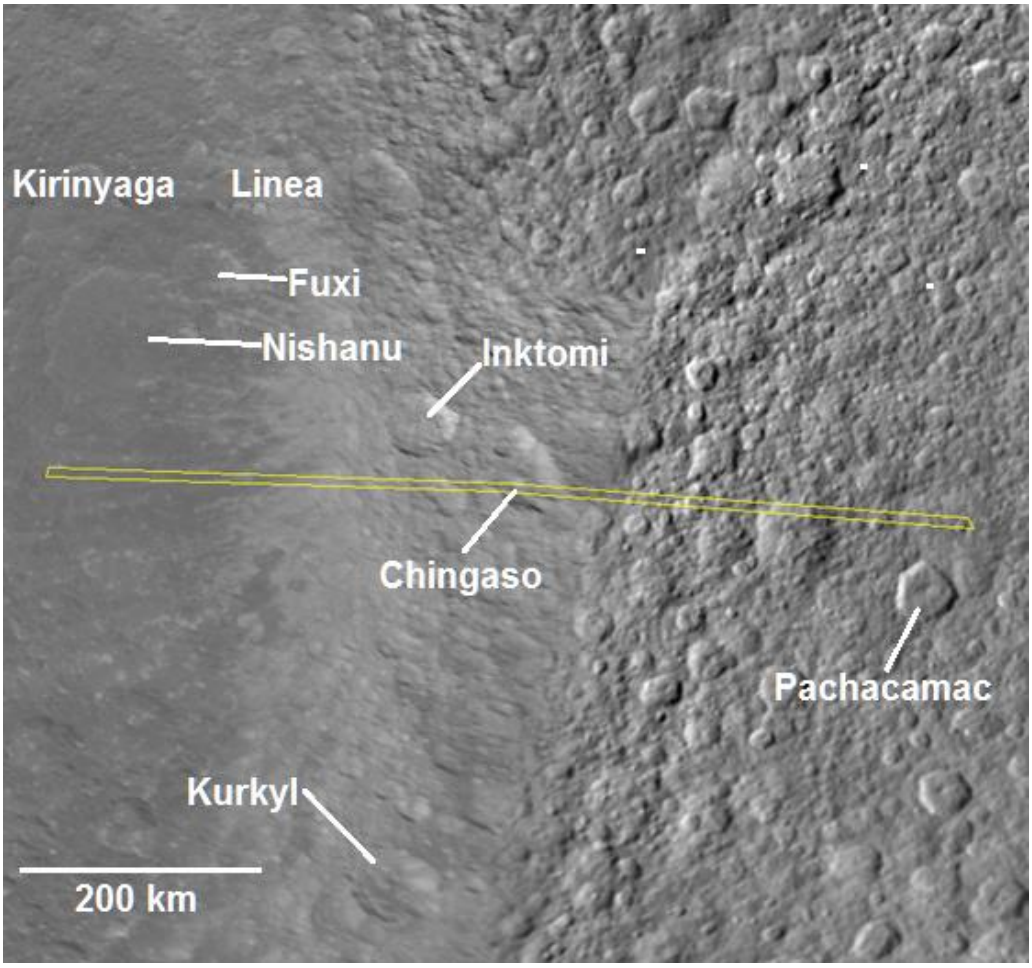

Figure 6.10: Cassini UVIS/FUV slit field of view (FOV) for the August 30, 2007 01:35 UT observation. The slit field of view is located on Rhea's leading hemisphere, and is calculated using JPL SPICE kernels and the Geometer computer code developed by the Cassini UVIS team. The FOV passes through the 47.8 km diameter impact crater Chingaso located at 17.1˚S, 106˚W.

Figure 6.11 shows the model spectra fits to the UVIS data. The best fits occur for hydrazine monohydrate and trichloromethane below a layer of water-ice.

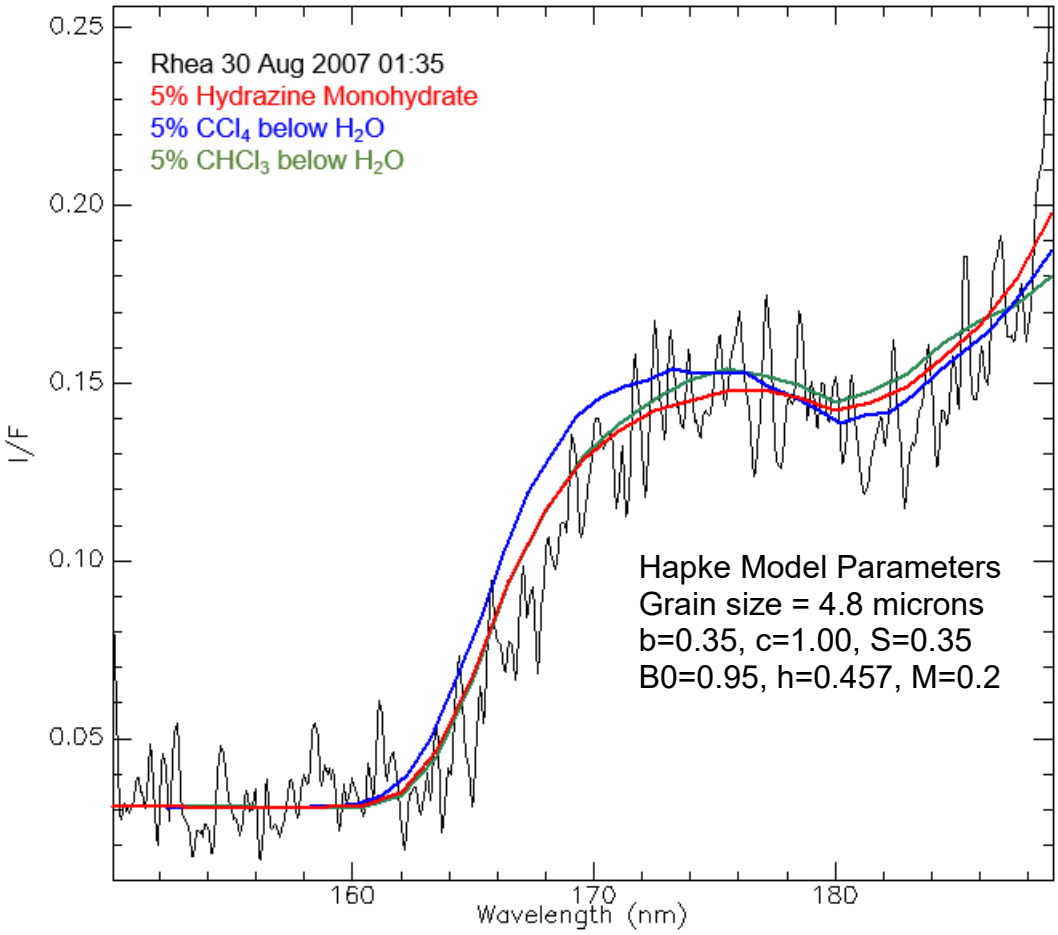

Figure 6.11: Theoretical model fits to the August 30, 2007 01:35 UT UVIS observation for trichloromethane and tetrachloromethane under water ice, and hydrazine monohydrate. The modelled spectra are based on Hapke's formulism and laboratory measurements of the absorbance. All three molecules could explain the absorption between ~179 and 189 nm.

Model spectra of hydrazine monohydrate and simple chloromethane molecules fit all of the remaining UVIS spectra shown below.

The next UVIS observation was collected during the same Cassini 2007 flyby of Rhea at slightly larger distance of 9249 km from Rhea. The phase angle of the observation was 18.2 degrees, and the integration time was 60 seconds using the high resolution slit state. The UVIS/FUV slit field of view (Figure 6.12) is located on the leading hemisphere of Rhea just north of the previous UVIS observation shown in Figure 6.10. The slit field of

view passes directly through the impact crater Inktomi and a portion of the larger impact crater Dohitt.

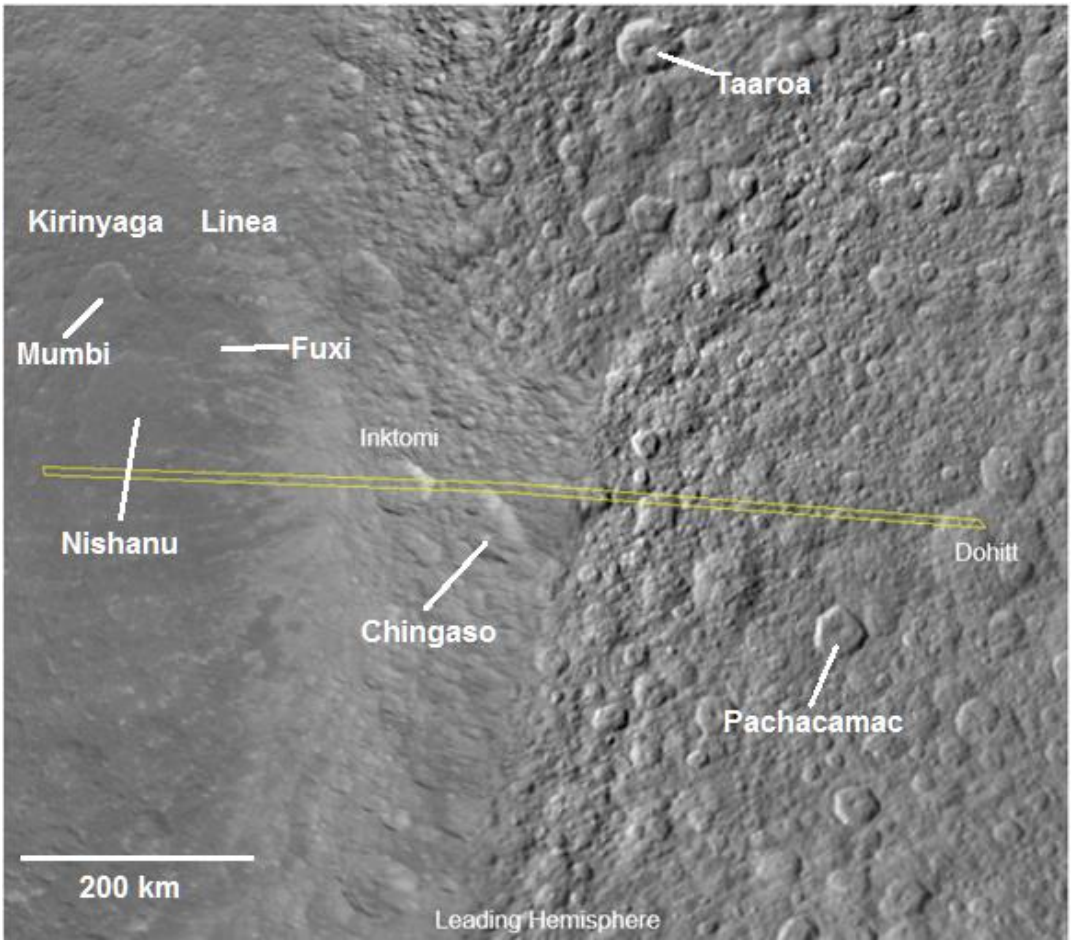

Figure 6.12: Cassini UVIS/FUV slit field of view (FOV) for the August 30, 2007 01:38 UT observation. The slit field of view is located on Rhea's leading hemisphere, and was calculated using JPL SPICE kernels and the Geometer computer code developed by the Cassini UVIS team. The FOV passes directly through the centre of Inktomi, a 47.2 km diameter impact crater located at 14.1˚S, 112.1˚W.

Laboratory UV spectra of hydrazine monohydrate ($N_2H_4 \cdot H_2O$) and trichloromethane (CH_3Cl) (shown in Chapter 4) can explain the broad absorption between ~179 – 189 nm (Figure 6.13). Tetrachloromethane fits the 184-nm absorption feature, but does not fit the UV falloff between about ~162 – 172 nm as well as the other two molecules. Again, it is of interest that the two chloromethane molecules must be located beneath a thin layer of water-ice to produce satisfactory fits to the UVIS data. When these two chloromethane molecules are mixed with water-ice, they do not fit the UVIS far-UV spectra (shown in Chapter 5).

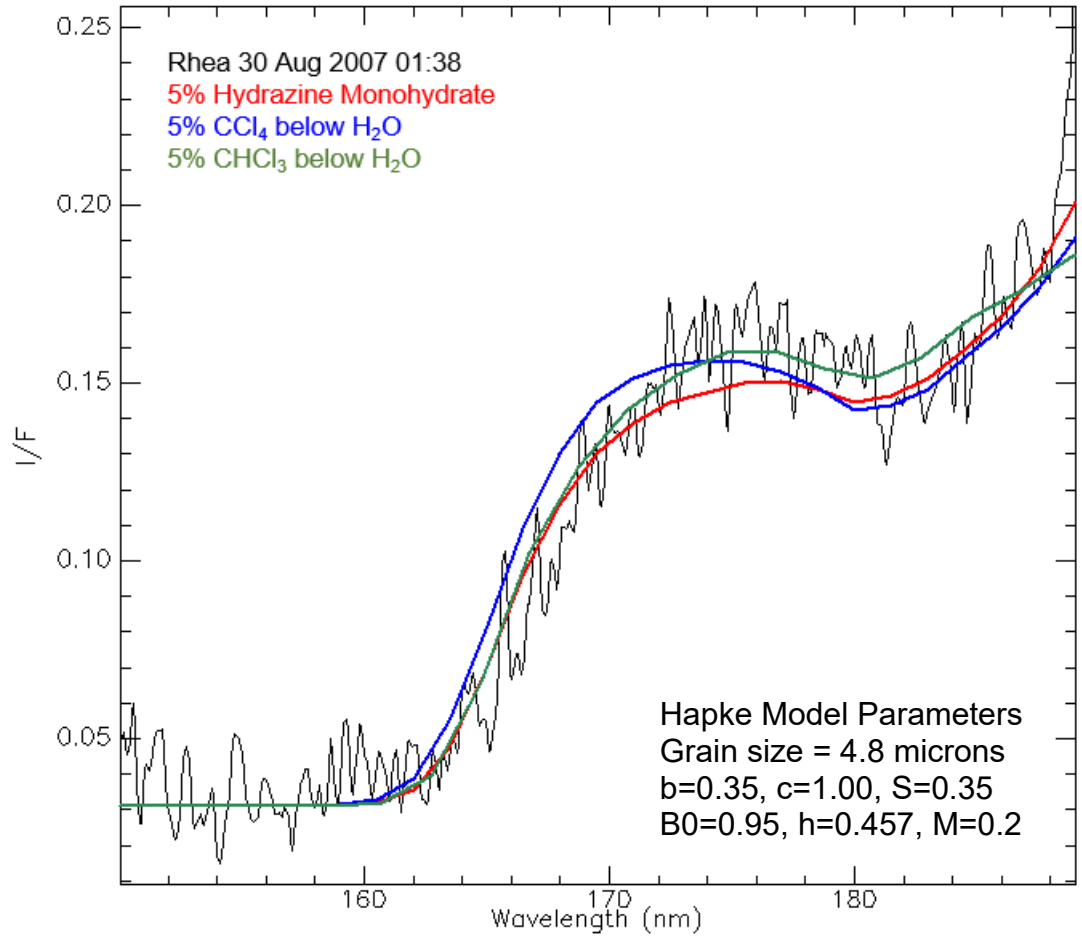

Figure 6.13: Theoretical model fits to the August 30, 2007 01:38 UT UVIS observation for trichloromethane ($CHCl_3$) and tetrachloromethane (CCl_4) under water ice, and hydrazine monohydrate ($N_2H_4 \cdot H_2O$). All three molecules can explain the broad absorption between ~179 – 189 nm, although only hydrazine monohydrate and trichloromethane fit the UV falloff between ~162 – 172 nm.

Moving outward to a slightly greater distance from Rhea's surface on the leading hemisphere a UVIS observation was collected at a range of 10065 km from Rhea at a phase angle of 19.7 degrees on August 30, 2007 01:40 UT. The integration time was 60 seconds using the high resolution slit state on the UVIS/FUV instrument. The UVIS/FUV slit field of view (Figure 6.14) passes directly through the impact crater Nishanu, which has evidence of past mass movement (Parekh, Vijayan, and Sivaraman, 2016).

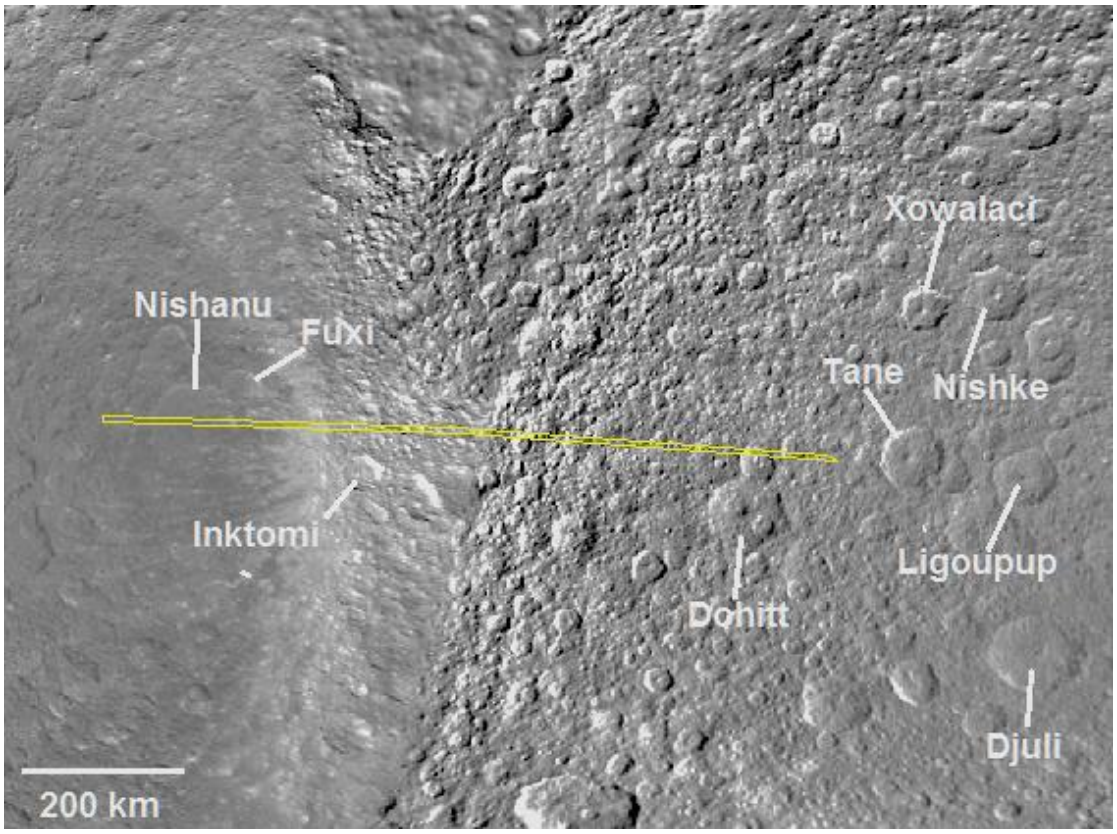

Figure 6.14: Cassini UVIS/FUV instrument field-of-view (FOV) for the August 30, 2007 01:40 UT observation. The slit field of view is located on Rhea's leading hemisphere, and was calculated using JPL SPICE kernels and the Geometer computer code developed by the Cassini UVIS team. The FOV passes directly through the large (103.4 km diameter) impact crater Nishanu located at 9˚S, 129˚W.

The three modelled spectra for hydrazine monohydrate, tetrachloromethane (CCl_4) and trichloromethane ($CHCl_3$) below a layer of water-ice are shown in Figure 6.15. Similar to the previous UVIS data, all three of these molecules can explain the broad absorption between ~179 – 189 nm. A Savitzky-Golay smoothing filter (Savitzky and Golay, 1964; Gorry, 1990) was applied to the UVIS reflectance spectrum by convolving the polynomial smoothing kernel with the raw data. This reduces significant noise that is inherent in the far-UV spectral data. The hydrazine is mixed with water-ice to a concentration of five percent whilst CCl_4 and $CHCl_3$ ice are located beneath a layer of water-ice. Once again, it is interesting to note that only simple chloromethane molecules beneath an overlying layer of water-ice fit the UVIS data, and not mixtures of chloromethane/water-ice.

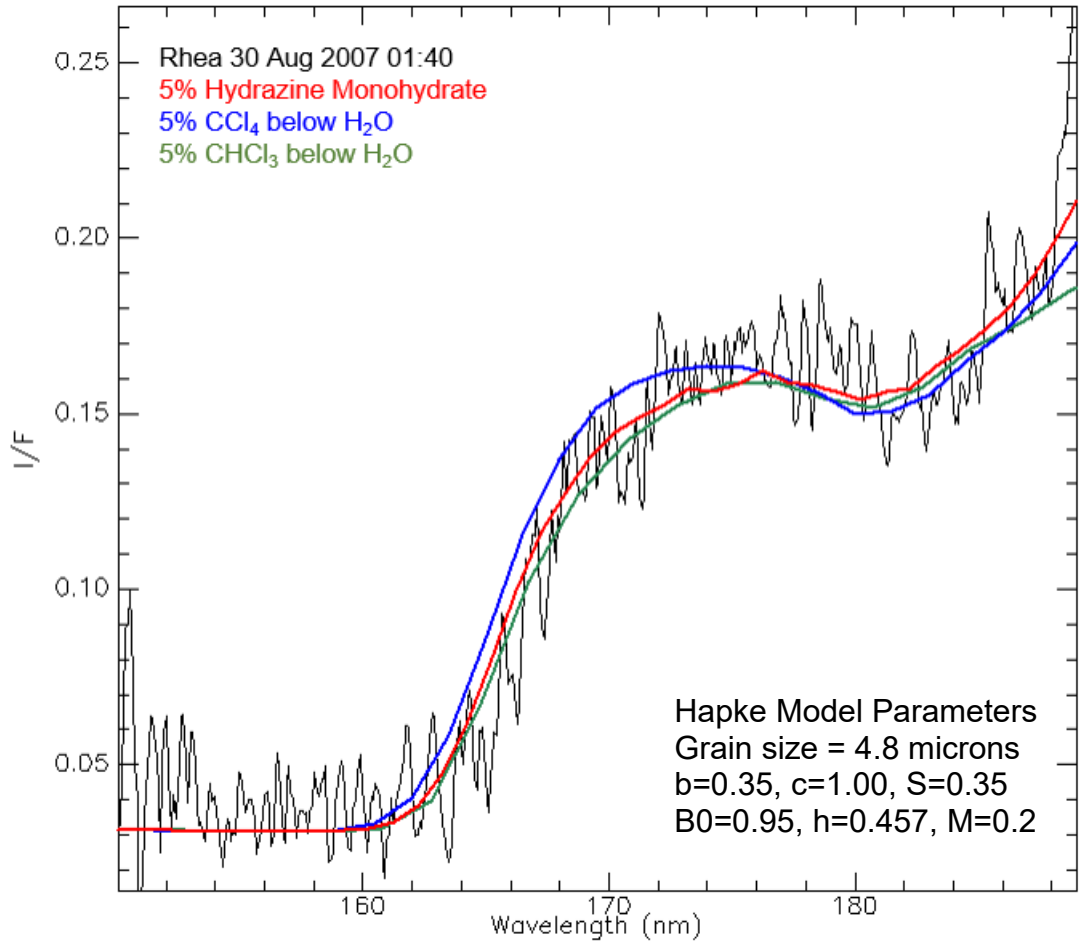

Figure 6.15: Theoretical model fits to the August 30, 2007 01:40 UT UVIS observation for trichloromethane and tetrachloromethane under water ice, and hydrazine monohydrate. The two modelled spectra based on Hapke's formulism and laboratory measurements of the absorbance. All three molecules could explain the broad absorption feature from ~179 – 189 nm. The grain size used in the modelled spectra is 4.8 microns.

Another UVIS data set was collected at the same latitude as the August 30, 2007 01:40 UT spectrum approximately 3 minutes later, at a range of 10990 km from Rhea and phase angle of 21.5 degrees (Figure 6.16). The greater distance from Rhea resulted in a larger slit field of view across Rhea's leading hemisphere. The slit field of view passes directly through the large impact crater Nishanu and through the northern rim of a small impact crater just north of Dohitt – a complex crater with a central peak.

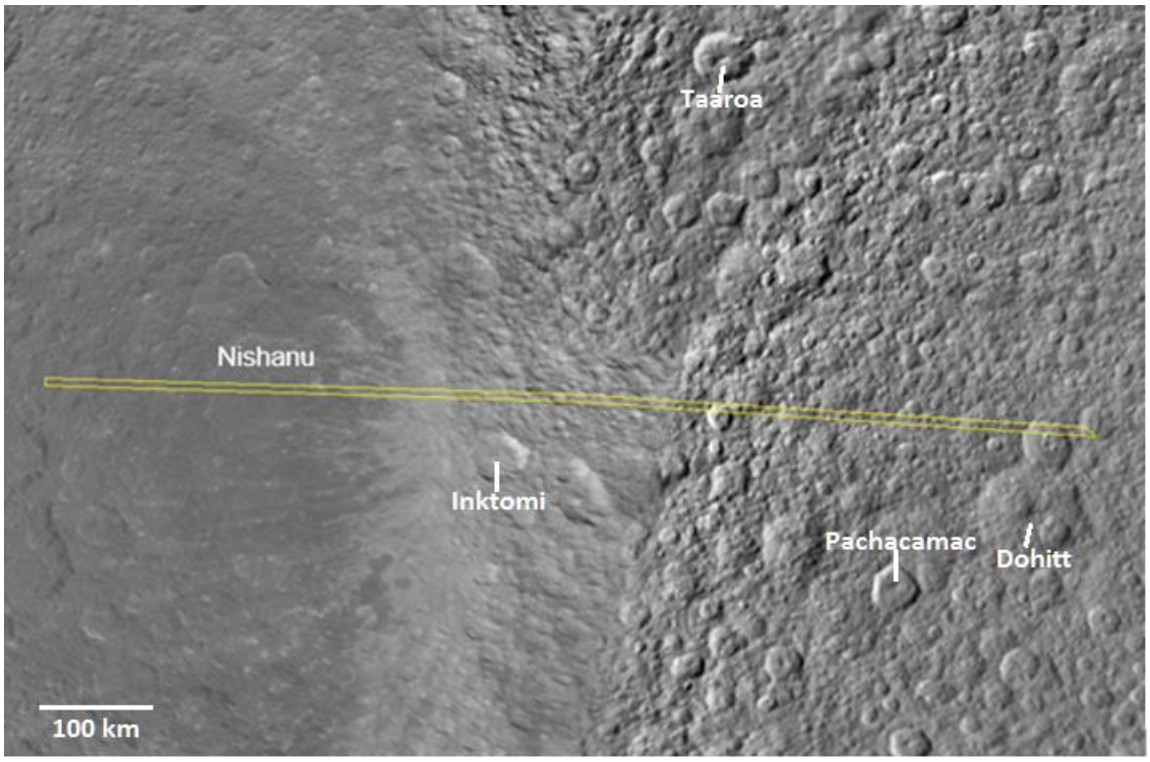

Figure 6.16: Cassini UVIS/FUV slit field of view (FOV) for the August 30, 2007 01:43 UT observation. The slit field of view passes through a large impact crater named Nishanu. The UVIS/FUV slit field of view was calculated using JPL SPICE kernels and the Geometer computer code developed by the Cassini UVIS team. The FOV passes through the impact crater Nishanu (103.4 km diameter) located at 9˚S, 129˚W.

The two molecules with the closest fit to the UVIS observation are Hydrazine Monohydrate and Trichloromethane ice just below a thin layer water-ice. The fit to the broad absorption band centred near 184 nm is excellent, and the model spectra fit the overall spectral slope of the UVIS spectra (Figure 6.17). The difference in spectral slope between the two modelled molecules is much less than the overall noise envelops of the Cassini UVIS/FUV data, resulting in a spectral ambiguity.

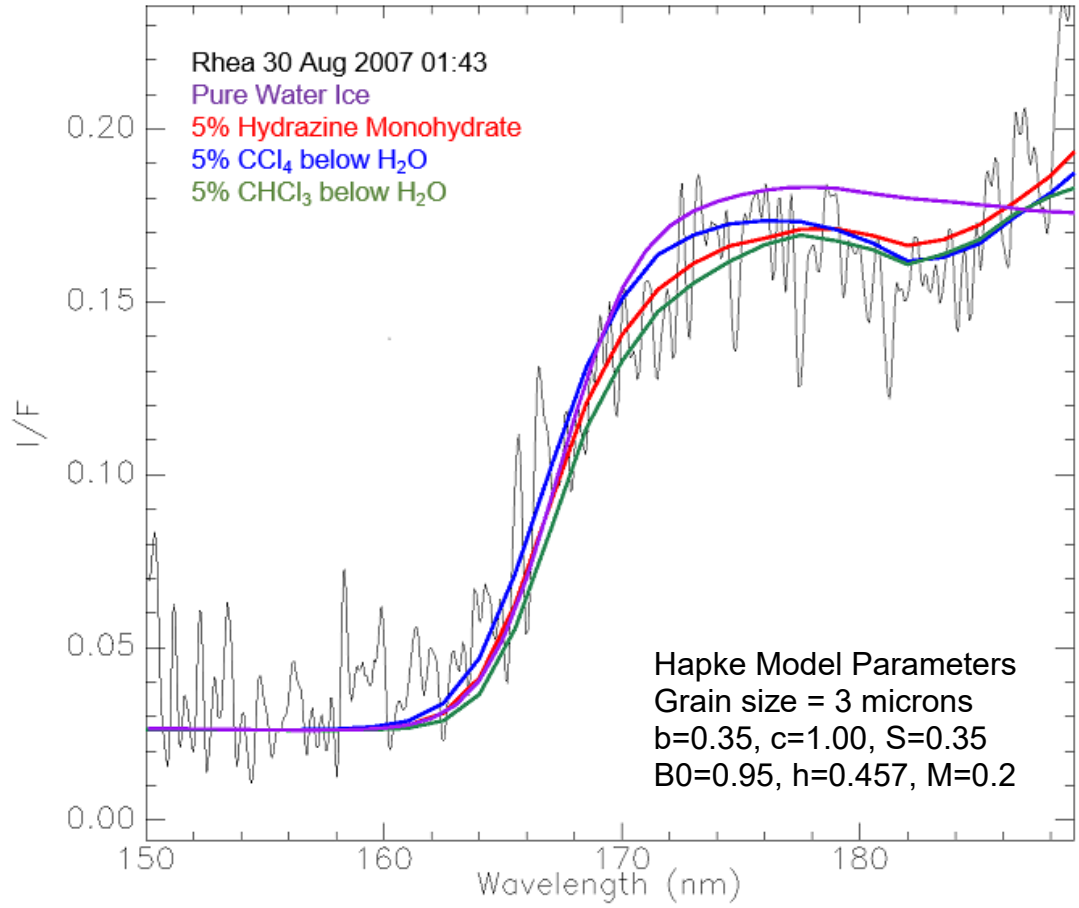

Figure 6.17: Theoretical model fits to the August 30, 2007 01:43 UT UVIS observation for tetrachloromethane (CCl_4) and trichloromethane ($CHCl_3$) under water ice, and hydrazine monohydrate. All three molecules fit the broad absorption feature between ~179 – 189 nm, as well as the overall spectral slope of the UVIS data. A model spectrum of pure water-ice does not fit the 184-nm absorption feature.

The next Cassini UVIS observation was recorded on Rhea's leading hemisphere, covering the two impact craters, Dohitt and Inktomi (Figure 6.18). The instrument field-of-view passes just south of the crater Nishanu. It should be noted, as it the case for all of the spatial-spectral UVIS observations, the final reflectance spectrum represents the integrated reflectance for the surface under the Cassini UVIS footprint.

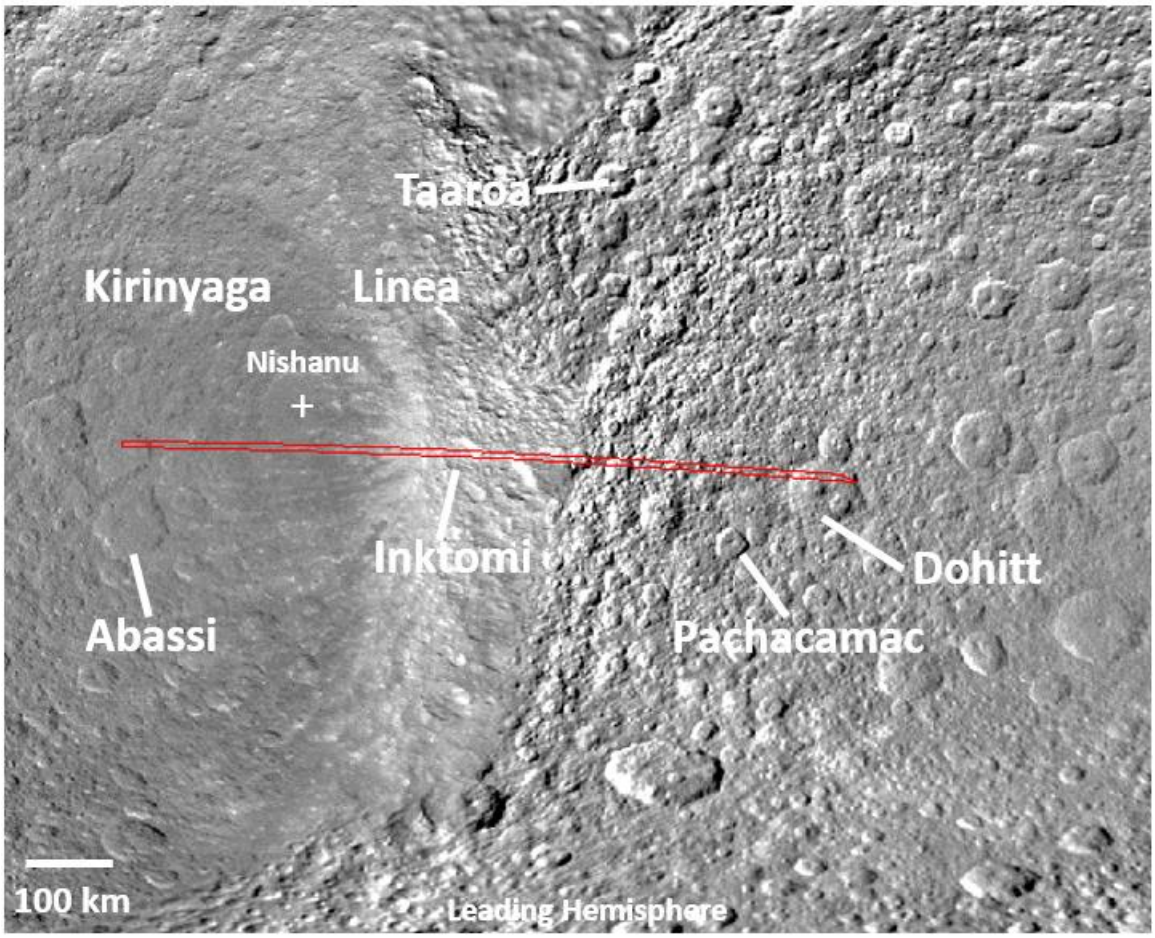

Figure 6.18: Cassini UVIS/FUV slit field of view (FOV) for the August 30, 2007 01:46 UT observation. The slit field of view passes just south of the crater named Nishanu and directly through the 47 km diameter crater Inktomi. The slit FOV also passes directly over the 93 km diameter crater Dohitt located just northeast of Pachacamac. The UVIS/FUV slit field of view was calculated using JPL SPICE kernels and the Geometer computer code developed by the Cassini UVIS team. The FOV passes through the impact craters Inktomi (diameter of 47.2 km, located at 14.1˚S, 112.1˚W) and Dohitt (diameter of 93.4 km, located at 18˚S, 74.1˚W).

In the case of the UVIS/FUV observation carried out on 30 August 2007 01:46 UT at a distance of 11851 km from Rhea's leading surface, trichloromethane ($CHCl_3$) and tetrachloromethane (CCl_4) below water-ice, as well as hydrazine monohydrate provide excellent fits to the UVIS data (Figure 6.19). Note the improvement in the baseline fit short-ward of 160 nm. A close examination of the spectral plot shows that hydrazine monohydrate and $CHCl_3$ below a layer of water-ice represent the best fits to the UVIS data. The CCl_4 laboratory spectrum does not fit the UV absorption edge due to water-ice as well as the two previously mentioned molecules.

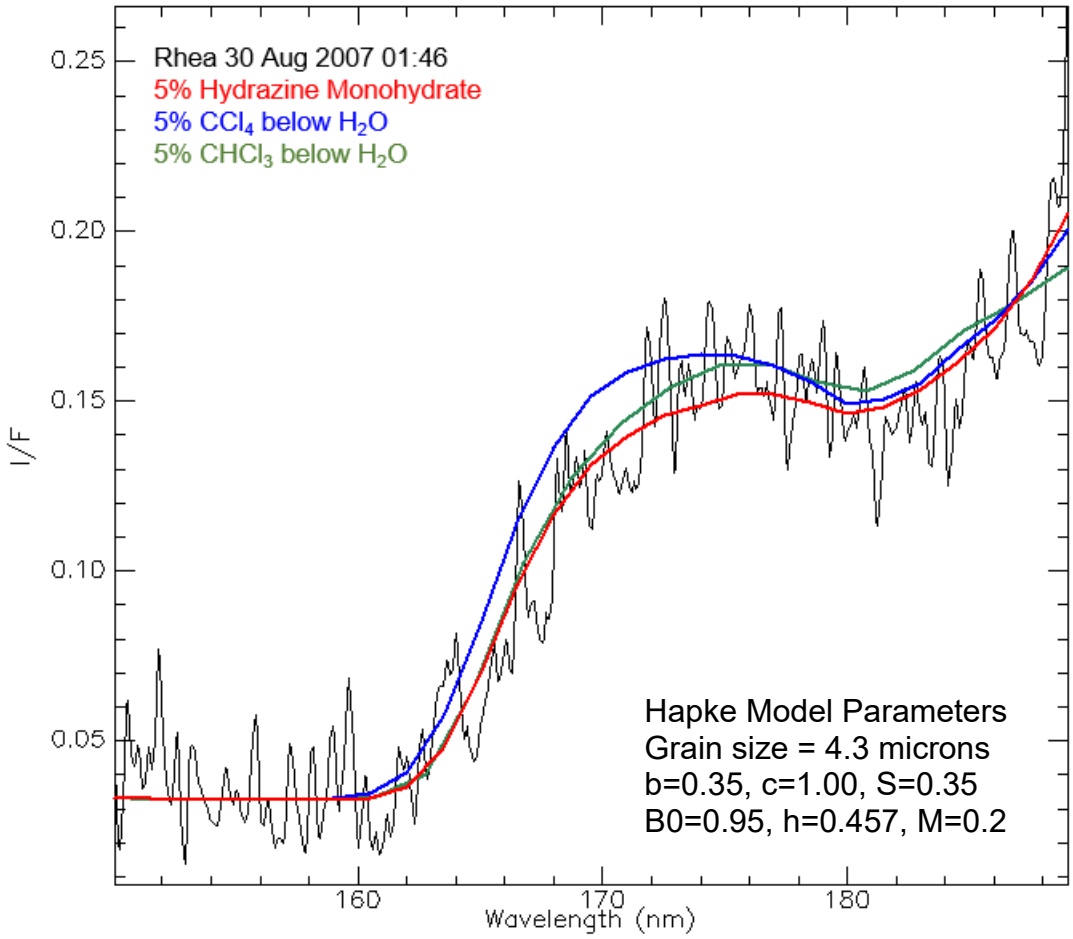

Figure 6.19: Theoretical model fits to the August 30, 2007 01:46 UT UVIS observation for tetrachloromethane (CCl_4) and trichloromethane ($CHCl_3$) under water ice, and hydrazine.

The next UVIS spectrum was collected closer to Rhea's equator on its leading hemisphere (Figure 6.20), and was collected on August 30, 2007 01:51 UT at a distance of approximately 13766 km from Rhea. The phase angle was 26.3 degrees, and the integration time was 60 seconds using the high resolution slit state.

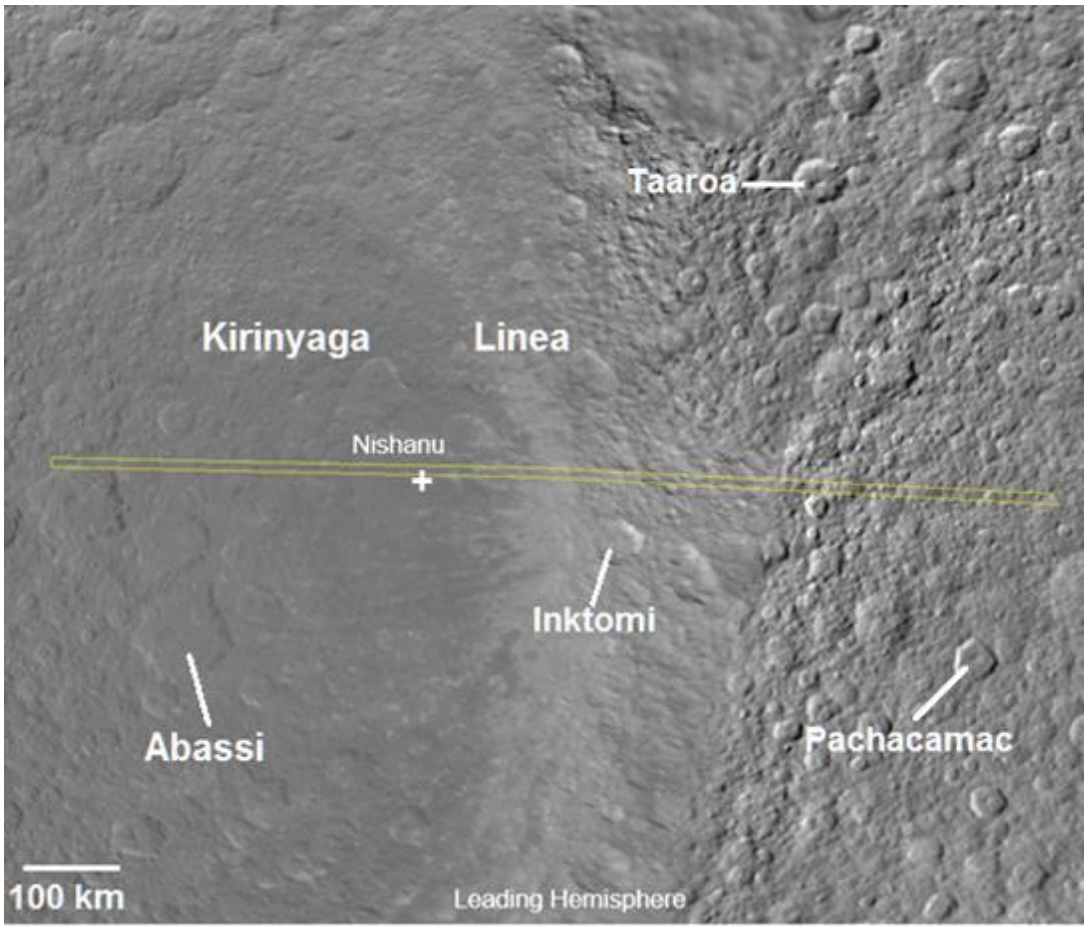

Figure 6.20: Cassini UVIS/FUV instrument footprint for the August 30, 2007 01:51 UT observation. The slit field of view was calculated using JPL SPICE kernels and the Geometer computer code developed by the Cassini UVIS team. The UVIS/FUV slit field of view traverses the large crater Nishanu (diameter of 103.4 km, located at 9˚S, 129˚W).

Modelled spectra consisting of a layer of solid phase tetrachloromethane (CCl_4) below water-ice and hydrazine monohydrate were fitted to the August 30, 2007 01:51 UT UVIS spectrum. Both molecules could explain the weak absorption feature centred near 184 nm. (Figure 6.21). The modelled spectra were produced assuming a temperature of 70 K under near-vacuum conditions. No satisfactory fits to the UVIS spectrum could be found using the modelled spectrum of trichloromethane ($CHCl_3$).

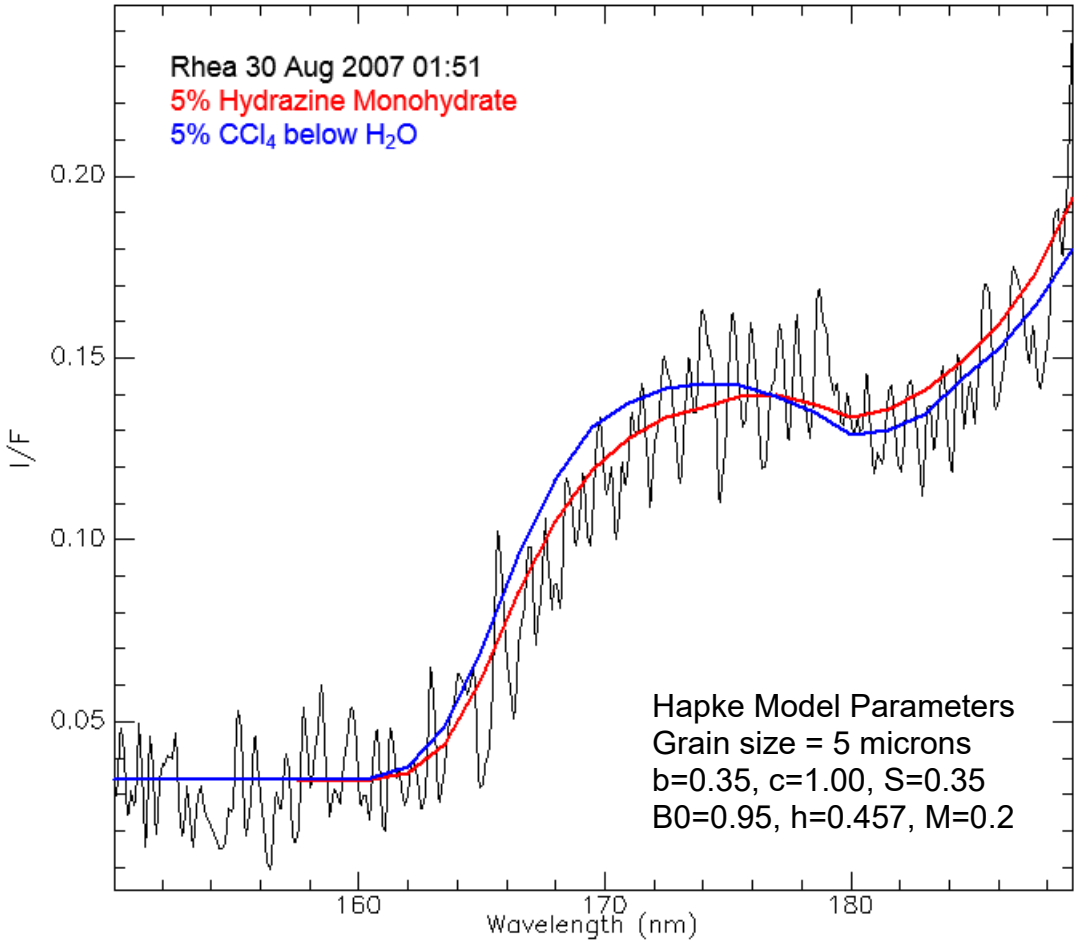

Figure 6.21: Theoretical model fits to the August 30, 2007 01:51 UT UVIS observation for and tetrachloromethane (CCl_4) under a thin layer of water ice, and hydrazine monohydrate (N_2H_4). The two molecules provide reasonable fits to the UVIS spectrum, although hydrazine monohydrate represents a better fit to the UV absorption edge due to water-ice.

The final UVIS observation used in this study for the Cassini 2007 flyby of Rhea, was collected on August 30, 2007 01:54 UT. The distance to Rhea was 14768 km at the start of the observation, and the phase angle was 27.4 degrees. The UVIS slit field of view is located on Rhea's leading hemisphere, just south of the equator (Figure 6.22).

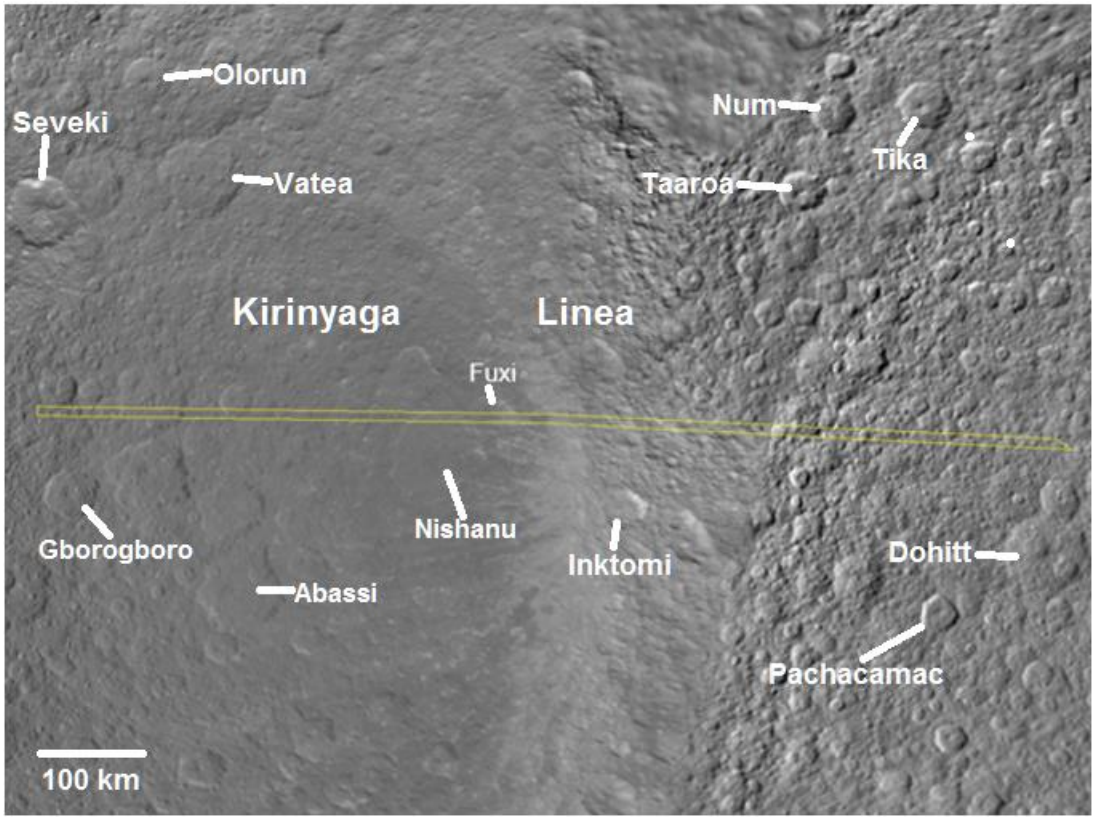

Figure 6.22: Cassini UVIS/FUV slit field of view for the August 30, 2007 01:54 UT observation. The footprint was calculated using JPL SPICE kernels and the Geometer computer code developed by the Cassini UVIS team. The slit field of view passes through the small crater Fuxi and through the northern rim of the 103.4 km diameter crater Nishanu.

Once again, three molecular species provided the best fit to the UVIS spectrum (Figure 6.23); Hydrazine Monohydrate ($N_2H_4 \cdot H_2O$), Tetrachloromethane (CCl_4) under water-ice, and Trichloromethane ($CHCl_3$) below a thin layer of water-ice. For reference, a modelled spectrum based on absorbance measurements of irradiated water-ice at a temperature of 70 K, has been plotted (purple line) along with the three modelled spectra. Although the irradiated water-ice spectrum provides a good fit to the absorption edge (i.e. the steep drop in reflectance at wavelengths less than about 170 nm) due to water-ice, it does not explain the broad absorption between ~178 nm to 189 nm. It is also interesting to note that the absorption edge due to pure water ice, whose midpoint is normally located near 165 nm, appears to be shifted to longer wavelengths. This could be explained by the

particular structure of the ice grain, the size of the ice grains, minor contaminants within the ice matrix, or a combination of these effects.

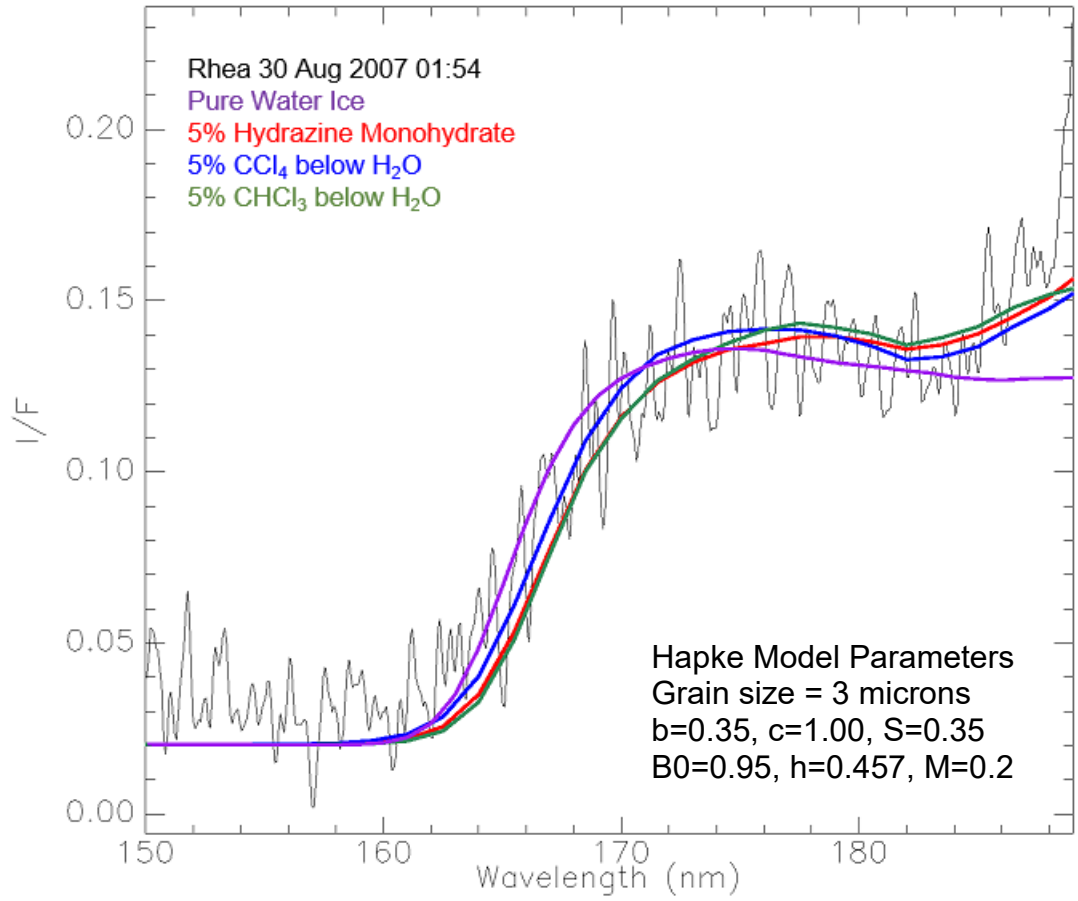

Figure 6.23: Theoretical model fits to the August 30, 2007 01:54 UT UVIS observation for Trichloromethane and Tetrachloromethane under a thin layer of water ice, and hydrazine monohydrate. All three molecules provide reasonable fits to the UVIS spectrum. A model water-ice spectrum does not fit the 184-nm absorption feature.

During the Cassini 2010 targeted flyby of Rhea, several high-resolution UVIS observations were made. Two of these observations were chosen for further analysis based on the signal-to-noise of the data. The two far-UV spectra sample Rhea's trailing hemisphere (Figure 6.24), and were collected on March 2, 2010 18:20 UT and 18:25 UT. The distances from Rhea were 19551 km and 22437 km with very high phase angles, 0.86 and 1.6 degrees, respectively. The integration times were 120 seconds using the low resolution slit state. Two UVIS/FUV slit field of views transect both chasmata and linea features, as well as several small impact craters.

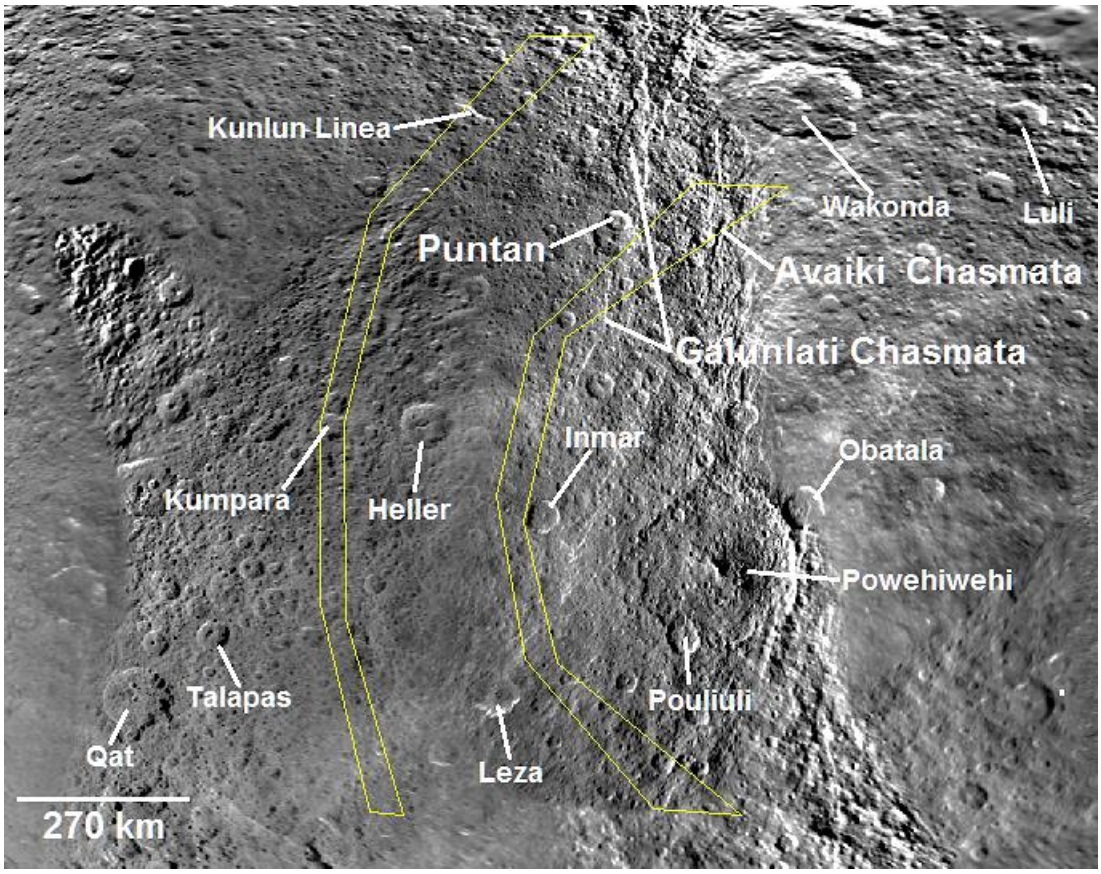

Figure 6.24: UVIS/FUV slit field of views (FOV) for the March 2, 2010 18:20 UT (right field of view) and 18:25 UT (left field of view) trailing hemisphere observations during the Cassini 2010 targeted flyby of Rhea. The polygonal approximations of the footprints were calculated using JPL SPICE kernels and the Geometer computer code developed by the Cassini UVIS team. The latitude and longitude points were used in ENVI to produce the overlays. The 18:25 observation was collected at a greater range, resulting in a larger slit field of view projected onto Rhea's trailing hemisphere. The FOVs for these observations passes through various linea, chasmata, and small impact craters. For geographical reference, the impact crater Heller is located at 10.1˚N, 315.1˚W.

The same procedure described earlier in this chapter was used to compare model spectra of chloromethane and hydrazine molecules with the two UVIS spectra. The best fit to the two UVIS observations is a model spectrum of tetrachloromethane (CCl_4) below water-ice and trichloromethane ($CHCl_3$) located beneath a layer of water-ice. Hydrazine monohydrate also fits the UVIS data (Figure 6.25). The presence of any of these molecules on Rhea's leading and trailing hemispheres indicates a global process responsible for their presence within the surface ice.

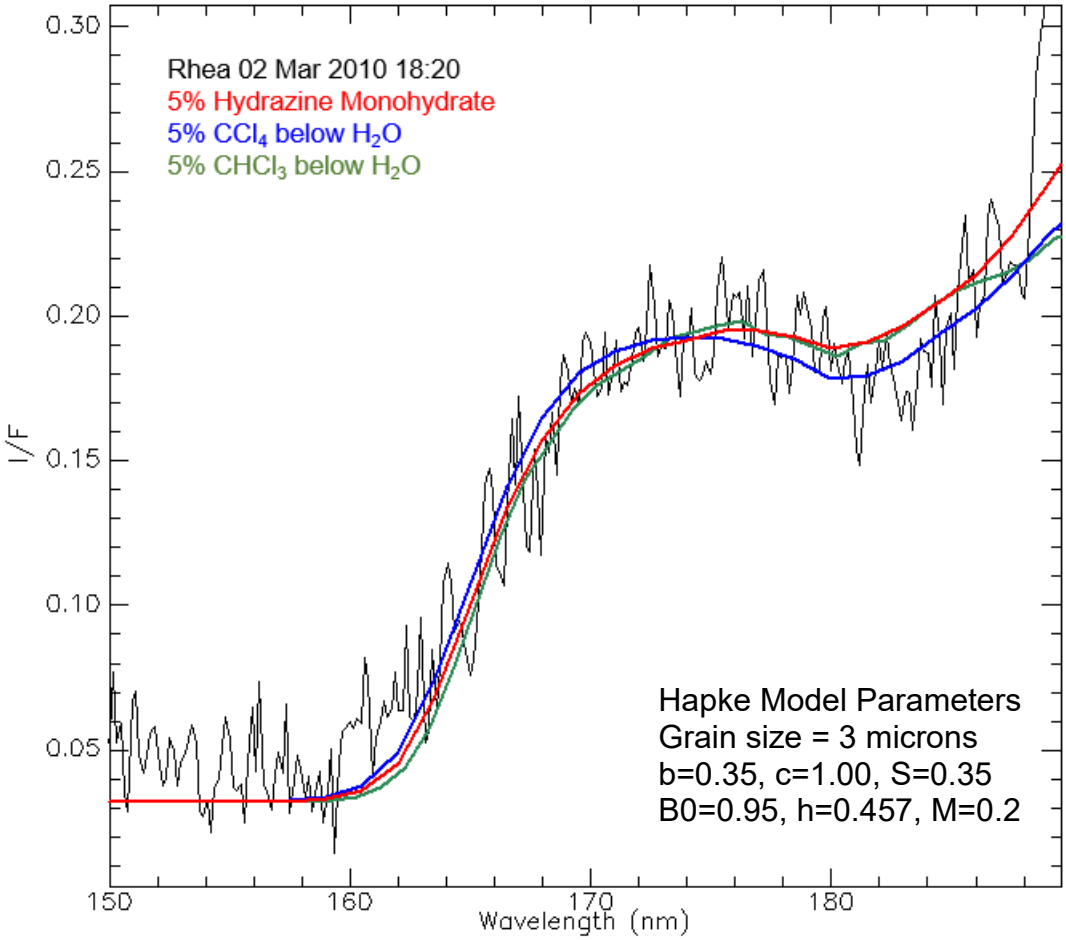

Figure 6.25: Theoretical model fits to the March 2, 2010 18:20 for tetrachloromethane (CCl_4) and trichloromethane ($CHCl_3$) under a thin layer of water ice and hydrazine monohydrate. All three molecules appear to fit the broad absorption between ~179 – 189 nm. The disagreement between the UVIS data and model spectra shortward of ~160 nm is most likely due to an inadequate background subtraction. A model water-ice spectrum does not fit the 184-nm absorption feature.

Since Rhea's trailing surface completely filled the UVIS/FUV slit field of view, only the background for the Cassini's radioisotope thermoelectric generators (RTGs) was subtracted. This explains the mismatch between the UVIS data and model spectra below ~160 nm. The second UVIS observation recorded during Cassini's 2010 targeted flyby of Rhea yields similar results to the first observation. Simple chloromethanes beneath a layer of water-ice or hydrazine monohydrate could explain the broad absorption between ~179 – 189 nm (Figure 6.26). It is of interest to note the higher level of noise present in the 2010 flyby data, relative to the 2007 data. However, by applying a Savitzky-Golay smoothing

filter (Savitzky and Golay, 1964; Gorry, 1990) to the UVIS spectrum, the broad absorption feature between ~ 179 – 189 nm is visible in the data.

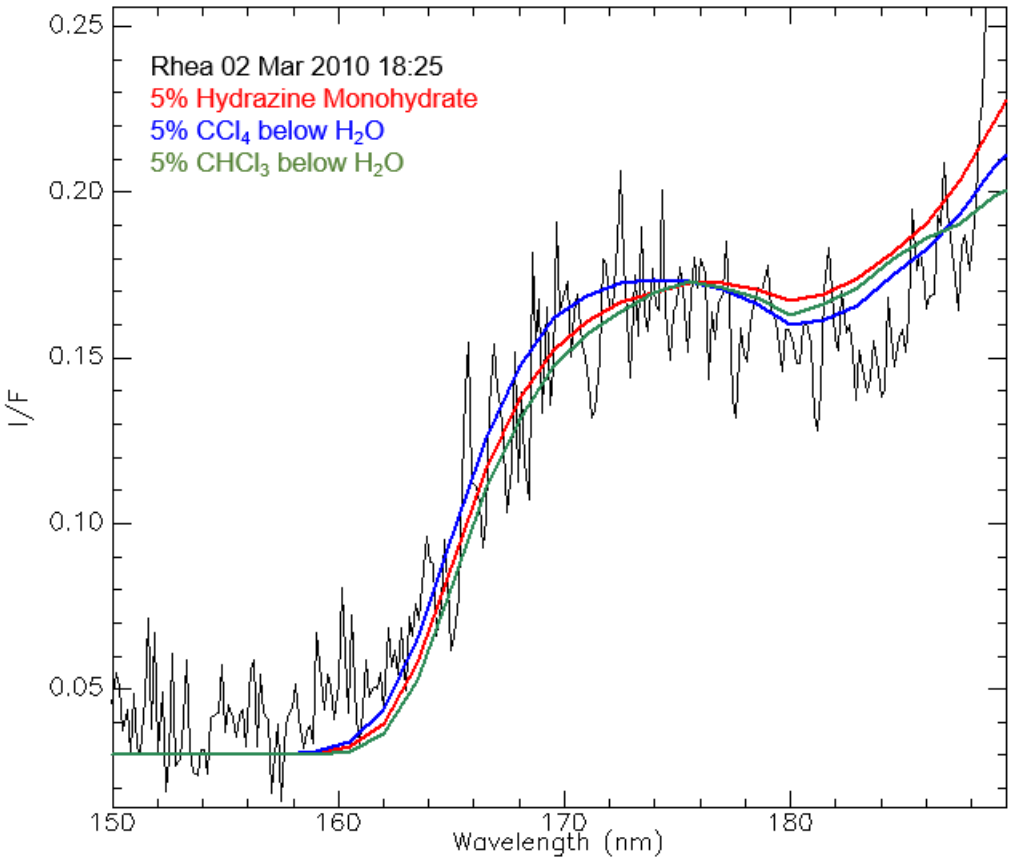

Figure 6.26: Theoretical model fits to the March 2, 2010 18:25 UT UVIS observation for Tetrachloromethane under a thin layer of water ice, trichloromethane under a thin layer of water ice, and hydrazine monohydrate. The correlation between Tetrachloromethane (CCl_4) and the UVIS observations is higher than for hydrazine monohydrate.

The final two UVIS observations to be examined were made during the Cassini 2011 targeted flyby of Rhea. The UVIS/FUV slit field of views for these two observations cross the boundary between the leading and trailing hemispheres (Figure 6.27) of Rhea. The two spectra were collected on January 11, 2011 05:40 UT and 06:04 UT at distances of 22088 km and 33579 km, respectively. Both spectra were collected at a phase angle near 15 degrees using the low resolution slit state on the UVIS instrument.

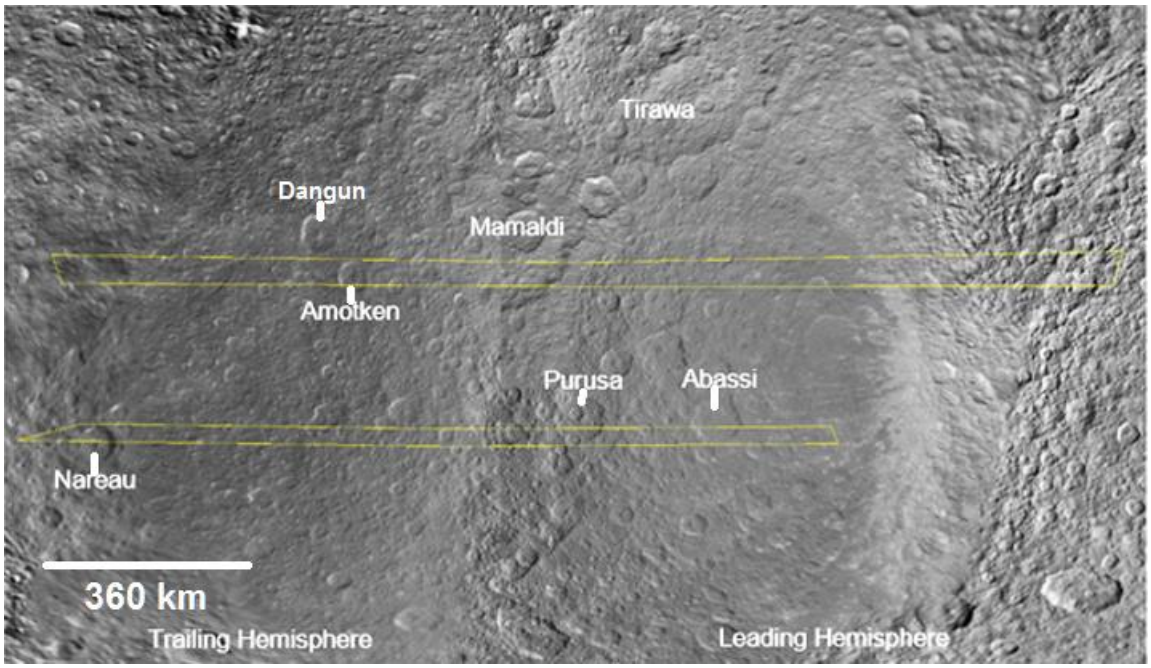

Figure 6.27: UVIS/FUV slit field of view for the January 11, 2011 06:04 observation (top field of view projection) during the Cassini 2011 targeted flyby of Rhea. The top field of view traverses a portion of the large impact crater Mamaldi and the crater Amotken. For geographical reference, the large impact basin Tirawa is located at 34.12˚N, 151.42˚W.

Both CCl_4 below water-ice, $CHCl_3$ below water-ice, and hydrazine monohydrate fit the broad absorption between ~179 – 189 nm (Figure 6.28). Spectral ambiguities between the three modelled spectra arise because the differences in the spectral profiles are less than the overall noise envelop of the UVIS/FUV data. Excessive noise in the January 11, 2011 05:40 observation prevented its analysis.

Because the UVIS/FUV slit field of view for the January 11, 2011 06:04 UT observation crosses the leading and trailing hemispheres on Rhea, the presence of any of the three molecules in the surface ice implies a global mechanism for their origin – i.e. the process for the formation and/or delivery of any of these molecules on Rhea appears to operate over both hemispheres.

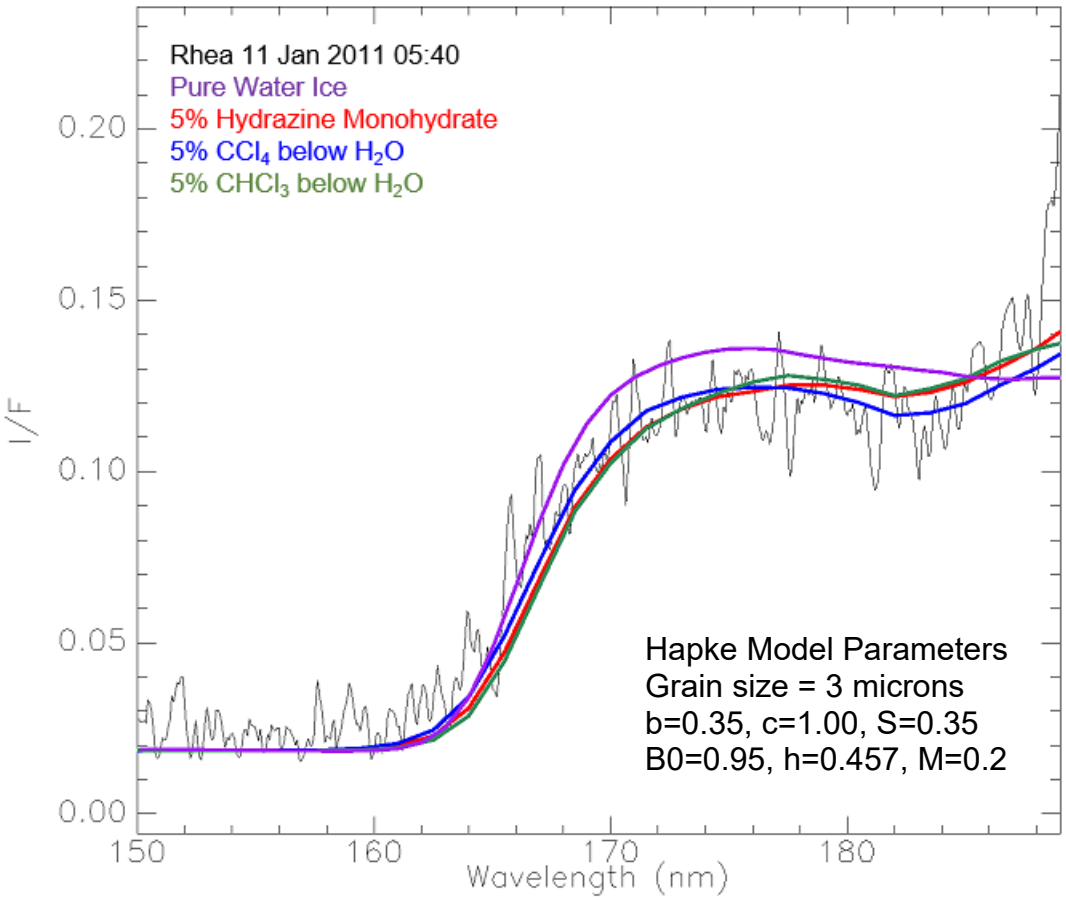

Figure 6.28: Theoretical model fits to the January 11, 2011 05:40 UT UVIS observation for tetrachloromethane (CCl_4) under a thin layer of water ice, trichloromethane ($CHCl_3$) beneath water-ice, and hydrazine monohydrate. The three molecules fit the absorption feature between ~179 – 189 nm, as well as the UV falloff between ~162 – 172 nm. A model water-ice spectrum does not fit the 184-nm absorption feature.

Examination of the modelled spectra presented here clearly show that either hydrazine monohydrate or simple chloromethane molecules can explain the weak, broad absorption seen between approximately 179 to 189 nm. To determine the relative strength of the absorption, continuum-removed spectra of four observations that sample both hemispheres of Rhea are shown. The continuum was removed by fitting a polynomial to the data. A piecewise linear segment fit was also tried, but the polynomial method produced better results (Figure 6.29).

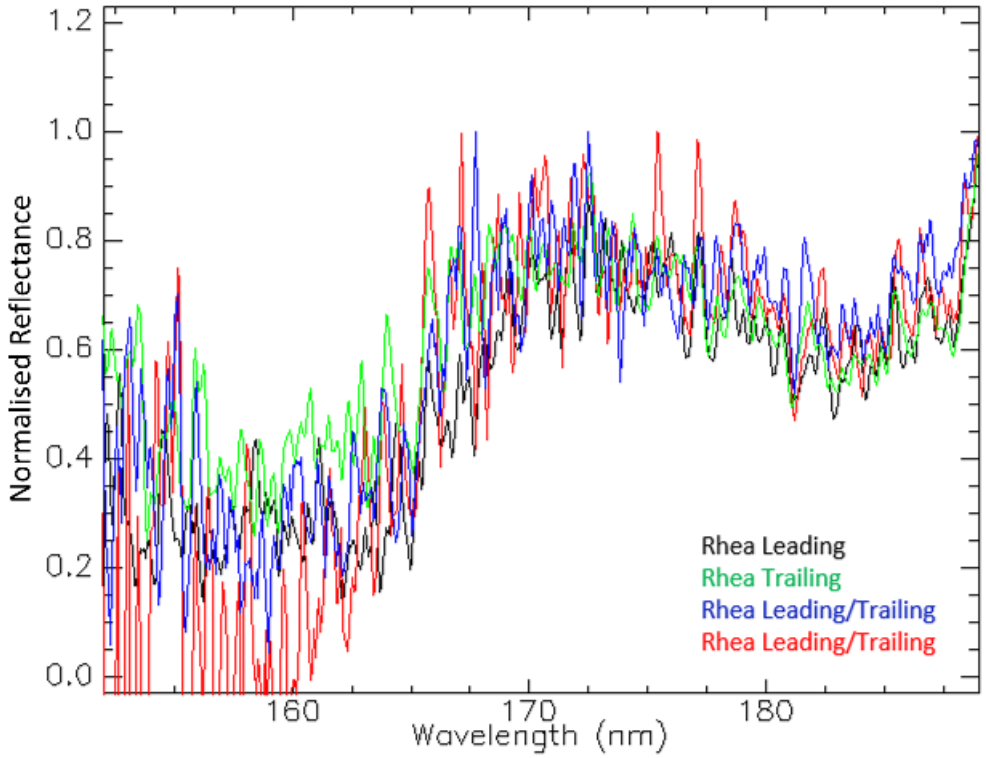

Figure 6.29: Normalised spectra showing the relative depth of the 184-nm absorption feature and the relative positions of the water-ice absorption edge. To within the error limits of the UVIS data, there is no significant differences in the strength of the 184-nm absorption feature as a function of location on Rhea's surface. A minor change in the position of the UV absorption edge due to water-ice is noted. The cause for the minor shift may be the result of different ice grain sizes and/or minor contaminants within the ice matrix. The continuum has been removed by fitting a polynomial to produce the normalized reflectance spectra.

Within the error limits of the UVIS data, no significant change in the relative depths of the 184-nm absorption feature is detected. This implies that whatever process is responsible for producing the 184-nm absorption feature, it does not depend on the geographical location on Rhea.

It should be noted that the above fits to the UVIS data are based on mixtures of water-ice and hydrazine and/or chloromethane molecules. The darkening of Rhea surface at far-UV wavelengths greater than 170 nm also implies an additional UV absorber (e.g. organics) that has not been included in the modelling process.

6.4.1 The Problem of Abundance Estimation

In an attempt to demonstrate the spectral ambiguity that arises between varying amounts of hydrazine relative to water-ice, laboratory ice spectra of hydrazine and pure water-ice were used to construct mixed spectra. A spectral mixing approach was used by averaging different proportions of water-ice and hydrazine. Figure 6.30 shows the effect of varying different proportions of hydrazine relative to the water-ice. The modelled spectra of hydrazine were produced, with abundances ranging from 25% down to 2.6%. As seen in Figure 6.30, the effect of varying proportions of hydrazine mixed with water ice on the depth of the broad absorption feature between ~178 – 189 nm, is extremely small. The same problems arise when simulating varying amounts of chlorine molecules on the depth of the absorption observed between ~178 – 189 nm.

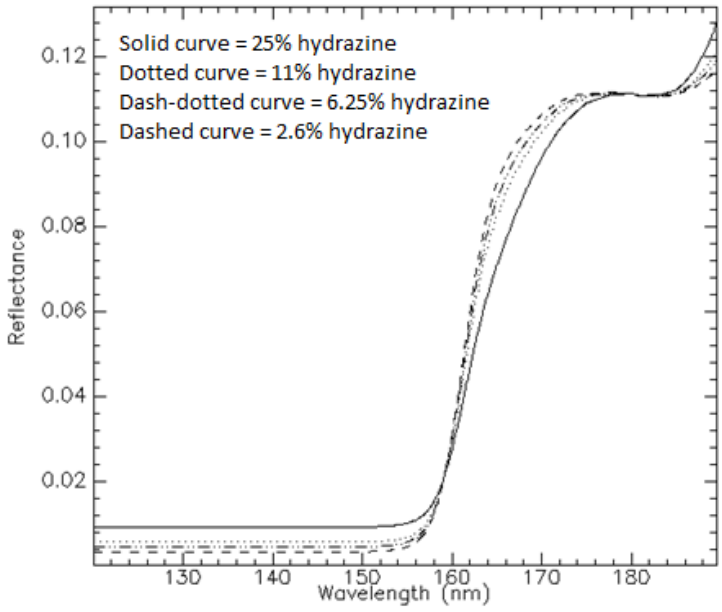

Figure 6.30: Simulated mixed water-ice/hydrazine spectra with varying amounts of hydrazine. The solid black curve represents 25% hydrazine, 11% is shown by the black dotted curve, 6.25% is shown by the dash-dotted curve, and the dashed profile represents 2.6% hydrazine. The effect of varying amounts of hydrazine in the ice mixture on the depth of the absorption between ~178 – 189 nm is very small.

The small differences between the modelled spectral profiles lies well within the overall noise envelope of the UVIS data, thus preventing the degeneracy between spectra from being removed (i.e. spectral ambiguity exists). However, it is still important to note that the detection of non-water-ice molecules on an icy satellite over nine astronomical units (i.e. the mean distance from the centres of the Earth and Sun) from the Sun is in itself a remarkable achievement.

6.5: A Search for the 184-nm Absorption Feature on Dione and Tethys

Assuming hydrazine monohydrate on Rhea is the result of satellite-to-satellite transfer of materials originating from Titan, far-UV spectra of Rhea were compared to observed UVIS spectra of Saturn's mid-sized moons Dione and Tethys (Figure 6.31). These mid-sized icy satellites all show signs of past endogenic features, including large impact craters that appear to have undergone partial relaxation (White *et al*. 2017), ridges, grabens and extensional faults (Rhea), and plains unit boundaries (Tethys). In order of increasing radial distance from Saturn's largest moon Titan, Rhea, Dione and Tethys are dominated by water-ice, with minor amounts of impurities.

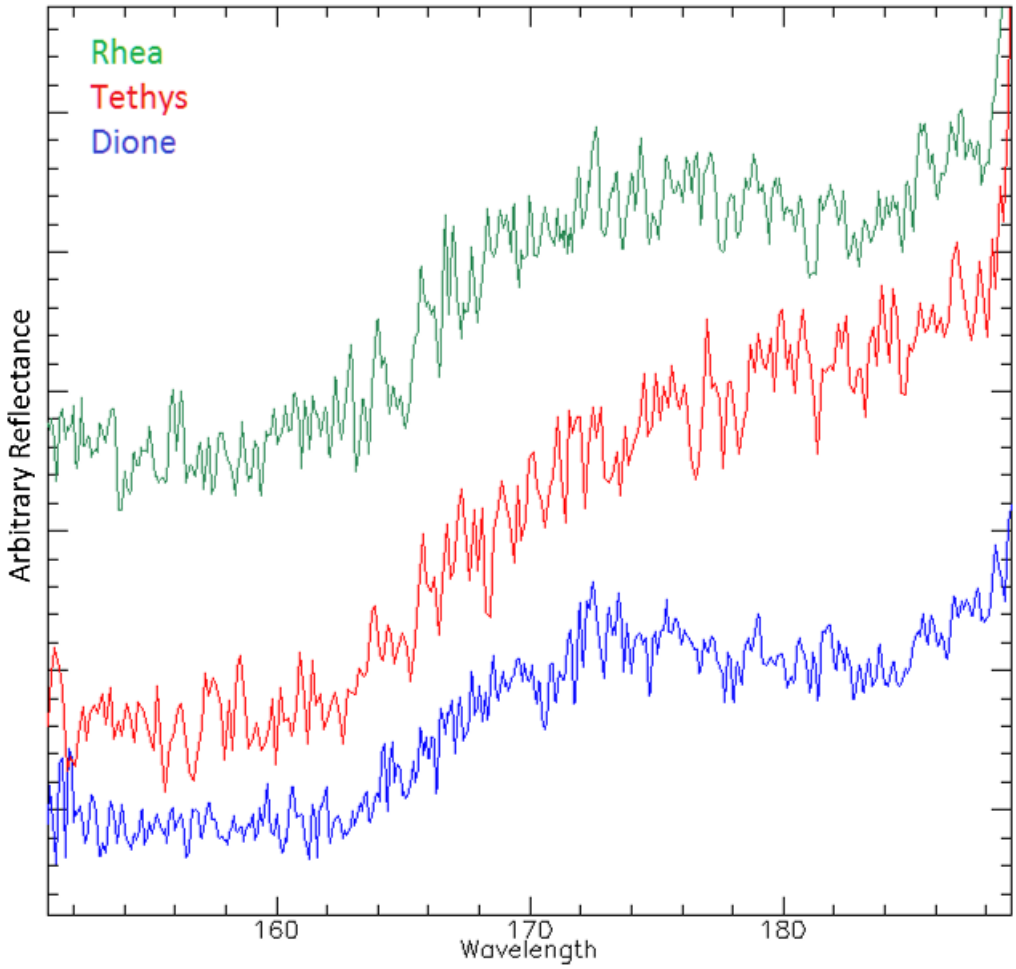

Figure 6.31: An example comparison of disk-resolved far-UV reflectance spectra of Rhea (green), Tethys (red), and Dione (blue). A Savitzky-Golay smoothing filter has been applied to each spectrum to reduce noise. The reflectance spectra in arbitrary units have been offset in the y-axis to facilitate a clear comparison between the UV absorption edge and the 184-nm absorption feature. Rhea and Dione show the strongest absorption from ~179 – 189 nm, while Tethys shows weaker absorption across the same wavelength. All three spectra show the steep 165-nm absorption edge due to water-ice.

All three spectra show the 165-nm absorption edge due to water-ice. Rhea (green) and Dione (blue) show a broad absorption feature centred near 184 nm, which can be explained by the presence of either hydrazine monohydrate or simple chloromethane molecules based on comparisons with laboratory ice sample measurements presented in Chapter 4. The 184-nm absorption is very weak (or non-existent) in the spectrum of Tethys trailing hemisphere (Figure 6.31, red spectrum). The same lack of absorption over the wavelength region of ~ 179 – 189 nm is seen in several other disk-integrated spectra of Tethys. This pattern of absorption centred near 184 nm is intriguing in that Dione is the icy

satellite that is furthest from Saturn's moon Titan. If the source of hydrazine originates from Titan's atmosphere, one might speculate that the two closer satellites Rhea and Dione would receive a higher amount of the material. The possibility that hydrazine could be transferred from Titan to Rhea and Dione is explored further in Chapter 7.

Modelled spectra based on laboratory absorbance measurements of tetrachloromethane (CCl_4) below H_2O ice, trichloromethane ($CHCl_3$) below H_2O ice and hydrazine monohydrate ($N_2H_4 \cdot H_2O$) were compared to UVIS spectra of Dione's leading and trailing hemispheres for ranges of about 4700 km, 37234 km, and 49000 km (Figure 6.32).

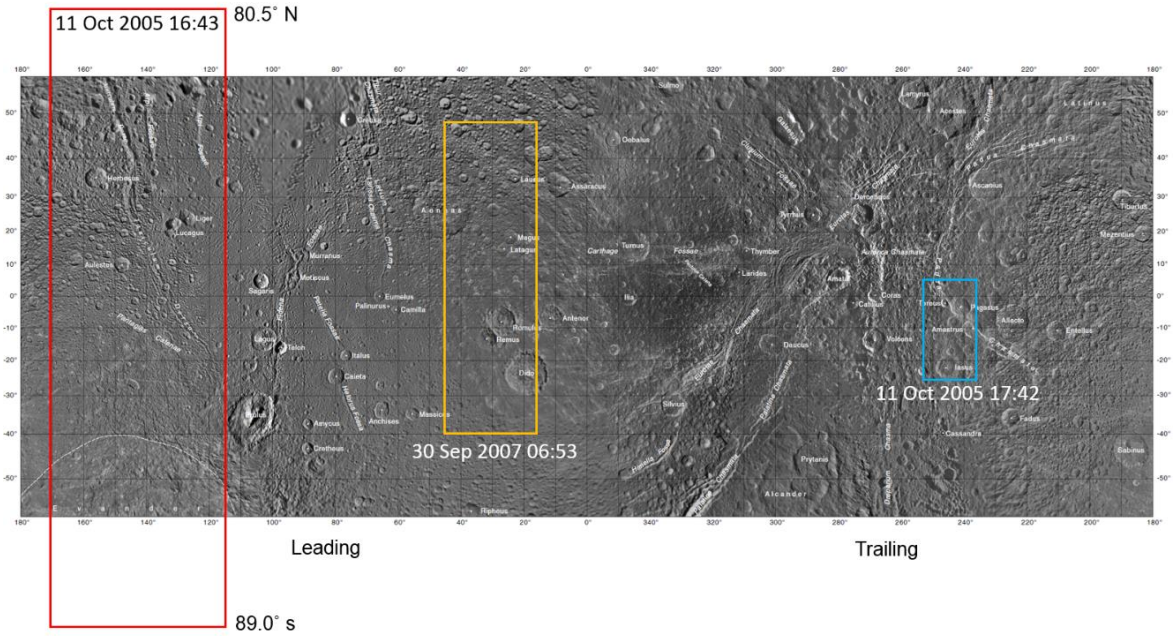

Figure 6.32: Cassini UVIS spectrometer field-of-views projected onto Dione's leading and trailing hemispheres. Due to the limited latitude coverage of the map of Dione, the instrument field of view for the observation carried out on 11 Oct 2005 extends beyond the map limits.

Similar to the case for Rhea, the absorption between ~179 and 189 nm can be explained by the possible presence of CCl_4 below a thin layer of water-ice, $CHCl_3$ below water-ice, or hydrazine monohydrate (Figures 6.33, 6.34 and 6.35). Since the differences between the modelled spectra are much less than the overall noise envelope of the UVIS data, the spectral ambiguity between the different molecules cannot be removed. It is

therefore possible that either of these chemical species could be present in the upper ice layers on Dione and Rhea.

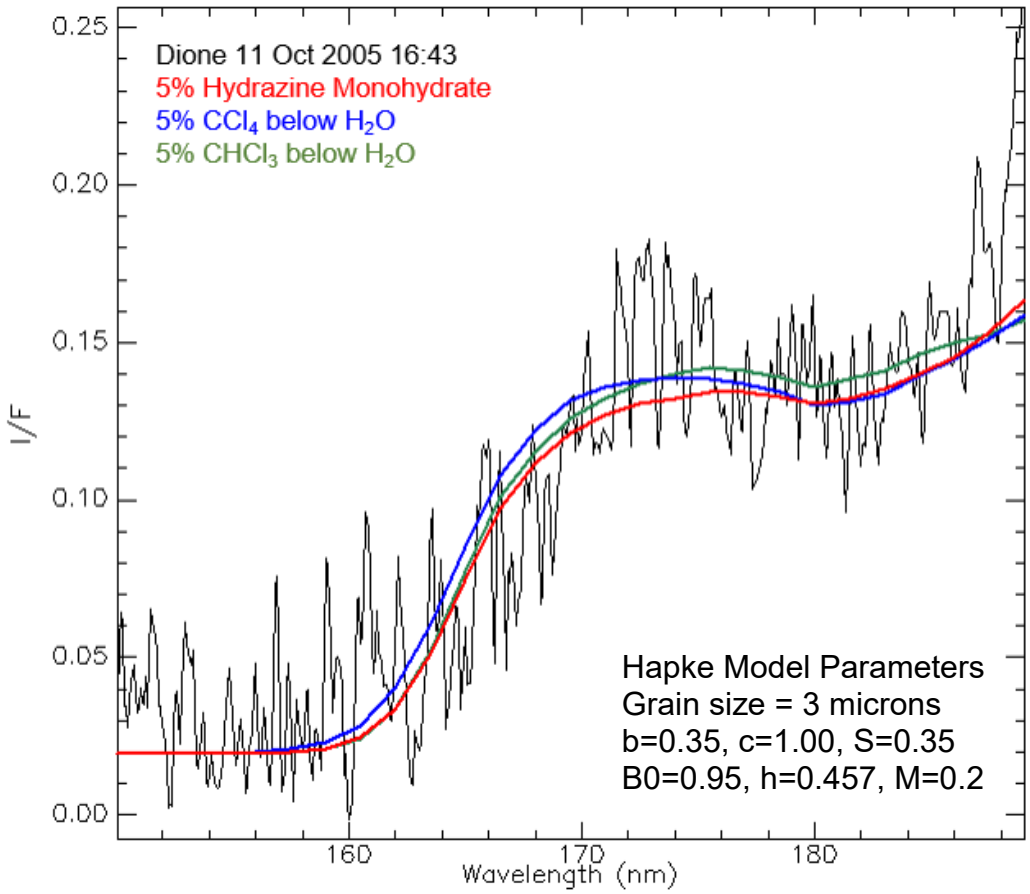

Figure 6.33: Model spectral fits to the Dione 11 Oct 2005 16:43 UT UVIS/FUV observation. The UVIS/FUV reflectance spectra were recorded on the leading hemisphere of Dione using the high-resolution slit state with an integration time of 30 seconds. The distance from Dione at the time of observation was 37234 km, and the phase angle was 22.1 degrees.

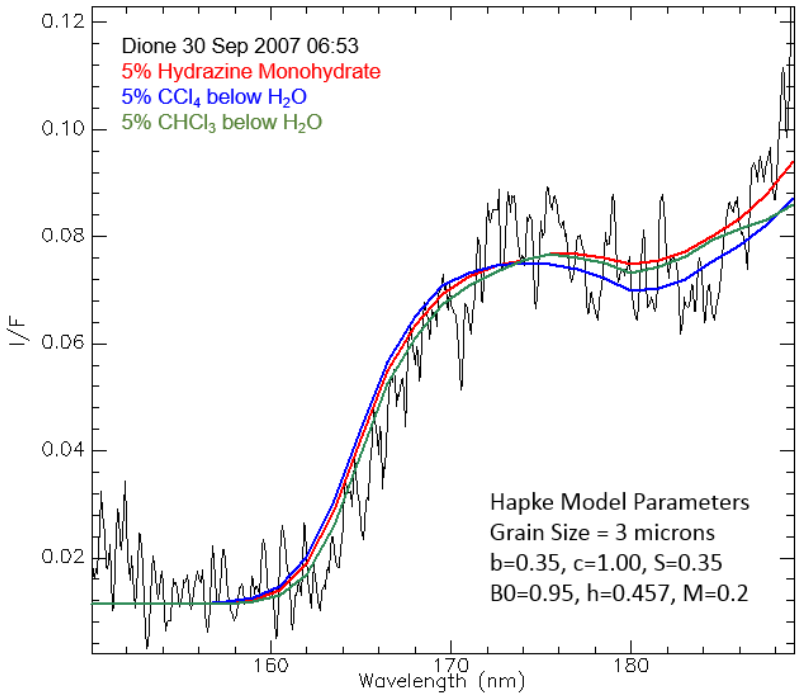

Figure 6.34: Model spectral fits to the Dione 30 Sep 2007 06:53 UT UVIS/FUV observation. The slit field of view covers Dione's leading hemisphere. The range from Dione was 49300 km, and the phase angle was 26.2 degrees.

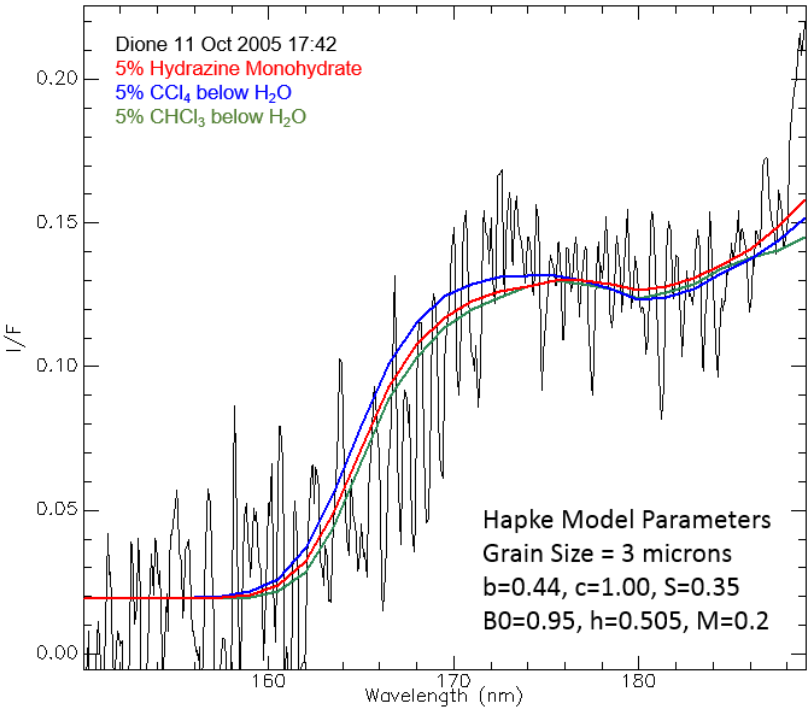

Figure 6.35: Model spectral fits to the Dione 11 Oct 2005 17:42 UT UVIS/FUV observation. The Dione spectrum was acquired over the satellite's trailing hemisphere at a range of 4700 km from the surface. The observation was carried out at a phase angle of 16 degrees, and the integration time was 30 seconds.

6.6: Summary

In Chapter 6, for the first time, results of a comparative analysis between spatially-resolved Cassini UVIS reflectance spectra with experimental data of ice samples for chemical species that are suspected to exist in the Saturnian system is presented. Spectral models are created using laboratory absorbance measurements of different ice mixtures in the far-UV, and Hapke theory. The model spectra are then compared with the Cassini UVIS spectra to determine which chemical species that are suspected to exist within the Saturnian system fit the observational data. The results of the comparative analysis show that the 184-nm absorption feature and the spectral slope of the 165-nm absorption edge due to water-ice observed in the UVIS spectra can be explained by the presence of simple chloromethane molecules or hydrazine monohydrate. It was not possible to remove the spectral ambiguity between these two chemical species due to the high noise level inherent in the Cassini UVIS data. However, it is possible to investigate which chemical species (hydrazine monohydrate or simple chlorine molecules) is likely to exist in the surface ices of Rhea and Dione by exploring the various chemical pathways that lead to their formation, as well as their source (or sources). Chapter 7 discusses the possible chemical pathways for the formation of simple chlorine molecules and hydrazine and their potential sources. The chapter concludes by examining the scientific implication of the potential discovery of a new chemical species in the Saturnian system.

CHAPTER 7

SCIENTIFIC IMPLICATIONS AND DISCUSSION OF RESULTS

7.1 Scientific Implications of the Possible Detection of Hydrazine Monohydrate on Rhea and Dione

The production of hydrazine monohydrate is easier to explain than the presence of any chlorine containing derivatives as it can be produced in chemical reactions involving water-ice and ammonia (Loeffler and Baragiola, 2010), or possibly delivered from Titan's nitrogen-rich atmosphere where the compound could be synthesised (Zheng *et al*., 2008). However, one possible source of hydrazine is contamination of the UVIS data by the hydrazine propellant from the Cassini spacecraft.

7.1.1 Does Hydrazine signal come from space craft propellant contamination?

Reviewing the mission files showed that the hydrazine thrusters did not fire at the time of the UVIS observations. However, hydrazine could remain as a possible contaminant around the space craft or even on the spectrometer optics, in which case this 184 nm feature should be seen in ALL far-UV spectra. However, disk integrated spectra acquired from Tethys show no indication of absorption near 184 nm (Figure 7.1). The Tethys spectra only show the H_2O absorption edge in the FUV near 165 nm. A spectrum of Enceladus during 2007 (Hendrix *et al*. 2010) also shows no absorption near 184 nm. Furthermore, a calibration UVIS/FUV spectrum was obtained of the star epsilon CMa during the T41 I occultation on February 23, 2008 (Koskinen, *et al*. 2011). The spectrum shows no indication of the broad absorption feature seen between ~179 and 189 nm in spectra of Rhea and Dione. This

decreases the likelihood that the 184-nm absorption feature is the result of contamination by the Cassini hydrazine thrusters.

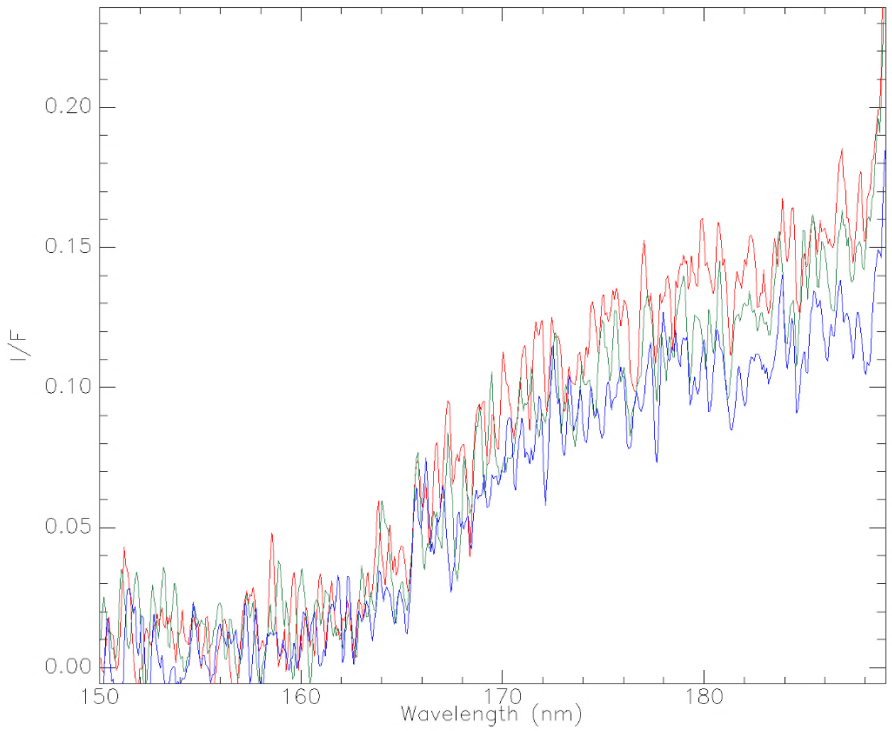

Figure 7.1: Cassini UVIS/FUV disk-integrated spectra of the trailing hemisphere of Saturn's icy satellite Tethys acquired during 2015. The observations were collected near a phase angle of ~29 degrees. All three spectra are dominated by water-ice as indicative of the steep far UV drop-off between ~160 and 170 nm. None of the spectra show the presence of the 184-nm absorption feature that is seen in UVIS/FUV spectra of Rhea and Dione.

7.1.2 Can hydrazine monohydrate be synthesised on Rhea and Dione?

The presence of hydrazine monohydrate on Rhea and Dione raises some interesting possibilities, as the molecular compound is a strong reducing agent. Large impacts onto the surfaces of these two icy satellites could raise the temperature to the point where nitrogen oxides are released through the process of molecular decomposition. Various functional groups can be reduced by hydrazine, including nitro groups, alkenes, and carbonyl molecules. The possible detection of hydrazine on Rhea and Dione is also important in that many hydrazine-based salts are soluble in water. If these salts are present in the deep interiors of Rhea and Dione, they could act to depress the freezing point of a water-

hydrazine salt solution (hydrazine hydrate has a melting point of 221.65 K; Singanahally, T. A. and Patil, K. C., 2014). Hydrazine salts can form when hydrazine hydrate is neutralised with an acid. The presence of ammonium salts in a solution of water and hydrazine in the deep interiors of Rhea and Dione can also lead to the production of hydrazine-based salts. The most significant difference between hydrazine and ammonium-based salts lies in the low reducing potential of ammonium salts and the fact that hydrazine salts have a lower thermal stability than ammonium salts. Apart from these two differences, hydrazine salts resemble ammonium salts, and this is why hydrazine-base salts are also soluble in water (Singanahally, T. A. and Patil, K. C., 2014).

The presence of hydrazine monohydrate (N_2H_4) on Rhea may also provide an explanation why ammonia (NH_3) was not detected by UVIS in the icy top layer of Rhea's surface. It is already known that irradiation of water-ice molecules by ions from Saturn's magnetosphere produces radicals, such as OH, O, H, and HO_2, which are unstable (Cooper *et al*. 2007). The irradiation of water-ice also leads to stable molecules, including O_2, H_2, and hydrogen peroxide (H_2O_2). Hydrogen peroxide, although it might exist on Rhea is not observable since it has a far-UV spectral signature that is located lower than 165 nm where water-ice dominates the UV absorption. In contrast, irradiation of ammonia ice leads to the breakup of NH_3 molecule into H_2 and N_2 via chemical pathways involving radicals of NH, H, and NH_2. Small amounts of HN_3, N_2H_2, and hydrazine (N_2H_4) are also produced. Lyman alpha photons with an energy of 10.2 eV (121.6 nm) can also irradiate solid ammonia ice, dissociating the molecule leading to the production of NH_2 and N_2H_4 (hydrazine) (Zheng *et al*., 2008).

A possible chemical pathway to the formation of hydrazine is illustrated by the following chemical reactions (adapted from Zheng *et al*., 2008):

$$H_2O + h\nu \rightarrow H + OH$$
$$H_2O + h\nu \rightarrow H_2 + O$$
$$NH_3 + OH \rightarrow NH_2 + H_2O$$
$$NH_2 + O \rightarrow NH + OH$$
$$NH + NH \rightarrow N_2H_2$$
$$\rightarrow N_2 + H_2$$
$$N_2 + 2H_2 \rightarrow N_2H_4$$

The destruction rate of any hydrazine produced on Rhea is governed by the number of radicals via the chemical pathway (adapted from Zheng *et al*., 2008):

$$N + H_2H_4 \rightarrow N_2H_3 + H_2$$
$$N_2H_4 + NH_2 \rightarrow N_2H_3 + NH_3$$

The main difficulty of this scenario is explaining the source of ammonia on Rhea and the extremely slow reaction rates at T = 70 K. The presence of minor amounts of ammonia mixed with water ice can lead to the production of hydrazine detected by UVIS through the chemical pathway where H_2O_2 (hydrogen peroxide) is produced from irradiation of water-ice molecules by charged particles originating from Saturn's magnetosphere. The source of ammonia could be primordial (Mandt, K. E. *et al*. 2014), incorporated into the interior of Rhea during its formation. The ammonia could also originate from a deep subsurface aqueous layer (i.e. endogenic source). This could explain the wide distribution of hydrazine across Rhea's surface. On the other hand, if Rhea is a uniform mixture of rock and ice (undifferentiated), then minor amounts of ammonia may be present over a large percentage of the satellite's surface. This would also explain why hydrazine appears to be present over a geographically wide area as sampled by the UVIS observations over Rhea's surface.

Laboratory experiments involving the irradiation of ammonia ice were carried out to determine if it is possible to observe the formation of hydrazine (Zheng *et al*. 2008). Zheng and his team irradiated ammonia ice over a temperature range 10 – 60 K in the lab. Their IR spectrum during irradiation of the ammonia did not show the absorption bands

from hydrazine (N_2H_4) because of interference from overlapping ammonia features in the measured spectrum. However, during the warm-up phase of the experiment, absorption features due to hydrazine became visible in the IR spectrum (Figure 7.2).

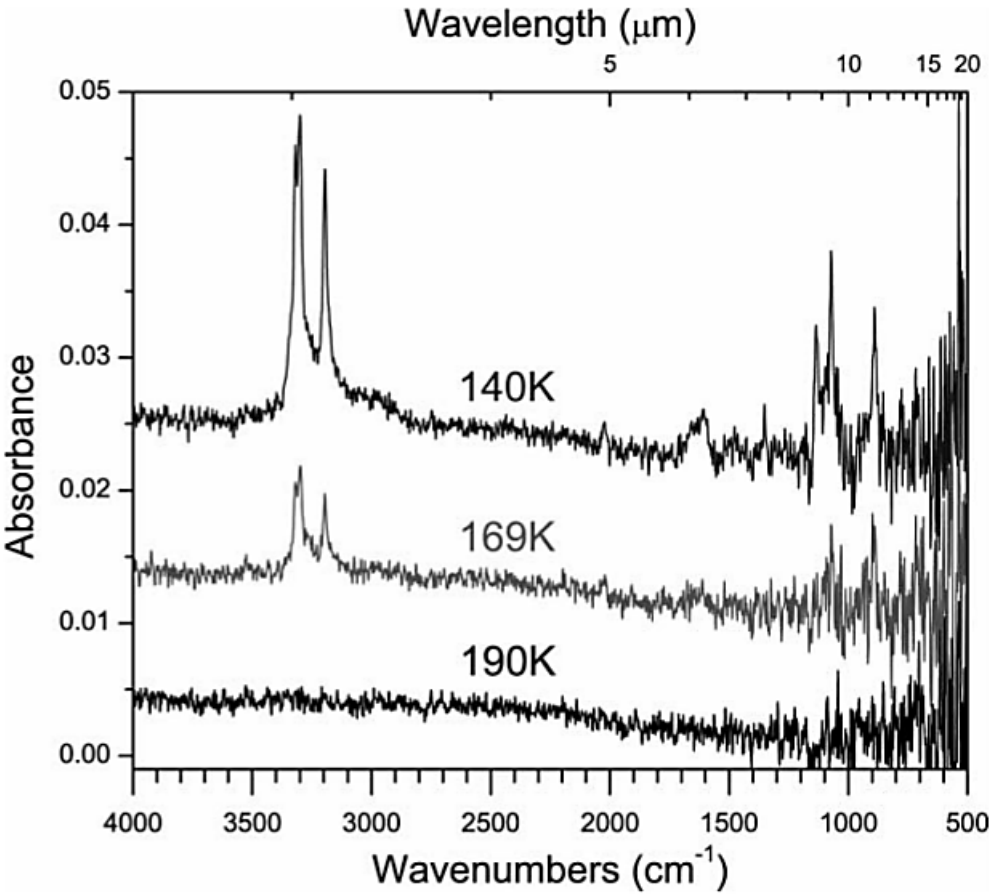

Figure 7.2: Evolution of absorbance features due to hydrazine (N_2H_4) during the warm-up phase of ammonia irradiation experiments carried out by Zheng et al. (2008). Two strong absorbance peaks due to hydrazine are seen at wavelengths of 3310 cm-1 (3.021 microns) and 3200 cm-1 (3.125 microns).

The appearance of the previously masked hydrazine absorbance peaks can be explained by the sublimation of ammonia in its solid phase. As the ammonia sublimates, the strength of the hydrazine bands increases, up to the point where all of the molecular compound has been sublimated. The IR spectra measured by Zheng *et al*. (2008) collected after the irradiation phase shows absorbance peaks of hydrazine at wavelengths of 4.926, 6.238, 8.881, 9.381, and 11.848 microns, in addition to two strong peaks at 3.021 and 3.125 microns. The absorption bands are due to the rocking, stretch, and deformation

modes of the hydrazine molecule (Table 7.1). The laboratory experiments conducted by Zheng and his team illustrate that it is possible to produce hydrazine via radiolysis of solid ammonia. Thus, if ammonia is present within the surface ice of Rhea, it could explain the possible presence of hydrazine monohydrate on Rhea.

Table 7.1: IR Absorption Features for Hydrazine (N_2H_4) from Literature and Experiments Involving Hydrazine Production from Solid Ammonia

Species	Literature (μm)	Experiment (μm)	Feature
N_2H_4	11.31	11.24	ν_6; NH_2 rock
N_2H_4	9.38	9.33	ν_{12}; NH_2 rock
N_2H_4	8.88	8.80	ν_5; N-N stretch
NH_2	6.67	6.61	Photodissociation product of NH_3
N_2H_4	6.24	6.23	ν_3; NH_2 deformation
N_2H_4	3.13	3.13	ν_2; NH_2 symmetrical stretch
N_2H_4	3.02	3.03	ν_1; NH_2 asymmetrical stretch
N_2H_4	3.02	3.01	ν_8; NH_2 asymmetrical stretch

References. Literature values for hydrazine taken from Durig *et al*. 1966. Experimental values for N_2H_4 and NH_2 are from Zheng *et al*. 2008. Literature values for NH_2 taken from Milligan & Jacox 1965.

There are also several processes that can reduce the production rate or prevent the synthesis of hydrazine within the upper surface ice layer of Rhea. Since water-ice is most likely to host solid ammonia ice, the probability of UV photons with energy 10.2 eV (121.6 nm) or less of destroying NH_3 decreases. This is due to the strong absorption of the Lyman-alpha photons by the water-ice matrix. This scenario applies for the case where the ammonia is located beneath the water-ice, and a photon path length short enough to allow sampling by UV/IR spectroscopy. Other impurities, such as hydrazine or chlorine may also be shielded against destruction by UV photons beneath a thin layer of water-ice. Lower energy (<6.05 eV or <205 nm) radiation, however, can penetrate further into the surface ice layer, with the potential to destroy any underlying impurities, such as NH_3, chlorine and hydrazine molecules. Instability due to longer wavelength photons may therefore explain why no ammonia has been detected on Rhea over the wavelength range sampled by the Cassini UVIS instrument. Ammonia could, in theory, be more stable if it exists on

icy satellites in the form of a hydrate mixture - i.e. ammonia in the form of a hydrate minimises the energy in thermodynamic equilibrium. The concentration of any hydrazine synthesised in chemical reactions between NH_3 and H_2O depends on several factors, including the dissociation rate of ammonia by energetic electrons from Saturn's magnetosphere, localised heating due to micrometeoroid bombardment. Localised heating tends to bring fresh NH_3 to the surface, where it is susceptible to destruction by radiolysis. Destruction of NH_3 by sublimation due to localised heating can also occur, since ammonia is more volatile than water-ice. An alternative source for the possible production of hydrazine in monohydrate form is examined in section 7.7.1.

Any N_2 and H_2 formed on Rhea by the irradiation of energetic particles from Saturn magnetosphere, in addition to minor abundances of NO and N_2O might become trapped with the surface ice at defect points. The amount of H_2 and N_2 produced, trapped within the ice, and removed, should be dependent on the degree of sputtering. There may be a temperature dependence to consider for the sputtered molecular hydrogen, as the efficiency at which water-ice traps H_2 molecules may be temperature dependent.

The process of dimerization is a chemical reaction involving two monomers, which react to form a dimer. Radiolysis of ammonia ice leads to the dissociation of the molecule into N_2 and H_2 through a series of intermediate chemical reactions involving the radicals N, NH, and NH_2. These reactions also produce minor amounts of NH_2NH_2 and HN_3. If ammonia (NH_3) is not present at the surface of Rhea, then it may indicate that hydrazine monohydrate (N_2H_4) is not destroyed via radiolysis, since reactions of hydrazine with radicals (including NH_2) can lead to the destruction of hydrazine through the chemical reaction $NH_2 + N_2H_4 \rightarrow NH_3 + N_2H_3$.

To summarise, the presence of minor amounts of ammonia ice on Rhea could play a key role in explaining the possible detection of hydrazine monohydrate based on an analysis of Cassini UVIS data. There are chemical pathways involving water-ice and

ammonia that can lead to the production of hydrazine in an environment where Rhea's surface layers are bombarded by energetic electrons and ions originating from Saturn's magnetospheric plasma. Water ice molecules are dissociated when they are irradiated with 5-250 eV electrons (Johnson *et al*. 2005). This leads to the production of unstable radicals, including H, O, OH, and HO_2. The irradiation of the water-ice also results in the production of stable molecular products, including H_2O_2, O_2, and H_2. Irradiation of any ammonia molecules present in the ice mixture leads to the production of N_2 and H_2 through chemical pathways involving the radicals H, NH, and NH_2. The irradiation of ammonia ice also produces the transient products N_2H_2, HN_3, and hydrazine (N_2H_4). The hydrazine produced in these reactions may not be stable due to dissociation by radiolysis to reform N_2 and H_2. Furthermore, the products formed in the chemical reactions leading to the production of hydrazine can collide with surrounding molecules in the solid phase ice to reform the original molecules. The production radiation yield (defined as the number of products produced by 100 eV of deposited energy) of hydrazine may be therefore be several times smaller than the case for free molecules. As the temperature increases the production yield should increase, so the abundance of hydrazine should vary as a function of latitude on Rhea. The yield increase with increasing temperature is due to an increase in the pliability of the molecular "matrix or cage" (i.e. the surrounding molecules).

7.1.3 Does Hydrazine Originate from Saturn's Largest Moon Titan?

Titan is Saturn's largest moon and orbits the planet at ~20 Saturnian radii, with an orbital period of 15.945 days (JPL Horizons; https://ssd.jpl.nasa.gov). The satellite's most notable feature is its thick atmosphere, dominated by molecular nitrogen (~98.4%) with minor amounts of hydrocarbons, including methane (CH_4). Solar UV photons dissociate methane in Titan's atmosphere, leading to the production of more complex hydrocarbon molecules. Based on results from the Cassini-Huygens probe, Titan appears to have

ammonia (NH_3) on its surface. The ammonia may originate from cryovolcanic activity (Lopes 2007). The original source of the nitrogen on Titan could be from shock chemistry resulting from impacts. The shock induced chemistry converts the accreted ammonia (which occurred during Titan's formation) into N_2 (Jones and Lewis, 1987). If Titan was warmer in the past (>150 K), its vapour pressure of NH_3 would have been higher and photolysis of NH_3 could then lead to the formation of N_2.

Irradiation of ammonia by solar UV photons could lead to the formation of hydrazine in Titan's atmosphere. The chemical pathway leading to the production of hydrazine from irradiation of ammonia is described as follows: $NH_3 \rightarrow NH_2 + H$. In this reaction, NH_2 is an amino radical and NH_3 is ammonia. The two amino radicals can then react chemically to form hydrazine. The production rate of N_2 observed in Titan's atmosphere could be increased as a result of chemical reactions involving hydrazine and hydrocarbon radicals. If "R" denotes the hydrocarbon radical, then the following chemical pathway leads to the production of molecular nitrogen on Titan: $R + N_2H_4 \rightarrow N_2H_3 + RH$. The hydrazyl radical (N_2H_3) is then dissociated by UV photons, producing N_2H_2 and H. The diazene (N_2H_2) reacts with a hydrocarbon radical to form N_2H and RH. Photodissociation of N_2H then leads to the production of N_2 and H, with the H atom escaping Titan's atmosphere. The whole chemical pathway can be summarised in the following chemical reactions (Zheng *et al*. 2008):

$$4NH_3 + 4h\nu \rightarrow 4NH_2 + 4H$$
$$2NH_2 + 2NH_2 \rightarrow 2N_2H_4$$
$$2N_2H_4 + 2H \rightarrow 2N_2H_3 + 2H_2$$
$$N_2H_3 + N_2H_3 \rightarrow N_2H_4 + N_2 + H_2$$

It is assumed that these reactions take place under the presence of an inert molecule that allows for conservation of energy and momentum. These chemical reactions can be expressed in the form of the following net reaction (Zheng *et al*. 2008):

$$4NH_3 + 4h\nu \rightarrow N_2 + N_2H_4 + 3H_2 + 3H$$

The main difficulty with these reactions is their extremely low reaction rates at temperatures encountered on the surface of Rhea.

The efficiency of this chemical pathway on Titan should depend on the temperature, which determines the rate at which molecular nitrogen is produced in Titan's atmosphere. Thus, hydrazine could be produced in Titan's atmosphere from irradiation of ammonia, and hydrazine could accelerate the production of N_2 observed in its atmosphere. If hydrazine does exist on Titan, then future space probes or space-based telescopes equipped with infrared spectrometers may be able to detect its presence.

7.1.3.1 Could Hydrazine on Rhea Originate from Titan's Upper Atmosphere?

Although it is theoretically possible that hydrazine (N_2H_4) could be produced by irradiation of ammonia on Titan, there is still the question of whether or not the molecule could be ejected from Titan. To explore this question the Jeans escape mechanism (Shizgal and Arkos, 1996) was considered as a possible process for ejecting hydrazine from Titan. To determine the loss rate, the Maxwell-Boltzmann distribution was integrated above the escape velocity from Titan's exobase:

$$nf(v)dv = \frac{4n}{\sqrt{\pi}}\left(\frac{m}{2kT}\right)^{3/2} v^2 \exp\left(-\frac{mv^2}{2kT}\right)dv \quad (7.1)$$

Here *n* represents the total number density of the constituent being considered, and the escape flux is then

$$\Phi_{esc} = \int_{v_e}^{\infty} \Phi\, dv = \frac{n_{exob}}{\sqrt{\pi}}\left(\frac{m}{2kT}\right)^{3/2} \int_{v_e}^{\infty} v^3 \exp\left(-\frac{mv^2}{2kT}\right)dv$$

$$x = v^2,\ dx = 2vdv \quad (7.2)$$

$$\Phi_{esc} = \frac{n_{exob}}{\sqrt{\pi}}\left(\frac{m}{2kT}\right)^{3/2}\left(\frac{kT}{m}\right)\left(v_e^2 + \frac{2kT}{m}\right)\exp\left(-\frac{mv_e^2}{2kT}\right)$$

In other words, the probability function is integrated for all molecules moving upwards at a speed that is greater than the escape velocity from Titan's exobase. Particles of given mass that populate the high-energy tail of the Maxwell velocity distribution at Titan's exobase (where the scale height equals the mean free path) escape. The Jeans escape mechanism described here assumes that there is no evaporative cooling taking place at Titan's exobase, and that there are no distortions in the velocity distribution function.

The results of the integration imply a residence time for hydrazine molecules of 7.1×10^{18} yr. This timescale is much greater than Titan's age, and thus Titan would hold on to any hydrazine that is produced in its atmosphere. For N_2, the residence time based on a similar integration of the Maxwell-Boltzmann distribution is 6.2×10^{15} yr. This timescale is also much greater than the age of Titan. Thus, the Jeans escape mechanism cannot remove hydrazine or molecular nitrogen from Titan's upper atmosphere. This agrees with the fact that the flux rate based on Jeans escape decays exponentially with the mass of the particle. Thus, Jeans escape does not play a significant role on Titan for molecules with masses equal to or heavier than molecular nitrogen. Therefore, an alternative escape processes must be considered as a source of hydrazine and/or nitrogen from Titan, including photochemical escape augmented by "sputtering." Sputtering is a non-thermal process that is an effective escape mechanism on small solar system bodies (e.g., Titan, Mars …) that have no inherent magnetic fields. Sputtering is the ejection of atoms/molecules from planetary surface upon impact from high-energy charged particles. Energetic ions deposit their energy in a planetary "regolith", which causes a cascade of events that leads to the ejection of atoms or molecules from the surface – i.e. the process is based on momentum transfer collisions with atoms in the surface, and by electronic excitation of atoms or molecules (Johnson and Leblanc, 2001).

So it is possible that N_2 (or the heavier molecule N_2H_4) is ejected from Titan's atmosphere via sputtering. Experiments conducted by DeLaHaye *et al*., 2007) lead to a

sputtering rate for N_2 on Titan of ~3.6×10^{28} amu/s (59.78 kg/s). Thus, over a geological timespan of 4 Gyr, the amount of N_2 ejected from Titan's atmosphere due to sputtering would be ~7.5×10^{18} kg or 5.6×10^{-5} Titan masses. The total mass of N_2 (or N_2H_4, since H_4 does not add a significant atomic mass to the hydrazine molecule) that Rhea could accumulate as it orbits Saturn would be equivalent to the typical mass of some of the more massive asteroids. It should be noted, however, that the above estimate assumes that N_2 or N_2H_4 has existed in Titan's atmosphere over the last 4 billion years and that it is destroyed before being accumulated onto Rhea's surface.

7.1.4 A Search for Hydrazine in Cassini CIRS Spectra of Titan's Atmosphere

The production of hydrazine via photolysis/radiolysis of ammonia described in the laboratory experiments performed by Zheng *at al*. 2008 raise the possibility of detecting the molecular compound in Titan's atmosphere. Cassini's Composite Infrared Spectrometer (CIRS) (Jennings *et al*. 2017) was a high-resolution (0.5 – 20 cm^{-1}) Fourier Transform spectrometer designed capture infrared energy over a wavelength range of 10 to 1400 cm^{-1} (1000 to 7 microns). This wavelength range covers the IR transitions for hydrazine (N_2H_4) described in the experimental results by Zheng *et al*. (2008). The IR transitions in hydrazine result from various deformation, stretch and rock modes of NH_2. These ro-vibrational modes occur at 3.02, 3.13, 6.23, 8.80, 9.33, and 11.24 microns (Zheng *et al*. 2008). The last four IR transitions fall within the range of the Mid-IR channel on the CIRS instrument (Focal Plane 3: 9-16.7 microns, Focal Plane 4: 7-9 microns). Fully calibrated Cassini CIRS spectra were therefore obtained through the Planetary Data System (PDS) archive in an attempt to search for hydrazine in Titan's atmosphere. All spectra were collected at a spectral resolution of 0.5 cm^{-1} (~0.0062 microns or 6.2 nm at a central wavelength of 11 microns). The wavenumber units of the CIRS spectra were

converted to units of microns in order to search for the aforementioned hydrazine IR transitions described in experiments carried out by Zheng *et al*. (2008).

Simulated CIRS spectra were produced using NASA's Planetary Spectrum Generator (Villanueva *et al*. 2018), which is based on the Planetary and Universal Model of Atmospheric Scattering. Figure 7.3 shows how the visibility of the hydrazine ν_5 N-N stretch mode (near 8.8 microns) changes as a function of the concentration of hydrazine (N_2H_4) in the atmosphere of Titan. The simulated infrared spectra assumed a limb geometry observation at an altitude of 200 km using a spectral resolution of 6.2 nm. The composition of Titan's atmosphere is set at 98.4 percent N_2, 1.4 percent CH_4, 7 ppmv C_2H_6, and two different concentrations (1 and 10 ppmv) of hydrazine (N_2H_4).

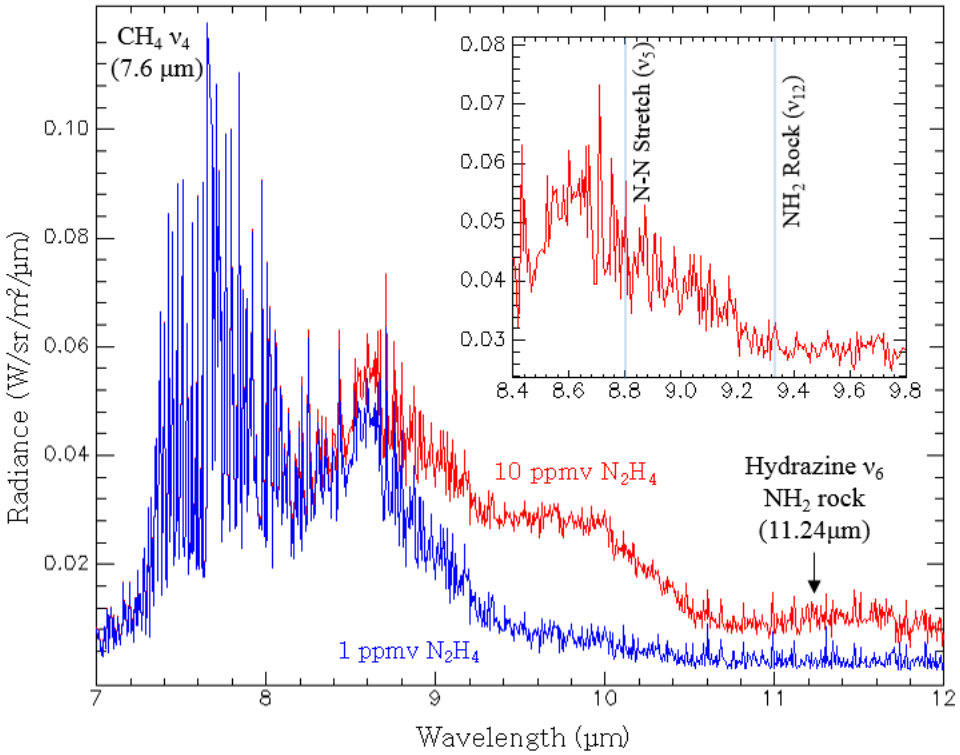

Figure 7.3: A synthetic spectrum of Titan's atmosphere produced using a limb geometry observation at an altitude of 200 km. The simulation used gas concentration of 98.4 percent N_2, 1.4% methane, 7 ppmv C_2H_6, 2.5 ppmv acetylene, and 1.0 ppmv (blue spectrum) and 10 ppmv (red spectrum) H_2N_4 (hydrazine). The spectrum is dominated by the presence of methane (CH_4), and shows the change in emission between 1 ppmv and 10 ppmv N_2H_4. There is a very subtle change in emission near 11.24 microns, at the location of the NH_2 rock band of hydrazine.

The synthetic IR spectrum in Figure 7.3 shows strong emission due to the ν_4 7.6-micron band of CH_4.. Differences between the two spectra are noted over the wavelength range ~9 to 12 microns. It is interesting to note that near the locations of the hydrazine N-N stretch (ν_5), NH_2 rock (ν_{12}), and NH_2 rock (ν_6) bands, there are distinct emission features visible in the simulated spectra. The same type of weak emission features (described below) are also noted in real CIRS spectra of Titan's upper atmosphere at the same wavelength locations.

Using information gained from the synthetic IR spectra, hydrazine was searched for in Cassini CIRS spectra of Titan's atmosphere. The spectra were collected in a limb geometry mode at a tangential altitude of approximately 200 and 300 kilometres. The spectra shown in Figure 7.4 were acquired using the FP3 at 30˚ N latitude at the limb near a tangential altitude of 200 km at a spectral resolution of 0.5 cm^{-1} (6.2 nm).

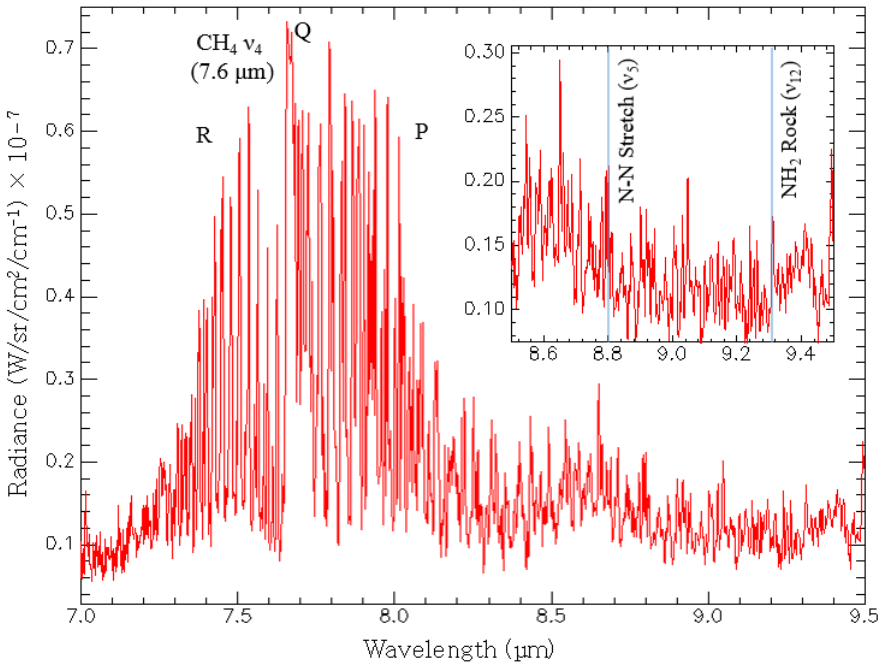

Figure 7.4: A Cassini CIRS spectrum of Titan's atmosphere acquired at a tangential altitude of 200 km in a limb mode geometry. The spectral resolution is 6.2 nm. The spectrum is dominated by the 7.6-micron band of methane. The blue horizontal lines in the inset mark the locations of the N-N stretch (~8.80 μm) and NH_2 rock mode (~9.33 μm) bands of hydrazine.

Similar to the case for the simulated CIRS spectra (Figure 7.3), the observed spectrum is dominated by the ro-vibrational transitions due to the methane (CH_4) 7.6 ν_4 band. The locations in wavelength space of the hydrazine N-N stretch (ν_5) and NH_2 rock (ν_{12}) are marked by the vertical blue lines in the inset plot. It is interesting to note that there are two spikes in the spectra at these locations. However, no claim of hydrazine detection has been made, as these features in the spectrum could be due to other hydrocarbons in Titan's atmosphere. The 8.8-micron N-N stretch band of hydrazine would be difficult to observe due to contamination of the nearby 7.6-micron absorption band of methane.

Figure 7.5 shows another CIRS spectrum over the same wavelength region and spectral resolution of the previous spectrum, but at a higher tangential altitude of 300 km.

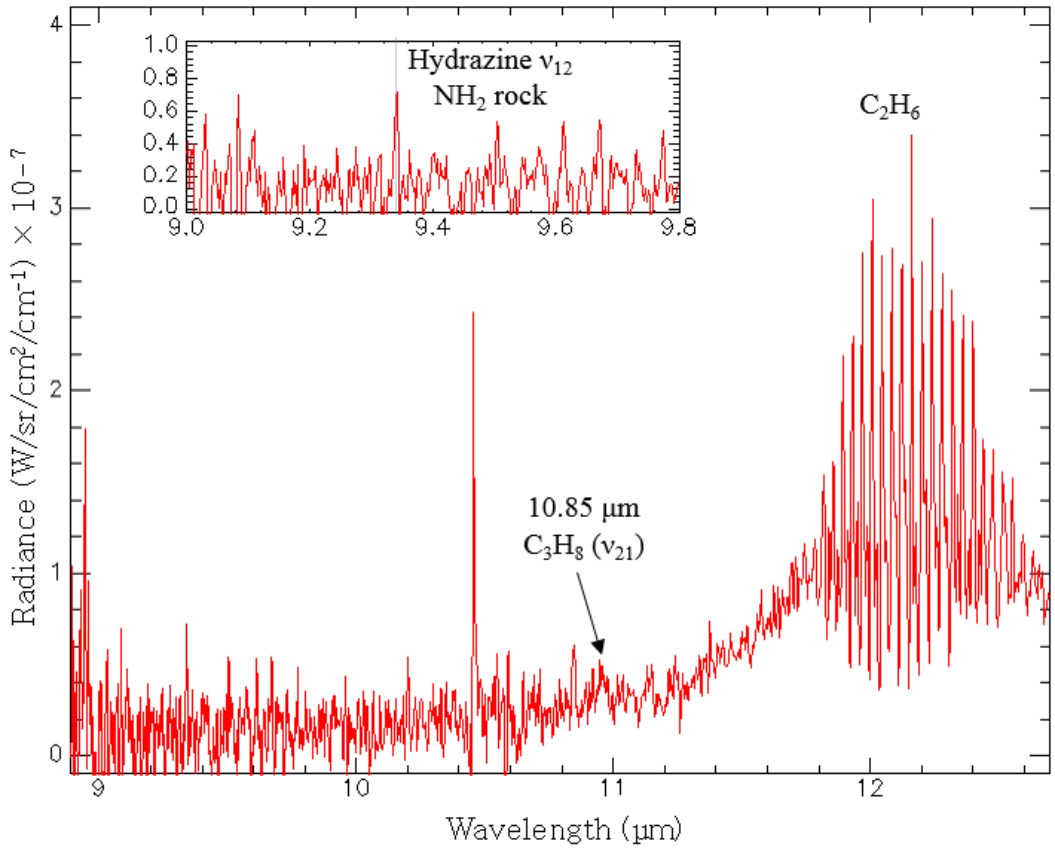

Figure 7.5: A Cassini CIRS spectrum of Titan's atmosphere acquired at a tangential altitude of 200 km in a limb mode geometry. The spectral resolution is 6.2 nm. The spectrum is dominated by the 7.6-micron band of methane. The blue horizontal lines in the inset mark the locations of the N-N stretch (~8.80 μm) and NH_2 rock mode (~9.33 μm) bands of hydrazine.

The spectrum is dominated by CH_4 emission in Titan's upper atmosphere, and the same two spike features occur near the locations of the hydrazine N-N stretch and NH_2 rock bands. The close proximity of the N-N stretch band of hydrazine to methane prevents a reliable detection. In contrast, the NH_2 rocks bands of hydrazine located near 9.33 and 11.24 represent the best features to conduct a search. Figure 7.6 shows a Cassini CIRS spectrum of Titan's extended atmosphere acquired in limb geometry mode with a tangent height of ~115 km. The spectrum covers the wavelength range from 7 to 9.5 microns, including the region where the 8.8-micron and 9.33-micron bands of hydrazine are located.

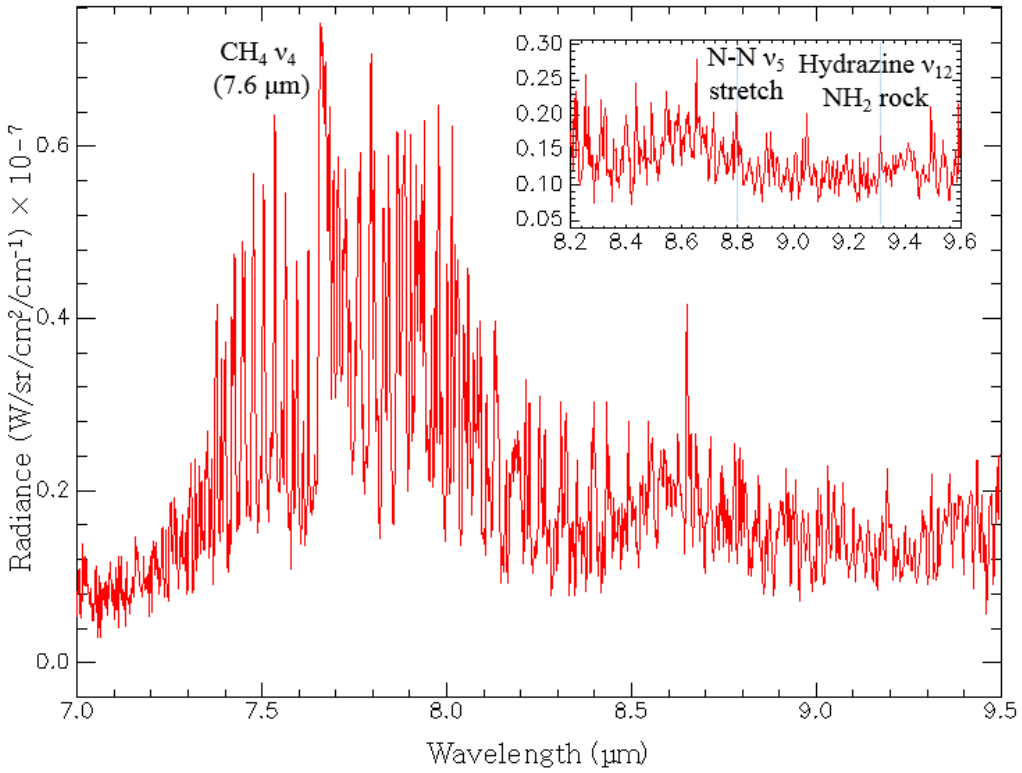

Figure 7.6: A Cassini CIRS spectrum of Titan's atmosphere acquired at a tangential altitude of 115 km in a limb geometry mode. The spectral resolution is 6.2 nm. The IR spectrum is dominated by the 7.6-micron CH_4 band. Two emission spikes are located near the hydrazine N-N stretch (8.8 microns) and NH_2 rock (9.33 microns) bands, which were observed during the warm-up phase of laboratory experiments carried out by Zheng et al. (2008).

The synthetic and observed Cassini CIRS spectra show that the detection of hydrazine in Titan's atmosphere is possible given the spectral resolution and wavelength coverage of the instrument. However, several of the hydrazine bands are located in close

proximity to strong hydrocarbon bands (e.g. CH_4), making their detection problematic. Several sharp emission features are noted at the locations of the hydrazine N-N stretch and NH_2 rock transitions.

Assuming hydrazine can be synthesised in the atmosphere of Titan, there are several factors that would govern the amount that could be produced. For example, if the temperature drops below the condensation point of hydrazine (N_2H_4), it would snow out of the atmosphere. In contrast, if the temperature is high enough, large amounts of water vapour could exist (Cottini *et al*. 2012) and UV photolysis of H_2O molecules would produce OH radicals. The OH radicals react with NH_2 produced by photolysis of ammonia, thus limiting the formation of hydrazine. Thus, it is the temperature that plays an important role in determine the concentration of hydrazine in Titan's atmosphere. Furthermore, if ammonia is not present on Titan, then there is no chemical pathway to its production and one would not expect to detect its presence in Cassini CIRS spectra. In this case, the weak emission line features seen in the CIRS spectra (Figures, 7.4, 7.5 and 7.6) are most likely due to other hydrocarbons in Titan's atmosphere.

7.1.5 A Search for Hydrazine in Cassini CIRS Spectra of Rhea's Icy Surface

The potential detection of hydrazine monohydrate on Rhea in the far-UV (Chapters 5 and 6) has raised the question of whether hydrazine (or NH_2) could be detected using data returned from the Cassini Composite Infrared Spectrometer (CIRS). Since the 7.6-micron bending mode band of methane (CH_4) lies within the spectral range (7.2 – 9.1 microns) of the CIRS focal plane 4 (FP4), it was decided to use the CIRS focal plane 3 (FP3). The CIRS FP3 covers the wavelength range 9.1 – 16.7 microns, where the NH_2 9.33-micron and 11.24-micron rock modes of hydrazine are located (Zheng et al. 2008).

After an extensive search of the NASA Planetary Data System (PDS) using the Outer Planets Unified Search (OPUS) tool (https://tools.pds-rings.seti.org/opus), two CIRS

spectra sampling Rhea's leading and trailing hemisphere were selected for analysis. The spectra were selected based on the quality of the observations, including signal-to-noise, with requirement that the observations be acquired under sunlit surface conditions, and that there are few detector artefacts present in the data. The two spectra analysed are averaged spectra from the individual spectral samples. The mean solar phase angle for the leading hemisphere observation is 40.3 degrees and the mean range to Rhea is 188610 km. For the trailing hemisphere observation, the mean solar phase angle is 80.9 degrees and the mean range to Rhea is 101483 km. The CIRS FOVs for each observation are shown in figure 7.7. The number of spectra averaged for the leading and trailing hemisphere observations are 1769 and 1319, respectively.

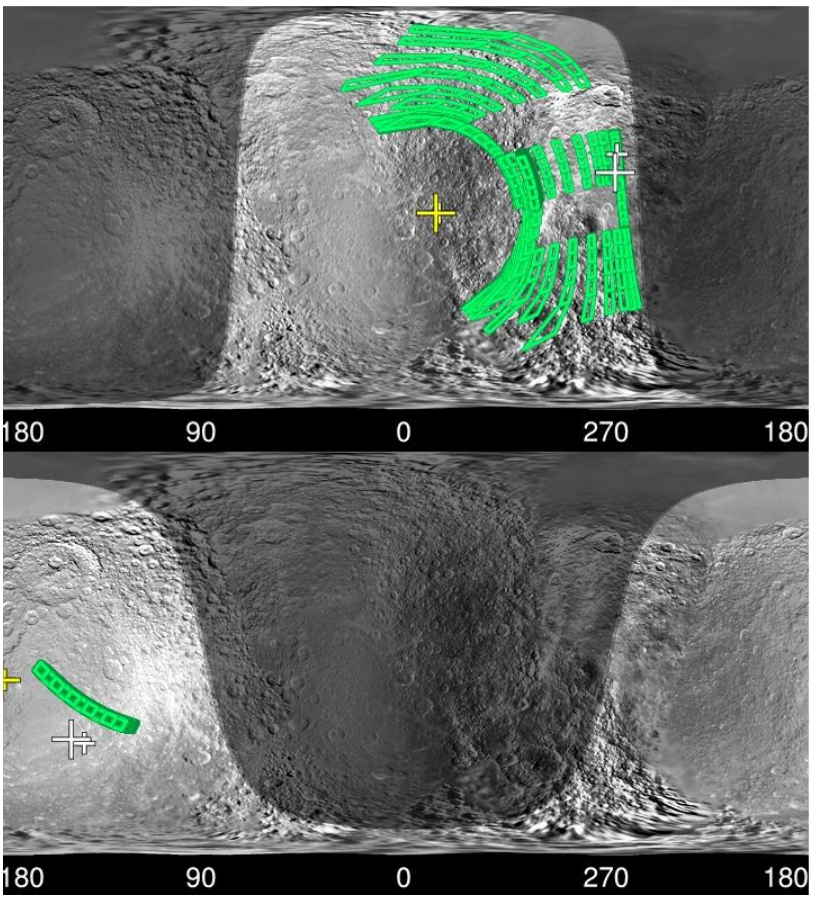

Figure 7.7: Cassini CIRS instrument FOVs for Rhea's trailing (top) and leading (bottom) hemispheres. The final spectra used in the analysis represent the average of individual spectral samples.

The mean spectra for Rhea's leading and trailing hemisphere are presented in figure 7.8. The original wavenumber units of the CIRS spectra have been converted to microns to maintain consistency in wavelength units used in this research.

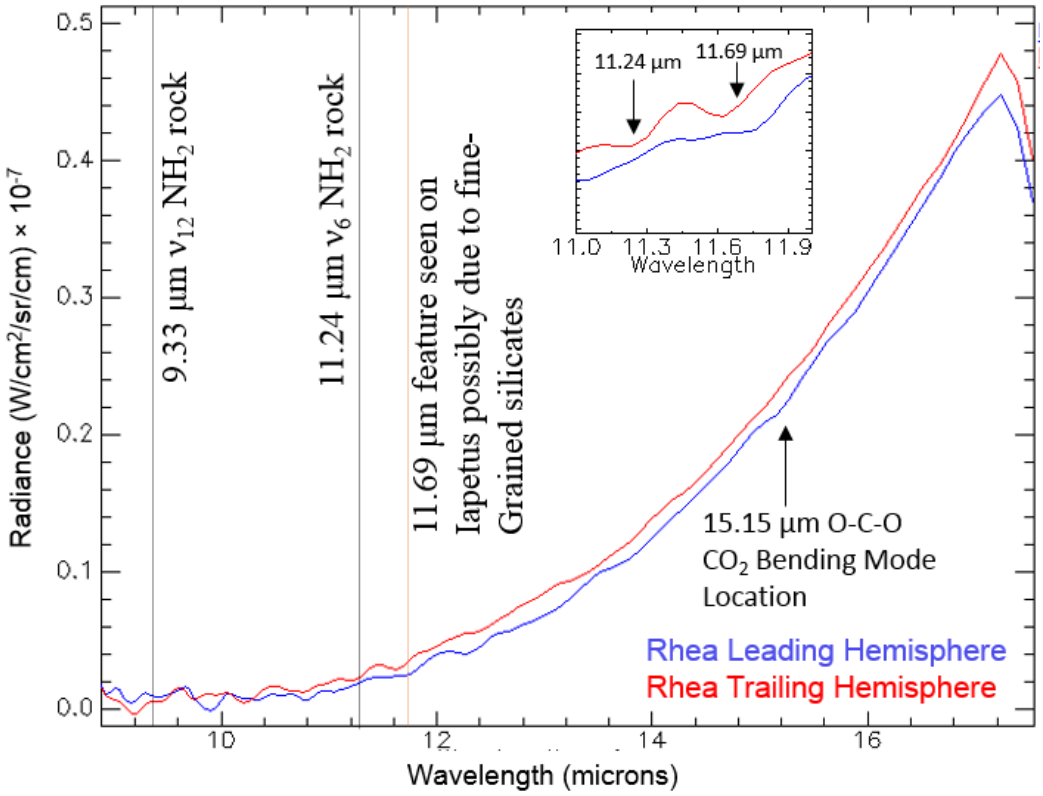

Figure 7.8: Cassini CIRS spectra of Rhea's leading and trailing hemispheres. Note the differences between weak absorption features between the two hemispheres. The locations of NH_2 features observed in IR spectra of thin ice measurements of irradiated ammonia carried out by Zheng et al. (2008) are marked by grey vertical lines. The location of an absorption feature at 11.7 microns, which has been attributed to fine-grained silicates (similar to that found in meteorites) on Iapetus by Young, et al. 2015, is denoted by the orange vertical line. The black arrow denotes the location where CO_2 ice has a transition at 15.15 microns due to the single or doublet O-C-O bending mode.

The CIRS spectra show a couple of weak absorption features not far from the locations where the 9.33-micron and 11.24-micron NH_2 rock modes of hydrazine are expected to be present. In addition, there is a weak absorption feature close to the expected location of the 11.695-micron silicate band that has been previously detected in CIRS spectra of Iapetus (Young *et al.* 2015). No claim as to the detection of the silicate feature can be made since the position of the silicate feature can shift depending on the crystalline

structure of the mineral. Furthermore, no constraints can be placed on its detection because there are no laboratory spectral measurements of silicates made at temperatures and pressures similar to Rhea's surface. Although the absorption features seen in the CIRS spectra do not lie exactly at the expected wavelengths where hydrazine and the silicate absorption are expected, it is important to note that spectral bands can shift due to changes in the phase and temperature. It is also interesting to note that there are minor differences in the position of absorption features observed in the spectra between the leading and trailing hemispheres of Rhea. For example, the weak absorption feature seen near 11.24 microns occurs in the spectrum of Rhea's trailing hemisphere and not in the leading hemisphere. The weak absorption feature located at 15.15 microns only occurs in the spectrum of Rhea's leading hemisphere. It is of interest to note that this feature lies at the location at of the O-C-O single (or doublet) bending mode of CO_2. However, the UVIS observations did not confirm the presence of CO_2 on Rhea.

To increase the signal to background or signal to noise ratio, the second derivative spectrum is computed. It is important to note that the derivative of the original spectrum does not increase the sensitivity of the analysis, because it is not valid to compare amplitudes of spectra and their derivatives since they are in different units. The units of the original CIRS spectrum are Radiance and that of the second derivative are Radiance/micron^2. Thus, it is meaningless to compare different units. It is therefore appropriate to state that the second derivative improves the signal to noise or signal to background ratio of the original CIRS spectrum – i.e. the derivative accentuates weak absorption features in the CIRS spectra. Figure 7.9 shows the comparison of the second derivative spectra for Rhea's leading and trailing hemisphere.

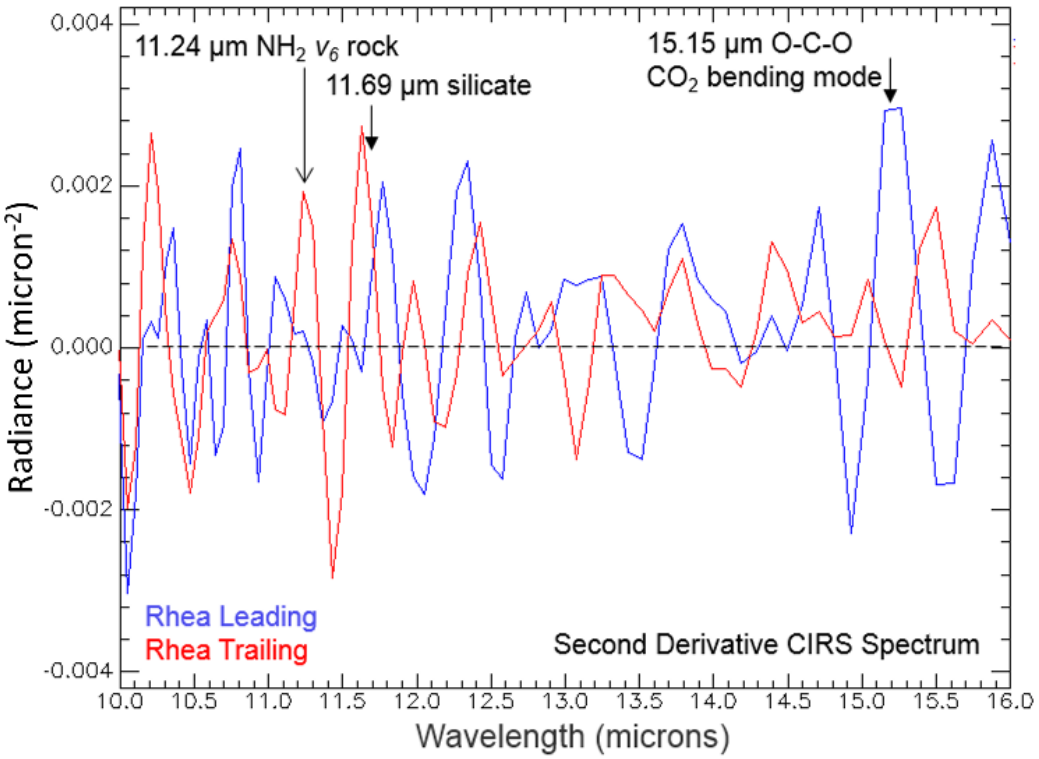

Figure 7.9: Second derivative CIRS spectrum of Rhea showing peaks, which mark the position of weak absorption features in the original spectrum. Black vertical lines denote the positions of two NH_2 rock bands of hydrazine observed in thin ice spectra involving the irradiation of ammonia ice (Zheng et al. 2008). Note the peak near 11.24 microns, the location where one of the NH_2 features is expected. Two derivative peaks are located just short-ward and long-ward of the 11.695-micron feature due to fine silicates, observed in CIRS spectra of Iapetus (Young et al. 2005). The black arrow denotes the location of where the O-C-O 15.15-micron bending mode of CO_2 occurs in the IR. The other sharp peaks (not annotated) in the second derivative spectra are unidentified.

The second derivative spectra show notable differences between Rhea's leading and trailing hemispheres in terms of weak absorption features. There are no significant peaks located near the expected position of the 9.33-micron NH_2 feature in hydrazine. On the other hand, a peak is seen near the location of the NH_2 11.24-micron feature in the second derivative spectrum of Rhea's leading hemisphere. No such peak is observed in the spectrum of the trailing hemisphere. This result confirms the Cassini UVIS data showing the potential detection of hydrazine on Rhea. None of the weak absorption features appears at locations in wavelength space where CIRS instrument artefacts are known to exist (10.42 and 12.99 microns). The weak dip around 15.15 microns (denoted by the black arrow in Figure 7.9) lies at the location of the CO_2 ice is known to have a singlet (or

doublet) transition produced by the O-C-O bending mode. However, the strength of this feature is close to the noise level of the CIRS data.

7.2 Scientific Implications of the Possible Detection of Simple Chlorine Molecules on Rhea

Chlorine is synthesised during oxygen burning by the addition of abundant alpha nuclei in massive stars being a minor product resulting from hydrostatic and explosive oxygen-burning that occurs in massive stars (Loon, 2010; Wallerstein *et al*. 1997). The chlorine is then ejected into the interstellar medium (e.g. planetary nebulae) when intermediate-mass stars (0.8 to 8 solar masses) expel their layers during the late asymptotic giant (AGB) phase of stellar evolution. The interstellar medium from which the primordial solar nebula was formed contained minor abundances of alpha-processed elements, including sulphur, argon, calcium, titanium, chromium, and chlorine (Wallerstein *et al*. 1997). CV chondritic meteorites that are oxidised show signs of being affected by metasomatic (i.e. mass transfer) that resulted in the enrichment in sodium, potassium, iron, and chlorine. Since chlorine (a halogen) is highly reactive, it is typically never found in its free state. Chlorine found in meteorites is in the form of chlorides. Varying amounts of chlorine have also been associated with phyllosilicates in carbonaceous chondrite meteorites. Varying abundances of chlorine among similar classes and different classes of meteorites have been found using neutron irradiation. The neutron irradiation produces the nuclear reaction for dating the meteorite samples, and this reaction can be used to calculate the elemental Cl concentration (Garrison, et al. 2000). Based on the analysis of the Garrison et al. (2000), the range in chlorine in their meteorite samples ranged from 15 to 177 ppm for ordinary chondrites, 12 to 507 ppm for iron silicate meteorites, 4 to 177 ppm for eucrites meteorites, and approximately 24 to 650 ppm for enstatites. It is possible that chlorine, a moderately volatile trace element in asteroidal objects could be delivered to the surfaces of icy

satellites during the course of their evolutionary history. It is also possible that redistribution of condensed chlorine molecules due to sputtering induced by charged particle bombardment originating from Saturn's magnetospheric plasma, could produce the geographically wide distribution (i.e. chlorine detected on the leading and trailing hemispheres) of simple chlorine molecules observed on Rhea. Thus, it is suspected that chlorine was incorporated into the rocky/silicate cores of solar system objects (e.g. planets, satellites) during their accretion phase.

The 184-nm absorption feature seen in UVIS spectra of Rhea's surface can also be explained by a layer of tetrachloromethane beneath a layer of water ice. Water and tetrachloromethane (CCl_4) are immiscible, because the CCl_4 cannot form hydrogen bonds to water. In other words, the critical size of a CCl_4 molecule and the hydrogen bond structure of amorphous solid ice would restrict diffusion of CCl_4 through the ice. Thus, if one were to put water and CCl_4 together in a localised container, and shake, the chemicals would rapidly separate out. On Rhea, there might be a source for CCl_4 (e.g., endogenic), with a fresh layer of water ice delivered on top of the tetrachloromethane (CCl_4) from Saturn's E-ring. Ejection of water-ice molecules from plumes originating from the southern sulci on Enceladus provide the source of E-ring water-ice (Postberg *et al*., 2008). Since E-ring material could coat both hemispheres of Rhea (from orbit geometry), it would explain why CCl_4 below water-ice is seen in all of the UVIS spectra analysed in this research. Based on the mass flux rate of ~0.026 kg/sec derived from Cassini CDA measurements of the amount of water coming from Enceladus' plumes (Kempf, *et al*. 2010), one can calculate the equivalent depth of water-ice deposited across the entire surface of Rhea using the mass flux rate and the mean density of water-ice. At approximately 90 K, the mean density is 934 kg/m^3 (Lide, 2005). The total surface area of Rhea based on its radius of 764 km (Roatsch *et al*. 2009) is 7.3×10^{12} m^2. Using these values, and the 0.026 kg/sec mass flux, the equivalent layer thickness of water-ice can be calculated using

$$thickness = \frac{flux}{density \times area}. \quad (7.3)$$

Assuming a continuous eruption of water-ice molecules from Enceladus' plumes, an equivalent thickness of water-ice of ~1.2×10^{-10} meters per year, or about 1.2×10^{-4} microns per year would form. Since UV reflectance spectroscopy is sensitive to the upper few microns, I see that a layer of chloromethane molecules beneath water-ice could be readily detectable.

Tetra chloromethane (also known as perchloromethane) has a melting point of 250.23 K, and has a density higher than liquid water. It can form a solution in chloroform ($CHCl_3$), formic acid and CS_2. Methylene chloride (CH_2Cl_2) has a melting point of 176.5 K, and is denser than liquid water (Lide 1989). The organic halogen compound is miscible in $CHCl_3$ and CCl_4, two other simple chlorine molecules that also fit the UVIS data. Chloroform is another organic halogen compound that is formed when organic molecules in water react with chlorine. Chloroform has a density higher than that of water, and its melting point is 209.7 K. It is also miscible in CCl_4, diethyl ether and CS_2. If the source of the two organic halogen molecules, $CHCl_3$ and CH_2Cl_2 is endogenic in nature, it could also indicate the presence of organic molecules in the interior of Rhea. The presence of these simple chlorine molecules in the deep interior of Rhea would lower the melting temperature of the ice to the point where an aqueous layer could exist. If Rhea is differentiated or partially differentiated the existence of an ocean in contact with a rocky/silicate core would provide a source for the chlorine molecules since a small amount of these volatile chemicals would be incorporated into the core material at the time of Rhea's formation.

The geographically wide distribution of simple chlorine molecules on Rhea's icy surface limited by the sampling of the UVIS observations seems to favour an endogenic source, since an exogenic source from Saturn's E-ring should result in an asymmetric or

localised distribution. An exogenic source resulting from a copious number of cometary and/or asteroid impacts could produce the geographically broad distribution of chlorine molecules on Rhea's surface. It is also possible that redistribution of condensed chlorine molecules due to sputtering induced by charged particle bombardment originating from Saturn's magnetospheric plasma, could produce the geographically wide distribution (i.e. chlorine detected on the leading and trailing hemispheres) of simple chlorine molecules observed on Rhea. The sputtering yield or number of molecules ejected per incident charged particle is a function of the surface temperature on Rhea, the energy of the incident ions and the angle of impact on the surface ice. The distribution of the observed chlorine species across Rhea's surface, in theory, should be determined by the velocity distribution of the sputtered molecules. The sputtering and radiolysis of water-ice molecules could also contribute to Rhea's exosphere, composed of O_2 and CO_2 (Teolis and Waite, 2016). Molecules with velocities exceeding Rhea's escape velocity travel on ballistic trajectories into space, with a certain percentage contributing to the satellite's tenuous atmosphere. Those molecules with velocities less than the escape velocity are redistributed to other location on Rhea's surface. It is also possible that free radical halogenation could occur due to irradiation of UV photons and/or charged particles leading to molecules with increased chlorination. If small amounts of methane (CH_4) are present in the ice, then the following chemical reactions might occur:

$$CH_4 + Cl_2 \rightarrow CH_3Cl + HCl$$
$$CH_3Cl + Cl_2 \rightarrow CH_2Cl_2 + HCl$$
$$CH_2Cl_2 + Cl_2 \rightarrow CHCl_3 + HCl$$
$$CHCl_3 + Cl_2 \rightarrow CCl_4 + HCl$$

Assuming carbon tetrachloride (CCl_4), chloroform ($CHCl_3$), and methylene chloride (CH_2Cl_2) have been detected on Rhea's surface using far-UV spectroscopy, they could be produced by the chemical reactions shown above. The source of the Cl_2 could originate from a subsurface ocean layer deep inside Rhea.

An alternative chemical pathway to the production of CCl_4 on Rhea would involve the following chemical reactions resulting from impact heating:

$$CH_4 + 4Cl_2 \rightarrow CCl_4 + 4HCl$$
$$CS_2 + 3Cl_2 \rightarrow CCl_4 + S_2Cl_2$$

However, the non-detection of hydrogen chloride (HCl) and the fact that carbon disulphide (CS_2) has not been detected on Rhea or Dione, suggests chemical barriers preventing the formation of carbon tetrachloride (CCl_4) from these two reactions.

7.2.1: Could Chlorine Molecules Explain the CO_2 in Rhea's Exosphere?

If simple chlorine molecules exist on Rhea, they might provide an explanation as to the source of the satellite's tenuous atmosphere composed of molecular oxygen and carbon dioxide. The following reactions might take place over very long-time scales due to the very low temperature (relative to room temperature) at the surface of Rhea (~70 K):

$$CH_2Cl_2 + O_2 \rightarrow CO_2 + 2HCl$$
or
$$CH_2Cl_2 + H_2O \rightarrow H_2CO + 2HCl$$
$$H_2CO + O_2 \rightarrow CO_2 + H_2O$$

The source of O_2 is radiolysis of water-ice molecules (H_2O) from ions and electrons originating from Saturn's magnetosphere (Cooper *et al*., 2008; Cassidy *et al*, 2010). It is possible that the source of the CO_2 in Rhea's exosphere could originate from these chemical reactions over long (geological) time spans. If the simple chlorine compound, CCl_4 does exist on Rhea's surface over a wide spatial distribution, then it might be possible for this chlorine compound to react with O_2 and/or H_2O to produce the CO_2 observed in Rhea's exosphere via the following chemical reactions that occur over very long time spans due to the low temperature environment:

$$CCl_4 + O_2 \rightarrow CO_2 + 2\,Cl_2$$
or
$$CCl_4 + 2\,H_2O \rightarrow CO_2 + 4\,HCl$$

The main unresolved questions on this scenario is whether or not there are any barriers to these reactions at the lower temperatures encountered on the surface of Rhea (and other icy satellites in the outer solar system). The question of whether these chemical reactions could take place at fast enough rates at low temperatures (<100 K) cannot be answered until laboratory measurements are performed.

If Cl or Cl_2 is present on Rhea, then it may also affect ozone synthesis, which may provide an explanation of why no ozone was detected in far-UV spectra collected by the Cassini UVIS instrument. In other words, ozone is destroyed by catalytic reaction. On the other hand, only weak absorption bands exist in the wavelength range cover by UVIS and any ozone present within the ice on Rhea may still be below the detection threshold of the spectrometer.

The formation of CO_2 from the second chemical reaction would also produce hydrogen chloride (HCl). Since HCl has not been detected on Rhea based on analysis of Cassini UVIS spectra, or is below the detection threshold of the UVIS instrument, the production of CO_2 from the second chemical reaction (shown above) is unlikely. The production of CO_2 from the first chemical reaction is possible, since O_2 can be synthesised by irradiation of water-ice molecules, and CCl_4 could originate from an endogenic source on Rhea. The production of the chlorine molecule (Cl_2) would be difficult to verify, since it is not detectable in the IR. The non-IR activity of Cl_2 is due to it having no dipole moment. The Cl_2 molecule does not have any absorption features that would allow its detection using the Cassini UVIS instrument in the wavelength range from ~150 – 190 nm. Thus, the production of CO_2 might be possible based on the chemical reaction between CCl_4 and O_2, assuming that carbon tetrachloride originates from an aqueous layer deep inside Rhea.

7.2.2: Problems Associated with the Possibility of Chlorine Molecules on Rhea

The production of chloromethane molecules on Rhea from methane ice and chlorine leads to the formation of hydrochloric acid (HCl) as seen from the chemical reactions presented in section 7.2. To examine the feasibility chloromethane molecules existing within the surface ice on Rhea, model spectra of deuterium chloride (DCl) were created using the measured absorbance of DCl ice from laboratory experiments. Hydrogen chloride (HCl) absorbance measurements were not feasible due to laboratory safety constraints at the Taiwan facility where the measurements were carried out. However, the molecular structure between HCl and DCl is similar enough to test whether HCl could be present on Rhea. As seen from the comparison plot (Figure 7.10), the fit between the observed spectrum and model spectrum is poor. The null detection of HCl on Rhea implies that the production of simple chloromethane molecules (CCl_4, $CHCl_3$) via the chemical reactions given in section 6.2 are unlikely to occur in Rhea's surface ice. Therefore, the potential detection of hydrazine monohydrate described in this research represents the most probable candidate between the two molecules that could explain the 184-nm absorption feature in the Cassini UVIS spectra.

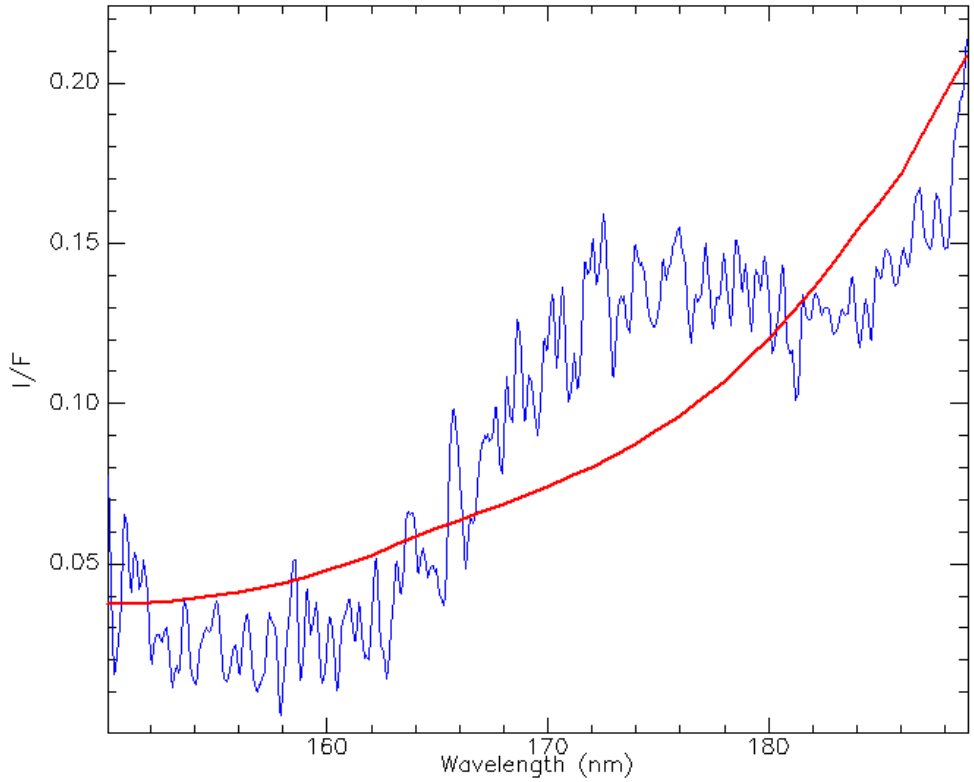

Figure 7.10: Best fit between the model spectrum of DCl ice and a Cassini UVIS spectrum of Rhea. The VUV ice spectrum was measured at 70 K at near-vacuum conditions, similar to the surface condition on Rhea.

7.3: A Search for Carbonic Acid and Carbon Dioxide on Rhea

If CO_2 is present in the water-ice surface layers on Rhea, irradiation from magnetospheric ions and electrons should produce carbonic acid (H_2CO_3). Previous work by Hage *et al*. (1998) has suggested the possibility that the 3.8-micron features seen in Galileo NIMS spectra of the two Jovian moons, Callisto and Ganymede are due to carbonic acid. Vacuum-UV laboratory spectra were collected of carbon dioxide and carbonic acid in solid phase at temperatures similar to the range encountered in the Saturnian system. Both CO_2 (Figure 7.11) and H_2CO_3 do not explain the weak absorption seen between ~179-189 nm on Rhea's leading and trailing hemispheres. Furthermore, the overall spectral profile of carbonic acid does not fit the general spectral slope of the UVIS spectra. The null detection of carbonic acid on Rhea can therefore be further evidence

against the possible existence of CCl_4 on Rhea as explained in section 7.7.2 – i.e. the non-detection of hydrogen chloride (HCl) needed to produce the simple chlorine compound.

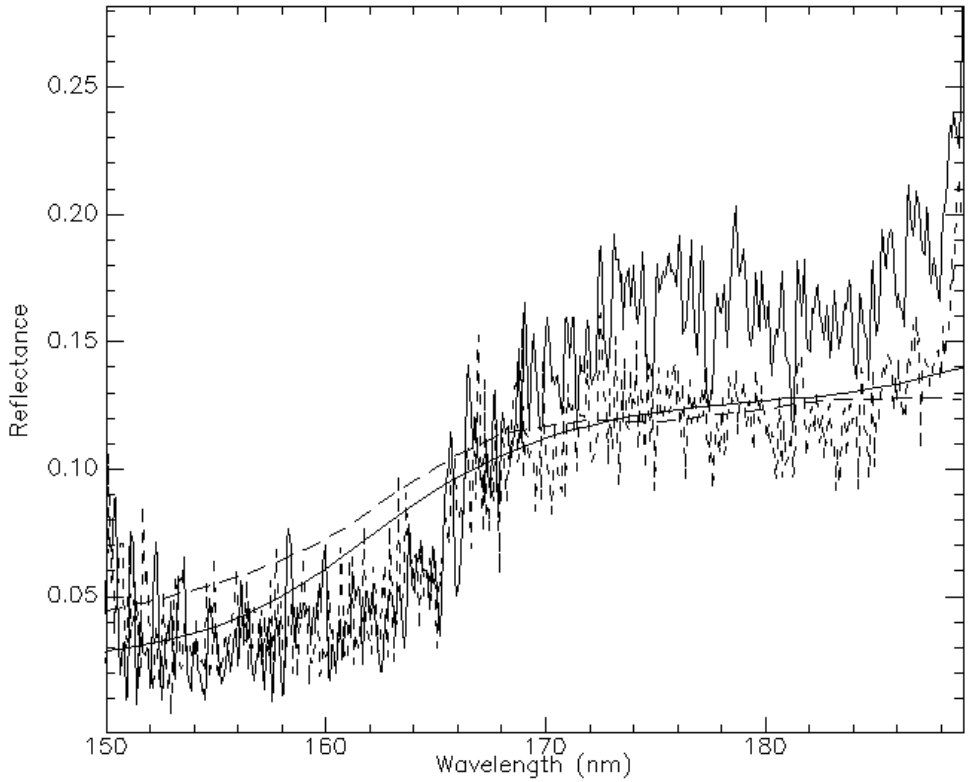

Figure 7.11: Modelled spectra of CO_2 (dashed curve) and H_2CO_3 (solid curve) ice compared with Cassini UVIS data over the leading (black solid UVIS spectrum) and trailing (black dashed UVIS spectrum) hemispheres of Rhea. The spectral slopes of the model spectra are similar in shape to the "UV drop-off" that occurs between ~160-170 nm.

On the other hand, the null detection of carbonic acid on Rhea (H_2CO_3) could be the result of concentrations below the detection threshold of the UVIS spectrograph. It is also possible that further irradiation of any carbonic acid present in Rhea's water-ice layers results in its recycling back to water and carbon dioxide. Another possibility, however unlikely is that CCl_4 is present on Rhea (and Dione), but the reaction with solid phase O_2 occurs on a reaction timescale that is extremely slow (i.e. on geological timescales). A certain percentage of CO_2 molecules would recombine after being dissociated via the chemical pathway reaction $CO_2 + h\nu \rightarrow CO + O$ (where the dissociation wavelength threshold for CO_2 is about 170 nm). Thus, the likelihood of detecting CO_2 ice on Rhea

depends on the timescales over which dissociation and recombination of the molecules occurs.

Another possible explanation for the null detection of CO_2 on Rhea surface in the far-UV region of the spectrum is the production rate of H_2O_2 from irradiation of CO_2 and H_2O. The relationship between the yield (i.e. *G* value), the amount of energy input (*E*), and timescale (*t*) of a chemical reaction, can be used to estimate the column density (N_c) of the molecular species produced in the reaction.

$$N_c = GEt \qquad (7.4)$$

The energy input at the radial distance of Rhea from Saturn amounts to 2.9×10^6 keV/cm^2 s from plasma ions, and 6.2×10^7 keV/cm^2 s from electrons (Delitsky & Lane, 2002). The total energy input to Rhea from plasma ions and electrons (not including UV photons) amounts to 6.5×10^7 keV/cm^2 s (Delitsky & Lane, 2002). Over a 1000-year time span, if CO_2 and H_2O ice are irradiated by plasma ions and electrons originating from the magnetosphere of Saturn, the column density of hydrogen peroxide (H_2O_2) produced at Rhea can be estimated as follows:

$$\begin{aligned} N_c &= GEt \\ &= \left(0.004\ molecules/eV\right)\left(6.5\times10^{10}\ eV/cm^2\ s\right)\left(3.156\times10^{10}\ s\right) \\ &= 8.21\times10^{18}\ molecules/cm^2 \end{aligned} \qquad (7.5)$$

In contrast, the amount of hydrogen peroxide produced when H_2O and CO_2 are irradiated on Europa is approximately 400 times greater $\left(N_c = 3.66\times10^{21}\ molecules/cm^2\right)$. Indeed, the higher column density for the production of hydrogen peroxide on Europa is due to the greater total energy input at Europa's distance from Jupiter's magnetosphere $\left(2.9\times10^{13}\ eV/cm^2\ s\right)$. Given the column density of hydrogen peroxide that could be produced at Rhea, the amount produced in terms of grams per cm^2 can be estimated using the relationship between the column density and molecular weight of H_2O_2 (34.0147 g/mol).

$$\frac{\left(8.21\times10^{18}\,cm^{-2}\right)\left(34.0147\,g/mol\right)}{6.023\times10^{23}\,mol^{-1}} = 4.64\times10^{-4}\,g/cm^{2} \quad (7.6)$$

The amount of H_2O_2 produced on Europa based on the previous column density estimate, is approximately 0.207 g/cm^2. The lower amount of hydrogen peroxide produced from the reaction among CO_2 and H_2O (relative to the amount produced on Europa) might explain why CO_2 has not been detected on Rhea based on analysis of far-UV spectra.

In contrast, on Europa, hydrogen peroxide has been detected over much of its leading hemisphere based on analysis of IR spectra obtained using the Keck II telescope. The detection of H_2O_2 on Europa's leading hemisphere implies the existence of CO_2, assuming H_2O_2 is produced by irradiation of CO_2 and H_2O. The lower column density of H_2O_2 on Rhea as calculated above, may imply an abundance of CO_2 that falls below the detection threshold of the UVIS instrument. No production of hydrogen peroxide was observed in laboratory experiments carried out at the Taiwan synchrotron facility involving the irradiation of water-ice, other than the synthesis of O_2. Analysis of Rhea far-UV spectra show no evidence for gaseous O_2 trapped within the ice matrix. This suggest that the formation of O_2 bubbles trapped within the ice may be suppressed by the low surface temperatures encountered on Rhea.

7.4: Evidence for a Subsurface Ocean on Rhea

The results of this research have provided evidence that can be used to establish the extent to which Rhea's chemical composition of surface ice is related to a possible internal aqueous layer. This research has also provided information on the evolution of endogenic molecules on Rhea's surface that have been exposed to the effects of radiolysis, space weathering, near-vacuum conditions and a range of extremely low surface temperatures. Results based on this research can be used to relate the geochemistry of Rhea's surface to possible subsurface ocean chemistry, an area of research that has been limited.

A few models predict that Rhea could harbour a subsurface ocean deep inside its interior. The location of an aqueous layer of water mixed with simple chlorine molecules and/or ammonia due to contact with a silicate rocky core, depends on the eutectic temperature of the solution. Small amounts of chlorine could originate from phreatic aquifers of limited areal extent. The perched aquifers composed of water, simple chlorine and/or hydrazine molecules, and small amounts of ammonia, could be located within a semi-pervious thick ice layer. Internal heat flow resulting from the radioactive decay of radioisotopes with long half-lives (^{232}Th, ^{40}K, ^{235}U, and ^{238}U), and impact heating over long time periods could produce regions deep within Rhea that become buoyant relative to their surroundings. A rough estimate of the heat produced in a rocky/silicate core can be made assuming the following radiogenic heat production rates: $H_U = 9.71\times10^{-5}$ W/kg, $H_K = 3.58\times10^{-9}$ W/kg, and $H_T = 2.69\times10^{-5}$ W/kg. The total concentration of ^{235}U and ^{238}U is based on the terrestrial value of 1.3×10^{-8} kg/kg, which is representative of the concentration found in carbonaceous chondrite meteorites. Using the ratio values of 3.968 and 1×10^{4} for Th/U and K/U, respectively (based on solar values), the calculated heat production rate within a rocky/silicate core is

$$\begin{aligned} H_r &= C_U\left(H_U + \frac{C_{Th}}{C_U}H_{Th} + \frac{C_K}{C_U}H_K\right) \\ &= 1.3\times10^{-8}\,\frac{kg}{kg}\left(9.71\times10^{-5}\,\frac{W}{kg} + 3.968\cdot 2.69\times10^{-5}\,\frac{W}{kg} + 1\times10^{4}\cdot 3.58\times10^{-9}\,\frac{W}{kg}\right) \\ &\approx 3.1\times10^{-12}\,\frac{W}{kg}. \end{aligned} \tag{7.7}$$

Mechanical pressure due to rising plumes originating from the deep aqueous layer heats the overlying ice causing it to melt. This process leads to the formation of perched aquifers. The pressure from the confined liquid solution in the aquifers could then produce cracks/fissures within the ice, or enlarge older cracks produced by previous impacts that have occurred over the history of Rhea (i.e. global fracture networks produced by very large impacts). The minimum tensile stress for crack propagation to occur based on a

balance between the work needed to overcome fracture toughness and the work available through tidal stresses, is given by Crawford and Stevenson (1988):

$$\sigma_{\min} = \frac{6}{4^{2/3}} \left(\frac{K}{\pi} \right)^{2/3} \left(g \Delta \rho \right)^{1/3} \qquad (7.8)$$

where K is the fracture toughness of the ice, g is the gravity at the surface, and $\Delta\rho$ is the density contrast of water-ice. For Rhea, g = 0.264 m/s^2, $\Delta\rho = 80\,kg/m^3$ and K = 10^5 Pa m$^{1/2}$. Substituting these values into equation 7.8 yields a minimum tidal stress of 6.1 kPa. Since Rhea's approximate diurnal tidal stress amounts to 17 kPa (Yoder, 1995), crack population is possible with the moon's ice shell.

However, no current evidence exists for any surface features (e.g. cryovolcanic features, chaotic terrain) created by subsurface aquifers on Rhea. If a deep internal aqueous layer does exist inside Rhea, then it is expected that the exterior impact craters on the satellite's surface would not be affected since a thick ice shell of a few hundred kilometres exists. In other words, there may be no geomorphological evidence at the surface of Rhea, even though a deep internal ocean layer could be present. There are tectonic features on Rhea (e.g. bright coloured wispy terrain and other tectonic related features) that indicate past geological activity occurred on the satellite. The tectonic features appeared to indicate that episodic events occurred in which interior water was extruded and condensed onto the surface of Rhea. Digital elevation models and Cassini ISS imagery of Rhea's trailing hemisphere show past evidence of extensional fault systems with a north-south trend (Schenk and Moore, 2007; Wagner *et al*. 2007). The graben (extensional fault systems) provide evidence of past endogenic activity on Rhea, and the digital terrain models based on Cassini ISS images show large scarps and/or ridges with a north-south orientation (Figure 7.12). Although ISS imagery shows no evidence for resurfacing events on Rhea, a few local regions show signs of recent tectonic stress (on geological timescales) based on the geological principle of superposition. Furthermore, several large impact craters show a

lack of smaller craters, indicative of relatively young ages of these craters. A geological study could be planned to search for cryovolcanic features on the surface of Rhea that might be related to subsurface aquifers.

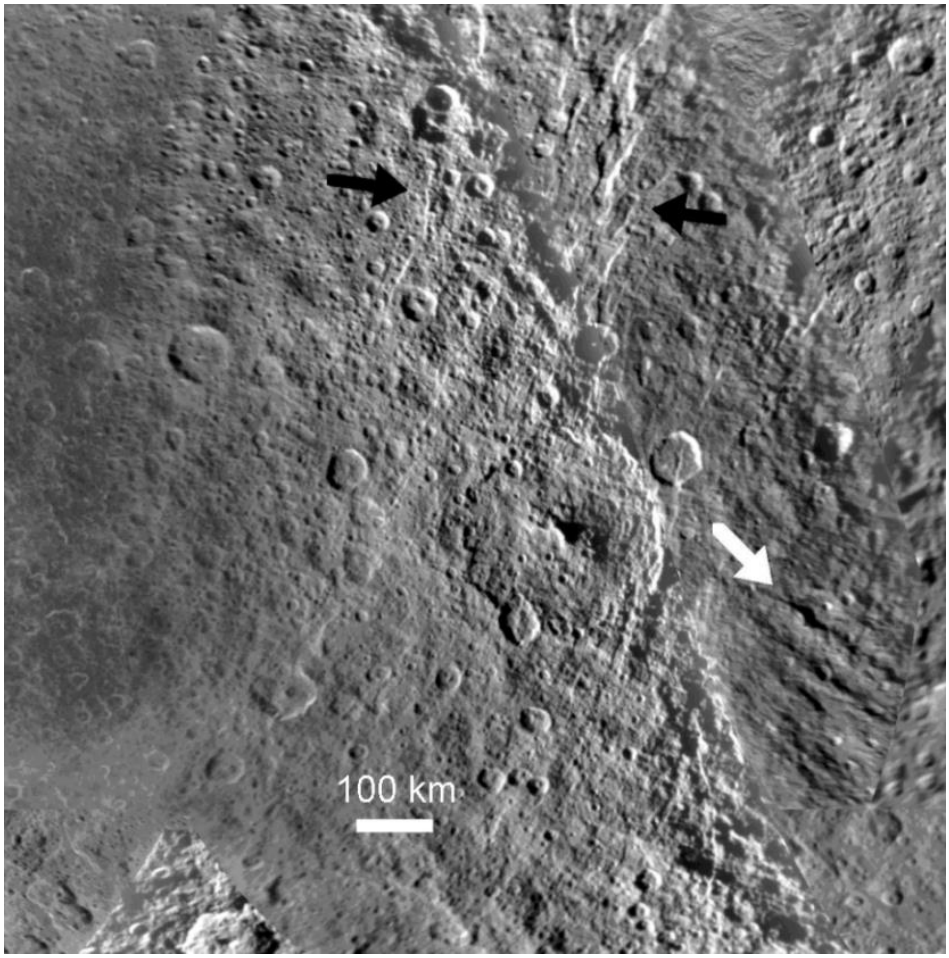

Figure 7.12: A Cassini ISS image of Rhea showing several ridges (white arrow) that appear to be orthogonal to the extensional tectonic feature (black arrows). The spatial resolution of the image is approximately 1 km (figure courtesy of Jaumann, et al. 2009).

The lack of observable tectonic features related to endogenic activity on or just below Rhea's surface, can be explained by estimating the depth at which a hypothetical subsurface ocean could exist in the interior of the satellite, as discussed in the following section.

7.4.1 Analytical Calculations of a Hypothetical Ocean Layer in Rhea's Interior

One can obtain a rough estimate for the depth of a hypothetical ocean on Rhea, assuming the satellite to be differentiated and that conduction is the primary mode of heat transfer within the object's interior. The analytical calculations shown below are based on the following list (Table 7.2) of molecules and their associated melting points.

Table 7.2: Melting points for chemical species that could exist in the interior ice of Saturn's icy moons.

Chemical Species	**Chemical Formula**	**Melting Point (K)**
Water Ice	H_2O	273
Ammonia	NH_3	167-195.4
Trichloromethane	$CHCl_3$	209.7
Methyl Tetrachloride	CCl_4	250.2
Methylene Chloride	CH_2Cl_2	176.5
Hydrazine	N_2H_4	221.5

The contribution from the initial accretion phase of icy satellites is assumed to be negligible, unless the accretion occurred sufficiently rapidly to allow minor melting to take place or the young-age scenario for the icy satellites is valid (Cuk, *et al*. 2016). For Saturn's mid-sized icy satellites, the decay of radioisotopes provides the main source of internal heating. If the satellites formed before the extinction of short-half-life radioisotopes (approximately 3.7 Myr after the formation of the Solar System; from Robuchon *et al*. 2010), such as ^{26}Al, ^{28}Al, ^{60}Fe and ^{53}Mn, then radioactive decay from these isotopes would contribute an early source of heating. If Rhea and Dione formed as a result of collisions between a previous generation of Saturnian satellites, then it is estimated that their ages may be about 100 Myr (Cuk, *et al*. 2016). In this scenario, the radiogenic heating in the interiors of Rhea and Dione due to short-half-life radioisotopes could help maintain an interior liquid ocean in the interiors of these moons. After about 3.5 Myr, the main source of heating due to radioactive decay of long-lived radioisotopes comes from ^{40}K, ^{232}Th, ^{235}U and ^{238}U. To determine if Rhea could have had an internal

ocean (and its depth) during its early evolution, data from the analytical calculations shown in the following section from Iess *et al*. (2007) and Robuchon *et al*. (2010) may be used.

For an icy moon with a silicate mass fraction, $f_{silicate}$, the heat flux at the surface resulting from the present-day decay of long half-life radioisotopes is given by the expression

$$\begin{aligned} q_s &= \left[1 + \left(\frac{1}{f_{silicate}} - 1 \right) \frac{\rho_{silicate}}{\rho_{ice}} \right]^{-1} \frac{\rho_{silicate} \dot{H} R}{3} \\ &= \frac{1}{3} \frac{f \rho_{ice} \rho_{silicate} \dot{H} R}{\left(\rho_{ice} - \rho_{silicate} \right) f_{silicate} + \rho_{silicate}} \end{aligned} \qquad (7.9)$$

where ρ_{ice} and $\rho_{silicate}$ are the mass densities of the ice and rocky components, respectively. The heat production rate is denoted by $\dot{H}$, and *R* is the radius of the satellite. To determine the depth of a hypothetical aqueous layer deep inside Rhea during its early evolution, the thermal conductivity for a silicate/water-ice mixture in terms of the volume fraction of silicate material and the thermal conductivities of silicate and ice, must be known.

$$\begin{aligned} k &= f_V k_{silicate} + \left(1 - f_V\right) k_{ice} \\ k_{ice} &= 0.4685 + 488.12 / T \quad \left[W / m / K \right] \\ f_V &= \frac{\rho_{Rhea} - \rho_{ice}}{\rho_{silicate} - \rho_{ice}} \end{aligned} \qquad (7.10)$$

For Rhea, the thermal conductivity is ~ 4.2 W/m/K, taken from Robuchon *et al*. (2010). The density of ice in Rhea's interior, that of silicates, and Rhea's mean density are assumed to be ρ_{ice} = 940 kg/m^3, $\rho_{silicate}$ = 3661 kg/m^3, and ρ_{Rhea} = 1233 kg/m^3, respectively (Iess *et al*. 2007). The silicate mass fraction in Rhea's interior is calculated using the relation

$$f_{silicate} = \rho_{silicate} f_V / \rho_{Rhea} \qquad (7.11)$$

where f_V is the volume fraction of silicate inside Rhea. For the model shown in Figure 7.13, the calculated silicate mass fraction for Rhea is 0.32. The surface heat flux can be calculated using equations 7 or 8. For a radius of 764 km and an initial rate of heating per unit mass of silicate of 4.08×10^{-11} W/kg just after Rhea's formation (the heating rate due to all long-half-life radiogenic isotopes based on the data from Robuchon *et al*. 2010), the heat flux at Rhea's surface would have amounted to 4.1 mW/m^2. The depth of a liquid layer inside Rhea shortly after its formation can be calculated using the following expression

$$d_{ocean} = \frac{k\left(T_m - T_s\right)}{q_s} \qquad (7.12)$$

where q_s is the surface heat flux (4.1 mW/m^2), k is the thermal conductivity of the ice and silicate, T_m is the melting temperature of the ice (including the non-ice components listed in Table 7.2), and T_s is the surface temperature of Rhea, assumed to be approximately equal to the temperature of the Saturnian primordial nebulae (70 K; Czechowski, 2012). Substituting the values for the surface temperature of Rhea (70 K), surface heat flux, thermal conductivity, and the range of melting points for ammonia (T_m ~167-195 K) for Rhea leads to a range for the depth of an internal ocean of approximately 100-128 km. Since the initial time and duration of Rhea's accretion are not known with good accuracy, it is not possible to determine the initial content of the short-lived radioisotopes that are important for the moon's later evolution. Thus, this calculation does not include heat contribution from Rhea's early accretion phase and short half-life radioactive isotopes (e.g. ^{26}Al). Although the internal heat contribution from long-half-life radioisotopes diminishes with time, the internal aqueous layer could be maintained if non-water-ice volatiles (e.g., ammonia, chlorine-based and hydrazine-based salts) reduce the melting temperature of the ice well below that of H_2O.

In this next section, the results from a sensitivity study on the effect of the silicate mass fraction of Rhea on the depth of a hypothetical liquid layer as a function of the melting temperature range for the chemical species listed in Table 7.2 are presented. The range of the silicate mass fraction used in the model presented below is 0.32-0.40 taken from Ellsworth and Schubert (1983). Figure 7.13 shows the results of the model for a range of melting temperature and silicate mass fractions.

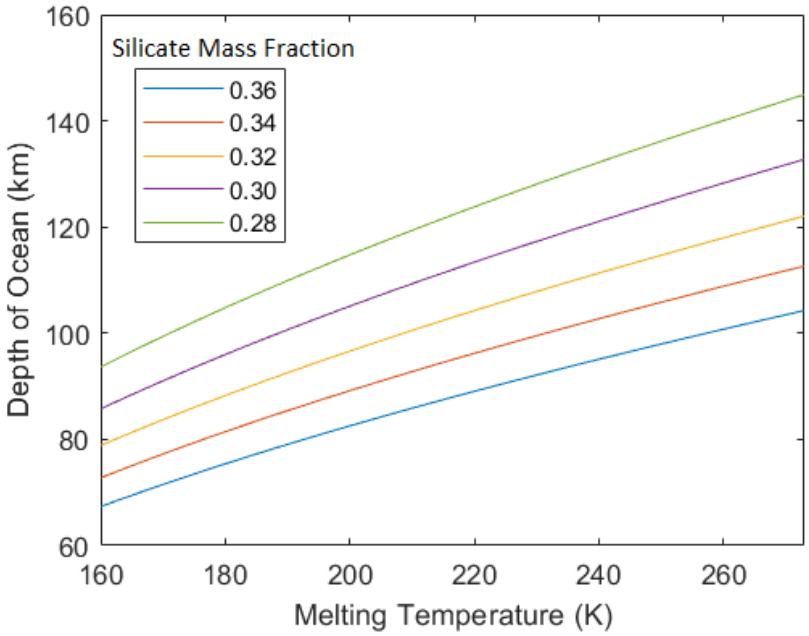

Figure 7.13: Depth of a hypothetical ocean layer inside Rhea as a function of melting temperature and silicate mass fractions. The depth of the internal aqueous layer increases as the silicate mass fraction decreases, and the depth of the internal ocean layer becomes shallower as the melting temperature decreases. The range of melting temperatures for these models was chosen based on the melting temperatures of ammonia, chloromethane and hydrazine based molecules (Table 7.2).

Based on the results of the internal ocean layer model computations, it is apparent that the depth at which the liquid layer occurs increases with melting temperature as is expected. The results of the model calculations also indicate that the internal ocean layer occurs at shallower depths for greater silicate mass fractions.

The great depths calculated for the case of Rhea also imply that no observable tectonic activity should take place at or near the surface layers of the satellite. This is indeed the case as no evidence exists for current endogenic activity on Rhea's surface,

although evidence for past endogenic activity has been observed in Cassini ISS imagery in the form of tectonic features and partially relaxed impact craters. The ocean model calculations also demonstrate the problem associated with an endogenic source for the existence of chloromethane or hydrazine-based molecules observed on the surfaces of Rhea and Dione. Any chloromethane or hydrazine molecules from a deep internal ocean would have to migrate at least 70 km through small fissures/cracks in the ice shell to reach the surface.

7.4.2: Can Accretion Provide an Additional Source of Internal Heat in Rhea?

An additional source of heating in the interior of Rhea is due to the release of energy during the satellite's formation through the process of accretion. The potential energy released as heat during the gravitational accretion can be derived by integration over a series of shells, each of thickness dr and mass $dm = 4\pi r^2 \rho\, dr$, where ρ is the mass density. Each shell contributes an additional potential gravitational energy $dE_p = Gm\, dm / r = (16/3)\pi^2 G\rho^2 r^4 dr$. Integration over the radius of the planet (or moon) yields

$$E_p = \int_0^{r_\oplus} dE_p = \int_0^{r_\oplus} \frac{Gm}{m} dm = \frac{3}{5}\frac{GM^2}{R} \qquad (7.13)$$

where M is the mass of Rhea, and R is the satellite's radius. Assuming all of the energy goes into heating, the maximum temperature change due to accretion can be expressed as

$$\Delta T_{acc} = \frac{3}{5}\frac{GM}{C_p R} \qquad (7.14)$$

where C_p is the specific heat capacity. For the mass and radius of Rhea, the amount of potential energy released as heat energy is 2.79×10^{26} J, assuming a constant density throughout the moon. The true variation in density in Rhea modifies this value by about 10

percent (Clauser, 2011). For a specific heat of 750 J/kg/K calculated from the relation $f_{silicate}c_{p,sil} + (1 - f_{silicate})c_{p,ice}$ (Czechowski, 2012) using a silicate mass fraction of 0.30, the change in temperature due to the accretion of Rhea amounts to ~ 161 K. This value agrees to within about 25 percent of the value obtained from numerical modelling (~215 K) described in Squyres *et al*. (1988). These accretion temperatures are below the melting point of pure water-ice (~273 K). However, minor amounts of ammonia and salts could depress the melting temperature to the point where additional heat from accretion could play a role in creating an internal liquid layer inside Rhea and Dione during their early formation histories. The amount of heat energy retained in the satellite's interior would depend on whether accretion occurred by many small impactors or if accretion took place by a small number of large impacts. In the latter case, most of the energy is deposited in the satellite's interior region. If Rhea was recently formed (~100 Mya) from the collision of primordial satellites orbiting Saturn (Cuk, *et al*. 2016), then there would be less time for the satellite to dissipate internal heat due to both accretion and radioactive decay of both short- and long-term radioisotopes. This scenario would increase the likelihood of a present-day subsurface ocean in Rhea's interior.

The above estimation of the depth of the liquid layer does not include any internal heating due to accretion, which could be important if the formation of Rhea occurred recently (~100 Myr) as reported by Cuz *et al*. 2016. Cuz *et al*. base their claim of Rhea's young age on simulations which indicate that Rhea, Dione and Tethys have not crossed as many orbital resonances as they should have if they are ancient satellites. This implies that Dione, Tethys and Rhea formed at distances not far from their present location. Based on this distance, the ages of these satellites are geologically young, less than 100 Myr. Thus, Dione, Tethys and Rhea may have been formed out of the debris resulting from collisions between previous moons in the Saturnian system. In the young satellite scenario set forth by Cuz *et al.* (2016), the high density of impact craters on Rhea can be explained by

planetocentric impacts. The calculated range of depths (~ 65-140 km) of an aqueous layer inside Rhea implies that there should be no present-day tectonic activity resulting from ongoing endogenic activity on Rhea. However, if Rhea accreted only 100 Myr ago, then liquid layers could have existed closer to the satellite's surface due to the additional heat input from accretion. This could explain the presence of tectonic features and relaxed craters observed at several locations on the surface of Rhea.

7.4.3: Possibility of Migration of Chlorine and Hydrazine through Internal Cracks

The detection of simple chlorine and/or hydrazine monohydrate on Rhea's surface is surprising. These molecules are observed on both hemispheres of Rhea for the limited number of disk-resolved observations is also intriguing. I now discuss how these molecules could be linked to a subsurface ocean layer inside Rhea. Aqueous effluents (ammonia, simple chlorine and hydrazine molecules) can propagate from the internal reservoirs through self-propagating cracks in Rhea's brittle ice shell to the surface, where they are detected using far-UV spectroscopy. The cracks and/or fissures could be initiated by large asteroid/comet impacts that have occurred since the time of Rhea's formation. Based on linear elastic fracture mechanics, the equation relating the stress at the tip of a crack to the stress from a large impact that initiated the crack is Crawford and Stevenson (1988)

$$K_{tip} = \sqrt{(\pi l)}\left[K_{imp} - 2g\left(\rho_{aq} - \rho_{ice}\right) l / \pi \right] \qquad (7.15)$$

where l is the lengths of the cracks, ρ_{ice} is the mass density of the ice, ρ_{aq} is the mass density of the liquid in the reservoir, g is the gravitational acceleration, K_{imp} is the initial impact stress, and K_{tip} is the stress at the tip of the crack. Internal cracks inside Rhea could contain an aqueous mixture, which transmit pressure upwards to the tip of the cracks. Propagation of cracks in the interior of Rhea continue to propagate as long as the stress exceeds the critical value for water-ice (6×10^6 N/m$^{3/2}$) (Crawford and Stevenson (1988)).

Linear elastic fracture modelling carried out by Crawford and Stevenson (1988) show that the propagation velocity of internal crack can reach several meters per second. For example, using a propagation velocity of 3 m/s, a crack could propagate a distance of approximately 260 km over a time span of one day. This distance is greater than the depth at which internal liquid reservoirs could exist inside Rhea's interior, based on analytical calculations performed in this thesis.

The density of the aqueous mixture in the internal reservoirs depends on the molecules comprising the liquid mixture and the temperature of the liquid mixture. Assuming that chloromethane, hydrazine (possibly hydrazine derived salts) and ammonia could exist within aqueous reservoirs deep inside Rhea's interior, the density of the liquid should be greater than that for pure water. As ice expands upon freezing, the resulting stresses can initiate cracks within the ice. Overpressures due to the freezing of trapped reservoirs of liquid surrounded by ice could force liquid to the surface of Rhea through cracks (conduits). This occurs because the liquid within the trapped reservoir is incompressible. Analysis of high-resolution imagery of Rhea's surface should therefore be performed to search for indications of past extrusions of these aqueous substances onto Rhea's surface.

7.4.4: Crater Relaxation as Evidence for Endogenic Activity on Rhea

Crater relaxation is the result of surface ice layers responding to an elastic-viscous-plastic like deformation process that occurs as a mechanical response to gravity loaded topography. The rate of the relaxation is a function of the size and thermal structure of the layer(s). The formation of large craters (Figure 7.14) across the surface of Rhea can be used as a probe for layering – i.e. as an indirect method of sampling any internal oceans that may exist in the interior of the satellite. Future work should involve morphological studies of Rhea's large impact craters (Figure 7.14) – i.e. measuring the d/D ratios for any

fresh craters that exist on the satellite's surface, where *d* is the crater depth and *D* is the crater diameter. On icy satellites, such as Europa, a plot of the crater diameter against depth shows a steep falloff in the depth of craters for diameters greater than about 10 km. This indicates relaxation due to an elastic-viscous-plastic like ice layer, most likely the result of recent endogenic activity linked with a subsurface aqueous layer. Two large Jovian satellites, Callisto and Ganymede show no steep falloff in the crater depth for diameters greater than about 10 km, indicative of no (or very little) crater relaxation (Schenk 2002). In other words, on Callisto and Ganymede there are no fresh large craters. The apparent absence of large craters that show no observable evidence of relaxation does not favour recent endogenic activity on these satellites. However, internal oceans located at depths far below the surface on Ganymede and Callisto (<100 km) would not be manifested in the geomorphology of surface features (e.g. large craters that have undergone relaxation, and other tectonic features associated with near-surface endogenic activity). The same scenario may apply to Saturn's second largest moon Rhea.

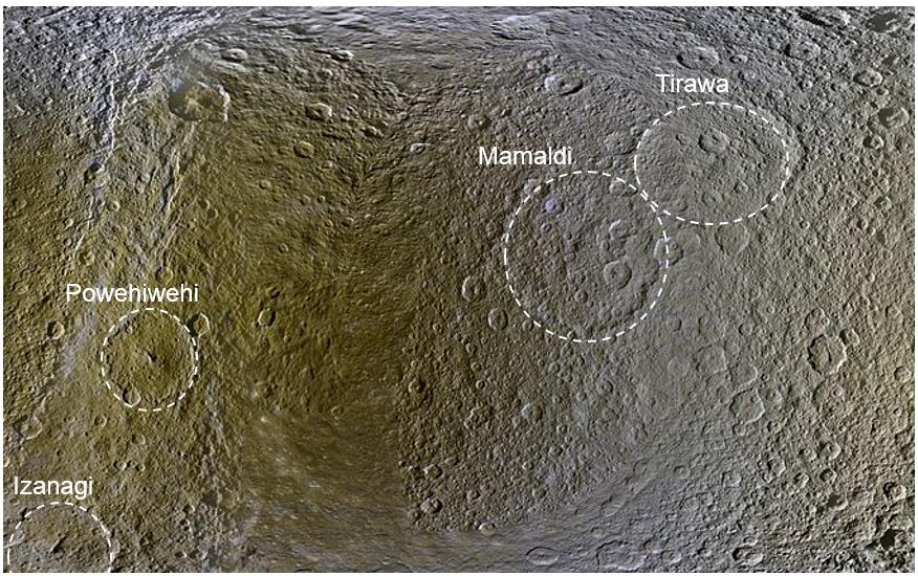

Figure 7.14: The large impact craters "Tirawa (151.7 W, 34.2 N), Powehiwehi (280.4 W, 8.2 S), Mamaldi (180 W, 17 N) and Izanagi (310.2 W, 49.4 S) on Rhea shows signs of possible relaxation. The colour composite Cassini ISS image is constructed using IR-Green-UV filters displayed as Red, Green and Blue. Adapted from colour composite map constructed by Dr. Paul Schenk (LPI, Houston).

7.4.5: Cryovolcanism on Rhea

There is as yet no definite evidence for the existence of features on Rhea's surface associated with current of past cryovolcanism (Wagner *et al*. 2010; Wagner *et al*. 2007). If cryovolcanic activity did occur sometime during Rhea's evolutionary history, it would result from the melting of water-ice and/or complex mixtures of water-ice and non-water-ice volatile components, such as ammonia, hydrazine, brines, and/or simple chlorine molecules. One of the main problems with cryovolcanism associated with the melting of pure water-ice in the interior of an icy moon is the higher density of liquid water upon undergoing a phase transition from a solid to a liquid. This makes it difficult for the extrusion of the liquid through an ice shell of finite thickness onto the surface of Rhea. Since Rhea does not undergo any significant tidal variations, cryovolcanic eruptions due to the over-pressurisation of the liquid reservoirs cannot occur. It is possible to speculate that a recrystallisation or refreezing of a liquid reservoir or ocean could lead to the required pressurisation.

A water-ammonia ice mixture heated by radiogenic isotope decay is another possible driving mechanism for cryovolcanism. However, an extremely high concentration of ammonia would be required to lower the density in the liquid reservoir to the point where the liquid could extrude to the surface, without the requirement for tectonic stresses over large scales to provide an additional external force.

The destabilisation of ammonia in the form of a hydrate by local sources of radiogenic heat could provide an alternative driving mechanism for cryovolcanic activity. However, based on cosmological constraints, only a few percent ammonia is predicted to have been incorporated into the icy satellites during the formation (Hersant *et al*. 2008), and no evidence for the presence of ammonia on the surface of Rhea was found from the analysis of UVIS spectra. However, the detection of hydrazine monohydrate on Rhea

based on analysis of UVIS spectral data implies the presence of ammonia, since there are chemical pathways that lead to the production of hydrazine from water-ice and ammonia. If the wide-spread distribution (i.e. observed on both leading and trailing hemispheres on Rhea) of simple chlorine and/or hydrazine molecules recently detected in Cassini UVIS spectra originate from Rhea's interior, then it is of interest to determine their role, if any, in promoting the extrusion of cryomagma on Rhea.

In summary, the possible detection of either hydrazine monohydrate and chloromethane molecules on Rhea and Dione is intriguing as there has been no prior detections of these chemicals in the outer solar system. Hydrazine monohydrate could be explained via chemical pathways involving the irradiation of ammonia ice, or production on Titan with subsequent transfer to Rhea and Dione. The result that hydrazine monohydrate is not seen in the spectrum of Tethys may be explained by its further radial distance from Titan.

The presence of chloromethane molecules on Rhea and Dione is more difficult to explain, since these would require the existence of a subsurface ocean on these satellites. Numerical models and analytical calculations (presented in 7.9.1) show that it is indeed possible for Rhea and Dione to harbour internal oceans with heat generated from the decay of long-lived radioisotopes acting as the main heat source. However, it is highly unlikely (but not impossible) that chlorine molecules could migrate upward through small fissures/cracks over tens (or even hundreds of km) to the surface layers of Rhea and Dione. For these reasons, the most likely candidate to explain the 184-nm absorption feature seen in far-UV spectra of Rhea and Dione is hydrazine monohydrate.

7.4.6: Summary

This chapter has presented several plausible scenarios that could explain the existance of hydrazine monohydrate and chloromethane molecules observed in the far-UV

spectra of Rhea (and Dione). The existance of chloromethane molecules on the surfaces of these icy satellites requires an endogenic source that originates from a possible interior ocean layer. However, analytical calculations show that it is highly unlikely that chlorine-based molecules could migrate up to the surface over distances of greater than 100 km. In contrast, hydrazine monohydrate can be produced via irradiation of ammonia ice. The source of the ammonia could be indigenous to Rhea, or Saturn's largest moon Titan. Laboratory experiments described in this chapter demonstrate that hydrazine can be synthesized when ammonia ice is irradiated by high-energy particles, and it is shown that hydrazine could, in theory, be transferred from Titan to Rhea (and Dione).

CHAPTER 8

CONCLUSIONS AND FUTURE RESEARCH

8.1 Summary of Results

This final chapter provides a brief summary of the key results of this thesis work and discuss some ideas for future studies. The primary research objectives were the following:

- to determine the presence of any chemicals that may be trapped within the ice matrix;
- to determine the possible source(s) of any chemical species identified;
- to discuss the scientific implications of non-water-ice molecules identified on Rhea and Dione.

The thesis presented the first-time analysis of disk-resolved far-UV spectra of Rhea and Dione acquired by the former Cassini UVIS instrument. The spectra were compared with model spectra produced using newly measured laboratory VUV spectra. The results of the first detailed geochemical survey of the surfaces of Rhea and Dione point to the possible discovery of a new chemical species in the Saturnian system.

From this extensive analysis and comparison with laboratory ice data I have shown that the surface of Rhea is dominated by water-ice of different grain sizes using the technique of derivative spectroscopy. This is demonstrated by a shift of the first-derivative peak relative to the nominal 165-nm absorption edge due to pure water-ice (Chapter 5).

The change in spectral slope of the UV absorption edge is caused by minor impurities of an unknown UV absorber within the water-ice matrix. The two most likely candidates for the minor contaminant in Rhea's surface ice are hydrazine monohydrate

($NH_2NH_2•H_2O$) or simple chloromethane molecules (CCl_4 below water-ice or $CHCl_3$ below water-ice). It is highly unlikely that both of hydrazine and chlorine molecules exist in the ice, since there is no chemical link between these species – i.e. chloromethane molecules cannot be produced from hydrazine and vice versa). None of the other vacuum-UV spectra (e.g. complex organic molecules, esters, alcohols, ozone, ammonia, carbon dioxide, various acids) collected in laboratory experiments matches the 184-nm absorption feature seen in the UVIS spectra.

Two scenarios for an endogenic source of chlorine and hydrazine have been discussed. The first scenario involved a deep subsurface aqueous layer composed of a solution of water, hydrazine and/or chlorine molecules, with minor amounts of ammonia incorporated during Rhea's formation. Over geological timescales, small amounts of chlorine and/or hydrazine may migrate their way to Rhea's surface through cracks/fissures produced by long-term impacts from asteroids and comets. The second scenario is one in which Rhea is an undifferentiated uniform mixture of ice and rock. The chlorine and/or hydrazine molecules are uniformly distributed with minor amounts present in the upper surface layer of Rhea. Both of these scenarios face difficulties, as any subsurface ocean on Rhea would be tens of kilometres deep, and it is highly unlikely that chlorine and/or hydrazine-based salts could migrate to the surface over the large radial distance. The uniform mixture scenario also faces similar difficulty in that it is difficult to explain why chlorine or hydrazine would be present in the outer surface layer that is probed by UV reflectance spectroscopy.

The other, more probable scenario is that chlorine molecules, known to be present in meteorites (Garrison, *et al.*, 2000), were deposited across the surfaces of Rhea and Dione by impacts occurring over geologically long timescales. However, this scenario also faces problems in that it is difficult to explain why the chloromethane molecules would be located beneath a layer of water-ice. One possibility involves the emplacement of the

chlorine molecules during the earlier histories of Rhea and Dione, followed by a thin coating of water-ice deposited on the satellite's surfaces from Saturn's E-ring.

It has also been shown that chlorine molecules (CCl_4 and $CHCl_3$) can be produced from methane and the simple chlorine radical, with the source of the Cl_2 radical originating from an interior liquid layer through cracks and fissures. This scenario was also explored by searching for hydrochloric acid (HCl) in the far-UV reflectance spectra. In addition to CCl_4, HCl is a product from the chemical reaction between CH_4 and Cl_2. However, HCl was not detected on the surfaces of Rhea or Dione thus ruling out this scenario.

The unlikelihood of any of the scenarios described above occurring on Rhea and/or Dione leads to the conclusion that hydrazine monohydrate represents the best candidate to explain the 184-nm absorption feature seen in the Cassini UVIS spectra.

Hydrazine monohydrate is less difficult to explain than chlorine molecules. The irradiation of any ammonia present on the surfaces of Rhea and Dione by charged particles originating from Saturn's magnetosphere results in the dissociation of NH_3 molecules to produce N_2H_2 and hydrazine (N_2H_4). Lyman alpha photons with wavelengths of 121.6 nm can also dissociate NH_3 in its solid phase to synthesise hydrazine. The source of the ammonia could be primordial, incorporated into the interiors of Rhea and Dione during their formation phase, and brought to their surfaces during a period when these satellites had endogenic activity. Evidence for past regional endogenic activity on Rhea is apparent in Cassini ISS imagery in the form of morphological features, including relaxation of large impact craters, curvilinear grabens, and orthogonal ridges. Transfer of ammonia observed in the plumes of Enceladus to Rhea's surface is unlikely due to Rhea's distance from Enceladus and the instability of NH_3 to photo- and radiolytic dissociation. The probability of Lyman alpha photons with a wavelength of 121.6 nm or less (i.e. >10.2 eV) of dissociating ammonia ice molecules is diminished due to the strong absorption of the

Lyman alpha photons by the water-ice matrix. This scenario applies when the NH_3 ice is located beneath a thin layer of water-ice, where the photon path length is short enough to allow sampling by UV or IR spectroscopy. However, instability of the NH_3 molecule to longer wavelength radiation (< 205 nm) can occur within the ice layer leading to its destruction. This may explain why ammonia was not detected on Rhea or Dione over the wavelength region sampled by the Cassini UVIS detector. Ammonia could, in theory, be more stable if it exists on icy satellites in the form of a hydrate mixture - i.e. ammonia in the form of a hydrate minimises the energy in thermodynamic equilibrium. The concentration of hydrazine via chemical reactions between water and ammonia ice is dependent on several factors. These include the dissociation rate by energetic electrons, localised heating due to impacts where ammonia ice is brought to the surface and is vulnerable to destruction by radiolysis, and the high volatility of NH_3 making it more susceptible to sublimation as a result of localised heating. For these reasons, an exogenic source of hydrazine was favoured.

Saturn's largest moon Titan, orbits exterior to Rhea, Dione and Tethys at approximately 20 Saturnian radii with an orbital period of 15.945 (JPL Horizons; https://ssd.jpl.nasa.gov/?horizons) days. Solar UV photons irradiate the Titan's thick atmosphere (composed mostly of N_2 with minor amounts of hydrocarbons; Horst, 2017) leading to the dissociation of methane. This leads to the synthesis of more complex hydrocarbon molecules. Ammonia (NH_3) has also been detected on the surface of Titan based on analysis of Cassini-Huygens probe data. The source of the NH_3 may be cryovolcanism (Lopes 2007). Irradiation of ammonia by solar UV photons can lead to the formation of hydrazine (see Chapter 6 for detailed description of the chemical pathways). If hydrazine can escape from Titan's atmosphere, then it is possible that Rhea could accumulate it as it orbits Saturn. Rough estimates show that the Jean's escape mechanism

is not sufficient to eject hydrazine from Titan's atmosphere. Thus, an alternative ejection mechanism is required to eject N_2H_4 from Titan's atmosphere.

Sputtering is a non-thermal process that is an effective escape mechanism on small solar system bodies (e.g. Titan, Mars …) that have no inherent magnetic fields. This scenario is supported by the observation that the 184-nm absorption feature is seen in Cassini UVIS spectra of Rhea and Dione, but not in spectra of Tethys, which is located furthest from Titan. At the radial distance of Tethys from Titan, hydrazine may be destroyed or diminished to the point where it is below the detection threshold of the UVIS instrument, before reaching Tethys. An alternative scenario is that any hydrazine present on Tethys is covered up by a fresh layer of water-ice grains originating from Enceladus.

Future research work on the details associated with the production, ejection and transfer of hydrazine from Titan's atmosphere are therefore needed to assess whether satellite-to-satellite transfer of materials can explain the possible presence of hydrazine monohydrate on Rhea.

8.2 Future Work

Future space probes equipped with IR and UV imaging spectrometers (i.e. hyper-spectral sensors) could explore the surfaces of Saturn's mid-sized icy moons. The UV hyperspectral instrument (Figure 8.1) would improve upon the previous Cassini UVIS instrument, which was not a true hyperspectral imaging system.

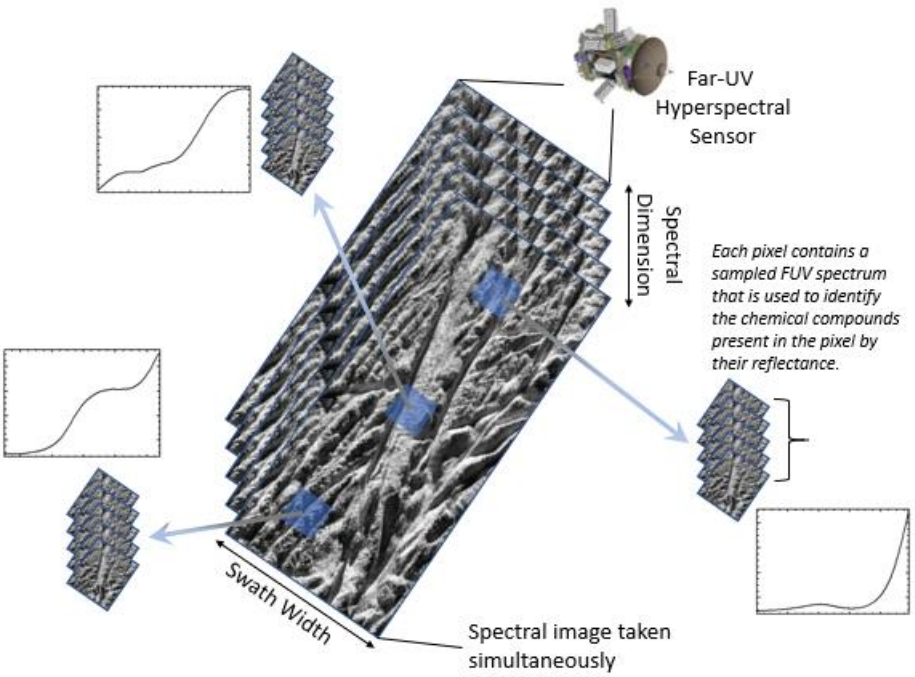

Figure 8.1: Illustration of a future far-UV hyperspectral sensor concept for carrying out a geochemical survey of Saturn's icy satellites. In a true hyperspectral (i.e. imaging spectrometer), each pixel in the image bands contains both spatial and spectral information. The spectral dimension consists of 100s of contiguous spectral bands across the far-UV region of the electromagnetic spectrum. Hyperspectral would allow detailed geochemical maps to be created over selected regions of interest. Diagram created by R. Mark Elowitz.

Advanced spectral mapping approaches, such as principle components analysis, minimum noise fraction transforms, matched filters and spectral feature fitting methods could be used to produce the first-time, high-resolution geochemical survey maps of the entire surfaces of the icy moons. Derivative spectral cubes would accentuate any subtle or weak absorption features that may be present in the spectrum of every pixel in the spectral cube. False-colour composite maps of the icy satellite surfaces based on the derivative spectral cubes would enhance different chemicals mixed in the surface ice. These proven methods have been extensively applied in the terrestrial remote sensing community (Kale *et al*. 2017). The detailed spectral maps would be used to characterise the spatial variability of the abundance of hydrazine monohydrate or chloromethane molecules, which could not be performed using the previous Cassini UVIS data due to limitations resulting from low signal-to-noise.

Hydrazine has several vibrational features in the IR region of the spectrum, which was searched for using IR spectra from the previous Cassini CIRS instrument. Several tantalizing features were seen in the CIRS spectra near wavelengths of the vibrational features, although no firm conclusions could be drawn from the data since the spectral features could have been due to the presence of other hydrocarbon molecules. Future far-UV and IR imaging spectrometers with higher sensitivities could be used to probe the upper ice layers of Rhea, Dione and Tethys for the presence of hydrazine monohydrate or chlorine molecules.

Although the laboratory experiments were able to provide VUV spectra of a variety of organic molecules, halogens and water-ice, no collection of minerals found in carbonaceous chondrite meteorites was performed due to the technical challenges of measuring such samples. To explore whether the 184-nm absorption feature could be due to the presence of phyllosilicates and other minerals associated with chondrites, it is of interest to acquire additional spectra of these samples.

Direct *in-situ* sampling of the surface of Saturn's mid-sized icy satellites using mass spectrometers/gas chromatographs (MS/GC) (Niemann *et al*. 2004) on surface landers could search for the presence of hydrazine or chlorine molecules. These are proven techniques that have been used on the Curiosity rover to detect the presence of dichloromethane on Mars. Future MS/GC instruments with improved sensitivity may be able to verify the presence hydrazine or chloromethane on the Saturn's icy satellites.

References

Acton, C. H., 1996. Ancillary Data Services of NASA's Navigation and Ancillary Information Facility; Planetary and Space Science, Vol. 44, No. 1, pp. 65-70.

Action, C. H., *et al*. 2017. A look toward the future in the handling of space science mission geometry; Planetary and Space Science (2017); DOI 10.1016/j.pss.2017.02.013; http//doi.org/10.1016/j.pss.2017.02.013.

Aruna, *et al.*, 2014. Hydrazine Salts. Inorganic Hydrazine Derivatives: Synthesis, Properties and Applications, pp. 37-82. 10.1002/9781118693599.ch02.

Asplund, M., Grevesse, N., and Sauval, A. J., 2005. ASP Conf. Ser. 336: Cosmic Abundances as Records of Stellar Evolution and Nucleosynthesis, eds., Bash, F. N., & Barnes, T. G., Brigham Young University, 25.

Asplund, M., *et al.*, 2009. The Chemical Composition of the Sun. Annu. Rev. Astron. Astrophys., 47, pp., 481-522.

Anderson, J. D., & Schubert, G., 2007. Saturn's Satellite Rhea is a Homogeneous Mix of Rock and Ice. Geophys. Res. Lett., 34.

Anderson, J. D., & Schubert, G., 2010. Rhea's Gravitational Field and Interior Structure Inferred from Archival Data Files of the 2005 Cassini Flyby. Phys. Earth Planet. Inter., 178 (2), pp. 176-182.

Bagenal, F. & Delamere, P. A., 2011. Flow of Mass and Energy in the Magnetospheres of Jupiter and Saturn. J. Geophys. Res., 116, A05209.

Baragiola, R. A. & Bahr, D. A., 1998. Laboratory Studies of the Optical Properties and Stability of Oxygen on Ganymede. J. Geophys. Res., 103.

Benit, J., Brown, W. L., Maclennan, C. G., 1991. Computer Simulation of Sputtering of Oxygen and Water Molecules from Thin Films of Water Ice. Methods in Phys. Res. B59/60, pp. 68-71.

Bergner, J. B., *et al*. 2018. A Survey of CH_3CN and HC_3N in Protoplanetary Disks. Astrophys. J. 857, 69.

Beuthe, M., *et al*. 2016. Enceladus's and Dione's Floating Ice Shells Supported by Minimum Stress Isostasy. Geophys. Res. Lett., 43, pp. 10088-10096.

Billes, F. and Ziegler, I., 2007. Vibrational Spectroscopy of Phenols and Phenolic Polymers. Theory, Experiment, and Applications. Applied Spectroscopy Reviews, 42, pp. 369-441.

Birnbaum, M. M., 1982. Voyager Spacecraft Images of Jupiter and Saturn. Applied Optics, 21, pp. 214-227.

Biver, N., *et al*., 2015. Ethyl Alcohol and Sugar in Comet C/2014 Q2 (Lovejoy). Sci. Adv., Vol. 1, No. 9.

Boduch, P., *et al*., 2011. Production of Oxidants by Ion Bombardment of Icy Moons in the Outer Solar System. Adv. Astron., Vol. 2011, ID 327641.

Brown, R. H., *et al*., 2004. The Cassini Visual and Infrared Mapping Spectrometer (VIMS) Investigation. Space Sci. Rev., 115, pp. 111-168.

Brown, R. H., *et al*., 2006. Composition and Physical Properties of Enceladus' Surface. Science, 311, pp. 1425-1428.

Buratti, B., 1984. Voyager Disk Resolved Photometry of the Saturnian Satellites. Icarus, 59, pp. 392-405.

Buratti, B. J., et al., 2008. Infrared Photometry of Phoebe from the Cassini Visual Infrared Mapping Spectrometer. Icarus, 193, 309.

Calvin, W. M., Johnson, R. E., & Spencer, J. R., 1996. O_2 pm Ganymede Spectral Characteristics and Plasma Formation Mechanisms. Geophys. Res. Lett., 23, 673.

Canup, R. M., & Ward, W. R., 2006. A Common Mass Scaling for Satellite Systems of Gaseous Planets. Nature, 441, pp. 834-839.

Carbary, *et al*., 2009. L. Shell Distribution of Energetic Electrons at Saturn. Geophys. Res. Lett., 114.

Carbary, J. F., *et al*., 2009. Saturn from Cassini-Huygens, Ed. Dougherty, M. K., Esposito, L. W., and Krimigis, S. M., Springer Science & Business Media.

Carlson, R. W., *et al*., 2009. Europa's Surface Composition. Europa, Univ. of Arizona Press, pp. 283-327.

Carrasco, N., et al., 2018. The Evolution of Titan's High-Altitude Aerosols Under Ultraviolet Irradiation. Nature Astronomy, 2, pp. 489-494.

Cassidy, T. (2010). Radiolysis and Photolysis of Icy Satellite Surfaces: Experiments and Theory. Space Sci. Rev., **153**, pp. 299-315.

Castillo-Rogez, J., 2006. The Internal Structure of Rhea. J. Geophys. Res., 111.

Celliers, P. M., et al., 2018. Insulator-Metal Transition in Dense Fluid Deuterium. Science, 361, pp. 677-682.

Chapman, C. R., 2004. Space Weathering of Asteroid Surfaces. Annu. Rev. Earth Planet Sci., 32, pp. 539-567.

Cheng, A. F., Haff, P. K., Johnson, R. E., & Lanzerotti, L. J., 1986. Interactions of Magnetospheres with Icy Satellite Surfaces. Satellites, pp. 403-436.

Chyba, C. F., 2000. Energy for Microbial Life on Europa. Nature, 403, pp. 381-382; Erratum, Nature 406 (2000), 368.

Ciarniello, M., *et al*., 2011. Hapke Modelling of Rhea Surface Properties Through Cassini-VIMS Spectra. Icarus, 214, pp. 541-555.

Clark, R. N., *et al*., 1984. Saturn's Satellites: Near-infrared Spectrophotometry of the Leading and Trailing Sides and Compositional Implications. Icarus, 58, pp. 265-281.

Clark, R. N., *et al*., 1986. Satellites, Univ. of Arizona Press, Tucson, pp. 437-491.

Clark, R. N., *et al*., 2005. Compositional Maps of Saturn's Moon Phoebe from Imaging Spectroscopy. Nature, 435, pp. 66-69.

Clark, R. N., *et al*., 2008. Compositional Mapping of Saturn's Satellite Dione with Cassini VIMS and Implications of Dark Material in the Saturn System. Icarus, 193, pp. 372-386.

Clark, R. N., *et al*., 2008. Saturn after Cassini-Huygens, London, July, 2008.

Clark, R. N., *et al*., 2009. Reflectance Spectroscopy of Organic Compounds. J. Geophys. Res., 114.

Clark, R. N., et al., 2010. Detection and Mapping of Hydrocarbon Deposits on Titan. J. Geophys. Res., 115.

Clark, R. N., *et al*., 2012. The Surface Composition of Iapetus: Mapping Results from Cassini VIMS. Icarus, 218, pp. 831-860.

Collins, G. C., et al., 2009. Tectonics of the outer planet satellites, in Planetary Tectonics, edited by R. A. Schultz and T. R. Watters, pp. 264–350, Cambridge Univ. Press, Leiden.

Consolmagno, G. J., & Lewis, J. S., 1978. The Evolution of Icy Satellite Interiors and Surfaces. Icarus, 34, pp. 280-293.

Consolmagno, G. J., 1985. Resurfacing Saturn's Satellites: Models of Partial Differentiation and Expansion. Icarus, 64, pp. 401-413.

Cooper, P. D., et al., 2003. Infrared Measurements and Calculations on $H_2O{\cdot}HO$. J. Am. Chem. Soc., 125, pp. 6048-6049.

Cooper, P. D., et al., 2006. Infrared detection of HO_2 and HO_3 radicals in water ice. J. Phys. Chem. A, 110, pp. 7985-7988.

Cooper, P. D., et al., 2008. Radiation Chemistry of $H_2O + O_2$ Ices. Icarus, 194, pp. 379-388.

Coradini, A., et al. 2008. Identification of Spectral Units on Phoebe. Icarus, 193, pp. 233-251.

Cottini, V., *et al*., 2012. Water Vapor in Titan's Stratosphere from Cassini CIRS Far-infrared Spectra. Icarus, 220, pp. 855-862.

Cowell, J., 2004. LASP, University of Colorado.

Cravens, T. E., *et al*., 2011. Electron Energetics in the Enceladus Torus. J. Geophys. Res., 116, A09205.

Crawford, G. D., & Stevenson, D. J., 1988. Gas-driven Water-Volcanism in the Resurfacing of Europa. Icarus, 73, pp. 66-79.

Croft, S. K., Lunine, J. I., and Kargel, J., 1988. Equation of State of Ammonia-Water Liquid – Derivation and Planetological Applications. Icarus, 73, pp. 279-293.

Cruikshank, D. P., *et al*., 2005. A Spectroscopic Study of the Surfaces of Saturn's Large Satellites: H_2O Ice, Tholins, and Minor Constituents. Icarus, 175, pp. 268-283.

Cruikshank, D. P., *et al*., 2007. Surface Composition of Hyperion. Nature, 448, pp. 54-56

Cruikshank, D. P., *et al*., 2008. Hydrocarbons and Saturn's Satellites Iapetus and Phoebe. Icarus, 193, pp. 334-343.

Cruikshank, D. P., *et al*., 2010. Carbon Dioxide on the Satellites of Saturn: Results from the Cassini VIMS Investigation and Revisions to the VIMS Wavelength Scale. Icarus, 206, pp. 561-572.

Cruikshank, D. P., *et al*., 2014. Aromatic and Aliphatic Organic Materials on Iapetus: Analysis of Cassini VIMS Data. Icarus, 233, pp. 306-315.

Cruz-Diaz, G. A., *et al*., 2014. Vacuum-UV Spectroscopy of Interstellar Ice Analogs II. Absorption Cross-Sections of Nonpolar Ice Molecules. Astronomy and Astrophysics, 562, A120.

Cuk, M., Dones, L., and Nesvorny, D., 2016. Dynamical Evidence for a Late Formation of Saturn's Moons. ApJ, 820 97.

Czechowski, L., 2012. Thermal History and Large Scale Differentiation of the Saturn's Satellite Rhea. Acta Geophysica, 60, pp. 1192-1212.

Czechowski, L., & Losiak, A., 2013. Differentiation, Mineralogy and Melting of Rhea. Geophys. Res. Abs., 15, EGU2013-9122.

Daintith, J., 2004. A Dictionary of Chemistry, Oxford University Press, UK.

Dalton, J. B., 2008. Determination of Icy Satellite Surface Composition from Spacecraft Observations: Mission-Critical Cryogenic Laboratory Spectral Measurements. Lunar and Planetary Science XXXIX (2008), Abstract 2395.

Dalton, J. B., et al., 2010. Chemical Composition of Icy Satellite Surfaces. Space Sci. Rev., 153, pp. 113-154.

Dawes, A., *et al*., 2018. Probing the Interaction Between Solid Benzene and Water Using Vacuum Ultraviolet and Infrared Spectroscopy. Physical Chemistry Chemical Physics 20, 15273-15287.

Delitsky, M.L. and Lane, A.L., 1998. Ice Chemistry on the Galilean Satellites. J. of Geophys. Res., 103.

Delitsky, M. L. and Lane, A. L., 2002. Saturn's Inner Satellites: Ice Chemistry and Magnetosphere Effects. J. Geophys. Res.: Planets, 107, E11.

Domingue, D., & Hapke, B., 1989. Fitting Theoretical Photometric Functions to Asteroid Phase Curves. Icarus, 78, 330.

Domingue, D., *et al*., 1991. Europa's Phase Curve: Implications for Surface Structure. Icarus, 90, pp. 30-42.

Domingue, D. L., et al., 1998. Supplementary Analysis of Io's Disk-integrated Solar Phase curve. Icarus, 134, pp. 113-136.

Durham, W. B., 1993. Flow of Ices in the Ammonia-Water System. J. Geophys. Res., 98, pp. 17,667-17,682.

Ellsworth, K., & Schubert, G., 1983. Saturn's Icy Satellites – Thermal and Structural Models. Icarus, 54, pp. 490-510.

Emery, J. P., *et al*., 2005. Near-infrared Spectroscopy of Mimas, Enceladus, Tethys, and Rhea. A&A., 435, pp. 353-362.

Esposito, L. W., *et al*., 2004. The Cassini Ultraviolet Imaging Spectrograph Investigation. Space Sci. Rev., 115, pp. 299-361.

Esposito, L. W., *et al*., 2014. Cassini User's Guide, Laboratory for Atmospheric and Space Physics (LASP).

Estrada, P. R., & Mosqueira, I., 2006. A Gas-Poor Planetesimal Capture Model for the Formation of Giant Planet Satellite Systems. Icarus, 181, pp. 486-509.

Fanale, F. P., *et al*., 1998. Laboratory Simulations of the Chemical Evolution of Europa's Aqueous Phase. Lunar Planet. Sci., 29, abstract 1248.

Filacchione, G., et al., 2016. Seasonal Exposure of Carbon Dioxide Ice on the Nucleus of Comet 67P/Churyumov-Gerasimenko. Science, 354, pp. 1563-1566.

Fortney, J. J. and Hubbard, W. B., 2003. Phase Separation in Giant Planets: Inhomogeneous Evolution of Saturn. Icarus, 164, pp. 228-243.

Gaffey, S. J., *et al*., 1993. Laboratory spectra of Geological Materials, in Remote Geochemical Analysis: Elemental and Mineralogical Composition. Cambridge University Press, Cambridge, pp. 43-78.

Garrison, D., *et al*., 2000. Chlorine Abundances in Meteorites. Meteoritics & Planetary Science, 35, pp. 419-429.

Gittus, J., 1978. Irradiation Effects in Crystalline Solids, Appl. Sci., London, 1978.

Glein, C. R., et al., 2008. The Oxidation State of Hydrothermal Systems on Early Enceladus. Icarus, 197, pp. 157-163.

Glein, C. R. & Shock, E. L., 2010. Sodium Chloride as a Geophysical Probe of a Subsurface Ocean on Enceladus. Geophys. Res. Let., 37.

Gorry, P. A., 1990. General Least-Squares Smoothing and Differentiation by the Convolution (Savitzky-Golay) Method. Anal. Chem, 62, pp. 570-573.

Graedel, T. E. & Keene, W. C., 1996. The Budget and Cycle of Earth's Natural Chlorine. Pure & Appl. Chem., 68, pp. 1689-1697.

Grundy, W. M. and Schmitt, B., 1998. The Temperature-Dependent Near-Infrared Absorption Spectrum of Hexagonal H_2O Ice. J. Geophys. Res., 103, pp. 25809-25822.

Hage, W., *et al*., 1998. Carbonic Acid in the Gas Phase and its Astrophysical Relevance. Science, 279, pp. 1332-1335.

Hall, D. T., *et al*., 1995. Detection of an Oxygen Atmosphere on Jupiter's Moon Europa. Nature, 373, pp. 677-679.

Hansen, G. B., & McCord, T. B., 2004. Amorphous and Crystalline Ice on the Galilean Satellites: a Balance Between Thermal and Radiolytic Processes. J. Geophys. Res., 109, E01012.

Hansen, C. J., *et al*., 2005. Ice Grain Size Distribution: Differences Between Jovian and Saturnian Icy Satellites from Galileo and Cassini Measurements. Bull. Am. Astron. Soc., 37, 729.

Hapke, B., 1981. Bidirectional Reflectance Spectroscopy: 1. Theory. J. Geophys. Res., 86, pp. 3039-3054.

Hapke, B., & Wells, E., 1981. Bidirectional Reflectance Spectroscopy: 2. Experiments and Observations. J. Geophys. Res., 96, pp. 3055-3060.

Hapke, B., 1986. Bidirectional Reflectance Spectroscopy: 4. The Extinction Coefficient and the Opposition Effect. Icarus, 67, pp. 264-280.

Hapke, B., 1993. Theory of Reflectance and Emittance Spectroscopy, 455 pp., Cambridge Univ. Press, New York.

Hawkes, I., & Mellor, M. 1972. Deformation and Fracture of Ice Under Uniaxial Stress. Journal of Glaciology, 11, pp. 103-131.

Hemmingway, D. J., *et al.* 2016. Dione's Internal Structure Inferred from Cassini Gravity and Topography, *47th Lunar and Planetary Science Conference*. Abstract #1314.

Hendrix, A. R., Barth, C. A., and Hord, C. W., 1999. Ganymede's Ozone-Like Absorber: Observations by the Galileo Ultraviolet Spectrometer. J. of Geophys. Res., 104.

Hendrix, A. R. & Hansen, C. J., 2008. Ultraviolet Observations of Phoebe from the Cassini UVIS. Icarus, **193**, pp. 323-333.

Hendrix, A. R., & Johnson, R., 2009. Europa: A new look at Galileo UVS data. Lunar Planet. Sci. Abstract 2526. XL., Houston, TX (CD-ROM).

Hendrix, A. R., Hansen, C. J, and Holsclaw, G. M., 2010. The Ultraviolet Reflectance of Enceladus: Implications for Surface Composition. Icarus, 206, pp. 608-617.

Hendrix, A. R., *et al*., 2018. Icy Saturnian Satellites: Disk-Integrated UV-IR Characteristics and Links to Exogenic Processes. Icarus, 300, pp. 103-114.

Hersant, F., *et al.*, 2008. Interpretation of the Carbon Abundance in Saturn Measured by Cassini. Planet. Space Sci., 56, pp. 1103-1111.

Hillier, J. K., *et al.* 2007. The Composition of Saturn's E Ring. MNRAS, 377, pp. 1588-1596.

Hogenboom, D. L., *et al.*, 1997. The Ammonia-Water System and the Chemical Differentiation of Icy Satellites. Icarus, 128, pp. 171-180.

Horanyi, M, Burns, J. A., and Hamilton, D. P., 1992. The Dynamics of Saturn's E Ring Particles. Icarus, 97, pp. 248-259.

Horst, S. M., 2017. Titan's Atmosphere and Climate. J. Geophys. Res. Planets, 122, pp. 432-482.

Howett, C. J. A., *et al.*, 2014. Thermophysical Property Variations Across Dione and Rhea. Icarus, 241, pp. 239-247.

Howett, C. J., A., *et al*., 2016. Thermal Properties of Rhea's Poles: Evidence for a Meter-Deep Unconsolidated Subsurface Layer. Icarus, 272.

Hsu, Hsiang-Wen, *et al*., 2015. Ongoing Hydrothermal Activities within Enceladus. Nature, 519, pp. 207-210.

Hubbard, W. B. and Smoluchowski, R. 1973. Structure of Jupiter and Saturn. Space Sc. Rev., 14, pp. 599-662.

Huber M.C.E., Pauluhn A., Culhane J.L., Timothy J.G., Wilhelm K., Zehnder A. (eds) Observing Photons in Space. ISSI Scientific Report Series, vol 9. Springer, New York, NY.

Hudson, R. L. & Moore, M. H., 2004. Reactions of Nitriles in Ices Relevant to Titan, Comets, and the Interstellar Medium: Formation of Cyanate Ion, Ketenimines, and Isonitriles. Icarus, 172, pp. 466-478.

Hudson, R. L, et al., 2014. Infrared Spectra and Optical Constants of Astronomical Ices: 1. Amorphous and Crystalline Acetylene. Icarus, 228, pp. 276-287.

Hussmann, H., *et al.* 2006. Subsurface Oceans and Deep Interiors of Medium-Sized Outer Planet Satellites and Large Trans-Neptunian Objects. Icarus, 185, pp. 258-273.

Iess, L., *et al.*, 2007. Gravity Field and Interior of Rhea from Cassini Data Analysis. Icarus, 190, pp. 585-593.

Jacobson, *et al.*, 2006. The Gravity Field of the Saturnian System from Satellite Observations and Spacecraft Tracking Data. AJ, 132, pp. 2520-2526.

Jaumann, R., *et al.*, 2006. High-Resolution CASSINI-VIMS Mosaics of Titan and the Icy Saturnian Satellites. Planet. Sp. Sci., 54, pp. 1146-1155.

Jaumann, R., *et al.*, 2008. Distribution of Icy Particles Across Enceladus' Surface as Derived from Cassini-VIMS Measurements. Icarus, 193, pp. 407-419.

Jaumann, R., *et al.*, 2009. Icy Satellites: Geological Evolution and Surface Processes. In Saturn from Cassini-Huygens (eds. Dougherty, M. K., Esposito, L. W., Krimigis, S. M.) Springer, New York, pp. 637-681.

Jennings, D. E., et al., 2017. Seasonal Evolution of Titan's Stratosphere Near the Poles from Cassini/CIRS Data. Applied Optics, 56, 18, pp. 5274-5294.

Jenniskens, P. & Blake, D. F., 1996. Crystallisation of Amorphous Water Ice in the Solar System. ApJ, 473, pp. 1104-1113.

Jerousek, R. G., et al., 2016. Small Particles and Self-Gravity Wakes in Saturn's Rings from UVIS and VIMS Stellar Occultations. Icarus, 279, pp. 36-50.

Johnson, R. E., 1982. Planetary Applications of Ion Induced Erosion of Condensed-Gas Frosts. Nucl. Instrum. Methods, 198, pp. 147-157.

Johnson, R. E. and Jesser, W. A., 1997. O_2/O_3 Microatmospheres in the Surface of Ganymede. Astrophys. J., 480, L79-L82.

Johnson, R. E. & Quickenden, T. I. (1997). J. Geophys. Res., 102, pp. 10985-10996.
Johnson, R. E., 1998. Sputtering and Desorption from Icy Surfaces, In: Schmitt, B., de Bergh, C., Festou, M. (Eds.). Solar System Ices, 303-334.

Johnson, R. E., 1997. Polar "Caps" on Ganymede and Io Revisited. Icarus, 128, pp. 469-471.

Johnson, R. E. and Leblanc, F., 2001. The Physics and Chemistry of Sputtering by Energetic Plasma Ions. Astrophys. and Space Sci., 277, pp. 259-269.

Johnson, R. E., *et al.*, 2005. Production of Oxygen by Electronically Induced Dissociations in Ice. J. Chem. Phys., 123, 184715.

Johnson, R. E., *et al.*, 2006. The Enceladus and OH Tori at Saturn. ApJ, 644 (2): L137.

Johnson, T. V., 2005. Geology of the Icy Satellites. Space Sci. Rev., 116, pp. 401-420.

Jones, G. H., *et al.*, 2009. Rhea's interaction with Saturn's magnetosphere: Evidence for a plasma source. Paper presented at American Geophysical Union, Fall Meeting 2009, San Francisco.

Jones, T. D. and Lewis, J. S., 1987. Estimated Impact Shock Production of N_2 and Organic Compounds on Early Titan. Icarus, 72, pp. 381-393.

Kale, K. V., *et al*., 2017. A Research Review on Hyperspectral Data Processing and Analysis Algorithms. Proc. Natl. Acad. Sci., India, Sect. A Phys. Sci., 87(4), pp. 541-555.

Kargel, J. S., 1991. Brine Volcanism and the Interior Structures of Asteroids and Icy Satellites. Icarus, 94, pp. 368-390.

Kargel, J. S., 1992. Ammonia-Water Volcanism on Icy Satellites: Phase Relations at 1 Atmosphere. Icarus, 100, pp. 556-574.

Kartal, B., *et al*. 2011. Molecular Mechanism of Anaerobic Ammonium Oxidation. Nature, 479, pp. 127-130.

Kempf, S., 2005. Composition of Saturnian Stream Particles. Science, 307, pp. 1274-1276.

Kempf, S., *et al.*, 2010. How the Enceladus Dust Plume Feeds Saturn's E Ring. Icarus, 206, pp. 446-457.

Klinger, J., 1981. Some Consequences of a Phase Transition of Water Ice on the Heat Balance of Comet Nuclei. Icarus, 47, pp. 320-324.

Kochubey, S. M. and Kazantsev, T. A. 2012. Derivative Vegetation Indices as a New Approach in Remote Sensing of Vegetation. Front. Earth Sci., 6(2), pp. 188-195.

Koskinen, T. T., *et al*. 2011. The Mesosphere and Lower Thermosphere of Titan Revealed by Cassini/UVIS Stellar Occultations. Icarus, **216**, pp. 507-534.

Kouchi, A. and Kuroda, T., 1990. Amorphisation of Cubic Ice by Ultraviolet Irradiation. Nature, 344, pp. 134-135.

Lange, M. A., & Ahrens, T. J., 1987. Impact Experiments in Low-Temperature Ice. Icarus, 69, pp. 506-518.

Lanzerotti, L. J., *et al*. 1984. Production of Ammonia-Depleted Surface Layers on the Saturnian Satellites by Ion Sputtering. Nature, 312, pp. 139-140.

Leto, G., et al., 2005. The Reflectance Spectrum of Water Ice: Is the 1.65 μm Peak a Good Temperature Probe? Mem. Soc. Astron. Ital., 6 (Suppl.), pp. 57-62

Lewis, J. S., 1972. Low Temperature Condensation from the Solar Nebula. Icarus, 16, pp. 241-252.

Lide, D. R., 2005. CRC Handbook of Chemistry and Physics (86 ed.). Boca Raton, Florida: CRC Press.

Liu, Y., et al., 2016. End-Member Identification and Spectral Mixture Analysis of CRISM Hyperspectral Data: A Case Study on Southwest Melas Chasma, Mars. J. Geophys. Res. Planets, 121, pp. 2004-2036.

Lodders, K., 2003. Solar System Abundances and Condensation Temperatures of the Elements. ApJ, 591, 1220.

Loeffler, M. J. and Baragiola, R. A., 2010. Photolysis of Solid NH_3 and NH_3-H_2O Mixtures at 193 nm. J. Chem. Phys., 133, 214506.

Lopes, R. M. C., *et al.*, 2007. Cryovolcanic Features on Titan's Surface as Revealed by the Cassini Titan Radar Mapper. Icarus, 186, pp. 395-412.

Lupo, M. J., & Lewis, J. S., 1979. Mass-Radius Relationships in Icy Satellites. Icarus, 40, pp. 157-170.

Mandt, K. E., *et al*., 2014. Protosolar Ammonia as the Unique Source of Titan's Nitrogen. ApJL., 788: L24.

Martens, H. R., *et al.*, 2008. Observations of Molecular Oxygen Ions in Saturn's Inner Magnetosphere. Geophys. Res. Lett., 35, p. L20103.

Martinez, *et al*., 2007. Hybrid Molecular Ions Emitted from CO-NH_3 Ice Bombarded by Fission Fragments. Int. J. Mass Spectrom., 262, pp. 195-202.

Martonchik, J. V., Orton, G. S., and Appleby, J. F., 1984. Optical Properties of NH_3 Ice from the Far Infrared to the Near Ultraviolet. Appl. Opt., 23, pp. 541-547.

Mason, N. J., Dawes, A., Holton, P. D., *et al.*, 2006. VUV Spectroscopy and Photo-Processing of Astrochemical Ices: An Experimental Study. Faraday Discussions, 133, 311.

Mastrapa, R. E. and Brown, R. H., 2006. Ion Irradiation of Crystalline H_2O – Ice: Effect on the 1.65-µm Band. Icarus, 183, pp. 207-214.

Mastrapa, R. M., *et al*., 2008. Optical Constants of Amorphous and Crystalline H_2O-Ice in the Near Infrared from 1.1 to 2.6 µm. Icarus, 197, pp. 307-320.

Mastrapa, R., M., *et al.*, 2009. Optical Constants of Amorphous and Crystalline H_2O-Ice: 2.5-22 µm (4000-455 cm^{-1}) Optical Constants of H_2O-Ice. ApJ, 701, pp. 1347-1356.

Matson, D. L. and Brown, R. H., 1989. Solid-State Greenhouse and Their Implications for Icy Satellites. Icarus, 77, pp. 67-81.

McClintock, W. E., *et al.*, 1993. Optical Design of the Ultraviolet Imaging Spectrograph for the Cassini Mission to Saturn. Opt. Eng., 32, 3038.

McClintock, W. E., Rottman, G. J., & Woods, T. N., 2000. Proceedings of the SPIE, Earth Observing System V, 4135, pp. 225-234.

Melosh, H. J., 1989. Impact Cratering, 245pp, Oxford Univ. Press.
Milligan, D. E., & Jacox, M. E., 1965. J. Chem. Phys., 43, 4487.

Moore, R. M., 2004. Methyl Bromide and Methyl Chloride in the Southern Ocean. J. Geophys. Res., 109.

Moore and Hudson, 2000. IR Detection of H_2O_2 at 80 K in Ion-Irradiated Laboratory Ices Relevant to Europa. Icarus, 145, pp. 282-288.

Moore, J. M., 1984. The Tectonic and Volcanic History of Dione. Icarus, 59, pp. 205-220.

Moore, J. M. & Schenk, P. M., 2007. Topography of Endogenic Features on Saturnian Mid-Sized Satellites. Lunar Planet. Sci. Conf. XXXVIII, 2136.

Morrison, D., 1982. The Satellites of Jupiter and Saturn. ARA&A, 20, pp. 469-495.

Mumma, M. J., et al., 2003. Remote Infrared Observations of Parent Volatiles in Comets: A Window on the Early Solar System. Adv. Space Res., 31, pp. 2563-2575.

Nelson, R. M. and Lane, A. L., 1987. Planetary Satellites. Exploring the Universe with the IUE Satellite. Astrophysics and Space Science Library, Vol. 129, Springer, Dordrecht, pp. 67-99.

Nicholson, P. D., et al., 2000. Saturn's Rings I: Optical Depth Profiles from the 28 Sgr Occultation. Icarus, 145, pp. 474-501.

Nimmo, F., 2004. Stresses Generated in Cooling Viscoelastic Ice Shells: Application to Europa. J. Geophys. Res., 109, E12001.

Nimmo, F. B., et al., 2010. Geophysical Implications of the Long-Wavelength Topography of Rhea. J. Geophys. Res., 115.

Nna-Mvondo, D., et al., 2008. Experimental Impact Shock Chemistry on Planetary Icy Satellites. Icarus, 194, pp. 822-835.

Noland, M. J., *et al.*, 1974. Six-Colour Photometry of Iapetus, Titan, Rhea, Dione, and Tethys. Icarus, 23, pp. 334-354.

Noll, K. S., *et al.*, 1996. Detection of Ozone on Ganymede. Science, 273, pp. 341-343.

Noll, K. S., *et al.*, 1997. Detection of Ozone on Saturn's Satellites Rhea and Dione. Nature, 388, pp. 45-47.

Oliver, M., et al., 2015. Methane Clathrates in the Solar System. Astrobiology, 15 (4), pp. 308-326.

Orlando, T. M. and Sieger, M. T., 2003. The Role of Electron-Stimulated Production of O_2 from Water Ice in the Radiation Processing of Outer Solar System Surfaces. Surface Science, 528, pp. 1-7.

Ozaki, Y., *et al*. 2012. Far-Ultraviolet Spectroscopy in the Solid and Liquid States: A Rev. Appl. Spectrosc., 66, pp. 1-25.

Paranicas, C., *et al.*, 2010. Asymmetries in Saturn's Radiation Belts. J. Geophys. Res., 115, 7216.

Parker F.S. (1971) Amides and Amines. In: Applications of Infrared Spectroscopy in Biochemistry, Biology, and Medicine. Springer, Boston, MA.

Pavithraa, S., *et al.* 2018. Vacuum Ultraviolet Photoabsorption of Prime Ice Analogues of Pluto and Charon. Molecular and Biomolecular Spectroscopy, 190, pp. 172-176.

Plescia, J. B., 1983. The Geology of Dione. Icarus, 56, pp. 255-277.

Phillips, C. B., *et al.*, 2012. Stereo Imaging, Crater Relaxation, and Thermal Histories of Rhea and Dione. Lunar Planet. Sci. Conf. XLIII, 2571.

Porco, C. C., *et al*., 2004. Cassini Imaging Science: Instrument Characteristics and Anticipated Scientific Investigations at Saturn. Space Sci. Rev., 115, pp. 363-497.

Postberg, F., *et al*., 2008. The E-ring in the Vicinity of Enceladus II. Probing the Moon's Interior – The Composition of E-ring Particles. Icarus, 193, pp. 438-454.

Postberg, F., *et al.*, 2009. Sodium Salts in E-ring Ice Grains from an Ocean Below the Surface of Enceladus. Nature, 459, pp. 1098-1101.

Rashmi, S., *et al*., 2014. International Journal of Innovative Science, Engineering & Technology, Vol. 1 Issue 4., June 2014.

Roatsch *et al.*, 2009. Cartographic Mapping of the Icy Satellites Using ISS and VIMS Data. Saturn from Cassini Huygens, pp. 763-781.

Rocard, F., *et al.*, 1986. Erosion of Ices: Physical and Astrophysical Discussion. Radiation Effects, 99, 97.

Roessler, K., 1991. Solid-State Astrophysics, Bussoletti, E., Strazzula, G., eds., North Holland, Amsterdam.

Rojas, F. S., et al. 1988. Derivative Ultraviolet-Visible Region Absorption Spectrophotometry and its Analytical Applications. Talanta, Vol. 35, No. 10, pp. 753-761.

Ross, J. E., & Aller, L. H., 1976. The Chemical Composition of the Sun. Science, 191, pp. 1223-1229.

Sack, N., et al., 1992. The Effect of Magnetospheric Ion Bombardment on the Reflectance of Europa's Surface. Icarus, 100, pp. 534-540.

Saur, J., Neubauer, Stobel, D. F., and Neubauer, F. M., 1998. Interaction of the Jovian Magnetosphere with Europa: Constraints on the Neutral Atmosphere. J. Geophys. Res., 103.

Savitzky, A. & Golay, M. J., 1964. Smoothing and Differentiation of Data by Simplified Least Squares Procedures. Anal. Chem., 36, pp. 1627-1639.

Schenk, P. M., 1989. Crater Formation and Modification on the Icy Satellites of Uranus and Saturn: Depth/Diameter and Central Peak Occurrence. J. Geophys. Res., 94, pp. 3813-3832.

Schenk, P. M., 2002. Thickness Constraints on the Icy Shells of the Galilean Satellites from a Comparison of Crater Shapes. Nature, 417, pp. 419-421.

Schenk, P. M., & Moore, J. M., 2007. Impact Crater Topography and Morphology on Saturnian Mid-Sized Satellites. 38th Lunar and Planetary Science Conference, Houston, abstract # 2305.

Schenk, P., *et al*., 2011. Plasma, Plumes and Rings: Saturn System Dynamics as Recorded in Global Colour Patterns on its Midsize Icy Satellites. Icarus, 211, pp. 740-757.

Scherzer, B. M. U., 1983. Development of surface topography due to gas ion implantation, in *Sputtering by Particle Bombardment II, edited by R. Behrisch*, pp. 271-342, Springer-Verlag, New York, 1983.

Schmitt, B., *et al.*, 1998. Optical Properties of Ices from UV to Infrared. In: Schmitt B, de Bergh C, Festou M (eds) Solar System Ices, Kluwer Academic, Norwell, pp. 199-240.

Schriver, L., *et al*., 1990. Infrared Spectroscopic and Photochemical Study of Water-Ozone Complexes in Solid Argon. Chem. Phys., 140, pp. 429-438.

Schubert, T., Spohn, T., & Reynolds, R. T., 1986. Thermal Histories, Compositions and Internal Structures of the Moons of the Solar System. Satellites, Univ. of Arizona Press, Tucson, pp. 224-292.

Shin, K., *et al*., 2013. Methanol Incorporation in Clathrate Hydrates and the Implications for Oil and Gas Pipeline Flow Assurance and Icy Planetary Bodies. Proc. Natl. Acad. Sci. U. S. A., 110(21): 8437-8442.

Shizgal, B. D. and Arkos, G. G., 1996. Nonthermal Escape of the Atmospheres of Venus, Earth, and Mars. Rev. of Geophys., 34, pp. 483-505.

Sieger, M. T., *et al*., 1998. Production of O_2 on Icy Satellites by Electronic Excitation of Low-Temperature Water Ice. Nature, 394, pp. 554-556.

Singanahally, T. A. and Patil, K. C., 2014. Patil, K. C., and Tanu Mimani Rattan. Inorganic Hydrazine Derivatives: Synthesis, Properties and Applications, John Wiley & Sons, Incorporated, 2014. ProQuest Ebook Central, https://ebookcentral.proquest.com/lib/open/detail.action?docID=1602920.

Sivaraman, B., *et al*. 2008. Electron, Proton and Ion Induced Molecular Synthesis and VUV Spectroscopy of Interstellar Molecules in the Ice Phase. Organic Matter in Space, Proceedings IAU Symposium No. 251.

Sivaraman, B., *et al*. 2012. VUV Spectroscopy of Formamide Ices. Chem. Phys. Lett., 554, pp. 57-59.

Sivaraman, B., *et al*. 2014. Vacuum Ultraviolet Photoabsorption of Pure Solid Ozone and its Implication on the Identification of Ozone on the Moon. Chem. Phys. Lett., 603, pp. 33-36.

Sivaraman, B., *et al*. 2014. Electron Impact Dissociation and VUV Photoabsorption of Frozen Formamide. Chem. Phys. Lett., 608, pp. 404-407.

Sivaraman, B., *et al*. 2016. Vacuum Ultraviolet Photoabsorption Spectra of Nitrile Ices for Their Identification on Pluto. ApJ, 825, 141.

Smith, B. A., *et al*., 1981. Encounter with Saturn: Voyager 1 Imaging Science Results. Science, 212, pp. 163-191.

Smith, B. A., *et al*., 1982. A New Look at the Saturn System: The Voyager 2 Images. Science, 215, pp. 504-537.

Smith, H. T., *et al*. 2008. Enceladus: A Potential Source of Ammonia Products and Molecular Nitrogen for Saturn's Magnetosphere. J. Geophys. Res., 113.

Spencer, J. R., *et al.*, 1989. Systematic Biases in Radiometric Diameter Determinations. Icarus, 78, pp. 337-354.

Spencer, J. R., 1989. A Rough-Surface Thermophysical Model for Airless Planets. Icarus, 83, pp. 27-38.

Spencer, J. R., Calvin, W. M., & Person, M. J., 1995. Charge-Coupled Device Spectra of the Galilean Satellites: Molecular Oxygen on Ganymede. J. Geophys. Res., 100, pp. 19049-19056.

Spencer, *et al.*, 2009. Enceladus: a cryovolcanic active satellite, Saturn from Cassini-Huygens, (M. Dougherty, L. Esposito and S. Krimigis, (eds.)), Springer, 2009.

Squyres, S. W., *et al*. 1988. Accretional Heating of the Satellites of Saturn and Uranus. J. Geophys. Res., 93, pp. 8779-8794.

Stedwell, Corey N. and Nicolas C Polfer. "Chapter 1 Spectroscopy and the Electromagnetic Spectrum." (2017).

Stephan, K.., *et al.*, 2010. Specular Reflection on Titan: Liquids in Kraken Mare. Geophys. Res. Lett. 37.

Stephan, K., *et al*., 2010. Dione's Spectral and Geological Properties. Icarus, 206, pp. 631-652.

Stephan, K., *et al.*, 2012. The Saturnian Satellite Rhea as Seen by Cassini VIMS. Planetary Sp. Sci., 61, pp. 142-160.

Stern, S. A., *et al*., 2007. Alice: The Rosetta Ultraviolet Imaging Spectrograph. Space Sci. Rev., 128, pp. 507-527.

Stern, S. A., *et al*., 2008. ALICE: The Ultraviolet Imaging Spectrograph Aboard the New Horizons Pluto-Kuiper Belt Mission. Space Sci. Rev., 140, pp. 155-187.

Sunshine, J. M., and Pieters, C. M., 1990. Extraction of Compositional Information from Olivine Reference Spectra: A New Capability for Lunar Exploration. Lunar and Planetary Science XXI, pp. 962-963.

Teolis, B. D., *et al*., 2010. Cassini Finds and Oxygen-Carbon Dioxide Atmosphere at Saturn's Icy Moon Rhea. Science, 330, 1813.

Teolis, B. D., *et al*. 2011. Formation, Distribution and loss of Rhea's O_2 – CO_2 Exosphere, 42nd Lunar and Planetary Science Conference, 2663.

Teolis, B. D., & Waite, J. H., 2016. Dione and Rhea Seasonal Exospheres Revealed by Cassini CAPS and INMS. Icarus, 272, pp. 277-289.

Tokano, T., *et al*., 2006. Methane Drizzle on Titan. Nature, 442, pp. 432-435.

Tortora, P., *et al*. 2016. Rhea Gravity Field and Interior Modelling from Cassini Data Analysis. Icarus, 264, pp. 264-273.

Tsai, F. and Philpot, W., 1998, Derivative Analysis of Hyperspectral Data. Remote Sens. Environ., 66:41-51.

Verbiscer, A. and Veverka, J., 1992. Mimas: Photometric Roughness and Albedo Map. Icarus 99, pp. 63-69.

Verbiscer, A. J., *et al*., 2005. The Opposition Surge of Enceladus: HST Observations 338-1022 nm. Icarus, 173, pp. 66-83.

Verbiscer, A. J., *et al*., 2006. Near-Infrared Spectra of the Leading and Trailing Hemispheres of Enceladus. Icarus, 182, pp. 211-223.

Vidal, R. A., *et al*., 1997. Oxygen on Ganymede: Laboratory Studies. Science, 276, pp. 1839-1842.

Villanueva, G. L., Smith, M. D., Protopapa, S., Faggi, S., Mandell, A. M., Planetary Spectrum Generator: an accurate online radiative transfer suite for atmospheres, comets, small bodies and exoplanets, Journal of Quantitative Spectroscopy and Radiative Transfer, Volume 217, pp. 86-104 (2018).

Vinatier, S., *et al*., 2007. Vertical Abundance Profiles of Hydrocarbons in Titan's Atmosphere at 15° S and 80°N Retrieved from Cassini/CIRS Spectra. Icarus, 188, pp. 120-138.

Vinatier, S., *et al*., 2010. Analysis of Cassini/CIRS Limb Spectra of Titan Acquired During the Nominal Mission: 1. Hydrocarbons, Nitriles and CO_2 Vertical Mixing Ratio Profiles. Icarus, 205, pp. 852-866.

Wagner, J. K., *et al.*, 1987. Atlas of Reflectance Spectra of Terrestrial, Lunar, and Meteoritic Powders and Frosts from 92 to 1800 nm. Icarus, 69, pp. 14-28.

Wagner, R. G., *et al.*, 1997. The Global Geology of Rhea: Preliminary Implications from the Cassini ISS Data. Lunar Planet. Sci. Conf. XXXVIII, 1958.

Wagner, R. J. *et al*., 2005. The Geology of Saturn's Satellite Dione Observed by Cassini's ISS Camera. Bull. Am. Astron. Soc., 37 (3), 701 (Abstr. 36-02).

Wagner, R. J., et al., 2010. The Geology of Rhea. A First Look at the ISS Camera Data from Orbit 121 (Nov. 21, 2009) in Cassini's Extended Mission. Lunar Planet. Sci. Conf. XLI, LPI Contribution No. 1533, p. 1672.

Waite, J. H., *et al.*, 2006. Cassini Ion and Neutral Mass Spectrometer: Enceladus Plume Composition and Structure. Science, 311, pp. 1419-1422.

Waite, J. H., et al., 2009. Liquid Water on Enceladus from Observations of Ammonia and ^{40}Ar in the Plume. Nature 460, pp. 487-490.

Waite, H. H., et al., 2011. Enceladus' Plume Composition. EPSC-DPS2011-61-4, 2011.

Wallerstein, G., et al., 1997. Synthesis of the Elements in Stars: Forty Years of Progress. Rev. Mod. Phys., 69, pp. 995-1084.

Warren, S. G., 1982. Optical Properties of Snow. Rev. Geophys. Space Phys., 20, pp. 67-89.

Warren, S. G., 1984. Optical Constants of Ice from the Ultraviolet to the Microwave. Appl. Opt., 23, pp. 1206-1225.

Warren, S. G. and Brandt, R. E., 2008. Optical Constants of Ice from the Ultraviolet to the Microwave: A Revised Compilation. J. Geophys. Res., 113, D14220.

Whalley E., 1968. Structures of Ice and Water as Investigated by Infrared Spectroscopy. In: Baer W.K., Perkins A.J., Grove E.L. (eds) Developments in Applied Spectroscopy. Developments in Applied Spectroscopy, vol 6. Springer, Boston, MA.

White, D. W., Mastrapa, R. M. E., Sandford, S. A., 2012. Laboratory Spectra of CO_2 Vibrational Modes in Planetary Ice Analogues. Icarus, 221, pp. 1032-1042.

White, O. L., et al., 2013. Impact Basin Relaxation on Rhea and Iapetus and Relation to Past Heat Flow. Icarus 223, pp. 699-709.

White, O. L., et al., 2017. Impact Crater Relaxation on Dione and Tethys and Relation to Past Heat Flow. Icarus, 288, pp. 37-52.

Yoder, C. F., Astrometric and geodetic properties of Earth and the solar system, in Global Earth Physics, T. J. Aherns, ed., AGU, 1-32, 1995.

Zastrow, M., Clarke, J. T., Hendrix, A. R., and Noll, K. S., 2012. UV Spectrum of Enceladus. Icarus, 220, pp. 29-35.

Zheng, W., Jewitt, D., Kaiser, R. I., 2006. Formation of Hydrogen, Oxygen, and Hydrogen Peroxide in Electron-Irradiated Crystalline Water Ice. ApJ., 639, pp. 534-548.

Zheng, W., *et al.*, 2008. Formation of Nitrogen and Hydrogen-Bearing Molecules in Solid Ammonia and Implications for Solar System and Interstellar Ices. ApJ., 674, pp. 1242-1250.

Zolotov, M. Yu. & Shock, E. L., 2001. Composition and Stability of Salts on the Surface of Europa and Their Oceanic Origin. J. Geophys. Res., 106, pp. 32815-32827.

Appendix A: Candidate list of molecules suspected to exist in the interiors and on the surfaces of icy satellites

Water	H_2O
Deuterium Oxide	D_2O
Heavy Water	HDO
Hydrogen Peroxide	H_2O_2
Oxygen	O_2
Carbon Monoxide	CO
Carbon Dioxide	CO_2
Carbon Trioxide	CO_3
Formyl Ion	HCO
Formaldehyde	H_2CO
Formic Acid	H_2CO_2
Carbonic Acid	H_2CO_3
D-Carbonic Acid	D_2CO_3
Carbon Suboxide	C_3O_2
Methanol	CH_3OH
Ethanol	CH_3CH_2OH
Acetone	$CH_{32}CO$
Methyl Formate	$HCOOCH_3$
Glycolaldehyde	CH_2OHCHO
Ethyl Acetate	$CH_3CO_2CH_2CH_3$
Dimethyl Carbonate	$OCH_{32}CO$
Ethylene Glycol	CH_2OH_2
Methane	CH_4
Acetylene	C_2H_2
Ethylene	C_2H_4
Ethane	C_2H_6
Propane	C_3H_8
Propdiene	C_3H_4
1,3-Butadiyne	C_4H_2
Carbon Trimer	C_3
Cysteinesulfonic Acid	OCS
Nitrogen Oxide	NO
Nitrogen	N_2
Ammonia	NH_3
Ammonia Hydrate	$NH_3{\cdot}H_2O$
Hydrazine	N_2H_4
Hydrazine Monohydrate	$NH_2NH_2{\cdot}H_2O$
Carbon Tetrachloride	CCl_4
Methylene Chloride	CH_2Cl_2
Tetrachloromethane	$CHCl_3$
Hydrogen Isocyanide	HNC
Hydrogen Cyanide	HCN
Poly-HCN	poly HCN
Acetonitrile	CH_3CN

Ethylamine	CH_3CH_2CN
Vinyl Cyanide	CH_2CHCN
Propinonitrile	C_2H_5CN
Methyleyanoacetylene	CH_3C_3N
Cyanoacetylene	HC_3N
Cyanogen	C_2N_2
Dicyanoacetylene	C_4N_2
Ammonium Nitrate	NH_4NO_3
Hydroxylamine	NH_2OH
Cyanate Ion	OCN-
…	XCN-
Isocyanic Acid	HNCO
Methyl Isocyanate	CH_3NCO
Formamide	$HCONH_2$
…	HCO_2NH_2
Urea	H_2NCONH_2
Thiourea	H_2NCSNH_2
…	$HCOO^- + NH_4$
Ammonium Hydrosulphide	NH_4HS
Thiocyanic Acid	HNCS, HSNC
Hydrogen Sulphide	H_2S
Sulphur Dioxide	SO_2
Sulphur Trioxide	SO_3
Sulphuric Acid	H_2SO_4
Sulphur	S_2
Methyl Clathrate	$CH_4 \cdot H_2O$
CO_2 Clathrate	$CO_2 \cdot H_2O$
H_2O·graphite	…
Bisodium Sulphate	Na_2SO_4
Bisodium Carbonate	Na_2CO_3
Calcium Carbonate	$CaCO_3$
Magnesium Sulphate	$MgSO_4$
Dodecahydrate	$MgSO_4 \cdot 12H_2O$
Epsomite	$MgSO_4 \cdot 7H_2O$
Hexahydrite	$MgSO_4 \cdot 6H_2O$
Pentahydrite	$MgSO_4 \cdot 5H_2O$
Starkeyite	$MgSO_4 \cdot 4H_2O$
Bassanite	$2CaSO_4 \cdot H_2O$
Beryl	$Be_3Al(SiO_2)_6$
Bloedite	$Na_2Mg(SO_4)_2 \cdot 4H_2O$
Bronzite	$(Mg,Fe^{2+})_2 \cdot (SiO_3)_2$
Dolomite	$(Ca,Mg)(CO_3)_2$
Burkeite	$Na_6CO_3(SO_4)_2$
Calcite	$CaCO_3$
Cordierite	$Mg_2Al_4Si_5O_{18}$
Eugsterite	$Na_4Ca(SO_4)_3 \cdot 2H_2O$
Gaylussite	$Na_2Ca(CO_3)_2 \cdot 5H_2O$
Goethite	FeOOH
Gypsum	$CaSO_4 \cdot 2H_2O$
Hematite	Fe_2O_3
Jarosite	$KFe_3(SO_4)_2(OH)_6$
Kaolinite	$Al_2Si_2O(OH)_4$

Leonite	$K_2Mg(SO_4)_2 \cdot 4H_2O$
Lepidocrocite	FeOOH
Magnetite	$Fe(II)Fe(III)_2O_4$
Mirabilite	$Na_2SO_4 \cdot 10H_2O$
Montmorillonite	$(Na,Ca)_{0.3}(Al,Mg)_2Si_4O_{10}(OH)_2 \cdot nH_2O$
Nahcolite	$NaHCO_3$
Nontronite	$Na_{0.3}Fe^{3+}{}_2Si_3AlO_{10}(OH)_2 \cdot 4H_2O$
Natron	$Na_2CO_3 \cdot 10H_2O$
Olivine	$(Mg,Fe)_2SiO_4$
Palagonite	…
Iron Sulphide	FeS
Pyroxene Bronzite	$Mg_{0.8}Fe_{0.2}SiO_3$
Iron Oxide	FeO
Plagioclase	$(Na,Ca)(Si,Al)_4O_8$
Picromerite	$K_2Mg(SO_4)_2 \cdot 6H_2O$
Amorphic SiO_2 Quartz	SiO_2
Pirssonite	$Na_2Ca(CO_3)_2 \cdot 2H_2O$
Amorphic Pyroxene	$(Mg,Fe)SiO_3$
Polyhalite	$K_2Ca_2Mg(SO_4)_4 \cdot 2H_2O$
Pyrophyllite	$Al_2Si_4O_{10}(OH)_2$
Ortho-Pyroxene	$XY(Si,Al)_2O_6$
Clino-Pyroxene	$XY(Si,Al)_2O_6$
Serpentine	…
Syngenite	$K_2Ca(SO_4)_2 \cdot H_2O$
Tholin	e.g., $C_3H_5N_2$
Kerogen	$C_{200}H_{300}SN_5O_{11}$
Trona	$Na_3CO_3HCO_3 \cdot 2H_2O$

Molecules highlighted in red colour denote new candidate molecules (possibly) detected on Rhea's surface. Table adapted and amended from Dalton, J. B. Lunar and Planetary Science XXXIX (2008). Table updated by R. Mark Elowitz.